Spodumene textural variations in a deformed LCT-type pegmatite. A case study from the Musha-Ntunga area, Rwanda

Jolan Acke[1,4], Daniel Kwizera[3], Alastair Goodship[3], Stijn Dewaele[4], Renata Barros[5], Christian Burlet[5], Simon Nachtergaele[6], Anouk Borst[1,2]

[1] Department of Earth and Environmental Sciences, KU Leuven, Leuven-Heverlee, Belgium

[2] Geodynamics and mineral resources, Royal Museum for Central Africa, Tervuren, Belgium

[3] PIRAN Rwanda Ltd, St Peters Port, Guernsey, UK

[4] Mineralogy & Petrology Research Group, University of Ghent, Belgium

[5] Geological Survey of Belgium, Brussels, Belgium, Royal Belgian Institute of Natural Sciences, Brussels, Belgium

[6] Department of Urban and Environmental Engineering, University of Liège, Liège, Belgium

Abstract. Spodumene, the main lithium-bearing mineral of the Musha-Ntunga LCT-type pegmatite deposit in Rwanda displays a variety of textures. Two distinct groups are identified based on grain size, habit, textural intergrowth features, optical properties and associated mineral assemblages. Contrary to the uniform euhedral primary group 1 spodumene with thin rims of symplectitic quartz-spodumene intergrowths (SQUI), group 2 spodumenes display a variety of textures which are linked to primary spodumene deformation, recrystallisation and alteration. Under shear stress, spodumene tends to deform in a brittle way causing large grains to break down along weak spots, such as cleavage planes. In addition, fluid influx along grain boundaries and cleavage planes can modify the spodumene composition and texture. LIBS analyses confirmed that lithium is leached from primary spodumene crystals along grain boundaries and cleavage planes. In this study, the interplay between both mechanisms is investigated to determine the (re)distribution of lithium.

1 Introduction

Granitic pegmatites are complex coarse-grained rocks that generally form from the last bits of a solidifying granitic melt (London 2018). In that process, different economically valuable metals such as lithium, tantalum, niobium and tin can be concentrated due to fractional crystallisation and hydrothermal processes (e.g. Hulsbosch et al. 2016). Understanding the genesis, emplacement and mineralisation style of these pegmatites is thus a crucial step in their potential exploitation.

Lithium-cesium-tantalum (LCT) pegmatites in the Karagwe-Ankole and Kibara Mesoproterozoic belts in Central Africa are typically associated with granitic magmatism during the early Neoproterozoic (Fernandez-Alonso et al. 2012). Here, we study LCT-type pegmatites from the Musha-Ntunga area in Eastern Rwanda, an area that is currently exploited for coltan- and cassiterite-bearing kaolinised pegmatite and cassiterite-rich quartz veins through shallow (up to 50m) underground mining operations. A recent drilling campaign by the mining company discovered lithium enrichment in fresh to moderately weathered spodumene pegmatites at depths between 100-400m. These unique samples provide a rare insight in the mineralisation, deformation and alteration style of spodumene pegmatites and the associated distribution of lithium within a potential high-grade deposit.

2 Methods

Samples were taken from fresh unweathered to medium weathered pegmatite drill core, from depths between 150 and 400m. A total of 40 thin sections and corresponding slabs were prepared. Microscopic examination consisted of petrographic microscopy and cold cathodoluminescence (CL) microscopy at KU Leuven. A Tescan field emission gun scanning electron microscope (FEG-SEM) was operated with a Tescan Back-scatter electron detector (BSE) and an Oxford Instruments energy-dispersive X-ray spectroscopy detector (EDX) at KU Leuven, to compose high-resolution BSE images and detailed elemental maps. Operating parameters to obtain the BSE images were a working distance of 10 mm, an accelerating voltage of 15 Kev and a beam current of 300 pA. Operating parameters to produce elemental maps were a working distance of 15 mm, an accelerating voltage of 20 Kev and a beam current of 10 nA. Laser Induced Breakdown Spectroscopy (LIBS) was carried out at the Geological Survey of Belgium to map the lithium distribution (Figure 4). The device is equipped with a compact pulsed diode-pumped Nd:YAG laser and 2 spectrometers: a 4-channel Avantes Avaspec EVO 4096CL with covering wavelength range of 200-572 nm and 0.07-0.09 nm spectral resolution, and a single channel Avantes Avaspec EVO 2048CL, with a covering wavelength range of 570-686 nm and 0.18 nm spectral resolution. Laser spot size is 100 µm. A collection of standards were measured to ensure peak intensities are within 0.1 nm of standard values (Kramida et al. 2019).

3 Spodumene textures

Based on petrographic observations, the spodumene from Musha-Ntunga is subdivided in two major groups. The first group is characterised by large spodumene crystal with uniform grain size

(c-axis length ranges usually between 2-5 cm), an elongated, eu- to subhedral crystal habit, with a narrow rim of droplet-like quartz intergrowths on the margin of the crystal (Figure 1A). The crystals display characteristic simple twinning and two cleavages, with planes intersecting at an angle of approximately 90°.

The second group of spodumene crystals, which are much smaller in size, exhibit a variety of textures. On the contact with group 1 spodumene crystals, thin spodumene needles are sometimes observed and intergrown with quartz. This quartz-spodumene assemblage is almost exclusively observed in contact with feldspar, mostly albite, and to a lesser extent with microcline and sometimes muscovite. The needles are oriented more or less orthogonal to the group 1 spodumene grain boundary (Figure 1B, 2B). Solitary spodumene needles or clusters of needles also occur within the matrix, spatially separated from group 1 spodumene crystals. Secondly, subhedral spodumene grains, often with clearly visible cleavage planes, are observed as foliated ribbons, intergrown with fine quartz grains and interstitial anhedral apatite (Figure 1C). A third variety of group 2 spodumene occurs as irregular crystals with a variety of shapes, distinctly grouped together (Figure 2A). Intermediate textures of these three endmember groups are also observed. Figure 2 shows these different types of textures with cold CL microscopy.

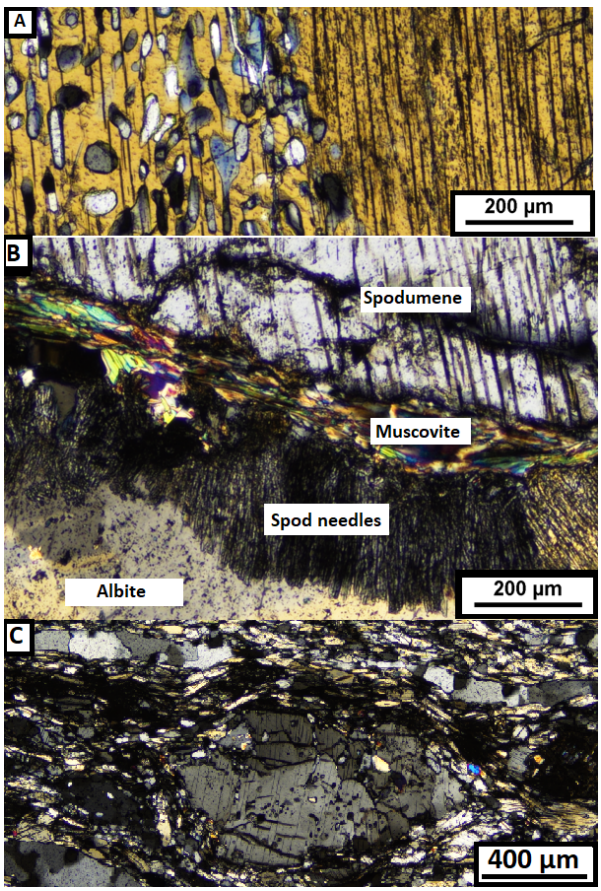

Figure 1. Overview of textural variations seen in association with large spodumene crystals. (A) Droplet symplectite of quartz-spodumene at the edge of the crystal. (B) Needle-like spodumene (spod needles) intergrown with quartz at spodumene border, surrounded by albite. (C) Spodumene fish surrounded by fine-grained foliated spodumene-quartz matrix, quartz ribbons and interstitial apatite.

4 Deformation structures

Different major minerals display typical deformation microstructures. Quartz grains within the matrix are often small and show traces of major ductile deformation, with pronounced lobate grain boundaries, indicative of elevated temperatures (Stipp et al. 2002). In addition, larger quartz grains show undulose and chessboard extinction. In the pegmatite zones with the highest degree of deformation observed, monomineralic quartz ribbons are present (Figure 1C, 3). Muscovite often defines the foliation in a sample, indicated by thin bands of stretched muscovite, with curved cleavage and 'mica fish'. Albite is mostly subhedral and displays intracrystalline deformation patterns, such as deformation twins and bookshelf sliding (Passchier and Trouw 2005).

Deformed spodumene crystals of both group 1 and group 2 can be observed. Large spodumene crystals behave in a more brittle way, as indicated by kinked spodumene twins and 'spodumene fish', with smaller group 2 spodumene grains in the strain cap area and recrystallised quartz in the strain shadow area (Figure 1C, 3). Similar to albite, large spodumene crystals display bookshelf sliding or micro-fracturing (Passchier and Trouw 2005). The mica fish, quartz ribbons, albite deformation twins and spodumene fish are all indicative of intense shear deformation, occurring during or shortly after pegmatite emplacement and crystallisation.

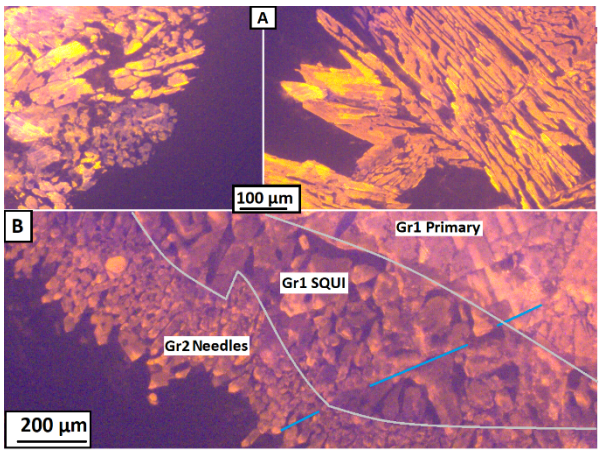

Figure 2. Cold cathodoluminescence microscopy images indicating textural variations of spodumene. (A) Group 2 spodumene textural variations. (B) Textural variation at the border of a large spodumene grain. Blue line indicates continuation of a cleavage plane from group 1 (primary crystal and SQUI) to group 2 spodumene (needles).

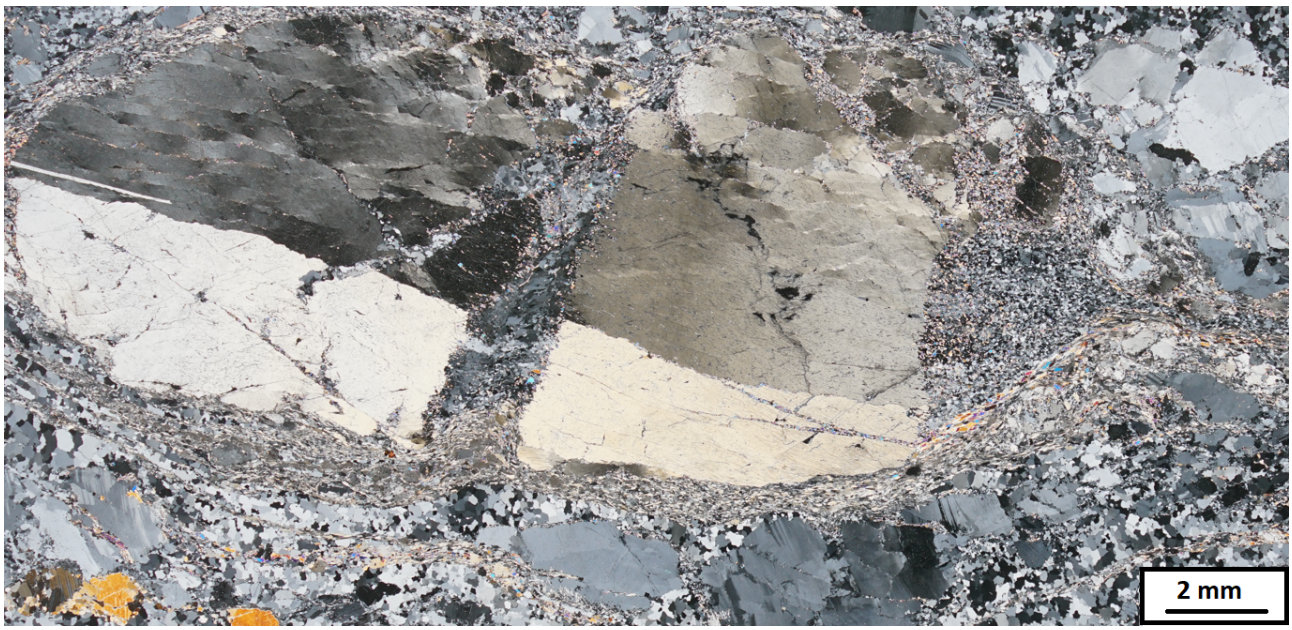

Figure 3. Overview of a thin section displaying a portion of a deformed pegmatite zone. The central spodumene 'fish' shows bookshelf sliding and is surrounded by a matrix of fine-grained spodumene, quartz and apatite. Primary albite grains show deformation twins.

5 Implications for lithium distribution

Using SEM-EDX analyses on the different textural varieties of spodumene, major elemental ratios of Si and Al appear to be identical, and no other major elements are detected. However, minor, trace- and major light elements cannot be measured using this technique. In order to map lithium distributions within the various spodumene textures, we carried out preliminary LIBS analyses. Figure 4 shows an overview map of a small core sample consisting of a moderately altered large, elongated spodumene grain, displayed as a lithium heat map. The spodumene grain is surrounded by albite and quartz. This heat map shows that lithium concentrations near cracks and cleavage planes are significantly lower (purple and dark blue colours) than in the center of the crystal (yellow-red colours). This suggests that lithium was partially leached from the crystal, whereby the cleavage planes, cracks and the external grain boundary provided fluid pathways for lithium to be disseminated. The leaching of lithium from spodumene is further evidenced by increased lithium concentrations in albitised zones near remnant spodumene grains.

6 Discussion

The largest spodumene crystals, belonging to group 1, occur in zones of the pegmatites showing the lowest degree of deformation. These large uniform crystals are considered to be of primary magmatic-hydrothermal origin. The quartz-spodumene boundary intergrowth that occurs on the boundary of group 1 spodumene crystals, as illustrated in Figure 1A and referred to as 'droplet symplectite SQUI', is also considered a primary growth feature. This is supported by the continuous cleavage from the large spodumene crystal into the SQUI droplet symplectite (Figure 1A). Group 2 spodumene has clearly crystallised later, however still strongly spatially associated with the large group 1 spodumene crystals. This is evidenced by the continuation of cleavage planes from group 1 to group 2 spodumene crystals as shown in Figure 2B. The wide variety of textural variations in group 2 is proposed to be due to the interplay between deformation mechanisms and fluid-assisted recrystallisation and alteration or overgrowth of primary spodumene. Alongside secondary spodumene, observed replacement and overgrowing products include albite, muscovite and apatite. As such, group 2 spodumene-quartz needles are the result of intense recrystallisation of primary spodumene. In an early stage, displayed in Figure 1B, recrystallisation only affected the margins of the large spodumene crystals whereas in a more progressive stage, as visualised in Figure 2A, large spodumene grains are completely replaced by group 2 spodumene. Here, spodumene cleavages likely acted as fluid pathways inducing primary spodumene breakdown and replacement along these weaker zones. This is manifested in the precipitation of secondary albite and muscovite within opened spodumene cleavages.

In the most intensely sheared and deformed zones, small elongated spodumene grains presumably formed from larger grains deformed in a brittle way, breaking apart along their main c-axis cleavage planes. These small spodumene grains inherited features (remnant cleavage) from their 'ancestor' large spodumene grains.

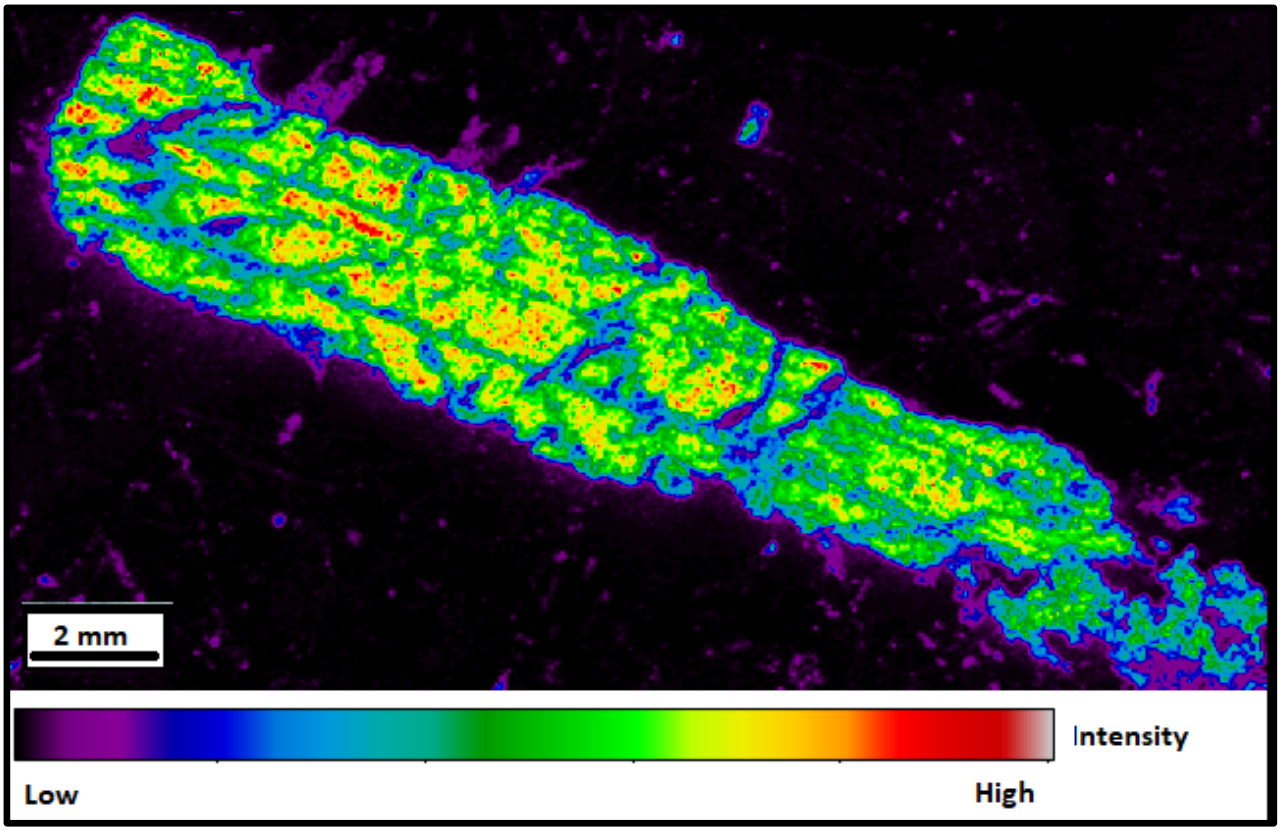

Figure 4. LIBS Lithium heat map of an elongated spodumene grain surrounded by albite.

7 Conclusions

The LCT-type pegmatite deposits in the Musha-Ntunga area in Rwanda offer a unique insight in the mineralisation, high temperature deformation and subsolidus alteration of a spodumene-rich pegmatite system. Based on grain size, two groups of spodumene are distinguished. Group 1 spodumene consists of large, euhedral and brittle deformed primary grains with droplet symplectite spodumene-quartz intergrowths (SQUI) along its rims, while group 2 represents a range of textural varieties of fine-grained secondary spodumene. The two main processes causing recrystallisation of primary spodumene are deformation (shear) and the presence of magmatic-hydrothermal fluids in the system. Although SEM-EDX analyses did not indicate a change of major elemental compositions between the different textural varieties, LIBS mapping shows that the concentration and distribution of lithium is strongly influenced by these two processes. Lithium is easily leached from the primary host and dispersed in the surrounding rock during the magmatic-hydrothermal stage.

Acknowledgements

Herman Nijs is thanked for thin section preparation. Lionel Sematuro and other colleagues from Piran Rwanda Ltd/TRINITY Metals Group are thanked for supplying the samples for this study.

References

Fernandez-Alonso M, Cutten H, De Waele B, Tack L, Tahon A, Baudet D, Barritt SD (2012) The Mesoproterozoic Karagwe-Ankole Belt (formerly the NE Kibara Belt): The result of prolonged extensional intracratonic basin development punctuated by two short-lived far-field compressional events. Precambrian Res. 216–219, 63–86. https://doi.org/10.1016/j.precamres.2012.06.007.

Hulsbosch N, Boiron M-C, Dewaele S, Muchez P (2016) Fluid fractionation of tungsten during granite–pegmatite differentiation and the metal source of peribatholitic W quartz veins: Evidence from the Karagwe-Ankole Belt (Rwanda). Geochim. Cosmochim. Acta 175, 299–318.

Kramida A, Ralchenko Y, Reader J, NIST ASD Team (2019) NIST Atomic Spectra Database (ver. 5.7.1). National Institute of Standards and Technology, Gaithersburg, MD. https://doi.org/10.18434/T4W30F.

London D (2018) Ore-forming processes within granitic pegmatites. Ore Geology Reviews, 101, 349–383. https://doi.org/10.1016/j.oregeorev.2018.04.020.

Passchier C and Trouw R (2005) Microtectonics (2nd, Revised and Enlarged ed.). Berlin, Heidelberg: Springer Berlin / Heidelberg. https://doi.org/10.1007/3-540-29359-0.

Stipp M, Stünitz H, Heilbronner R, Schmid S (2002) The eastern Tonale fault zone: A 'natural laboratory' for crystal plastic deformation of quartz over a temperature range from 250 to 700°C. Journal of Structural Geology, 24(12), 1861-1884. https://doi.org/10.1016/S0191-8141(02)00035-4.

Magmatic-Hydrothermal Mineral Formation Systems: A Geological Study

Jhoshua U. Aparicio[1]
[1]UNAL, Bogotá D.C, Colombia

Abstract. In this paper we will talk about magmatic-hydrothermal deposits, their importance as a source of valuable metals and their different uses nowadays. In addition, we will also cover one of the most important advances in the study of magmatic-hydrothermal deposits, Laser Ablation Inductively Coupled Plasma Mass Spectrometry (LA-ICP-MS), and how this analytical technique has greatly improved our ability to study the geochemistry of magmatic-hydrothermal mineral-forming systems, allowing us to gain new insights into the processes that control the formation of these deposits.

1 Introduction

Magmatic-hydrothermal mineral-forming systems are created from the interaction of magma and hydrothermal fluids. It has been revealed that these deposits form in three main stages:
1. Magma intrusion: Magma intrudes into the earth's crust and cools, releasing volatile fluids.
2. Circulation of hydrothermal fluids: Hydrothermal fluids rise through the surrounding rocks and mix with magmatic fluids forming complex mineral deposits. In some cases, these fluids may also come from external sources such as groundwater.
3. Mineral deposition: Hydrothermal fluids are deposited in the surrounding rocks forming mineral deposits, which are deposited by changes in saturation, temperature and pressure drop or Ph variations. These deposits are important sources of sulfides, oxides, sulfosalts and/or native elements (Espinoza 2020).

Magmatic-hydrothermal mineral forming systems are found all over the world, but are especially common in subduction areas, where one tectonic plate is forced under another. In these regions, intense tectonic activity provides the heat and energy necessary for the formation of these deposits, which are commonly located in places such as (Figure 1):
The Pacific Ring of Fire, which includes countries such as Japan, Indonesia, the Philippines and Chile.
The Andes Mountains in South America, which crosses countries such as Chile, Argentina, Peru and Bolivia.
The Iberian Peninsula in Europe, where copper, lead and zinc deposits are found in places such as the Iberian pyritic belt.
The Rhine river basin in Europe, where there are zinc, lead and copper deposits.
The Ferriferous Quadrilateral in Brazil, where there are important iron deposits (Berger 1985).

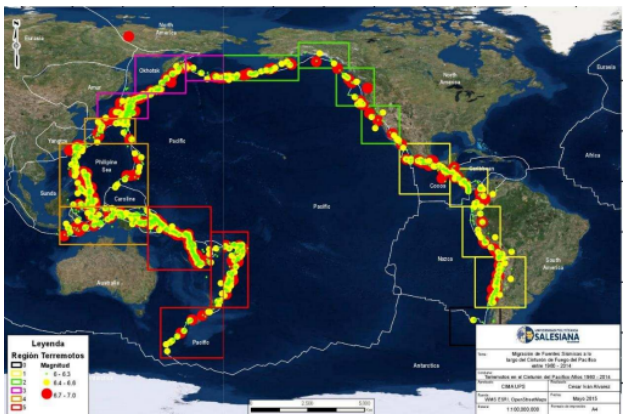

Figure 1. The geographic distribution of the fire belt is observed, where an ideal environment for finding magmatic-hydrothermal deposits is presented. López (2017).

These formation systems are important because they contain minerals of economic interest such as gold, silver, and copper, which are highly demanded in the industry.

It should be emphasized that the interest in this type of deposits is not merely economic, as exploration is necessary for the energy transition proposed in the Sustainable Development Goals (SDGs) developed by the UN in the last decade (Watari 2019).

One of the most widely used ways to study magmatic-hydrothermal deposits is Laser Ablation Inductively Coupled Plasma Mass Spectrometry (LA-ICP-MS) which will be discussed below.

2 Laser Ablation Inductively Coupled Plasma Mass Spectrometry (LA-ICP-MS)

The LA-ICP-MS analysis process can be divided into two main parts: sampling, which consists of laser ablation and ionization in a plasma, and mass spectrometry.

In inductively coupled plasma and laser ablation, the sample is vaporized using a high-energy pulsed laser beam, which is directed through the objective lens of the modified petrographic microscope. The sample surface is viewed with a charge-coupled device (CCD) camera mounted on the microscope, allowing precise laser spot location. Laser pulses cause energetic atoms, ions, molecules and solid particles to be ejected from the target. The removed aerosols are transported in argon or helium gas to the inductively coupled plasma. In the torch, which is heated by induction to approximately 10,000°C, the plasma formed provides a rich source of excited and ionized

atoms. The combination of ICP and MS technologies enables rapid quantitative elemental analysis with high precision and low detection limits (Adburiyim 2006).

In mass spectrometry, on the other hand, the device can analyse both chemical elements and small organic molecules. It requires the sample to be in a gaseous state, including solutions or solids. It measures the masses of elements or molecules of chemical compounds by separation of charged particles. The sample is ionized, and the ions are electrostatically directed to a mass analyser, where they are separated according to their m/z ratio and then sent to a detector, this is best understood by looking at Figure 2 (Adburiyim 2006).

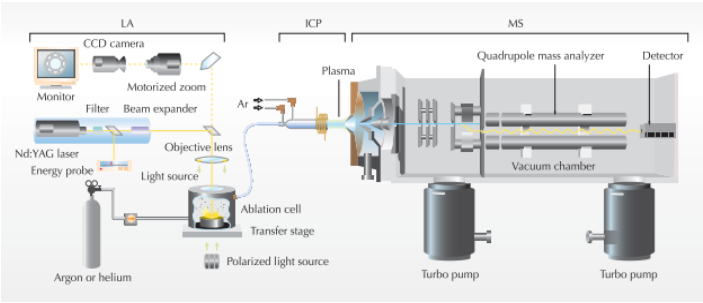

Figure 1. Graphical representation of how LA-ICP-MS is used. The sample is placed in the ablation cell and the laser beam is focused on the sample with the help of a CCD camera. The ablated material forms an aerosol, which is transported by an argon or helium carrier gas to the ICP-MS plasma. In the ICP, the laser-ablated particles are vaporized and ionized. The ions are extracted by the vacuum interface and guided to the mass analyser, where they are separated by their mass-to-charge ratio and finally detected. Adburiyim (2006).

Knowing how LA-ICP-MS data acquisition works, it is used in the search for magmatic-hydrothermal deposits to measure trace element concentrations in minerals and rocks. Briefly, the technique uses a laser to vaporize a small amount of sample, which is then ionized and fed into a mass spectrometer (Adburiyim 2006). The resulting signal provides us with information about the chemical composition of the sample.

2.1 LA-ICP-MS and its use for the study of magmatic-hydrothermal deposits.

One of the most important advances in the study of magmatic-hydrothermal deposits has been with LA-ICP-MS. This analytical technique has greatly improved our ability to study the geochemistry of magmatic-hydrothermal mineral-forming systems, allowing us to gain new insights into the processes that control the formation of these deposits.

LA-ICP-MS has been used to study the distribution of trace elements in magmatic-hydrothermal ore deposits. This has allowed us to identify the processes that control the mobility of these elements, which in turn has improved our understanding of the genesis of mineral deposits.

3 Conclusions

In conclusion, the formation of magmatic-hydrothermal ore-forming systems and their related hydrothermal systems, as well as the formation of ores associated with highly fractionated silicic magmas, are important areas of research for geologists and mining professionals for our development as a society.

Understanding the geochemistry and geology of these systems is critical to identifying new deposits and optimizing mining methods in a responsible and sustainable manner. Recent advances in analytical techniques have improved our understanding of these systems, enabling more effective exploration and mining strategies.

Importantly, magmatic-hydrothermal deposits can be very valuable to the mining industry, as they may contain deposits of precious metals and other minerals of high economic value. However, their exploitation can have significant environmental impacts and it is important to manage these resources responsibly and sustainably.

Acknowledgements

We would like to thank the UNAL for its constant support in the search for information and significant contributions at the time of writing the document, as well as the SGA for allowing us to have the opportunity to write this scientific article.

References

Abduriyim, A., and Kitawaki H (2006) APPLICATIONS OF LASER ABLATION–INDUCTIVELY COUPLED PLASMA–MASS SPECTROMETRY (LA-ICP-MS) TO GEMOLOGY https://www.gia.edu/doc/SU06A1.pdf

Berger B, and Bethke P,M., (1985) Geology and Geochemistry of Epithermal Systems https://pubs.geoscienceworld.org/segweb/books/book/1214/Geology-and-Geochemistry-of-Epithermal-Systems

Espinoza A.S., (2020) Apuntes de Yacimientos Magmático-Hidrotermales para el curso de Metalogenia de la Facultad de Ingeniería http://www.ptolomeo.unam.mx:8080/xmlui/bitstream/handle/132.248.52.100/17342/Material%20did%C3%A1ctico.pdf?sequence=5&isAllowed=y

López A., Álvarez C.I., and Villarreal E (2017) MIGRACIÓN DE FUENTES SÍSMICAS A LO LARGO DEL CINTURÓN DE FUEGO DEL PACÍFICO https://dialnet.unirioja.es/servlet/articulo?codigo=5969874

Watari T., McLellan B.C., Giurco D., Dominish E., Yamasue E., Nansai K., (2019) Total material requirement for the global energy transition to 2050: A focus on transport and electricity https://reader.elsevier.com/reader/sd/pii/S0921344919302290?token=5740989F265371B64A6D43FF8C7C610D03C6CA71A37F6D6A69AB9F076C4D0951BE94F2132755096C42E92EDD352A9F46&originRegion=us-east-1&originCreation=20230304030728

Diachronous tin mineralization in the Iberian Pyrite Belt

Iñigo Borrajo[1], Fernando Tornos[1, 2], Carmen Conde[1], Gonzalo Ares[1], John M. Hanchar[2], Markus Wälle[2,3], Rong-Qing Zhang[4], James Royal[5], Tim Moody[5]
[1]Instituto de Geociencias (IGEO, CSIC-UCM), Spain
[2]Department of Earth Sciences, Memorial University of Newfoundland, Canada
[3]Swiss Gemmological Institute (SSEF), Switzerland
[4]School of Earth Sciences and Engineering, Nanjing University, China
[5]Pan Global Resources Inc, Canada

Abstract. LA-ICP-MS U-Pb dates of cassiterite from two Sn-rich volcanogenic massive sulfide deposits in the Iberian Pyrite Belt (IPB) (La Romana and Neves Corvo), Spain and Portugal display an offset of ca. 17 Ma and suggest that major tin deposition took place coevally with the host massive sulfides at ca. 360 Ma but was later remobilized and reconcentrated along shear zones during the Variscan deformation and metamorphism around 336 Ma.

1 Introduction

The Iberian Pyrite Belt represents one of the most important metallogenic provinces in Europe. Here, volcanogenic massive sulfides (VMS) are interbedded with shale and felsic volcanic rocks and deposited at or close the seafloor; they generally include an underlaying stockwork-like feeder zone (Barriga 1990; Tornos 2006 and references therein). One key feature of the Iberian Pyrite Belt is the abundance of Sn hosted by cassiterite or less commonly by stannite. However, only few deposits host high (up to economic) contents of Sn, like the Lagoa Salgada deposit (measured + indicated resources of 10.3 Mt @ 0.16% of Sn; www.ascendantresources.com; Oliveira et al. 2013), the recently discovered La Romana prospect with yet unconstrained resources (www.panglobalresources.com) or the outstanding Neves Corvo deposit with a total endowment of 300,000 metric tons of Sn metal (Relvas et al. 2006a).

The origin of Sn in the Pyrite Belt is poorly constrained and remains enigmatic. Relvas et al. (2006a) have proposed that it is associated with magmatic-hydrothermal fluids related with underlying intrusions of peraluminous granitoids. However, Relvas et al. (2001) and Tornos (2006) have proposed that tin mineralization was hydrothermally leached from underlying (meta)-sediments in this belt as proposed for the tin-rich sediment-hosted Sullivan deposit in the British Columbia (Slack et al. 2020).

In this study, we present new U-Pb dating of cassiterite that shows that there were at least two individual events of cassiterite formation.

2 Geological context

The Iberian Pyrite Belt is a wide belt in the northernmost part of the South Portuguese Zone, southwest Iberia. It is dominated by igneous (volcanic and intrusive) and sedimentary rocks in a relatively simple geological sequence that includes form bottom to top (Fig. 1): Phyllite-Quartzite (PQ) Group, a monotonous detrital package of Late Devonian age; the Volcanic Sedimentary (VS) Complex, a heterogeneous unit of mafic-felsic volcanic rocks interbedded with shale, previously dated as late Famennian to middle Visean age, and that fills an intracontinental marine basin; and the Baixo Alentejo Flysch Group, a turbidite-like unit complex of early to Middle Carboniferous age.

The La Romana project is close to the Aznalcóllar-Los Frailes cluster, in the southeastern border of the IPB, partially covered by the sediments of the post-Miocene Guadalquivir Basin (Fig. 1). The mineralization occurs mostly as volcanic-hosted bodies located above a rhyodacite dome complex. Host rocks include coherent porphyritic dacite and rhyolite, different types of volcaniclastic rocks with monomictic and/or polymictic composition, and dark shale.

The Neves Corvo is located in the west part of the IPB in Portugal (Fig. 1). It is hosted by a sequence formed mainly of mudstone and felsic volcanic facies divided in three main sequences from bottom to top: rhyolite fiamme-rich facies, coherent porphyritic rhyolite interbedded with shale and volcaniclastic rocks, and a monomictic dacite breccia (Rosa et al., 2008). The mineralization is interbedded with shale or replaces permeable facies of the related coherent and volcaniclastic rocks.

Both, the La Romana and Neves Corvo deposits were affected by intense deformation during the different stages of the Variscan orogeny with widespread southward thrusting.

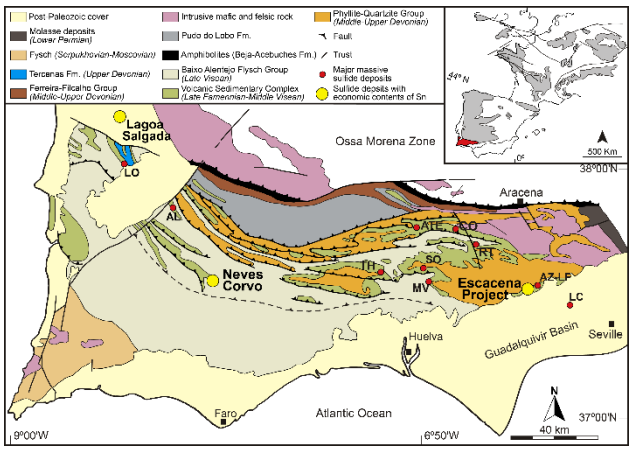

Figure 1. Geological map showing the location of the La Romana (Escacena) and Neves Corvo

deposits. LC: Las Cruces; LF: Los Frailes; Az: Aznalcollar; RT: Riotinto; SO: Sotiel; TH: Tharsis: ATE: Aguas Teñidas; CO: Concepcion; MV: Masa Valverde; AL: Aljustrel; LO: Lousal.

3 Mineralization at La Romana and Neves Corvo deposits

The mineralization at La Romana consists of stratabound massive sulfides replacing pervasively altered shale and probably formed by subseafloor replacement. It includes dominant pyrite with lesser amounts of chalcopyrite and traces of sphalerite and galena. The sphalerite includes micro-sized inclusions of cassiterite. However, the most prominent tin mineralization forms up to cm-sized mases of coarse-grained cassiterite with quartz, chalcopyrite and chlorite within shear bands that crosscut the massive sulfides (Fig 2A).

The Neves Corvo deposit encloses seven tectonically stacked massive sulfide orebodies, some of them including the originally underlying stockwork. The mineralization stands out for the high Cu and Zn, and locally very high Sn grades. The orebodies include different styles of mineralization: 1) massive sulfides, composed by Cu, Sn, Pb and Zn-rich ores; 2) stockwork, including Cu, Sn and Zn ores; and, 3) banded ore ("rubane") consisting in high grade Cu and Sn mineralization tectonically emplaced on the top of the massive sulfides. Cassiterite occurs as large, almost monomineral massive orebodies in the rubane ore (Fig. 2B) or within the stockwork as quartz-cassiterite-rich stringers. The Cu-rich massive sulfides also include minor fine grained cassiterite, stannite and complex Sn-bearing sulfosalts.

4 Methods

This research is focused on cassiterite from the rubane ore at Neves Corvo and that in shear zones at La Romana. Large (> 1 mm) grains of cassiterite were easily separated by handpicking and mounted in an epoxy disc and polished to expose the crystal centres. Areas free of cracks or inclusions were selected for U-Pb dating by using optical microscopy and BSE images.

LA-ICP-MS U-Pb dating of cassiterite was done at the Micro Analysis Facility (MAF) at Memorial University of Newfoundland, St, John's, Canada by using a Thermo Finnigan Element XR high-resolution single collector ICPMS interfaced to a Coherent GeoLas 193 nm Excimer laser. The U-Pb analysis were collected during a single session in December 2022. The conditions used were an energy density of 4 J/cm^2 and a pulse frequency of 10 Hz and a laser spot size diameter of 110 µm. Yankee and Cligga Head cassiterite was used as the primary standard and validation material (Carr et al. 2020; Tapster and Brighter 2020).

5 Results

Twenty-two spot analyses in the La Romana cassiterite sample yielded a lower intercept age on a Tera-Wasserburg diagram (Tera and Wasserburg, 1972) of 336.1 ± 4.0 Ma (2σ, MSWD = 3.1). Twenty-two analysis of the Neves Corvo cassiterite yielded an age of 360.6 ± 5 Ma (2σ, MSWD = 2.8). Approximate U and Th concentrations are 3.42 to 17.11 ppm and 0.18 to 3.86 ppm respectively in the sample from Neves Corvo and at La Romana U contents are between 6.66 and 62.50 ppm and Th contents between 0.06 and 25.80 ppm.

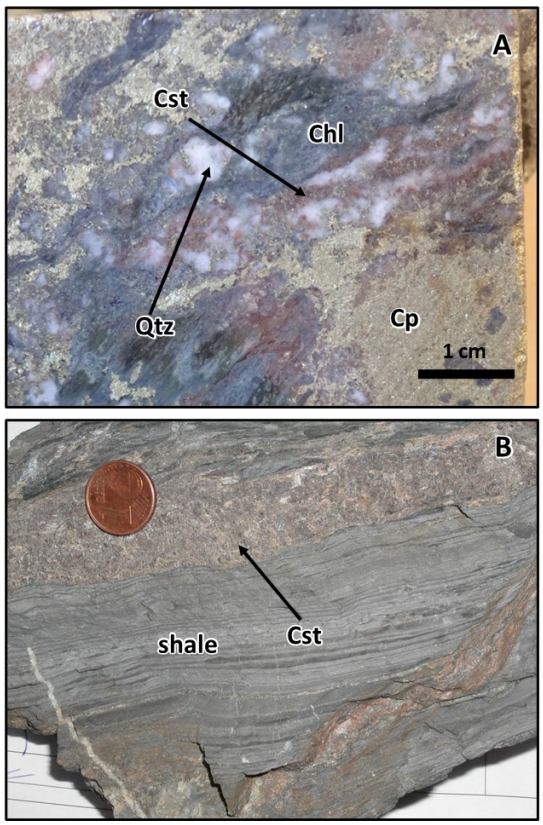

Figure 2. Textural relationships of cassiterite. **A** Late veins with quartz, chlorite, chalcopyrite and cassiterite at the La Romana. **B** Cassiterite interbedded with shale from the rubane ore at the Neves Corvo deposit. Cp: chalcopyrite; Qtz: quartz; Cst: cassiterite; Chl: chlorite.

Closure temperature of the U-Pb isotopic system in cassiterite has been estimated to be higher than 500 °C for grains of 1-µm radii (Zhang et al. 2011). Thus, the obtained dates in this study are interpreted as the crystallization age of the cassiterite mineralization.

6 Discussion

Palynostratigraphic studies (e.g. Pereira et al. 1996; Matos et al. 2011) along with U-Pb dating of the host volcanic rocks (Barrie et al. 2002; Paslawski et al. 2021; Pereira et al. 2021; Mello et al. 2022), between many others, have helped to constrain the timing of the mineralization in the IPB. However, direct absolute dating of VMS

deposits is still problematic because of the fine-grained size of the mineralization and the lack of good geochronometers. Mathur et al. (1999) obtained Re-Os dates in pyrite-rich ores for the giant Rio Tinto (346 ± 26 Ma) and Tharsis (353 ± 44 Ma) deposits, while Relvas et al. (2001) and Munhá et al. (2005) reported Re-Os (358 ± 29 Ma) and Rb-Sr (347 ± 25 Ma) dates for the massive and stockwork ores of the Neves Corvo deposit. All these dates display large analytical errors.

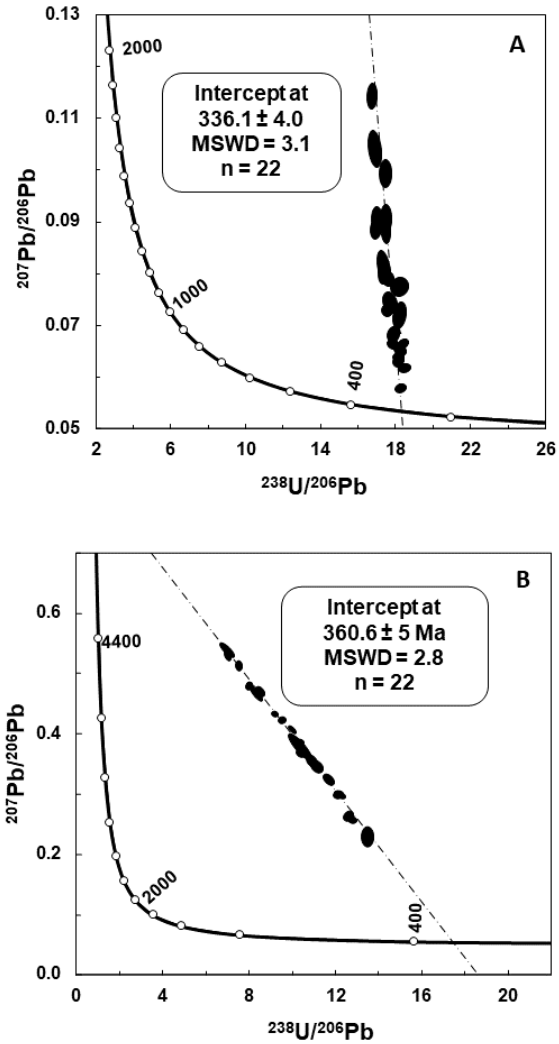

Figure 3. Tera–Wasserburg (Tera and Wasserbourg 1972) concordia diagrams of cassiterite from the IPB. **A** La Romana **B** Neves Corvo. Error envelopes are 2 sigma.

Recently, Li et al. (2019) reported U-Pb dates for cassiterite from the massive ore (364.4 ± 4.4), the fissural ore (367.5 ± 8.7) and the rubane ore (365.2 ± 5.3 and 363.4 ± 5.8) at Neves Corvo. All these dates overlap within errors with the result obtained in the present study. In the Neves Corvo area five different episodes of felsic volcanism between ca. 354 ± 2 Ma and 385 ± 2 Ma have been reported by Oliveira et al. (2013) by U-Pb dating of igneous zircon. Here, the main stage of massive sulphide deposition has been interpreted to have taken place during late Strunian time (ca. 360.0 - 361.5 Ma), associated with the black shales and rhyolites of the ca. 359 ± 3 Ma volcanic event (Pereira et al. 2021). This implies that the felsic volcanism, shale sedimentation and sulfide and cassiterite mineralization are essentially coeval.

At the La Romana deposit the absolute age of the associated igneous host rocks remains unknown.

Pereira et al. (1996) based on miospores collected from the black shales hosting the massive sulfides at the Los Frailes-Aznalcollar-La Romana orebodies suggested an uppermost Devonian age (Strunian: ca. 360.0-361.5 Ma). In contrast, Nesbitt et al. (1999) dated hydrothermal zircon in the stockwork zone of the Los Frailes deposit at 345.7 ± 4.7 Ma. This date is in good agreement with the U-Pb date in cassiterite from La Romana suggesting a late regional hydrothermal event in the area at ca. 343 Ma. This event is also broadly coeval with the late volcanism in the Riotinto area at ca. 340 Ma (e.g. Valenzuela et al. 2011; Mello et al. 2022) and several plutonic rocks in the Sierra Norte Batholith in the NE of the IPB (Paslawski et al. 2021; Fig. 1).

The geochronological data available do not constrain the sources of Sn but can provide important information when combined with field observations and other geochemical data. At Neves Corvo, the hydrogen, oxygen and Sr-Nd isotopic data of Relvas et al. (2001, 2006b) suggests that Sn was precipitated from hydrothermal fluids that were of different composition from those that formed the bulk of the massive sulfide mineralization. Tin-bearing fluids could be related to the upflow of magmatic-hydrothermal fluids related with a deep peraluminous granite (Relvas et al. 2006b; Marques et al. 2020). However, Tornos (2006) suggests that Sn is related to the same fluids forming the bulk of the VMS deposits and derived from the hydrothermal leaching of the siliciclastic sediments of the PQ Group or an underlying continental basement. The major problem of any magmatic-hydrothermal model is the lack of peraluminous magmatism in a magmatic arc with calk-alkaline felsic rocks. Collision-related peraluminous magmatism postdates the Sn mineralization at Neves Corvo by more than 30 Ma.

A further metal extraction from the basement reservoir or a remobilization of older mineralization during the polyphase Variscan deformation and metamorphism (Dallmayer et al. 1997) could have generated a second Sn-rich event at ca. 342 Ma at la Romana. This is consistent with the occurrence of cassiterite mineralization in syn-tectonic Variscan shear zones in this deposit.

This hypothesis agrees with the recent study of Romer et al. (2022) suggesting that in the Variscan Belt, Sn was remobilized during prograde metamorphism between 400 and 340 Ma.

Conclusions

U-Pb dating of cassiterite from La Romana and Neves Corvo in the Iberian Pyrite Belt reveals two events at ca. 336 ± 4.1 Ma and 360.6 ± 5Ma of tin mineralization. The first one is coeval with the formation of the massive sulfides with Sn being leached from the underlying siliciclastic rocks. The second event is of Variscan age and probably related with syn-tectonic deformation.

Acknowledgements

Funded by an internal research grant of Memorial University of Newfoundland, the iTARG3T Project (EIT Raw Materials of the European Union's Horizon 2020 Grant No. 18036) and the EIS Project (Horizon Europe Grant No. 101057357). The authors thank Pan Global Resources for supporting the research.

References

Barrie TC, Amelin Y, Pascual E (2002) U–Pb geochronology of VMS mineralization in the Iberian Pyrite Belt. Miner Depos 37:684–703. https://doi.org/10.1007/s00126-002-0302-7

Barriga F (1990) Metallogenesis in the Iberian pyrite belt. In: Dallmeyer RD, Martinez Garcia E (eds) Pre-Mesozoic geology of Iberia. Springer-Verlag, Berlin Heidelberg New Yor, pp 369–379

Carr P, Zink S, Bennett V, et al (2020) A new method for U-Pb geochronology of cassiterite by ID-TIMS applied to the Mole Granite polymetallic system, eastern Australia. Chem Geol 539:119539

Dallmeyer RD, Catalán JRM, Arenas R, Ibarguchi J, Gutiérrez G, Farias P, Bastida F, Aller, J (1997) Diachronous Variscan tectonothermal activity in the NW Iberian Massif: evidence from $^{40}Ar/^{39}Ar$ dating of regional fabrics. Tectonophysics 277:307-337.

Li X, Zhao K, Jiang S, Palmer M (2019) In-situ U-Pb geochronology and sulfur isotopes constrain the metallogenesis of the giant Neves Corvo deposit, Iberian Pyrite Belt. Ore Geol Rev 105:223–235

Marques AFA, Relvas JM, Scott SD, Rosa C, Guillong M (2020) Melt inclusions in quartz from felsic volcanic rocks of the Iberian Pyrite Belt: clues for magmatic ore metal transfer towards VMS-forming systems. Ore Geol Rev 126:103743.

Mathur R, Ruiz J, Tornos F (1999) Age and sources of the ore at Tharsis and Rio Tinto, Iberian pyrite belt, from Re-Os isotopes. Miner Depos 34:790–793. https://doi.org/10.1007/S001260050239

Matos JX, Pereira Z, Rosa CJP, et al (2011) Late Strunian age: a key time frame for VMS deposit exploration in the Iberian Pyrite Belt. In: 11th SGA Biennial Meeting: Let's Talk Ore Deposits

Mello C de, Tornos F, Conde C, et al (2022) Geology, Geochemistry, and Geochronology of the Giant Rio Tinto VMS Deposit, Iberian Pyrite Belt, Spain. Econ Geol 117:1149–1177

Munhá J, Relvas J, Barriga F, Conceição P (2005) Osmium isotope systematics in the Iberian Pyrite Belt. In: Mineral Deposit Research: Meeting the Global Challenge: Proceedings of the Eighth Biennial SGA Meeting Beijing, China, 18–21 August 2005. Springer Berlin Heidelberg, pp 663–666

Nesbitt RW, Pascual E, Fanning CM, et al (1999) U-Pb dating of stockwork zircons from the eastern Iberian Pyrite Belt. J Geol Soc London 156:7–10. https://doi.org/10.1144/GSJGS.156.1.0007

Oliveira D de, Matos J, Rosa C, et al (2011) The Lagoa Salgada orebody, Iberian Pyrite Belt, Portugal. Econ Geol 106:1111–1128

Oliveira JT, Rosa CJP, Pereira Z, et al (2013) Geology of the Rosário-Neves Corvo antiform, Iberian Pyrite Belt, Portugal: New insights from physical volcanology, palynostratigraphy and isotope geochronology studies. Miner Depos 48:749–766. https://doi.org/10.1007/S00126-012-0453-0

Paslawski LE, Braid JA, Quesada C, McFarlane CM (2021) Geochronology of the iberian pyrite belt and the sierra norte batholith: Lower plate magmatism during supercontinent amalgamation? Geol Soc Spec Publ 503:589–617. https://doi.org/10.1144/SP503-2020-5

Pereira Z, Matos JX, Rita Solá A, et al (2021) Geology of the recently discovered massive and stockwork sulphide mineralization at Semblana, Rosa Magra and Monte Branco, Neves–Corvo mine region, Iberian Pyrite Belt, Portugal. Geol Mag 158:1253–1268. https://doi.org/10.1017/S0016756820001284

Pereira Z, Ramos RS, Pons J, Oliveira J (1996) Edad devónica (Struniense) de las mineralizaciones de Aznalcóllar (Faja Pirítica Ibérica) en base a palinología. Geogaceta 20:1609–1612

Relvas J, Barriga F, Ferreira A, et al (2006a) Hydrothermal alteration and mineralization in the Neves-Corvo volcanic-hosted massive sulfide deposit, Portugal. I. Geology, mineralogy, and geochemistry. Econ Geol 101:753–790

Relvas J, Barriga F, Longstaffe F (2006b) Hydrothermal alteration and mineralization in the Neves-Corvo volcanic-hosted massive sulfide deposit, Portugal. II. Oxygen, hydrogen, and carbon isotopes. Econ Geol 101:797–804

Relvas J, Tassinari C, Munhá J, Barriga F (2001) Multiple sources for ore-forming fluids in the Neves Corvo VHMS Deposit of the Iberian Pyrite Belt (Portugal): strontium, neodymium and lead isotope evidence. Miner Depos 36:416–427. https://doi.org/10.1007/s001260100168

Romer R, Kroner U, Schmidt C, Legler C (2022) Mobilization of tin during continental subduction-accretion processes. Geology 50:1361–1365. https://doi.org/10.1130/G50466.1

Rosa CJ, McPhie J Relvas JM, Pereira Z, Oliveira T, Pacheco N (2008) Facies analyses and volcanic setting of the giant Neves Corvo massive sulfide deposit, Iberian Pyrite Belt, Portugal. Miner Depos 43:449-466.

Slack JF, Neymark LA, Moscati RJ, Lowers HA, Ransom P, W, Hauser RL, Adams, DT (2020) Origin of tin mineralization in the Sullivan Pb-Zn-Ag deposit, British Columbia: Constraints from textures, geochemistry, and LA-ICP-MS U-Pb geochronology of cassiterite. Econ Geol 115: 1699-1724.

Tapster S, Bright JW (2020) High-precision ID-TIMS cassiterite U–Pb systematics using a low-contamination hydrothermal decomposition: implications for LA-ICP-MS and ore deposit geochronology. GChron 2:425-441.

Tera F, Wasserburg GJ (1972) U-Th-Pb systematics in three Apollo 14 basalts and the problem of initial Pb in lunar rocks. Earth and Planet Sci Lett 14:281-304.

Tornos F (2006) Environment of formation and styles of volcanogenic massive sulfides: The Iberian Pyrite Belt. Ore Geol Rev 28:259–307

Valenzuela F, Donaire T, Pin C, et al (2011) Geochemistry and U–Pb dating of felsic volcanic rocks in the Riotinto–Nerva unit, Iberian Pyrite Belt, Spain: crustal thinning, progressive crustal melting and massive sulphide genesis. J Geol Soc London 168:717–731. https://doi.org/10.1144/0016-76492010-081

Zhang DL, Peng JT, Hu RZ, et al (2011) The closure of U-Pb isotope system in cassiterite and its reliability for dating. Geological Review 57:

http://www.ascendantresources.com. Accessed February 27, 2023

http://www.panglobalresources.com. Accessed February 27, 2023

Magmatic-hydrothermal stratabound W-(Sn) mineralization in the Iberian Variscan Massif: The Barxa deposit

Iñigo Borrajo[1], Fernando Tornos[1], John M. Hanchar[2], Jose M. Fuenlabrada[3], Tobias E. Bauer[4]
[1]Instituto de Geociencias (IGEO, CSIC-UCM), C/Severo Ochoa, 7, 28040 Madrid, Spain
[2]Department of Earth Sciences, Memorial University of Newfoundland, St. John's, NL, Canada A1C 5S7
[3]Unidad de Geocronología (CAI de Ciencias de la Tierra y Arqueometría), Universidad Complutense. 28040 Madrid, Spain
[4]Division of Geosciences and Environmental Engineering, Luleå University of Technology, Luleå SE-971 87, Sweden

Abstract. Stratabound scheelite mineralization distal to granitic rocks represents a minor group of deposits within the framework of the W-Sn metallogenic province of the European Variscan Belt; however, this style of mineralization can have large tonnages and grades. The recently discovered Barxa and Valtreixal deposits in NW Spain are somewhat different to the other scheelite-rich stratabound deposits in Iberia. They display a lateral zonation from the crosscutting Sn-rich veins that acted as feeder zones and include a proximal greisen-like alteration and a distal alteration that consists of an Al-rich calcic skarn. The εNd_i values of the stratabound orebodies range between those of the granitic dikes distal to the mineralization (εNd_i, between -6.5 and -5.5) and the host unaltered metapelites (εNd_i between -12 and -10.4). Mineralization in the skarn-like alteration shows values similar to those in the host metapelites, while the greisen-like assemblage has closer εNd_i values to those of the granitic dykes.

1 Introduction

Tungsten-(tin) mineralization worldwide usually occurs spatially associated with felsic intrusions giving rise to a wide spectra of magmatic-hydrothermal ore deposits including veins, skarns, pegmatites, disseminations in evolved granitic cupolas, porphyries, and breccia pipes (e.g. Derré 1982).

Perigranitic vein systems hosting high grade low tonnage W mineralization has been largely mined during the last centuries in the European Variscan Belt, where they represent the dominant mineralization style (e.g. Harlaux et al. 2018). Along with this classical mineralization, a short number of deposits are characterized by being related to stratabound scheelite-rich orebodies with an alteration somewhat similar to that of skarns. Many of these deposits show no obvious spatial relationship with Variscan granitoids (Schermerhorn 1981; Arribas 1983; Gaspar and Inverno 2000). The Mittersill deposit (Austria) belongs to this group and with more than 10 Mt @ > 0.4% WO_3 represents one of the largest tungsten deposits in Europe (Ordosch et al. 2019).

Two new stratabound scheelite deposits have been found in Western Iberia. They include the Valtreixal deposit with inferred resources of 10 Mt @ 0.28 WO3 (www.almonty.com) and the Barxa deposit with unknown resources. The high tonnage and high and homogeneous W grades make them an attractive target for mining and contrast with vein-like deposits being usually smaller in size and with more erratic ore grades.

In this study we present geological evidences and isotope geochemistry data of the Barxa deposit that support that, despite being unrelated to any magmatic intrusion, is a distal replacement of favourable rocks with a magmatic-hydrothermal origin.

2 Geological Context

The Barxa deposit is located in NW Iberia, close to the contact between the Central Iberian Zone (CIZ) and the Schist Domain of the Galicia-Tras-os-Montes Zone (GTMZ) (Martínez Catalán et al. 2004; Díez-Montes 2006). Within the studied region, the CIZ includes gneisses, metasediments and metavolcanic rocks, while the Schist Domain is mostly dominated by metapelitic rocks (Fig. 1). In detail, the rocks hosting the Barxa deposit consist of a monotonous succession of Late Cambrian to Silurian phyllites (Farias 1989; Farias et al. 2014) deformed and metamophosed during the Variscan Orogeny and intruded by younger granitic suites ranging from early syn- tectonic and late syn-tectonic to post-tectonic (Díez-Montes 2006; Fig. 1).

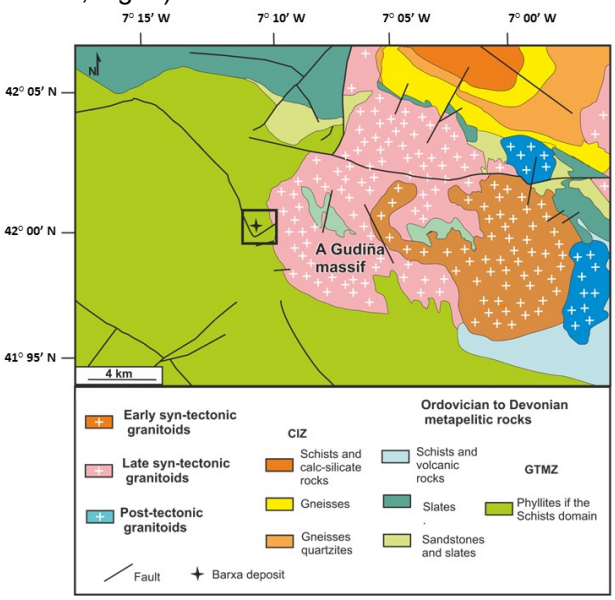

Figure 1 Regional geological map of the Barxa deposit area. Modified from Díez-Montes (2006).

The syn-tectonic A Gudiña granite is the closest intrusion to the Barxa deposit (Fig.1). It shows a clear intrusive contact with the host phyllites towards its SW border generating a contact metamorphic aureole. Here, there are several irregular granitic dykes with a pinch-and-swell morphology intruding parallel to the regional cleavage. Here, the granite displays a pervasive greisen-like hydrothermal alteration and host abundant Sn-rich quartz veins. One of these dykes with 3 m to 15 m thick and with a length of around 80 m is known as the Barxa granite.

3 The Barxa deposit

W-(Sn) mineralization is hosted by at least four stratabound calc-silicate bodies of decametric dimensions with a E-W trend and dipping 30-40° SW that are interbedded with the phyllites (Fig. 2). The mineralized bodies are adjacent to a NNE-SSW trending fault.

The orebodies are more competent than the host phyllite; they have a large-scale boudin morphology, edges are usually sheared and brecciated and are the preferential site for the formation of up to 2 m thick NE-SW-trending quartz and minor tourmaline veins (Fig. 2). When crosscutting the stratabound mineralization the veins have a well-developed selvage of quartz-muscovite-scheelite-cassiterite (greisen-like assemblage) that laterally prograde on a much larger zone of clinozoisite-quartz-scheelite (skarn-like assemblage).

Outside of these bodies there are little evidences of metasomatism. Locally, the phyllite enveloping the mineralization shows a muscovite-tourmaline-rich halo.

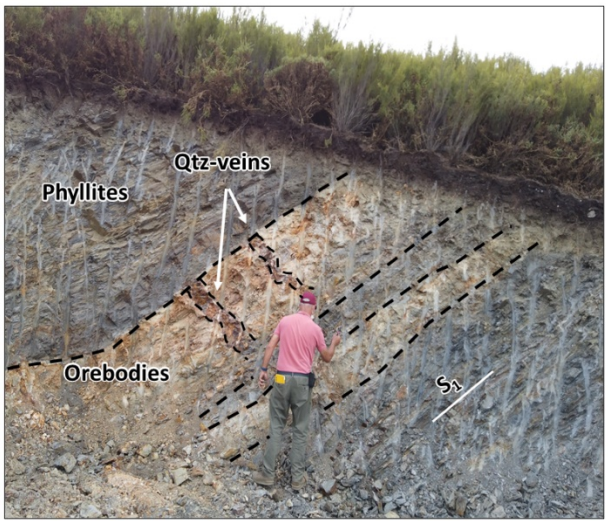

Figure 2 Outcrop of the Barxa stratabound orebodies that are subparallel to the layering of the host phyllites and are crosscut by NE-SW trending quartz veins which do not propagate throughout the host rock.

3 The stratabound orebodies

The mineralization includes two different metasomatic zones, a proximal greisen like-alteration and a distal, dominant skarn-like alteration. This latter is a coarse-grained massive brownish rock composed mostly of anhedral quartz crystals and large sub-euhedral unoriented and zoned clinozoisite crystals (Fig. 3A). Scheelite grains of up to 2 mm in size occur intergrown with clinozoisite and quartz (Fig. 3A). Only locally, this assemblage replaces a previous prograde calcic skarn made up aggregate of massive grossular with crystals of up to 0.7 cm in size and having a high intergranular permeability. This zonation is typical of iron-poor calcic skarns with the clinozoisite-quartz assemblage forming at temperatures below ca. 440°C for a fluid pressure close to 1 kb.

The garnet assemblage represents the oldest metasomatic rock but we have not found any evidences of the unreplaced protolith. This is probably caused by its complete replacement by the metasomatic assemblage, as reported in other scheelite-rich stratabound deposits in Iberia (Gaspar and Inverno 2000).

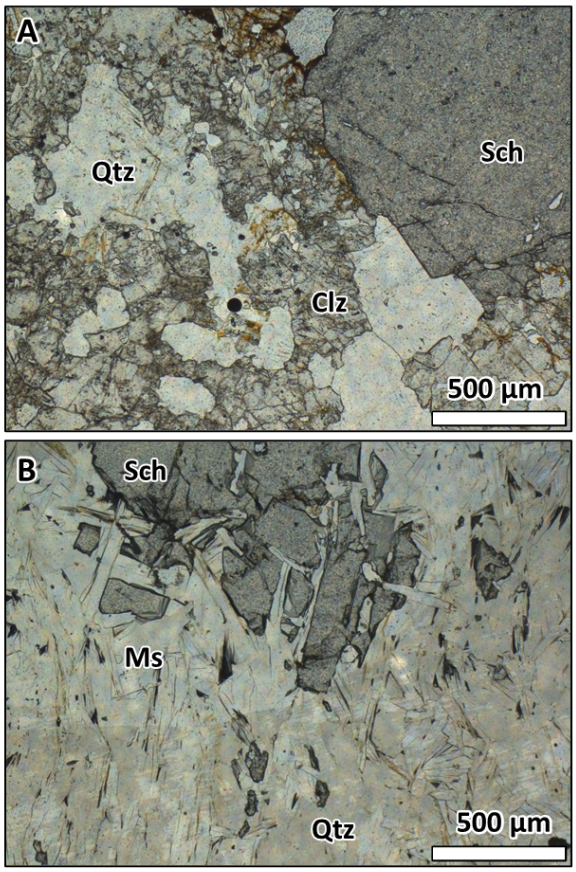

Figure 3 Plane-polarized transmitted light images showing mineralogical and textural features of scheelite from Barxa deposit. **A** Large scheelite (sch) grain intergrown with clinozoisite (Clz) and quartz (Qtz) in the skarn-like alteration. **B** Scheelite crystals intergrown with muscovite (Ms) in the greisen.

The greisen alteration progrades on the skarn-like assemblage. It includes two zones with contrasting W and Sn tenors. The W-rich greisen consists of medium-grained muscovite crystals of up to 500 µm in size, quartz, minor sub-millimetric apatite grains, scarce tourmaline and minor rutile, ilmenite and arsenopyrite. Scheelite aggregates of up to 1 mm in size are intergrown in this assemblage (Fig. 3B). Proximal to the quartz veins there is a Sn-rich greisen, with total thickness of less than 10 cm. It is dominated by large muscovite grains up to 1 mm in size (Fig. 4) and includes minor quartz and apatite. Cassiterite grains with sizes ranging between 15 µm and 500 µm occur intergrown with muscovite (Fig. 4).

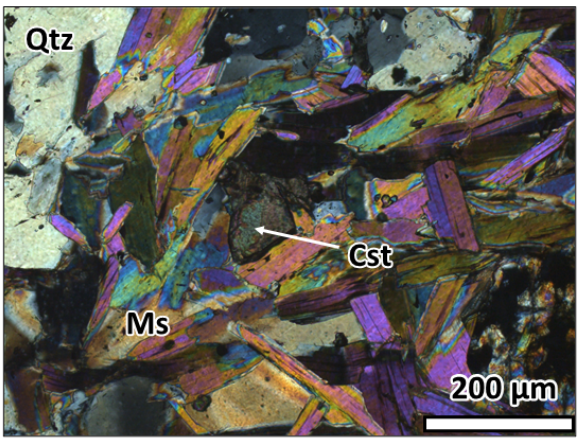

Figure 4 Cross polarized transmitted light image of a cassiterite (Cst) grain intergrown with coarse-grained muscovite (Ms) from the Sn-rich greisen of the Barxa deposit.

All the metasomatic rocks are locally crosscut by late mm-thick sulfide-rich veins with arsenopyrite, pyrite and minor chalcopyrite.

4 Fluid evolution and sources of Sr and Nd

The Rb, Sr, Sm and Nd concentrations and the $^{87}Sr/^{86}Sr$ and $^{147}Nd/^{144}Nd$ isotopic ratios of samples from the different metasomatic assemblages, the Barxa granite and the host unaltered phyllites were analyzed at the Centro de Geocronología y Geoquímica Isotópica (CAI de Ciencias de la Tierra y Arqueometría) of the Universidad Complutense de Madrid (UCM) using isotope dilution thermal ionization mass spectrometry (IDTIMS).

Syn-kinematic granites emplaced in the NW of the Iberian Variscan Massif between 325 and 310 Ma (Dias et al. 1998). Reported ages of other Sn-W deposits in the area range between 330 and 300 Ma (Melleton et al. 2011; Zhang et al. 2019). Therefore, initial isotopic ratios have been recalculated at an average age of 310 Ma.

The initial Sr isotope composition of the Barxa granite is homogeneous displaying strongly radiogenic $^{87}Sr/^{86}Sr_i$ ratios between 0.71825 and 0.71916. In contrast, the host phyllites show more heterogeneous values between 0.71458 and 0.72048. This isotopic heterogeneity is typical in the metasediments from the NW Iberia which sometimes show unexpected low $^{87}Sr/^{86}Sr$ values, interpreted as led by weathering and diagenetic processes due the high mobility of Rb and Sr (Villaseca et al. 2014). The metasomatic rocks also display a wide range in the $^{87}Sr/^{86}Sr_i$ ratios that range between 0.70799 and 0.72475.

The high variability and overlapping in the granite and metapelites $^{87}Sr/^{86}Sr_i$ ratios made it difficult to interpret the obtained results.

In contrast, $\varepsilon Nd_{310\ Ma}$ values in the phyllites and the Barxa granite lay in two contrasting and well-defined fields. The metapelites have εNd_i ratios that range between -12.0 and -10.4, consistent with a derivation from an old crustal reservoir; more juvenile $\varepsilon Nd_{310\ Ma}$ values between -6.4 and -5.1 were obtained for the Barxa granite, which are similar to those of the dominant peraluminous syn-kinematic granitic suite in NW Iberia ranging between -9 and -5 (Dias et al. 2002; Villaseca et al. 2009; Martins et al. 2013).

The stratabound mineralization has intermediate Nd isotopic compositions between the Barxa granite and the phyllites. This suggests that Nd mineralization is derived from the host sedimentary sequence and an external fluid in isotopic disequilibrium with the host rocks.

In detail, the □Nd$_i$ values track a trend of progressive fluid-rock reaction. Samples proximal to the quartz veins (Sn-rich greisen, W-rich greisen and the quartz-tourmaline veins) have εNdi values ranging between -9.6 and -8.4 and samples from the distal skarn-like alteration have more negative values between -10.4 and -9.6. This trend is consistent with the inflow of a fluid with higher $^{143}Nd/^{144}Nd$ values that circulated through the fluid channel ways now represented by the quartz veins. The most likely source for fluids is the Barxa granite, located ca. 2 km away, or any equivalent intrusion located beneath the stratabound mineralization. If that holds true, the magmatic-hydrothermal fluids exsolved from the granite during crystallization and that produced greisenization and Sn-rich mineralization are the same that formed the mineralization at Barxa W-Sn deposits.

4 Conclusions

The recently discovered Barxa deposit in NW Iberia includes at least four large scheelite-rich distal skarns dominated by quartz and clinozoisite formed at relatively low temperatures and replacing an unknown protolith. Nd isotope geochemistry suggests that the mineralization formed due to the reaction with the metasediments of fluids derived from a distal crystallizing granite and strongly suggest that in Fe-poor systems, W-rich fluids can travel far from the source till they

find a suitable lithology where to precipitate by fluid-rock interaction.

Acknowledgements

This research was conducted within the iTARG3T (Innovative targeting & processing of W-Sn-Ta-Li ores: towards EU's self-supply) project funded by the EIT Raw Materials of the European Union's Horizon 2020 (GA 18036) and Hugo Dummett Mineral Discovery Fund (SEG) grant to Iñigo Borrajo. Thanks to J. Ruiz, C. Rodríguez, I. Solaz, I. Losada, C. Casquet and E. Crespo for their constructive reviews and suggestions.

References

Arribas A (1983) Geología y metalogenia del yacimiento «Virgen de la Encina», Ponferrada (Léon). Tecniterrae 56:36–75

Derré C (1982) Caracteristiques de la Distribution des Gisements à Etain et Tungstene Dans L'Ouest de L'Europe. Miner Depos 17:55-77.

Dias G, Leterrier J, Mendes A, et al (1998) U–Pb zircon and monazite geochronology of post-collisional Hercynian granitoids from the Central Iberian Zone (Northern Portugal). Lithos 45:349–369

Dias G, Simões PP, Ferreira N, and Leterrier J (2002) Mantle and crustal sources in the genesis of late-Hercynian granitoids (NW Portugal): geochemical and Sr-Nd isotopic constraints. Gondwana Res 5:287-305

Díez-Montes A (2006) La Geología del Dominio "Ollo de Sapo" en las comarcas de Sanabria y Terra do Bolo. Universidad de Salamaca

Farias P (1989) La geología de la región del sinforme de Verín (Cordillera herciniana, NW de España). Universidad de Oviedo

Farias P, Casado B, Marcos A, et al (2014) U-Pb zircon SHRIMP evidence for Cambrian volcanism in the Schistose Domain within the Galicia-Trás-os. Montes Zone (Variscan Orogen, NW Iberian Peninsula). Geol Acta 209–218

Gaspar L, Inverno CM (2000) Mineralogy and metasomatic evolution of distal strata-bound scheelite skarns in the Riba de Alva Mine, Northeastern Portugal. Econ Geol 95:1259–1275

Harlaux M, Mercadier J, Marignac C, et al (2018) Tracing metal sources in peribatholitic hydrothermal W deposits based on the chemical composition of wolframite: The example of the Variscan French Massif Central. Chem Geol 479:58–85

Martínez Catalán JR, Martínez Poyatos D, Bea F (2004) Zona Centroibérica. In: Vera JA (ed) Geología de España SGE-IGME. Sociedad Geológica de España--Instituto Geológico y Minero de España, Madrid, pp 68–133

Martins HC, Sant H, Noronha F (2013) Late-Variscan emplacement and genesis of the Vieira do Minho composite pluton, Central Iberian Zone: Constraints from U–Pb zircon geochronology, AMS data and Sr–Nd–O isotope geochemistry. Lithos 162:221-235

Melleton J, Gloaguen E, Frei D, Lima A (2011) U-Pb dating of columbite-tantalite from Variscan rare-elements granites and pegmatites. In: Goldschmidt. p Vol. 75, No. 3, 1452

Ordosch A, Raith JG, Schmidt S, Aupers K (2019) Polyphase scheelite and stanniferous silicates in a W-(Sn) skarn close to Felbertal tungsten mine, Eastern Alps. Mineral Petrol 113:703–725. https://doi.org/10.1007/S00710-019-00675-X

Schermerhorn LJG (1981) Framework and evolution of Hercynian mineralization in the Iberian Meseta. Leidse Geolo Meded 52:23–56

Villaseca C, Bellido F, Pérez-Soba C, Billström K (2009) Multiple crustal sources for post-tectonic I-type granites in the Hercynian Iberian Belt. Mineral Petrol 96:197-211

Villaseca C, Merino E, Oyarzun R, Orejana D, Pérez-Soba C, and Chicharro E (2014) Contrasting chemical and isotopic signatures from Neoproterozoic metasedimentary rocks in the Central Iberian Zone (Spain) of pre-Variscan Europe: Implications for terrane analysis and Early Ordovician magmatic belts. Precambrian Res 245:131-145.

Zhang R, Ramos V, Leal S, et al (2019) U-Pb geochronology of cassiterites from primary Sn mineralizations in Sn-W Variscan Metallogenic Province, Portugal. In: In Advances in Understanding Hydrothermal Processes, Life with Ore Deposits on Earth—15th SGA Biennial Meeting. pp 357–360

https://almonty.com Almonty Industries - Leaders In Tungsten. Accessed February 27, 2023

The role of micas in the origin of granite-related Sn-W-Nb-Ta mineralization

Karel Breiter[1], Michaela Vašinová Galiová[1], Michaela Hložková[1]
[1]BIC, Purkyňova 648, 62100 Brno, Czech Republic

Abstract. About 3000 spot LA-ICP-MS analyses of micas from eight typical rare-metal granite plutons were evaluated to establish possible correlation among trace-element (Li, Nb, Sn, Ta, W) spectra of micas. Igneous and hydrothermal micas play a substantial role in rare metal accumulation and redistribution although behavior of rare metals during magmatic/hydrothermal evolution of granites is highly variable. Maximum contents of metals in granitic mica reach ca. 1200 ppm Sn, 350 ppm W, 2300 ppm Nb and 600 ppm Ta, while micas in greisens reached 1500 ppm Sn, 140 ppm W, 500 ppm Nb and 150 ppm Ta. With increasing granite fractionation, the contents of Li in mica increase, while the contents of rare metals usually decrease as a consequence of the crystallization of Li-mica after the crystallization of the rare metal-bearing accessories. In greisens, similar to granites, Li-poor micas (muscovite, annite) are relatively Sn, W, Nb, Ta-enriched, while Li-rich zinnwaldite tends to be Sn, W, Nb, Ta-poor. Among distinctly mineralized quartz–mica veins, intragranitic veins (+cassiterite, wolframite) at Cínovec contain HFSE-poor zinnwaldite, while exogranitic wolframite-bearing veins at Panasqueira contains W-rich muscovite.

1 Introduction

Micas are, besides quartz and feldspars, the most common rock-forming minerals in all prospectively fertile rare-metal granites (RMG). Among common minerals, micas are certainly the most important host of many trace elements, strategic metals (Sn, W, Nb, Ta) and rare alkalis (Li, Rb, Cs) in particular. A routine application of ICP-MS method coupled with laser ablation to geological material in the last two decades allowed to obtain a large amount of *in situ* trace elements data on micas from fertile granitoids and related mineralization (van Lichtervelde et al. 2008; Xie et al. 2015; Legros et al. 2018; Launay et al. 2021; Monnier et al. 2022; Breiter et al. 2019, 2022, 2023). A comprehensive overview of the behavior of trace elements in micas during magmatic and hydrothermal processes is, however, still missing. We attempt to partly fill this gap targeting on the changes in Li, Sn, W, Nb and Ta in micas during a transition from the magmatic to hydrothermal stage of system evolution.

2 Studied granite plutons

Eight typical geologically well documented RMG plutons of different ages, geotectonic positions, geochemical types, and styles of mineralization were selected for this review (Figure 1):

1. Madeira metaaluminous to peralkaline pluton (1824–1818 Ma), Pitinga province, Brazil (Costi et al. 2009). The youngest subintrusion, peralkaline albite (+riebeckite, annite, lepidolite) granite contains large cryolite bodies and disseminated Sn, Nb and Th-mineralization.
2. Wiborg batholith, Finland, (1.67–1.54 Ga) including a late Kimi Li-mica-bearing granite stock, represents the large Lower Proterozoic rapakivi-type plutons with small late RMG intrusions (Lukkari et al. 2009).
3. Orlovka, Transbaikal region, Russia, sub- to peraluminous Jurassic pluton forms a layered body consisting of the (ascending order) biotite, muscovite, zinnwaldite and lepidolite facies with disseminated Ta-minerals (Badanina et al. 2004).
4. Cínovec/Zinnwald sub- to peraluminous late-Variscan granite pluton, Eastern Erzgebirge, Czech Republic/Germany intruded after a collapse of the Upper Carboniferous Teplice-Altenberg caldera. It is composed of lower biotite and upper zinnwaldite facies, the latter affected by pervasive zinnwaldite-dominant greisenization, and intersected by flat quartz-zinnwaldite veins with cassiterite and wolframite (Johan et al. 2012; Breiter et al. 2017).
5. Nejdek, late Variscan peraluminous pluton in the Western Erzgebirge, is composed of several facies of biotite granites and small late zinnwaldite granite stocks. It contains cupola-shaped quartz-Li-biotite greisen bodies with wolframite, and numerous steep zones of fissure-related quartz-muscovite greisen with cassiterite (Breiter 2012).
6. Beauvoir Li, P, F-rich lepidolite leucogranite (~310 Ma) is vertically fractionated and contains disseminated Sn and Ta mineralization (Raimbault et al. 1995). On the other side, the extent of muscovite bearing greisen is limited and the exo-

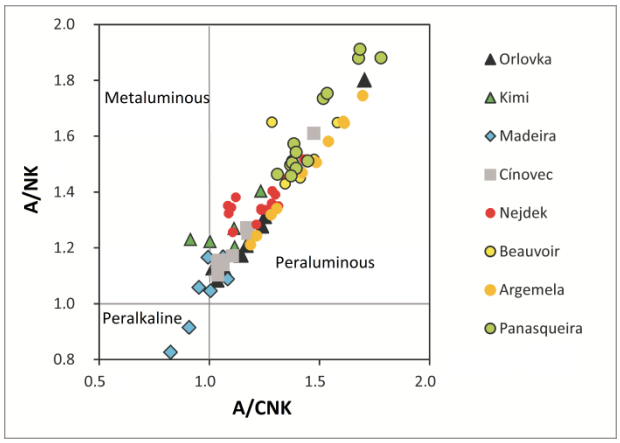

Figure 1. Classification of the studied granites according to their peraluminity/alkalinity (Badanina et al. 2004; Costi et al. 2009; Lukkari et al. 2009; Raimbault et al. 1995; author´s data).

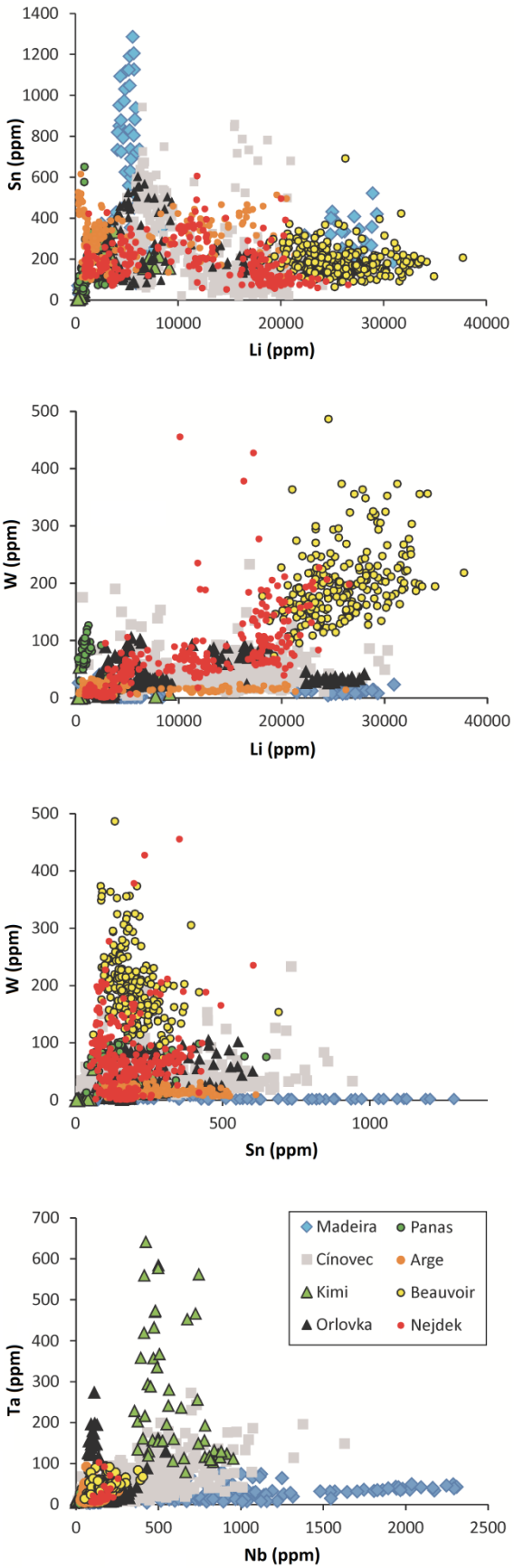

Figure 2. Sn, W, Nb and Ta contents in Li-bearing micas from fertile granitoids. Author's data.

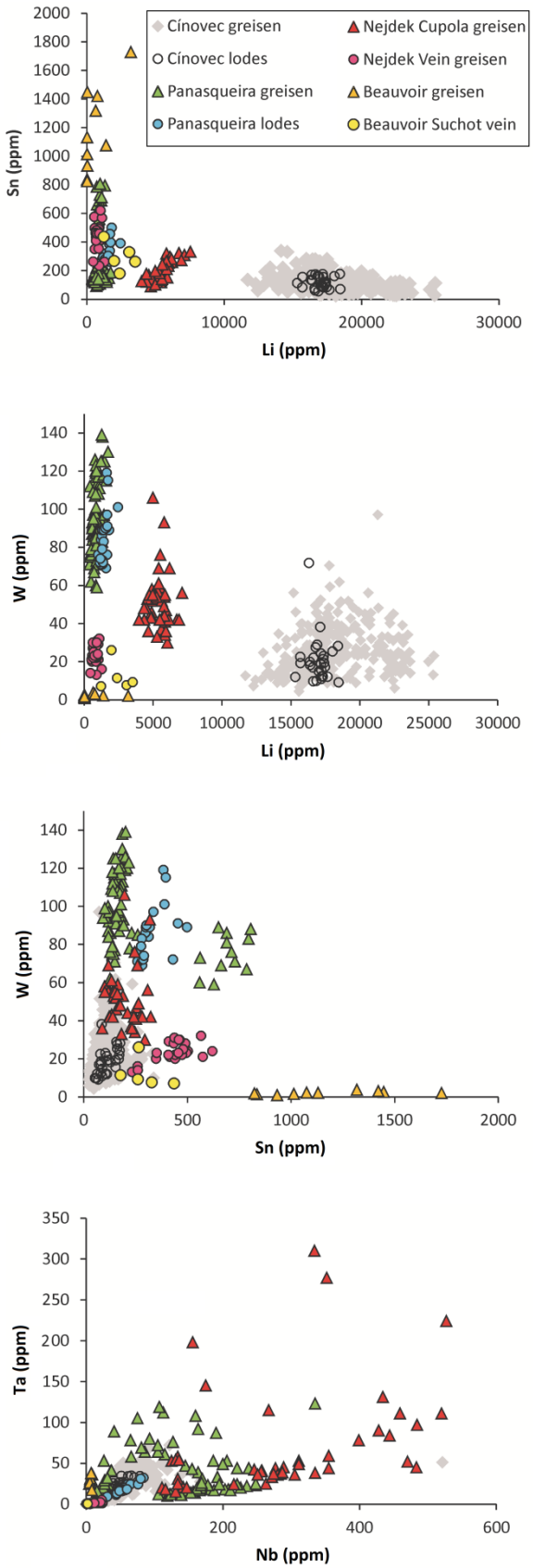

Figure 3. Sn, W, Nb and Ta contents in Li-bearing micas from greisen and granite-related veins. Data from the Beauvoir greisen and the Suchot vein from Monnier et al. (2022), other author´s data. Note the different scales in both figures.

contact aureole comprises only individual quartz veins (Monnier et al. 2022).
7. Panasqueira peraluminous pluton, Portugal, is composed of two-mica and muscovite facies, the later forming a greisenized cupola and a swarm of flat thick exocontact quartz-muscovite veins rich in wolframite (Marignac et al. 2020; Launay et al. 2021; Breiter et al. 2023).
8. Argemela stock, Portugal, is a small (<1 km^2) two-phase leucogranite intrusion rich in Li, P, and F, with distinctly zoned mica phenocrysts (muscovite to lepidolite), with scarce thin intragranitic quartz-wolframite veinlets (Charoy and Noronha 1996; Michaud and Pichavant 2020; Breiter et al. 2022).
The Beauvoir, Argemela, Panasqueira and Nejdek plutons represent strongly peraluminous, P-rich (S-type) (late)-orogenic granites, while Kimi, Orlovka and Cínovec represent mostly subaluminous, P-poor, post-orogenic (A-type) granites. Madeira albite granite is an example of scarce mica-bearing peralkaline granites.

The Cínovec deposits is the best example of pervasive Li-rich greisenization with addition of some mineralized intragranitic quartz veins, while the Beauvoir, Orlovka and Madeira deposits contain dominantly disseminated magmatic mineralization. The Panasqueira deposit is a typical exocontact vein-type deposit. In all these mineralization types, micas play an important role.

3 Analytical methods

The contents of trace elements in mica from Cínovec and Nejdek were analyzed using solid-state Nd:YAG laser (UP 213, New Wave Research, Inc., Fremont, California, USA) coupled to quadrupole-based ICP mass spectrometer Agilent 7500ce (Agilent Technologies, Inc., Santa Clara, California, USA) installed in the Department of Chemistry, Masaryk University, Brno. Other samples were analyzed at Faculty of Chemistry, Brno University of Technology and BIC Brno. Here, an ArF* excimer 193 nm laser ablation system Analyte Excite+ (Teledyne CETAC Technologies, Omaha, Nebraska, USA) was connected to the Agilent 7900 quadrupole ICP mass spectrometer (Agilent Technologies, Inc., Santa Clara, California, USA). For more details see Breiter et al. (2023).

4 Contents of Sn, W, Nb and Ta in micas from fertile granites

Tin, W, Nb, and Ta are high-field-strength-elements (HFSE); in the magmatic stage they commonly enter the early crystallized Ti oxides, or tend to form disseminated cassiterite, columbite or pyrochlore groups of minerals later. Their contents in mica thus depend on the timing of crystallization of mica *vs.* accessory minerals. The content of Li in mica is a relevant indicator of geochemical evolution of magmatic systems. Thus, the results are presented as bivariate Li *vs.* metal diagrams (Figures 2, 3).

Tin is one of ubiquitous trace elements in mica starting from common calc-alkaline granites (up to 100 ppm); reaching 600 ppm in phengite from Orlovka and in zinnwaldite from Piaotang, China (Legros et al. 2018), 800 ppm in biotite and zinnwaldite from Cínovec, and 1300 ppm in annite from peralkaline granite of Madeira. The contents of W reached about 100 ppm in muscovite from Panasqueira and in phengite and zinnwaldite from Orlovka, 200 ppm in zinnwaldite from Nejdek, and 350 ppm in lepidolite from Beauvoir. The Sn/W values, (18 in C1 chondrites, McDonough and Sun 1995) vary from >100 in micas in peralkaline Madeira granite to 0.5 in Beauvoir and Nejdek and do not correlate with Sn or W fertility of the pluton.
Niobium is the most common trace element in micas among all discussed HFSE, reaching about 1000 ppm in biotite from Cínovec, 1500 ppm in Li-annite from Huangshan, China (Zhu et al. 2018), and 2400 ppm in annite from peralkaline granite from Madeira. The highest values of Ta, up to 200 ppm, were found in micas from Orlovka, Cínovec, Nejdek and from the Tanco pegmatite (Van Lichtervelde et al. 2008). The Nb/Ta values in micas (Nb/Ta=17 in chondrite, McDonough and Sun 1995) are very variable: from ~50 in peralkaline granite of Madeira through ~5 in Beauvoir and Nejdek to 0.5 in zinnwaldite from Orlovka.
The contents of all HFSE in micas usually increase during initial stages of magmatic fractionation, while their behaviour in final stages of plutons evolution is very diverse. Generally, with increasing Li-contents, the contents of Sn, Nb and Ta decreased, while the contents of W increase or remain stable. An exception is the strong enrichment in Ta and Nb in late magmatic rims of lepidolite at Argemela (Breiter et al. 2022).

5 Micas from greisen and ore veins

The term “greisen” comprises a whole range of potentially ore-bearing quartz–mica dominated hydrothermal lithologies. The composition of greisen micas spans from muscovite across zinnwaldite to annite, whereas Li-enriched varieties are the most typical.

Pervasive greisens forming large pericontact bodies in granite cupolas are typical for shallow-level granite intrusions in the Erzgebirge: zinnwaldite-rich greisens in cupolas of strongly evolved granites usually contain cassiterite>> wolframite, while wolframite dominates in annite-bearing cupola-shaped greisens in less evolved granite facies. Lower-tempered fissure-related muscovite (phengite)-dominated greisens are usually cassiterite-bearing. In greisens, much like in granites, Li-poor micas (muscovite, annite) are Sn, W, Nb, Ta-enriched, while Li-rich zinnwaldite tends to be Sn, W, Nb, Ta-poor. Among distinctly mineralized quartz–mica veins, the intragranitic veins (+cassiterite and wolframite) at Cínovec contain HFSE-poor zinnwaldite, while the exogranitic wolframite-bearing veins at Panasqueira contain W-rich muscovite.

Lower contents of Sn and W in greisen micas at Cínovec compared to those in their magmatic precursors led Johan et al. (2012) to believe that magmatic annite was the main reservoir of Sn and W. During greisenization, the metals were, by the action of F-rich solutions, released forming cassiterite and wolframite in veins and greisen bodies. In contrast, Monnier et al. (2022) documented from Beauvoir, that, in this case a F-poor fluid destroyed magmatic cassiterite and W-enriched lepidolite; released tin was bound to newly formed Sn-rich (up to 1700 ppm) greisen muscovite, while W was transported away, forming exocontact vein-type wolframite mineralization.

6 Concluding remarks

Igneous and hydrothermal micas play a substantial role in HFSE accumulation and redistribution. The maximum contents reach ca. 1200 ppm Sn, 350 ppm W, 2300 ppm Nb and 200 ppm Ta.

With increasing fractionation of granite systems, demonstrated as vertical zoning (Cínovec, Orlovka, Beauvoir) or as a suite of subsequent intrusions (Madeira, Nejdek, Panasqueira), Li contents in mica increase, while the contents of HFSE usually decrease. Rather than the influence of the crystal structure, it is a consequence of the crystallization of Li-mica after the crystallization of the HFSE accessories. An exception is the Beauvoir granite with nearly identical contents of HFSE along the whole known vertical profile.

Micas from the peraluminous RMG are generally enriched in W, while micas from the subaluminous A-type granites are relatively enriched in Nb.

During greisenization, the share of mica in the HFSE budget usually strongly decreases and rutile, cassiterite and columbite become the main hosts of rare metals. However, an opposite example was recorded at Beauvoir. This illustrates the great variability in HFSE behavior during the magmatic/hydrothermal transition, which calls for further research.

Acknowledgements

This contribution was supported by the Czech Science Foundation, project EXPRO 19-29124X.

References

Badanina EV, Veksler IV, Thomas R et al (2004) Magmatic evolution of Li-F rare-metal granites: a case study of melt inclusions in the Khangilay complex, Eastern Transbaikalia (Russia). Chem Geol 210: 113–133

Breiter K (2012) Nearly contemporaneous evolution of the A- and S-type fractionated granites in the Krušné hory/Erzgebirge Mts., Central Europe. Lithos 151: 105–121

Breiter K, Ďurišová J, Hrstka T et al (2017) Assessment of magmatic vs. metasomatic processes in rare-metal granites: a case study of the Cínovec-Zinnwald Sn–W–Li deposit, Central Europe. Lithos 292: 198–217

Breiter K, Hložková M, Korbelová Z, Vašinová Galiová M (2019) Diversity of lithium mica compositions in mineralized granite–greisen system: Cínovec Li-Sn-W deposit, Erzgebirge. Ore Geol Rev 106: 12–27

Breiter K, Ďurišová J, Korbelová Z et al. (2022) Rock textures and mineral zoning – A clue to understanding rare-metal granite evolution: Argemela stock, Central-Eastern Portugal. Lithos 410–411: 106562

Breiter K, Ďurišová J, Korbelová Z et al. (2023) Granite Pluton at the Panasqueira Tungsten Deposit. Minerals 13, 163.

Charoy B, Noronha F (1996) Multistage growth of a rare-element, volatile-rich microgranite at Argemela (Portugal). J Petrol 37: 73–94

Costi HT, Dall´Agnol R, Pichavant M, Rämö OT (2009) The peralkaline tin-mineralized Madeira cryolite albite-rich granite of Pitinga, Amazonian craton, Brazil: petrography, mineralogy and crystallization processes. Canad Mineral 47: 1301–1327

Johan Z, Strnad L, Johan V (2012) Evolution of the Cínovec (Zinnwald) granite cupola, Czech Republic: composition of feldspars and micas, a clue to the origin of W, Sn mineralization. Canad Mineral 50: 1131–1148

Launay G, Sizaret S, Lach P et al (2021) Genetic relationship between greisenization and Sn-W mineralizations in vein and greisen deposits: insights from the Panasqueira deposit (Portugal). BSGF Earth Sci Bull 192: 2

Legros H, Marignac C, Tabary T et al (2018) The ore-forming magmatic-hydrothermal system of the Piaontang W-Sn deposit (Jiangxi, China) as seen from Li-mica geochemistry. Amer Mineral 103: 39–54

Lukkari S, Thomas R, Haapala I (2009) Crystallization of the Kymi topaz granite stock within the Wiborg rapakivi batholith, Finland: Evidence from melt inclusions. Canad Mineral 47: 1359–1374

Marignac C, Cuney M, Cathelineau M et al (2020) The Panasqueira rare metal granite suites and their involvement in the genesis of the world-class Panasqueira W-Sn-Cu deposit: a petrographic, mineralogical, and geochemical study. Minerals 10: 562

McDonough WF, Sun S (1995) The composition of the Earth. Chem Geol 120: 223–253

Michaud JAS, Pichavant M (2020) Magmatic fractionation and the magmatic-hydrothermal transition in rare metal granites: evidence from Argemela (Central Portugal). Geochim Cosmochim Acta 289: 130–157

Monnier L, Salvi S, Melleton J et al (2022) Mica trace-element signatures: highlighting superimposed W-Sn mineralizations and fluid sources. Chem Geol 600: 120866

Raimbault L, Cuney M, Azencott C et al (1995) Geochemical evidence for a multistage magmatic genesis of Ta–Sn–Li mineralization in the granite at Beauvoir, French Massif Central. Econ Geol 90: 548–596

Van Lichtervelde M, Grégoire M, Linnen RL et al (2008) Trace element geochemistry by laser ablation ICP-MS of micas associated with Ta mineralization in the Tanco pegmatite, Manitoba, Canada. Contrib Mineral Petrol 155: 791–806

Xie L, Wang RC, Groat LA et al (2015) A combined EMPA and LA-ICP-MS study of Li-bearing mica and Sn–Ti oxide minerals from the Qiguling topaz rhyolite (Qitianling district, China): the role of fluorine in origin of tin mineralization. Ore Geol Rev 65: 779–792

Zhu Z, Wang R, Marignac C et al (2018) A new type of rare metal granite with Nb-rich mica: the early Cretaceous Huangshan rare-metal granite suite, northeast Jiangxi Province, China. Amer Mineral 103: 1530–1544

Fluid evolution in the San Rafael Sn-Cu lode deposit, Peru: Constraints from fluid inclusion analyses and chlorite geochemistry

Malena Cazorla Martínez[1*], Kalin Kouzmanov[1], Alexandra Tsay[1], Zoltán Zajacz[1], Florence Bégué[1], Matthieu Harlaux[2], Miroslav Kalinaj[3], Lluís Fontboté[1]
[1]Department of Earth sciences, University of Geneva, Geneva, Switzerland
[2]BRGM – French Geological Survey, 45060 Orléans, France
[3]MINSUR S.A., Peru
**Present address: iCRAG, University College Dublin Belfield, Dublin 4, Ireland*

Abstract. We have studied the evolution of mineralizing fluids in the world-class San Rafael Sn-Cu lode district, Peru, by investigating the major and trace element compositions of fluid inclusions and hydrothermal chlorite from four major mineralization stages of the deposit. Hypersaline liquid, vapor, and liquid-vapor fluid inclusion assemblages in quartz, fluorite, and cassiterite have been analyzed by microthermometry, Raman spectroscopy and LA-ICP-MS. Salinity and homogenization temperature decrease from stage I to stage IV. Most element concentrations in the fluid inclusions (e.g., Zn, Pb, Na) decrease progressively from stage I to stage IV, except for B. Fluid mixing at 350-250ºC of a hypersaline, high-temperature, metal-bearing, magmatic fluid with a low-temperature and low-salinity fluid is proposed to explain the fluid dilution and the decrease in temperature and salinity. Widespread presence of CH_4 in fluid inclusions indicates the reduced character of the fluids. Constant B content throughout the four hydrothermal stages could result from the replacement of early-stage tourmaline by chlorite, bringing B into solution continuously. Copper, Zn, Pb, and Mn are enriched in chlorite belonging to stage IV. The Ti/Pb and Ni/Cu trace element ratios in chlorite correlate with fluid temperatures and could be used as proxies for temperature evolution at San Rafael.

1 Introduction

The Central Andean tin belt (CATB) of the South American Cordillera is a major metallogenic province that extends from southern Peru, through Bolivia, to northern Argentina (Lehmann et al. 1990). The CATB hosts numerous Sn-W±Ag-Cu deposits, including Mesozoic mesothermal Sn-W deposits in its northern sector, and Oligocene to Miocene polymetallic Sn-W deposits along the entire belt (Clark et al. 1990). The San Rafael Sn-Cu deposit, located in the northernmost tip of the CATB, is currently one of the largest hypogene Sn deposits worldwide (total past production + remaining resources of >1.5 Mt of Sn with an average grade of 3.7%; Harlaux et al. 2023). In 2020, Minsur S.A. has reported 195,300 t fine Sn in measured + indicated resources and 73,600 t fine Sn in inferred resources, while total reserves were estimated at 132,000 t fine Sn (Minsur S.A. 2021).
The geological and structural setting, the paragenetic sequence, and the rock and mineral geochemistry of the San Rafael deposit have been extensively studied (e.g., Arenas 1980; Palma 1981; Kontak and Clark 2002; Mlynarczyk et al. 2003; Mlynarczyk 2005; Mlynarczyk and Williams-Jones 2005, 2006; Wagner et al. 2009; Corthay 2014; Prado Flores 2015; Harlaux et al. 2020, 2021a, b). Fluid inclusion microthermometry data for San Rafael have been reported in some of the previous studies; however, no trace element data about the mineralizing fluids are available for this major Sn deposit.

In the present study, we report new fluid inclusion trace element analyses and chlorite mineral compositional data that provide new insights into the fluid evolution of the world-class San Rafael Sn-Cu lode deposit with emphasis on the origin of the mineralizing fluids and ore forming processes.

2 Geological setting

The San Rafael deposit is located in the Eastern Cordillera of southeast Peru. The San Rafael intrusive complex consists of several granitic bodies, which were emplaced during the Late Oligocene (ca. 24 Ma) into Carboniferous and Ordovician metasedimentary rocks, producing contact metamorphism (Kontak and Clark 2002; Harlaux et al. 2021a, 2023). The mineralization is hosted by NW-trending, quartz-cassiterite-sulfide veins and breccia bodies, both spatially associated with the granitic complex (Kontak and Clark 2002; Mlynarczyk et al. 2003), as well as late-stage polymetallic veins.

Four major mineralization stages have been identified at San Rafael (Arenas 1980; Palma 1981; Kontak and Clark 2002; Mlynarczyk et al. 2003; Wagner et al. 2009): (1) an early, pre-ore quartz-tourmaline stage I; (2) a main Sn ore stage II, occurring in quartz-chlorite-cassiterite veins and breccia bodies; (3) a sulfide-dominant stage III, associated to the major deposition of base metal sulfides (e.g., chalcopyrite, pyrrhotite, sphalerite, arsenopyrite, pyrite, and galena); and finally (4) a late, barren stage IV, consisting of banded silica, platy calcite, fluorite, adularia, with minor sulfides and carbonates.

3 Materials and methods

Thirty-two samples, both from surface outcrops and underground workings from the San Rafael mine

and the Quenamari prospect, representative of each of the mineralization stages have been selected. Mineralogy and textures were studied by optical microscopy, optical and SEM cathodoluminescence, BSE imaging, and QEMSCAN mapping at the Department of Earth sciences, University of Geneva.

Petrography of fluid inclusion assemblages (FIA) was followed by microthermometric measurements on a Linkam THMSG 600 stage mounted on a Leica DMLB microscope for transparent minerals, and a Linkam FTIR 600 stage mounted on an Olympus BH2 microscope for near-infrared microthermometry of opaque minerals. Raman spectroscopy analyses have been performed on the vapor, liquid, and solid phases in the FIs, using a LabRAM HR Evolution (HORIBA Scientific) Raman spectrometer. LA-ICP-MS analyses on individual FIs were conducted using a NWR 193 He Laser Ablation system coupled to an Agilent 8900 triple quadrupole mass spectrometer. Isotopes analyzed include ^{7}Li, ^{11}B, ^{23}Na, ^{29}Si, ^{34}S, ^{35}Cl, ^{39}K, ^{43}Ca, ^{55}Mn, ^{56}Fe, ^{65}Cu, ^{66}Zn, ^{75}As, ^{79}Br, ^{85}Rb, ^{88}Sr, ^{108}Ag, ^{118}Sn, ^{133}Cs, ^{137}Ba, ^{204}Tl, and ^{208}Pb.

Hydrothermal chlorites from 9 samples have been analyzed by EMPA for major and minor elements using a JEOL 8200 Superprobe and by LA-ICP-MS for trace elements using a NWR 193 He Laser Ablation system coupled to an Agilent 8900 triple quadrupole mass spectrometer.

4 Results

4.1 Fluid inclusion study

FIAs from the four mineralization stages have been studied (Figure 1): secondary hypersaline liquid (L-V-NaCl; “brines”), high-density vapor (V), and aqueous liquid-vapor (L-V) FIAs in stage-I quartz and tourmaline; primary and pseudo-secondary L-V and low-density V FIAs in stage-II quartz; primary and pseudo-secondary L-V FIAs in stage-III quartz; and primary, pseudo-secondary, and secondary L-V, solid-liquid-vapor (L-V-S), and boiling (liquid+vapor) FIAs in stage IV quartz and fluorite. Average homogenization temperatures for stages I, II, III and IV are 402 ± 27ºC, 287 ± 26ºC, 291 ± 47ºC, and 244 ± 35ºC, respectively. Fluid salinity ranges between 48.0 ± 2.5 wt% NaCl eq. for L-V-NaCl FIs, and 15.6 ± 4.5 wt% NaCl eq. for L-V FIs in stage I. Average salinity in stage II is 7.5 ± 6.3 wt% NaCl eq., 5.3 ± 3.0 wt% NaCl eq. in stage III, 4.1 ± 3.3 wt% NaCl eq. in fluorite-hosted FIAs from stage IV, and 0.6 ± 0.6 wt% NaCl eq. in banded silica-hosted FIAs from stage IV.

Raman spectroscopy analyses allowed identification of CH_4 in FIs from all the stages, boric acid in FIs from stages II and IV, calcite crystals in FIs from stage IV, and Fe-bearing hydroxychloride daughter crystals in brines from stage I (i.e., Fe-pyrosmalite $Fe_8Si_6O_{15}(OH, Cl)_{10}$ and hibbingite γ-$Fe_2(OH)_3Cl$).

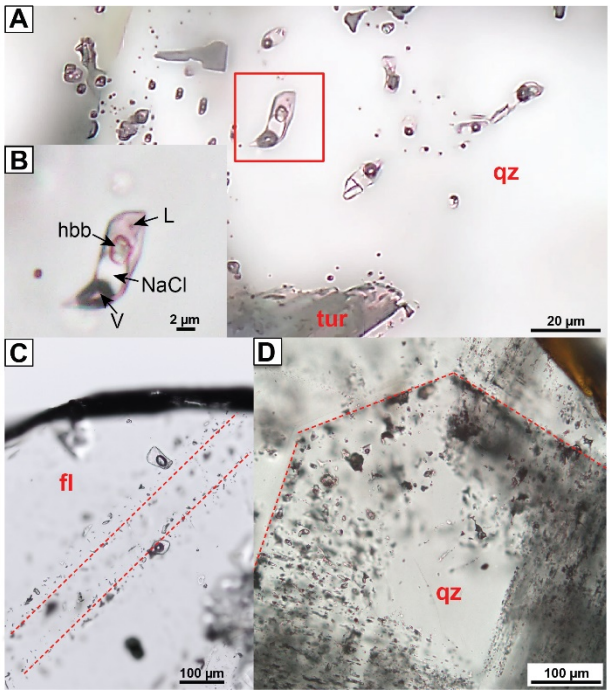

Figure 1. Fluid inclusion assemblages observed in studied samples from the San Rafael Sn-Cu deposit. A) Quartz-hosted L-V-NaCl FIs from stage I. B) Close up of the FI in A. C) Fluorite-hosted primary L-V FIs from stage IV. D) Quartz-hosted primary L-V FIs from stage IV. Dashed red lines represent primary growth banding. *Abbreviations:* fl - fluorite; hbb - hibbingite; L – liquid ; qz - quartz; tur – tourmaline; V - vapor.

LA-ICP-MS analyses of FIAs show variations of up to 3 orders of magnitude for Na, K, Ca, Cl, Sr, Mn, Tl, Zn, Pb, and Ba concentrations between FIs from stage I and those from stage IV (Fig. 2; e.g., 1,000-10,000 ppm Pb in stage I, and 1-10 ppm Pb in stages III-IV).

Elements such as B (and Li to a lesser extent) show similar contents in FIAs from all the stages with values of 1,000-10,000 ppm B. Iron, Sn, and Cu were not detected in most of the FIs. Nevertheless, brine FIAs belonging to stage I yield anomalously high Fe (1-10 wt.% Fe) and high Sn concentrations (200-2,000 ppm Sn). In addition, FIAs from stage I show higher values of Fe and Na/K ratio than most FIs from stages II, III, and IV.

4.2 Chlorite geochemistry

Chlorite is a major gangue mineral in stages II, III, and IV, typically intergrown with quartz, cassiterite and sulfides. Chlorite in veins and their alteration halos has been analyzed from the three stages of mineralization, although most analyses have been performed on vein chlorite.

Most of the studied chlorite aggregates at San Rafael is classified as Fe-chlorite (ripidolite and daphnite), except for several chlorites from Quenamari which correspond to Al-chlorite (diabentite). Furthermore, chlorites in samples

from stage IV at Quenamari are enriched in Mn (1-2.5 wt% MnO) relative to those from stages II and III at San Rafael (~0.3 wt% MnO).

The most abundant trace elements in the analyzed chlorites are Li (200-900 ppm), B (3-50 ppm), Ti (10-1,000 ppm), V (1-100 ppm), Co (1-1,000 ppm), Ni (1-1,000 ppm), Cu (0.01-1,000 ppm), Zn (20-5,000 ppm), Sr (0.1-10 ppm), Sn (10-1,000 ppm), and Pb (1-1,000 ppm). However, it must be noticed that the contents of several elements such as Pb, Cu, Zn, Ni, and Ti vary remarkably across chlorites from different stages. Concentrations of Cu, Zn, and Pb in stage IV chlorite are ~2 orders of magnitude higher than that in stages II and III. Conversely, Ni contents are within one sample systematically lower in stage IV than in stages II and III.

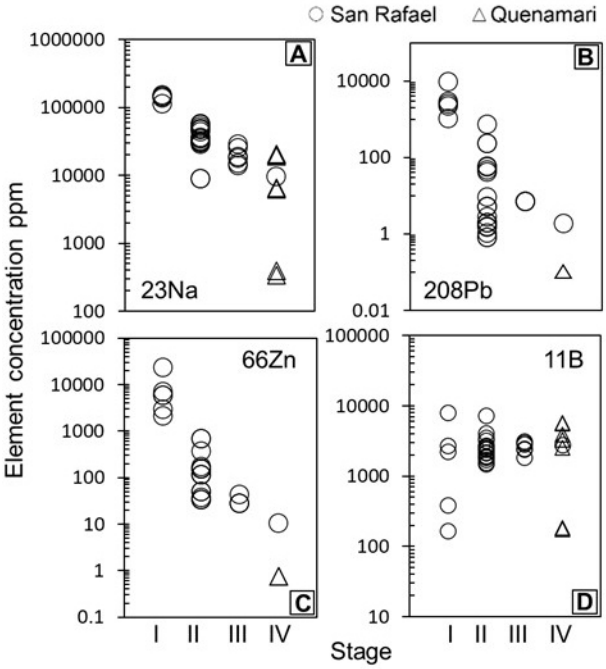

Figure 2. Element concentrations analyzed by LA-ICP-MS in individual quartz-hosted fluid inclusions from stages I, II, III, and IV. Each symbol corresponds to an individual fluid inclusion analysis. A) Sodium. B) Lead. C) Zinc. D) Boron.

5 Discussion

5.1 Fluid evolution

Fluids of magmatic origin were the dominant fluid type during the early stage of mineralization. They are characterized by high Fe concentrations (found in some FIs belonging to stage I, as indicated by LA-ICP-MS analyses and the presence of hibbingite and Fe-pyrosmalite daughter crystals), and relatively low Na/K ratios in comparison to FIs from the later stages. As proposed by some authors (Audétat et al. 1998; Harlaux et al. 2017), fluid mixing between an early, high-temperature, metal-rich magmatic fluid and a low-temperature, low-salinity, and metal-depleted fluid may cause the drop of 2-3 orders of magnitude of element concentrations within the evolution of the early- to the late-stage FIAs (Figs. 2A-C), in parallel to a constantly decreasing homogenization temperature (Figs. 3B-D) and salinity. The presence of CH_4 in the studied FIAs is indicative of the reduced character of the fluids, which is consistent with the mineral paragenesis of the ore assemblages. Previous stable isotope studies (Wagner et al. 2009; Harlaux et al. 2021a) demonstrated the importance of fluid mixing between magmatic fluids and meteoric waters for ore deposition at San Rafael.

Stage-I FIs show high concentrations of Sn (100-1000 ppm), which highlights the potential of these fluids to precipitate large amounts of cassiterite during the late stage. Boron concentrations in the fluid are constant from early to late stages of mineralization (Figs. 2D and 3A; 1,000-10,000 ppm), that could result from the shift from tourmaline alteration in stage I to chloritization, replacing tourmaline, from stage II onwards (this study; Mlynarczyk 2005). When tourmaline is replaced by chlorite, B is released again into the fluid, which seems to results in elevated and constant B concentrations in the fluid..

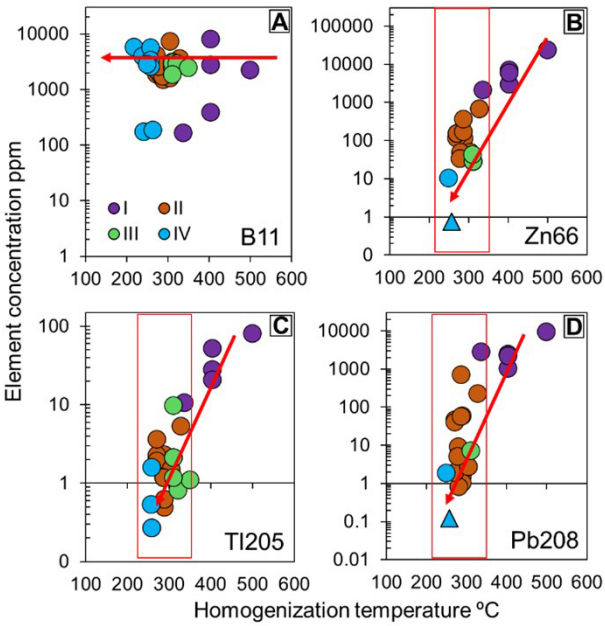

Figure 3. Element concentration in individual fluid inclusions. vs. homogenization temperatures plots of A) Boron, B) Zinc, C) Thallium, and D) Lead. Each spot represents an individual fluid inclusion. Red square represents the interpreted temperature range at which fluid mixing took place. Red arrows represent the general evolutionary trend from early to late stages.

5.2 Chlorite compositions

High Mn content in chlorite from the Quenamari prospect – stage IV – is attributed to the presence of a late well-developed Mn-rich assemblage in the Quenamari prospect (Corthay 2014), which is missing in the San Rafael deposit.

As proposed by Wilkinson et al. (2015), chlorite trace element ratios, such as Ti/Pb, can be used as

vectors for high-temperature centers in porphyry ore deposits. In the present study, chlorite trace element ratios of specific elements (following the methodology of Wilkinson et al. 2015) were compared to FI homogenization temperatures obtained for the same sample (Fig. 4). Results show that the samples with the lowest homogenization temperatures (Fig. 4A) are those yielding the lowest values for the Ni/Cu and Ti/Pb ratios (Figs. 4B-C), and vice versa.

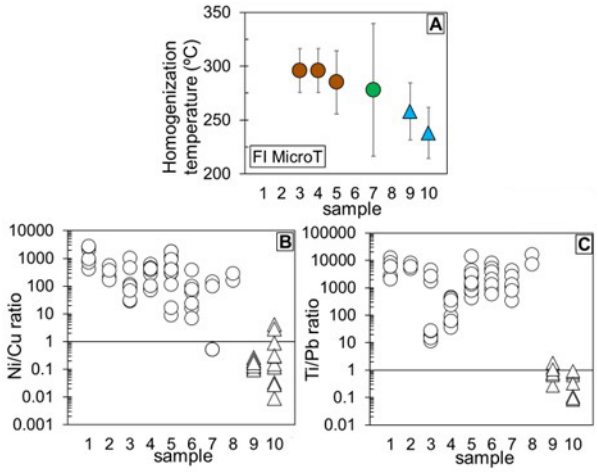

Figure 4. A) Average fluid inclusion homogenization temperatures for samples where chlorite geochemistry was studied. Error bars correspond to standard deviation. B) Ni/Cu and C) Ti/Pb ratios in chlorites from the San Rafael deposit.

6 Conclusions

Fluid inclusion analysis document a distinct decrease in trace element concentrations from early to late stages at San Rafael, consistent with a progressive decrease in temperature and salinity of the fluids. Fluid systematicsare interpreted to be related to fluid mixing at 250-350ºC of early hypersaline (40-50 wt% NaCl), hot (>400ºC), metal-rich (20,000-130,000 ppm Fe, 100-1,000 ppm Sn, 1,000-10,000 ppm Zn, 1,000-10,000 ppm Pb) magmatic fluids, with lower-temperature (~200ºC), low-salinity (~1 wt% NaCl), metal-poor meteoric waters. Constant B concentrations in early- to late-stage FIAs is interpreted to result from tourmaline replacement by chlorite, maintaining a constant release of B along the fluid flow path.

Mn-bearing chlorite at Quenamari are indicative of the presence of a Mn-rich stage developed in that part of the district, which has not been previously recognized at the San Rafael deposit. The Ti/Pb and Ni/Cu trace element ratios in chlorite at San Rafael are proposed as possible proxies for high-temperature mineralization centers, possibly unexposed in the Quenamari area.

References

Arenas MJ (1980) El distrito minero San Rafael, Puno – Estaño en el Perú. B Soc Geol Perú 66:1-11.

Audétat A, Günther D, Heinrich CA (1998) Formation of a magmatic-hydrothermal ore deposit: Insights with LA-ICP-MS analysis of fluid inclusions. Sciences 279(5359): 2091-2094.

Clark AH, Farrar E, Kontak DJ, Langridge RJ, Arenas FMJ, France LJ, McBride SL, Woodman PL, Wasteneys HA, Sandeman HA,Archibald DA (1990) Geologic and geochronologic constraints on the metallogenic evolution of the Andes of southeastern Peru. Econ Geol 85:1520-1583

Corthay G (2014) The Quenamari prospect, San Rafael tin District, southern Peru: Geology, mineral assemblages, fluid inclusion microthermometry, and stable isotopes. Unpubl. MSc thesis, University of Geneva, Switzerland.

Kontak DJ, Clark AH (2002) Genesis of the giant, bonanza San Rafael lode tin deposit, Peru: origin and significance of pervasive alteration. Econ Geol 97:1741-1777.

Harlaux M, Mercadier J, Bonzi WME, Kremer V, Marignac C, Cuney M (2017) Geochemical signature of magmatic-hydrothermal fluids exsolved from the Beauvoir rare-metal granite (Massif Central, France): Insights from LA-ICPMS Analysis of primary fluid inclusions. Geofluids:1-25.

Harlaux M, Kouzmanov K, Gialli S, Laurent O, Rielli A, Dini A, Chauvet A, Menzies A, Kalinaj M, Fontboté L (2020) Tourmaline as a Tracer of Late-Magmatic to Hydrothermal Fluid Evolution: The World-Class San Rafael Tin (-Copper) Deposit, Peru. Econ Geol 115:1665-1697.

Harlaux M, Kouzmanov K, Gialli S, Clark AH, Laurent O, Corthay G, Prado Flores E, Dini A, Chauvet A, Ulianov A, Chiaradia M, Menzies A, Villón Durand G, Kalinaj M, Fontboté L (2021a) The upper Oligocene San Rafael intrusive complex (Eastern Cordillera, southeast Peru), host of the largest-known high-grade tin deposit. Lithos 400-401:106409.

Harlaux M, Kouzmanov K, Gialli S, Marger K, Bouvier AS, Baumgartner LP, Rielli A, Dini A, Chauvet A, Kalinaj M, Fontboté L (2021b) Fluid mixing as primary trigger for cassiterite deposition: Evidence from in situ $\delta^{18}O$-$\delta^{11}B$ analysis of tourmaline from the world-class San Rafael tin deposit, Peru. Earth Planet Sci Lett 563:116889.

Harlaux M, Kontak DJ, Clark AH, Kouzmanov K, Holm-Denoma CS, Gialli S, Laurent O, Spikings R, Chauvet A, Dini A, Kalinahj M, Fontboté L (accepted) Depositing over 1.5 Mt of Sn within 1Ma of initial granitic intrusion in the San Rafael Sn (-Cu) deposit, southeastern Peru. Econ Geol.Lehmann B, Ishihara S, Michel H, Miller J, Rapela CW, Sanchez A, Tistl M, Winkelmann L (1990) The Bolivian tin province and regional tin distribution in the central Andes: A reassessment. Econ Geol 85:1044-1058.

Minsur S.A. (2021) Annual Report: March 28, 2022, 71 p., www.minsur.com.

Mlynarczyk MS, Sherlock RL, Williams-Jones AE (2003) San Rafael, Peru: geology and structure of the world's richest tin lode. Miner Deposita 38:555-567.

Mlynarczyk MSJ (2005) Constraints on the genesis of lode-style tin mineralization: Evidence from the San Rafael Tin-Copper deposit, Peru. PhD Thesis, Department of Earth and Planetary Sciences, McGill University, Montreal, Canada.

Mlynarczyk MS, Williams-Jones AE (2005) The role of collisional tectonics in the metallogeny of the Central Andean tin belt. Earth Planet Sci Lett 240:656-667.

Mlynarczyk MS, Williams-Jones AE (2006) Zoned tourmaline associated with cassiterite: implications for fluid evolution and tin mineralization in the San Rafael Sn–Cu deposit, southeastern Peru. Can Mineral 44:347-365.

Palma VV (1981) The San Rafael tin–copper deposit, Puno, SE Peru. Master's Thesis, Queen's University, Kingston, Ontario, United States of America.

Prado Flores E (2015) San Rafael Tin Mine, Peru: Geology, mineralogy, O and H stable isotopes, and fluid inclusions microthermometry of the deep level 3600m. Unpubl. MSc thesis, University of Geneva, Switzerland, 89 p.

Wagner T, Mlynarczyk MS, Williams-Jones AE, Boyce AJ (2009) Stable isotope constraints on ore formation at the San Rafael tin-copper deposit, Southeast Peru. Econ Geol 104: 223-248.

Wilkinson JJ, Chang Z, Cooke DR, Baker MJ, Wilkinson CC, Inglis S, Chen H, Gemmel JB (2015) The chlorite proximitor: A new tool for detecting porphyry ore deposits. J Geoch Explor 152: 10-26.

Multi-phase tungsten mineralisation at the world class Hemerdon deposit, south-west England

Eimear Deady[1,2], K. Moore[1], R.K. Shail[1], K.M. Goodenough[2] and S. Chenery[2]
[1]Camborne School of Mines, University of Exeter, UK
[2]British Geological Survey, UK

Abstract. Tungsten mineralisation in the form of wolframite is commonly hosted in greisen stockworks associated with peraluminous granites globally. Tungsten mineralisation at the world-class Hemerdon deposit, located in south-west England, has a complicated mineralogical and chemical history, which records repeated fluid-derived alteration, dissolution and (re)precipitation. Limited evidence for the coeval deposition of cassiterite with wolframite has been found at Hemerdon.

1 Introduction

The Variscan granite-related mineralisation at Hemerdon comprises one of the largest tungsten deposits in the world. It has a combined, JORC-compliant, mineral resource estimate of 351.5 Mt at 0.12% WO_3 and 0.03% Sn (Tungsten West, 2022). The Hemerdon Ball Granite is a G2 muscovite granite cupola and dyke (Simons et al. 2016), separate but adjacent to the Dartmoor Granite in Devon, south-west England. The Cornubian Batholith is subclassified into five different peraluminous granites, where G2 represents the muscovite granite. It hosts a greisen-bordered sheeted vein system with ferberite and wolframite (± cassiterite) mineralisation approximately 100+ m wide. Mineralisation extends into the metasedimentary host rocks. The deposit was recently exploited (2015–18) at the Drakelands Mine and is in the process of redevelopment by Tungsten West (2020–present).

This study uses combined optical microscopy, cathodoluminescence, SEM, EPMA, fluid inclusion microthermometry, stable and radiogenic isotopes and LA-ICP-MS point and mapping analysis to establish a detailed paragenetic succession for the mineralisation at the Hemerdon deposit. We also determine the concentration of major and trace elements in wolframite. Our aim is to provide new constraints on the physico-chemical evolution of sheeted vein wolframite deposits.

2 Petrography

2.1 Mineral assemblages and paragenetic relationships

Tungsten mineralisation is typically hosted in greisen, or greisen-absent quartz-dominated veins. The metallic mineral assemblages comprise wolframite and/or ferberite (the iron-rich end-member of the wolframite series) + arsenopyrite ± chalcopyrite, pyrite, native bismuth, cassiterite (Figure 1). Both wolframite and ferberite are present as primary phases at Hemerdon, while secondary, recrystallised ferberite is common along crystal boundaries, fractures, and occasionally as a replacement (or alteration) phase associated with the pervasive alteration of wolframite (Figure 2a).

Accessory phases in the tungsten-bearing veins include, in varying amounts, apatite, fluorite, monazite, tourmaline, rutile, scorodite, cassiterite, native bismuth, xenotime and zircon. The role the accessory phases, in particular the phosphates and fluorides, play in the deposition of wolframite (Wang et al., 2023) will be considered in the ongoing research.

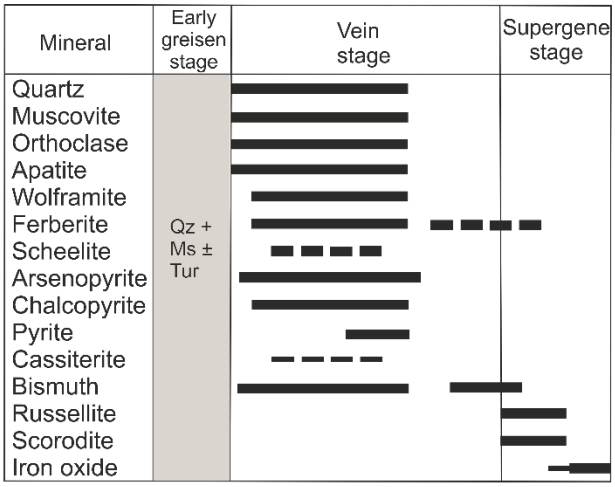

Figure 1. Generalised paragenesis at Hemerdon (this study, McAllister 2016, Cameron 1951).

The wolframite-quartz veins are part of a wider ore system that comprises multiple generations of barren and mineralised veins (McAllister, 2016, unpublished). The relationship between these veins is being investigated as part of this project.

2.2 Scanning Electron Microscopy (SEM) analysis of wolframite petrogenesis

SEM-based, back scattered electron microscopy has been used to identify the range of wolframite-ferberite textures that occur throughout the Hemerdon deposit. The mineralisation is dominated by the Fe-rich end member, ferberite, with variable distribution of wolframite. The textures range from heavily altered and porous, with secondary precipitation of ferberite, to unaltered, fresh wolframite (Figure 2A-D). The distribution of the alteration throughout the deposit is currently being assessed as part of this project

to inform mine planning. Limited evidence for the coeval deposition of cassiterite with wolframite has been found at Hemerdon.

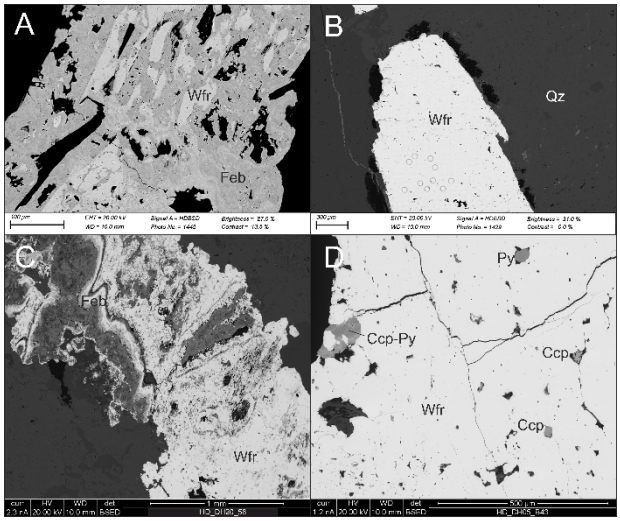

Figure 2. Back scatter electron (BSE) images of A wolframite with ferberite overgrowths; B unaltered wolframite with minor dissolution along crystal boundaries; C dissolution-reprecipitation of wolframite-ferberite; D fresh unaltered wolframite with sulfide inclusions. Wfr–wolframite, Feb–ferberite, Ccp–chalcopyrite, Py–pyrite (after Warr, 2021).

2.3 LA-ICP-MS major and trace element mapping

The textural variability and ferberite-wolframite relationships indicate that metallogenesis involved a complicated and protracted fluid history. The crystallographic and geochemical variations are indistinguishable under normal SEM BSE analysis conditions. However, variation on the microscale is apparent using LA-ICP-MS element mapping and it indicates that multiple fluids had variable Fe/Mn ratios and trace element budgets.

Mapping of individual crystals shows five stages of wolframite precipitation in an otherwise relatively fresh wolframite: 1. an initial Mn-rich, Fe-poor wolframite core with; 2. a subsequent Nb-Ta-rich, Fe-rich wolframite, with elevated Sn, followed by; 3. a Ti-Mn-rich wolframite which is depleted in the other major and trace elements. Stage 4 repeats stage 2, while stage 5 is a later stage of Bi-Mo ±Fe secondary mineralisation (Figure 3).

3 Further work

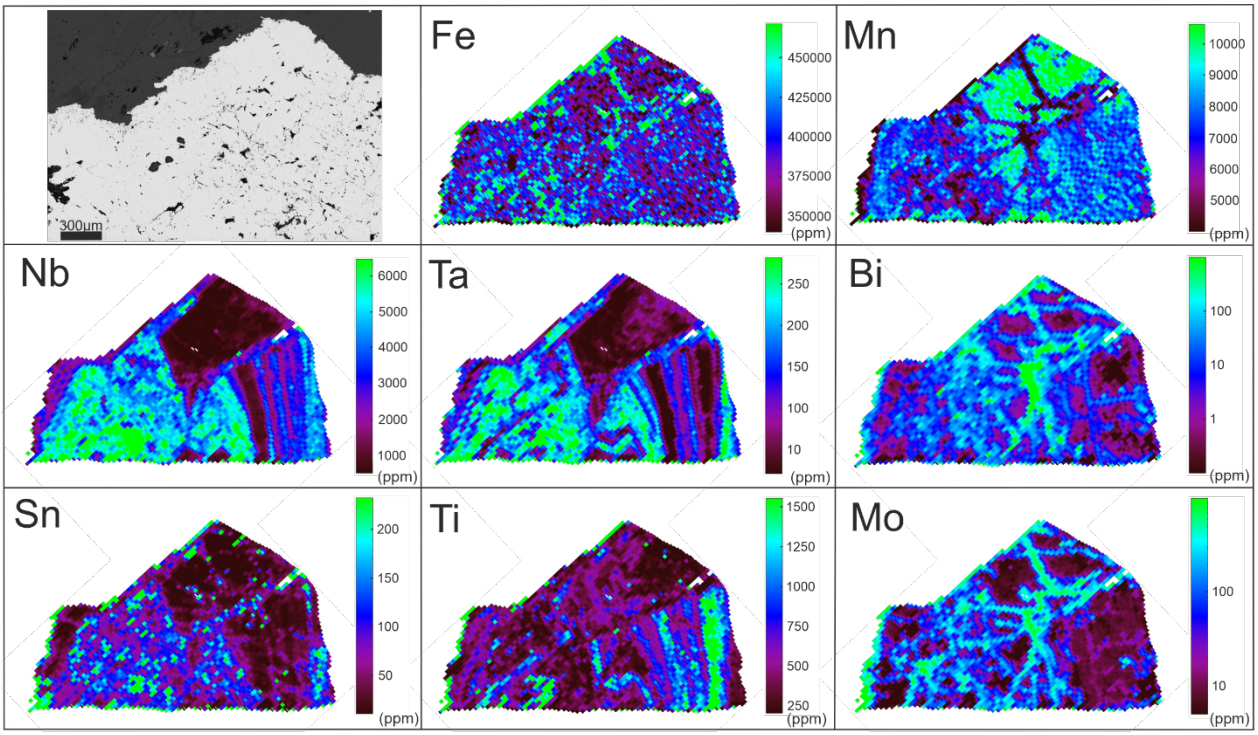

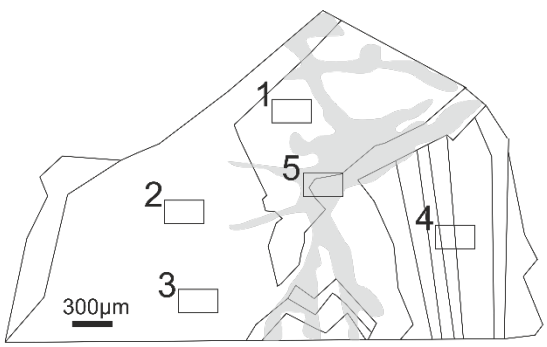

	1	2	3	4	5
Points (n)	67	50	62	88	65
Fe^{56} (ppm)	363646	408561	428620	388176	413816
Mn^{55} (ppm)	10258	5997	5832	7816	4492
Nb^{93} (ppm)	429	3830	9340	2935	1348
Ta^{181} (ppm)	19	193	305	36	68
Ti^{47} (ppm)	400	237	1595	1289	405
Sn^{120} (ppm)	9	84	262	32	76
Bi^{209} (ppm)	1	52	59	3	2165
Mo^{95} (ppm)	7	161	249	9	493

Figure 3. LA-ICP-MS mapping of wolframite from the Hemerdon deposit showing zones described in the text. Average composition data from five areas within the mapped region show the range of compositional variation.

Initial observations indicate a complex, multi-generational fluid history for wolframite-ferberite precipitation at Hemerdon. The tungsten-bearing veins form just one part of the system and so need to be put in the context of the later veins. Cassiterite mineralisation at Hemerdon appears to be hosted in a separate generation of fluids, based on the dearth of veins hosting co-precipitated cassiterite and wolframite, so, the relationship between these fluids and vein sets needs further analysis to interpret the relationship.

Acknowledgements

The authors thank staff at the Hemerdon deposit mine site (then Wolf Minerals, now Tungsten West) for facilitating access and sample collection at Hemerdon and fruitful discussions. John Fletcher (BGS) is thanked for the preparation of exemplary polished thin sections. The BGS Innovations Flexible Fund supported the development of the LA-ICP-MS mapping method.

References

Cameron J (1951) The geology of Hemerdon wolfram mine, Devon Transactions of the Institute of Mining and Metallurgy 61:1-14

Simons B, Shail RK, Andersen JC (2016) The petrogenesis of the Early Permian Variscan granites of the Cornubian Batholith: lower plate post-collisional peraluminous magmatism in the Rhenohercynian Zone of SW England Lithos 260:76-94 doi:https://doi.org/10.1016/j.lithos.2016.05.010

Wang X-S, Williams-Jones A, Hu R-Z, Jiang Z-Q, Shang L-B, Bi X-W (2023) Apatite and fluorite control the transport of tungsten in calcium-bearing hydrothermal fluids Geochimica et Cosmochimica Acta 346:1-14 doi:https://doi.org/10.1016/j.gca.2023.02.001

Warr LN (2021) IMA–CNMNC approved mineral symbols Mineralogical Magazine 85:291-320 doi:https://doi.org/10.1180/mgm.2021.43

U-Pb columbite-tantalite ages from NW-Amazonian Craton, Colombia

Jose A. Franco[1-2], Albrecht Von Quadt[3], Amed Bonilla[2], Alejandro Piraquive[2-4], Thomas Cramer[1-2], Zeze Amaya[2]
[1]Universidad Nacional de Colombia. Bogotá, Colombia
[2]Grupo de Estudios en Geología Económica y Mineralogía Aplicada (GEGEMA). Bogotá, Colombia
[3]Institute of Petrology and Geochemistry ETH. Zurich, Switzerland
[4]Geological Survey of Norway. 7491 Trondheim, Norway

Abstract. At E-Colombian Vichada and Guainía region, Mesoproterozoic rocks of the northwest part of the Amazonian Craton are potential sources of Columbite Group Minerals (CGM), cassiterite, and REE mineralizations. Columbite grains were extracted from colluviums and pegmatitic dykes at San Jose (LOC 5), from colluviums at Barranquilla (LOC 6) and as closely (LOC 2), from colluviums of La Fortuna and El Burro-Venezuela. In pan concentrates, the common mineral assembly is rutile-(Nb,Ta) and REE-minerals. In the latter, metallographic and SEM-EDX analyses revealed columbite-Fe grains containing inclusions of up to 0.2 mm length of ixiolite, rutile-(Nb,Ta), and occasionally tantalite-Mn and microlite. Major and trace elements concentrations obtained through XRF and EPMA reveal matrix variations in the Nb_2O_5 Ta_2O_5, TiO_2, and Fe_2O_3 contents. Sufficient U, Pb, and Th in single columbite crystals permitted conducting LA-ICP-MS U-Pb dating yielding concordant ages at ca. 1549 ± 5 Ma for (LOC 5) and 1531 ± 12 Ma for (LOC 6) and 1472 ± 12 Ma for Venezuelan columbites. The reported ages are coeval with ages of granitoid suites documented in the vicinity of the Orinoco River ranging betweenca.1600-1350 Ma, indicating thus a genetic link between columbite-Fe ores and early Mesoproterozoic magmatism.

1 Introduction

Minerals of the columbite-tantalite group (CT) constitute an isomorphic series $(Mn^{2+},Fe^{2+})(Ta,Nb)_2O_6$ with end members of Nb and Ta that include elements such as Fe, Mn, and substitutions to a lesser extent by cations such as Ti, Ca, Na, U, Th, Y, and REE. They crystallize mainly in the orthorhombic system and present dimorphism with minerals of the tapiolite series becoming the object of comprehensive studies (e.g. Cerny, 1989; Cerný et al., 2012; Ercit et al., 1995; Möller et al., 1989).

Columbite (Nb) and tantalite (Ta) minerals may present diverse paragenesis in rocks such as miazkites, nepheline syenites, carbonatites, or in (anorogenic) alkaline granites enriched in rare earth elements and their associated pegmatites.

Brazil and Canada are the main producers of niobium mineral concentrates, whereas Australia is the main producer of tantalum. The presence of Nb-rich ores associated with carbonatites in Brazil as is represented by the Araxá, and Six Lakes Carbonatites, the latter located in the vicinity of the Colombian border.

Most of the columbite-tantalite minerals in the world are extracted from weathered material derived from felsic pegmatitic rocks, especially in Rwanda, Sierra Leone, and Cameroon (Elsner, 2010). Much less common are Nb-rutiles or ilmenorutile $(Ti^{4+}, Nb^{5+}, Fe^{3+})O_2$ with more than 13 wt% Nb_2O_5 reported with columbite in pegmatites of Manitoba, Canada (Cerny et al. 1981).

(CT) are widespread in almost all continents and geological times. Although, the most important deposits seem to be associated with Archean and Paleoproterozoic rocks, Cenozoic columbites have been reported. In South America, columbites are found in Brazil, Argentina, and Bolivia and sporadically but less studied in Venezuela and Colombia, for which a late Mesoproterozoic age has been documented (Melcher et al. 2017)

In this study, we attempt to trace the possible sources for columbite-tantalite deposits in Colombia. For this purpose, we integrate a new comprehensive mineral characterization including BSE imagery, geochemical and isotopic analyses performed on columbite-tantalite crystals mainly collected from colluvial deposits covering Mesoproterozoic rocks in E-Colombia, which are part of the NW-Amazonian Craton. The columbite-tantalite ores are apparently related to enriched zones or pegmatites of anorogenic origin represented mainly by rapakivi granites outcropping locally along the Orinoco, Inírida, Guainía and Cuyari rivers (see

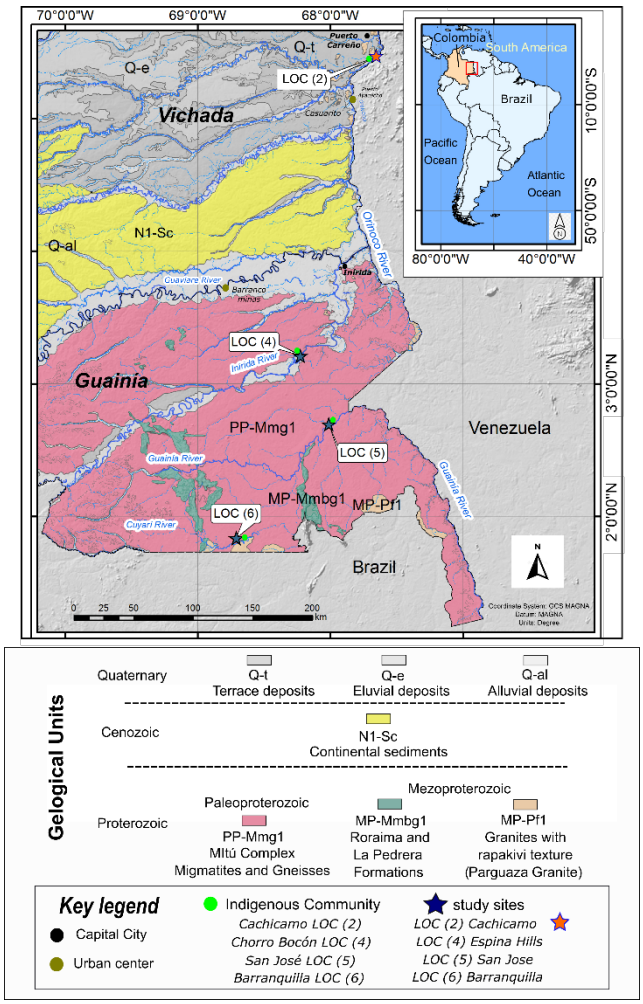

Figure **1**).

2 Geological Background

The ca. 1500-1550 Ma Parguaza Rapakivi Batholith, is found outcropping over 90% in Venezuela and some 10% in Colombia, where it intrudes the Amazon Craton Paleoproterozoic migmatitic complexes (Bonilla-Pérez et al., 2013; Gaudette et al., 1978; Gonzalez and Pinto, 1990). The Parguaza granites are well-documented as a primary ore for Sn, Nb, Ta, and REE minerals (Aarden and Davidson, 1977; Mariño-Pardo, 2012, 2013). Most of the batholith is covered by partially laterized Cenozoic sediments in plains and valleys, whereas fresh outcrops correspond to localized exposures in rivers and inselbergs. Alluvial-colluvial deposits in the Venezuelan localities of El Burro, La Fortuna, and Aguamena yield concentrations of cassiterite, rutile (Nb,Ta), columbite-tantalite and REE minerals. In the easternmost part of Colombia, the Parguaza Rapakivi suites occur in tributaries to the Orinoco River (

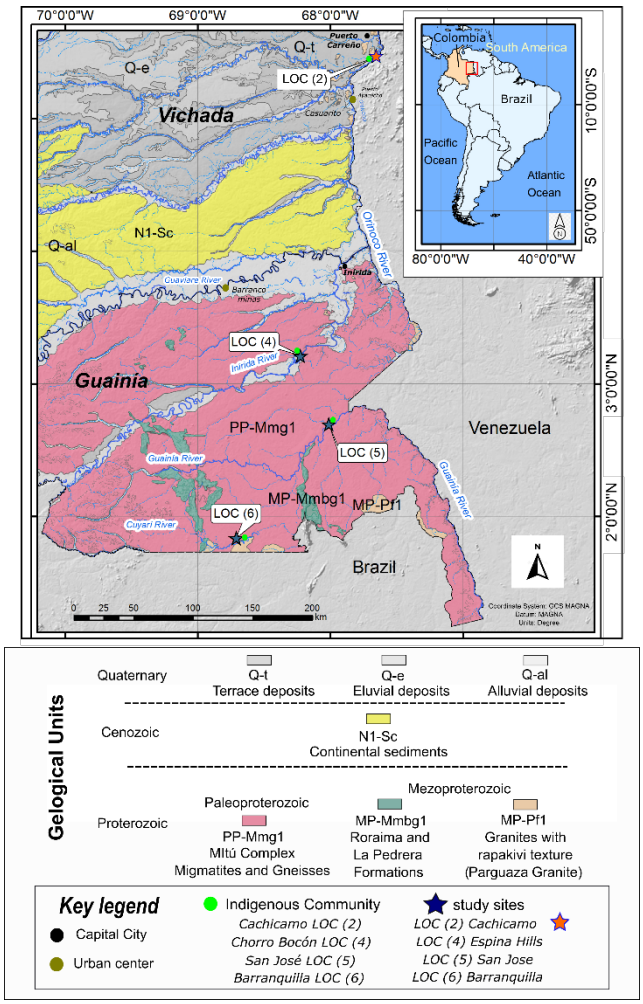

Figure **1**, LOC (2)). Similarly, other exposures are identified in the riverbanks of the Inírida River LOC (4), the Guainía River LOC (5), and the Cuyarí River LOC (6) (Bonilla Perez et al., 2016; Kroonenberg, 2019).

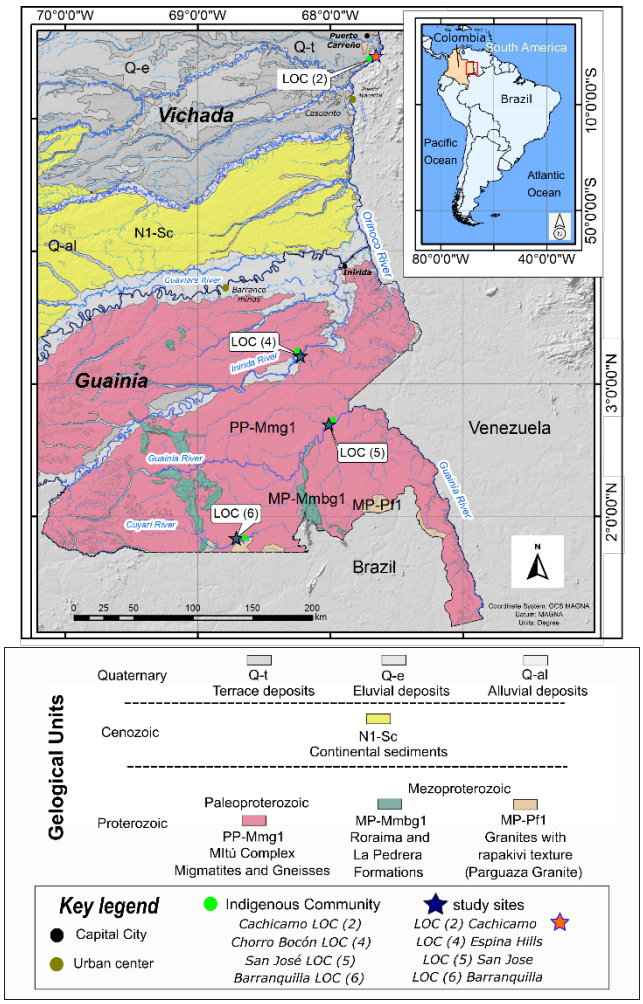

Figure 1. Geological map of E-Colombia showing the Guainía and Vichada departments, the studied locations LOC (5) and (6). For reference and comparison, LOC (2) and LOC (4) samples of rutile-(Nb, Ta) with columbite-Fe inclusions yielded an age of 1342 ± 27 Ma (Franco et. al. 2019). Modified from the Geological Map of Colombia (Gómez Tapias et al., 2015).

3 Methodology

From pan concentrates of each locality, 30 up to 0.5 cm long columbite-Fe crystals were handpicked and identified further using a Bruker Tracer III-V pXRF instrument. Fragments of the thirty crystals for LOC (5 and 6) were mounted in epoxy resin pucks. For Venezuelan columbite, we polished a 3 cm crystal long that we analyzed by EPMA and LA-ICP-MS. Remaining fragments were pulverized using an agate mortar and fused at 1200 °C to pearls for XRF analyses employing a PANanalyticalAXios instrument at the Universidad Nacional de Colombia. For EPMA analysis, the polished epoxy pucks were coated with graphite.

EPMA analysis of major elements was performed employing a JEOL JXA-8900 electron microprobe at LMA-CM-UFMG - Universidade Federal de Minas Gerais (UFMG), Brazil. The CGM geochemistry was confirmed by energy-dispersive X-ray spectroscopy (EDS).

BSE images of the columbite crystals allowed choosing the most homogeneous zones, free of inclusions or in very low proportion. LA-ICP-MS analyses were performed using a Thermo Scientific Element XR, with a single collector, high resolution, magnetic sector ICP-MS and an excimer Argon fluoride laser (193 nm) at the Institute of Geochemistry and Petrology of ETH-Zürich, following the methodology described by Von Quadt et al. (2019) and compared with Melcher et al. (2015, 2017) and Che et al. (2015).

For U-Pb dating, laser ablation of the grains was performed in spots of 40 microns, with a frequency of 5 Hz and an intensity of 7 J/cm^2 . T_X36 columbite-Fe standard and standard glass NIST-610 were used as primary reference materials for correcting laser-induced element fractionation and matrix effects, whereas GJ-1 zircon was analyzed as secondary reference material for monitoring age accuracy and reproducibility. Data over 20% discordant were excluded from the calculation of Concordia ages.

4 Results of characterization and LA-ICP-MS dating

4.1 LOC (5) San Jose - Guainía River

Columbite-Fe found in pegmatitic dykes and colluvial deposits near San Jose occurs together with crystals of rutile-Nb, monazite, xenotime, tourmaline, and magnetite. The pegmatite is hosted in the Paleoproterozoic Mitú Complex rocks and related to rapakivi granite intrusions as the Tabaquen Granite and other unnamed plutons along the Guainía River (Figure 1). The EPMA and ICP-MS analyses reveal an average composition in wt% of up to 52 % Nb_2O_5, 11 %Ta_2O_5, 16% TiO_2, 9 % Fe_2O_3, 7 % MnO and 1% WO_3. Among the minor elements appear up to 600 ppm of Si, W, and Al, up to 405 ppm of Mn, Zr, Cr, Y, and Pb, less than 50 ppm of Cr, P, and Hf, and below 10 ppm of La, Ce, Pr, Nd, Sm, Eu, Gd, Tb, Dy, Ho, Rb, Tm and Lu. The BSE images and-EDS composition show rutile-(Nb, Ta) inclusions and tantalite-Mn (Figure 2 A to B').

The LA-ICP-MS data yield a concordia age of 1549 ± 5 Ma (MSWD= 5; n=50) (Figure 2 C).

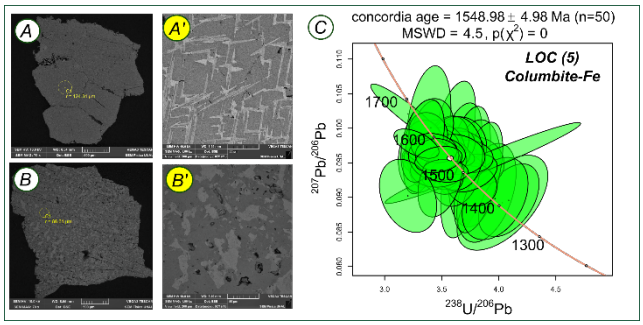

Figure 2. A. Columbite-Fe crystal with exsolutions and inclusion; **A'.** Zoom of the yellow circle zone showing the texture of columbite-Fe and tantalite-Mn (light gray); **B.** Columbite-Fe crystal with inclusion; **B'.** Zoom of the yellow circle zone showing tantalite-Mn (light gray), and **C.** U-Pb-Concordia diagram for columbite-Fe from San Jose LOC (5)

4.2 LOC (6) Barranquilla – Cuyarí River

The columbite-Fe crystals from Barranquilla are found in colluvial deposits with blocks of pegmatites composed of quartz and muscovite together with beryl and crystals of rutile-Nb, monazite, xenotime, tourmaline, REE-enriched zircons, and garnets near to the Cuyari river (

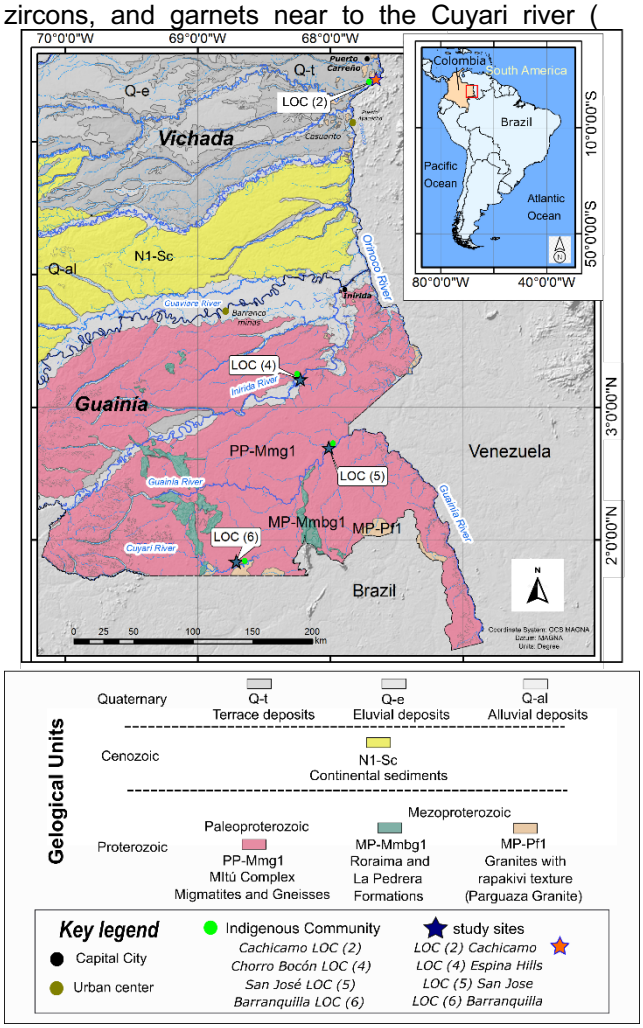

Figure **1**). The XRF analyses exhibit an average composition of up to 42 wt% Nb_2O_5, 32 wt% Ta_2O_5, 3 wt% TiO_2, 8 wt% Fe_2O_3, 9 wt% MnO, 2 wt% WO_3 and 1 wt% SiO_2. The minor elements are up to 600 ppm V, Ca, Zr, Hf, Zn, Ba, Nd, and Y. The SEM-EDS images reveal inclusions of tantalite-(Mn) and rutile-(Nb-Ta) (Figure 3 A to C).

The U-Pb LA-ICP-MS data yield a concordia age of 1531 ± 12 Ma (MSWD= 3; n=15) (Figure 3 D).

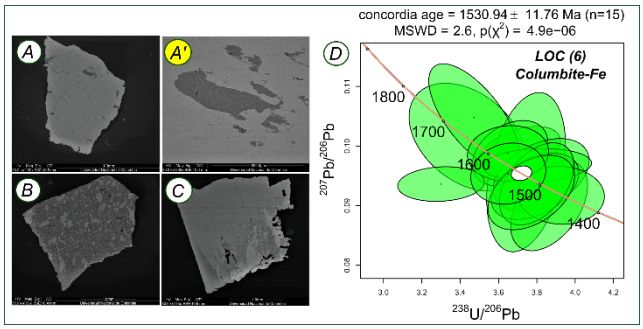

Figure 3. A. Columbite crystal with inclusions and **A'** ampliation showing rutile-(Nb,Ta) inclusion (Dark gray) columbite-Fe; **B.** Columbite crystal with tantalite-Mn inclusions (Light gray); **C.** Columbite crystal with tantalite-Pb inclusions (Light gray), and **D.** U-Pb concordia diagram of columbite-tantalite from Barranquilla-Cuyarí River LOC (6).

4.3 Columbite-tantalite from Venezuela

Samples of columbite-Fe and tantalite-Mn from Aguamena, El Burro y La Fortuna in Venezuela were found in colluvial deposits over the Parguaza Granite together with crystals of cassiterite, struverite, ilmenorutile, monazite, and tourmaline. The XRF and EPMA analyses exhibit an average composition of up to 35 wt% Nb_2O_5, 34 wt% Ta_2O_5, 4 wt% TiO_2, 11 wt% Fe_2O_3, 9 wt% Mn_2O_3, 3 wt% WO_3, 1 wt% SiO_2 and 0,5 wt% SnO_2. Among the minor elements are up to 600 ppm of Al and Zr, Hf, V, Ca, U, and Yb. The BSE-EDS images show a paragenesis with struverite, tantalite-Mn, cassiterite, and in some Ta-rich grains microlite (Figure 4 A to C').

The U-Pb LA-ICP-MS data yield a concordia age of 1472 ± 6 Ma (MSWD= 9; n=17) (Figure 4 D).

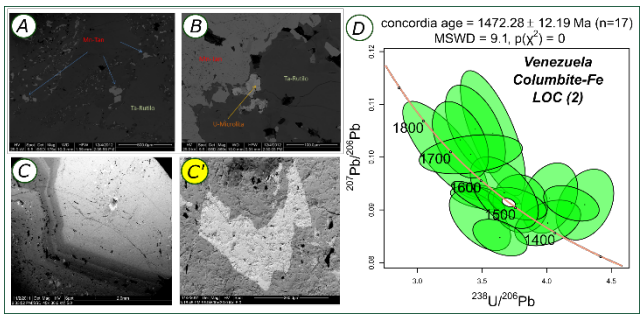

Figure 4. A. Picture of columbite-tantalite with inclusion of U-microlite and struverite; **C.** Rutile-(Nb,Ta) with zonation and inclusions; **C'.** Zoom showing the columbite- tantalite inclusions (withe), and **D.** U-Pb concordia diagram of columbite-tantalite crystals from El Burro and La Fortuna in Venezuela.

5 Discussion

5.1 Geochemical constrains.

The new XRF and EPMA data of major and trace elements in the columbites agree with the former data in their general composition and affiliation to the ferro-mangano columbite-tantalite series. Amazonian Craton columbites are enriched in rare earth elements (REE), especially in heavy REE. High radioactivity comparative measurements confirm the high U content up to 1 wt%, especially in the columbites from Venezuela. In general, minerals show a small variability within their matrix, but crystals with less than 10 wt% of TiO_2 and no inclusions provided the best results for LA-ICP-MS dating.

5.2 Age of mineralization and provenance

The columbite U-Pb crystallization ages found for LOC (5) of 1549 ± 5 Ma (MSWD= 5; n=50) overlap within age uncertainties with ages from LOC (6)

columbites of ca. 1531 ± 12 (MSWD=3; n=15) and correspond to previously obtained U-Pb ages from rutile-(Nb,Ta) at LOC (2) (Franco et al., 2021) of 1512 ± 12 Ma. Differently, Venezuelan columbite-tantalite samples exhibit younger U-Pb ages of 1472 ± 6 Ma (MSWD= 6; n=17). In summary, these results interpreted as crystallization ages comprise the time span from 1600 to 1470 Ma, bracketing the crystallization of the Parguaza-rapakivi batholith suites reported for this part of the Amazonian Craton. Besides, columbite concordant ages may indicate at least two generation events prior to the Early Mesoproterozoic major magmatic episode.

On the other hand, U-Pb-in rutile-(Nb,Ta) LA-ICP-MS ages acquired from LOC (5) and LOC (6) of 1377 ± 1 Ma and 1411 ± 5 Ma, respectively (Franco et al., 2019) can be correlated with 1411 Ma ages reported by Melcher et al. (2017) for Colombian CGM samples, based on U-Pb isotopes in wodginite–ixiolite, CGM, rutile, and cassiterite, with a mineralization age ranging from 1453 to 1277 Ma, although without reporting their exact provenances.

6 Conclusion

The acquired and compared ages suggest a major mineralization event for the Colombian columbite formation ranging from ca. 1550 to 1500 Ma and at least another younger mineralization or reworking event between ca. 1411 to 1370 Ma.

7 Acknowledgements

We express our gratitude to the indigenous communities of Cachicamo, San Jose y Barranquilla. Special thanks to the laboratories of the National University of Colombia, UFMG in Brazil, and GEGEMA group in Bogota.

8 References

Aarden, H., Davidson, M., 1977. Minerales de estaño, niobio, tántalo y titanio en la zona del Cano Aguamena, Estado Bolívar, analizados con microsonda de electrones, in: Memorias V Congreso Geológico Venezolano. Caracas, pp. 919–940.

Bonilla-Pérez, A., Frantz, J.C., Charão-Marques, J., Cramer, T., Franco-Victoria, J.A., Mulocher, E., Amaya-Perea, Z., 2013. Petrografía, Geoquímica y Geocronología del Granito de Parguaza en Colombia. Bol. Geol. 35, 83–104. https://doi.org/10.18273/revbol

Bonilla Perez, A., Frantz, J.C., Charão-Marques, J., Cramer, T., Franco Victoria, J.A., Amaya-Perea, Z., 2016. Magmatismo rapakivi en la cuenca media del Río Inírida, Departamento de Guainía, Colombia. Bol. Geol. 38, 17–32. https://doi.org/10.18273/revbol.v38n1-2016001

Cerny, P., 1989. Exploration strategy and methods for pegmatite deposits of tantalum, in: Möller, P., Cerny, P., Saupé, F. (Eds.), Lanthanides, Tantalum and Niobium: Mineralogy, Geochemistry, Characteristics of Primary Ore Deposits, Prospecting, Processing and Applications - Proceedings of a Workshop in Berlin, Nov. 1986. Springer, Berlin, Heidelberg, New York, London, Paris, Tokyo, pp. 274–302.

Cerný, P., London, D., Novák, M., 2012. Granitic Pegmatites as Reflections of Their Sources. Elements 8, 289–294. https://doi.org/10.2113/gselements.8.4.289

Che, X.D., Wu, F.Y., Wang, R.C., Gerdes, A., Ji, W.Q., Zhao, Z.H., Yang, J.H., Zhu, Z.Y., 2015. In situ U-Pb isotopic dating of columbite-tantalite by LA-ICP-MS. Ore Geol. Rev. 65, 979–989. https://doi.org/10.1016/j.oregeorev.2014.07.008

Elsner, H., 2010. Heavy Minerals of Economic Importance. BGR, Hannover.

Ercit, T.S., Wise, M.A., Cerny, P., 1995. Compositional and structural systematics of the columbite group. Am. Mineral. 80, 613–619.

Franco, J.A., Cramer, T., Bonilla, A., Piraquive, A., Campos, H., 2019. Nb-rutile: A reference mineral for timing of Sn, Nb-Ta, U-Th and REE mineralization at NW part of the Amazonian Craton. 15th Biennial Meeting of the Society for Geology Applied to Mineral Deposits: Life With Ore Deposit on Earth. Glasgow, Scotland Abstract Volumes 3.

Franco, J.A.; Cramer, T.; Bonilla, A.; Castañeda, A.J.; Poujol, M.; Amaya, Z. 2021. Mineralogía y geocronología de rutilo-(Nb,Ta) relacionado a casiterita y columbita-tantalita provenientes de rocas Mesoproterozoicas del Cratón Amazónico cerca de Cachicamo, Colombia. Boletín de Geología, 43(1), 99-126. https://doi.org/10.18273/revbol.v43n1-2021005

Gaudette, H.E., Mendoza, V.S., Hurley, P.M., Fairbairn, H.W., 1978. Geology and age of the Parguaza rapakivi granite, Venezuela. Geol. Soc. Am. Bull. 89, 1335–1340. https://doi.org/10.1130/0016-7606(1978)89<1335:GAAOTP>2.0.CO;2

Gómez Tapias, J., Montes Ramírez, N.E., Nivia Guevara, Á., Diederix, H., 2015. Mapa Geológico de Colombia, 1:1.000.000, in: Atlas Geológico de Colombia. SGC, Bogotá, p. 2 hojas.

Kroonenberg, S.B., 2019. The Proterozoic Basement of the Western Guiana Shield and the Northern Andes, in: Cediel, F., Shaw, R.P. (Eds.), Geology and Tectonics of Northwestern South America. Springer International Publishing, Cham, pp. 115–192. https://doi.org/10.1007/978-3-319-76132-9_3

Mariño-Pardo, N., 2013. Coltán (Nb y Ta): Ubicación, extracción ilegal y potencial minero en el Municipio Cedeño del Estado Bolivar, Venezuela, Propuestas. V Simposio Venezolano de Rocas Ígneas y Metamórficas, Auditorio de Geología, UCV, del 27 al 29/11/2013. UCV, Venezuela.

Mariño-Pardo, N., 2012. Potencial minero del Bajo Parguaza. Rev. Commod. Venez. 2, 44–47.

Melcher, F., Graupner, T., Gäbler, H.-E., Sitnikova, M., Henjes-Kunst, F., Oberthür, T., Gerdes, A., Dewaele, S., 2015. Tantalum–(niobium–tin) mineralisation in African pegmatites and rare metal granites: Constraints from Ta–Nb oxide mineralogy, geochemistry and U–Pb geochronology. Ore Geol. Rev. 64, 667–719. https://doi.org/10.1016/j.oregeorev.2013.09.003

Melcher, F., Graupner, T., Gäbler, H.-E.E., Sitnikova, M., Oberthür, T., Gerdes, A., Badanina, E., Chudy, T., 2017. Mineralogical and chemical evolution of tantalum–(niobium–tin) mineralisation in pegmatites and granites. Part 2: Worldwide examples (excluding Africa) and an overview of global metallogenetic patterns. Ore Geol. Rev. 89, 946–987. https://doi.org/10.1016/j.oregeorev.2016.03.014

von Quadt, A., M. Guillong, O. Laurent, I. Peytcheva, M. Galliski. 2019: U-Pb dating of columbite-bearing ores with a new columbite reference material. − Rev. Bulg. Geol. Soc., 80, 3–“Gesciences 2019”, 94–95.

Rare-earth element mineralization in altered pegmatites from the Djurkovo Pb-Zn deposit, Central Rhodopes

Sylvina Georgieva[1], Rossitsa D. Vassileva[1], Georgi Milenkov[1], Jan Cempírek[2], Radek Škoda[2]
[1] Geological Institute, Bulgarian Academy of Sciences, Sofia, Bulgaria
[2] Dept. of Geological Sciences, Masaryk University, Brno, Czech Republic

Abstract. The Djurkovo polymetallic vein deposit is formed by veins filling open space in various gneisses that compose the high-grade metamorphic complex in the Central Rhodopes. Abundant deformed concordant or crosscutting pegmatites of varying thickness are common in the metamorphic sequence. The studied pegmatite dykes consist mainly of plagioclase, K-feldspar, quartz, and minor micas. The main accessory minerals are allanite- (Ce), titanite, apatite and zircon. Late hydrothermal overprint and alteration of pegmatites led to formation of epidote-group minerals, adularia, albite, sericite, chlorite, carbonate, quartz and leucoxene. The secondary minerals also include rare earth element (REE+Y) and Th, U fluorcarbonate – phosphate – oxide assemblages. This mineral association typically occurs as very fine-grained (< 20 μm) anhedral disseminations, observed along fractures and dissolved zones in allanite and titanite that evidently are the main source for the REEs. This indicates remobilization of REEs followed by formation of new phases during the late-stage hydrothermal activity. Limited mobility of REEs is illustrated by precipitation of the newly-formed minerals within the grains of the altered accessory minerals. The studied pegmatites retain a significant amount of accessory minerals rich in incompatible elements and despite being hydrothermally altered they could be considered as their potential source.

1 Introduction

Rare-earth elements (REEs), along with Y, Th, and U, are generally incompatible in crystal structures of the main rock-forming minerals due to their geochemical properties (large ionic radii, high ionic charge). For this reason, these elements are usually concentrated in the upper continental crust through low-degree partial melting and fractional crystallization processes, and are commonly mobile in magmatic-hydrothermal systems having the ability to complex with F, Cl etc. (Ballouard et al. 2020 and references therein). Being of strategic importance and belonging to the critical materials list, most of these elements are crucial for high technology development. Recent increase of interest in pegmatites as sources of critical elements as well as industrial materials (ceramic feldspar) requires revision and detailed investigation of pegmatite-rich regions (Linnen et al. 2012).

Numerous pegmatite bodies with various size, shape and position are important rock constituents intruded in the metamorphic complex, hosting the main vein and metasomatic polymetallic ore mineralization in the Central Rhodopes, south Bulgaria. The current mining activity in the region facilitates the investigation of these pegmatite bodies with regards to their mineral and geochemical properties and to evaluate their resource potential for critical elements. This study provides preliminary data about the primary and secondary REE mineralization that occurs in pegmatites from the Djurkovo Pb-Zn deposit.

2 Methodology

Materials used in this study are hydrothermally altered pegmatite samples from the Eastern Apophysis area, level 472 of the Djurkovo Pb-Zn deposit. Prior to EPMA study, the mineral relationships and representative spots in the thin sections were chosen using optical and scanning-electron microscopy.

The chemical composition of the minerals was analysed with a Cameca SX100 electron microprobe (EMP) at the Joint Laboratory of Electron Microscopy and Microanalysis, Department of Geological Sciences, Masaryk University, and Czech Geological Survey, Brno. Wavelength-dispersive mode with an accelerating voltage of 15 kV, a beam current of 4-20 nA and a beam size 2–6 μm were applied. The following standards and X-ray *K*α and *L*α lines were used: sanidine (Si, Al, K), albite (Na), olivine (Mg), almandine (Fe), fluorapatite (Ca, P), tephroite (Mn), anatase (Ti), chromite (Cr), columbite (Nb), $ScVO_4$ (V), $SrSO_4$ (Sr), topaz (F), vanadinite (Cl), barite (Ba), $LaPO_4$ (La), $CePO_4$ (Ce), $PrPO_4$ (Pr), $NdPO_4$ (Nd), $SmPO_4$ (Sm), $GdPO_4$ (Gd), ThO_2 (Th), U (U).

3 Geological setting

The Djurkovo Pb-Zn deposit is located in the Laki ore region, situated in the northern part of the Central Rhodope metamorphic complex, south Bulgaria. This region hosts numerous hydrothermal Pb-Zn (±Ag) ore deposits and occurrences, accumulated in extensional tectonic settings (Marchev et al. 2005). The polymetallic mineralization is connected to several predominantly NNE ore-bearing faults that also crosscut the volcanics of the near Borovitsa caldera to the east. The ore mineralization occurs either as subvertical veins formed by open-space filling in the metamorphic rocks (mostly gneisses) or forms rich replacement ore bodies in the marble layers. The mineralization of the Djurkovo deposit is located in two major NNE-SSW trending ore veins, developed in gneisses and marbles, named Eastern Apophysis and West 2 (Buret and Kouzmanov 2011). Apart from the gneisses and marbles, abundant pegmatite bodies with different size, shape and position are important rock constituents cutting the metamorphic complex. These bodies are often

deformed, boudinaged, folded or cut by later faults (Fig. 1A, B).

Regarding the vein mineralization in the deposit, three main paragenetic stages are outlined (Buret and Kouzmanov 2011): 1) early quartz-pyrite; 2) polymetallic (galena, sphalerite); 3) late carbonate stage. A prograde skarn stage occurred during metasomatic replacement in the marbles due to fluid-rock interaction that generally resulted in formation of diopside (±olivine). The related hydrothermal alteration in pegmatites led to formation of adularia, epidote, chlorite, and later carbonatization (Vassileva et al. 2020 and references therein).

According to the $^{40}Ar/^{39}Ar$ thermochronology on hydrothermal K-feldspar from the Laki ore district, the age of the economic mineralization in the Djurkovo deposit is constrained between 32–30 Ma (Buret et al. 2013).

4 Results

Petrographic study showed that the quantity of quartz in the studied pegmatite bodies is about 20–25 % of the rock volume, and plagioclases prevail over K-feldspars. The studied pegmatites do not show clear zonal mineral distribution. Myrmekite intergrowth textures are typically observed on the borders between plagioclase and K-feldspar. Quartz forms irregularly distributed medium- to fine-grained anhedral grains, often occupying the interstitial space between plagioclase and K-feldspar. Undulate extinction and lobate grain boundaries are often observed in the quartz. Minor amounts of muscovite and biotite are present. Rare sub- to anhedral grains of garnet (up to 5 mm) with inclusions of K-feldspar, quartz, allanite, calcite, and chlorite occur among quartz and feldspars. The garnet contains dominant almandine (49.6–44.9 mol.%), and high amounts of grossular (28.8–20.9 mol.%), and spessartine (26.1–13.5 mol.%) components. The garnet mainly forms in the peripheral zone of some pegmatite bodies, close to the contact with gneisses, which suggests a metasomatic influence.

The main pegmatite accessory minerals are allanite, apatite, titanite, and zircon (Fig. 1C–F). Allanite typically forms brown, euhedral to subhedral crystals up to 1 mm large among feldspar and/or quartz grains. Frequently, the crystals are replaced or fragmented and intersected by late hydrothermal epidote (*sensu lato*) (see Fig. 1C). The dominant REE_2O_3 in the mineral are Ce_2O_3 (up to 8.5 wt%), La_2O_3 (3.9 wt%) and Nd_2O_3 (3.5 wt%). Thorium contents (up to 3.4 wt% ThO_2) are elevated. Because of the hydrothermal alteration, part of the mineral is transformed to REE-rich clinozoisite with patchy or irregular zonal patterns that can be observed clearly in back-scattered electron (BSE) images. Apart from epidote, late REE fluorcarbonates form in cracks and zones within the allanite grains.

Titanite is developed as euhedral to subhedral crystals (up to 2 mm long) in association with feldspars. Some of the crystals are deformed and cracked. Weak compositional zoning could be outlined in BSE images. The content of Fe_2O_3 in the mineral is less than 0.97 wt%, whereas Al_2O_3 reaches up to 8.97 wt%. The main trace elements incorporated in the mineral are Nb (≤3.23 wt% Nb_2O_5), Y (≤1.35 wt% Y_2O_3), Ce (≤0.3 wt% Ce_2O_3), Nd (≤0.23 wt% Nd_2O_3), and Ta (≤0.21 wt% Ta_2O_5). Titanite is partly or entirely replaced by leucoxene (mostly anatase according to Raman spectroscopic data; see Fig. 1E, F). Apatite forms euhedral crystals (up to 600 μm) within the feldspar and quartz matrix. Its content of F reaches up to 3.6 wt%, elevated are also Cl (up to 0.3 wt%) and Y_2O_3 (up to 0.3 wt%). It is chemically homogeneous; no apatite dissolution, alteration, or reaction textures were observed. Zircon occurs as euhedral crystals (up to 200 μm) associated with feldspars. Clear chemical zoning is defined by incorporation of HfO_2 (up to 2.68 wt%) and UO_2 (up to 1.12 wt%).

The pegmatite bodies are overprinted by clearly visible late hydrothermal alteration. The mineral association comprises epidote-group minerals, adularia, albite, sericite, chlorite, carbonates, REE fluorcarbonates, leucoxene, xenotime, thorite, uraninite and quartz. Rare thin veinlets and disseminations of galena, sphalerite and minor chalcopyrite are present. The main alteration assemblage is similar to those in pegmatites from other deposits in the region (e.g., Petrovitsa Pb-Zn deposit, Madan ore region, Georgieva et al. 2022).

Epidote-group minerals are the prevalent hydrothermal alteration products; they generally occur as sub- to euhedral prismatic crystals (up to 500 μm) or clusters which, along with carbonate, adularia, and sericite, form nests and veins among feldspars. Their composition generally varies between clinozoisite and Fe^{3+}-rich clinozoisite. Sericite, carbonate, adularia and albite replace almost the entire volume of feldspars, forming thin network of veinlets and nests. Monomineralic adularia veins (up to 500 μm thick) with well-shaped subhedral crystals were also observed. Chlorite is developed mainly replacing micas and also as thin veinlets and nests along with aforementioned secondary mineral assemblage.

Late carbonate-dominated rare-element (REE+Y, Th, U) mineral assemblage, typically developed as less than 20 μm large anhedral grains and aggregates, precipitated along the fractures and dissolved zones in allanite and titanite as their alteration product. It is represented by the minerals from the bastnäsite-synchysite series, including parisite and röntgenite intermediate members. Their EMP analyses show that the main REEs are Ce (14.84–25.90 wt% Ce_2O_3), La (7.10–12.23 wt% La_2O_3), Nd (3.76–10.96 wt% Nd_2O_3), Sm (0.35–2.76 wt% Sm_2O_3) and Gd (0.3–2.36 wt% Gd_2O_3). Part of the analyses shows high contents of ThO_2 (up to 25.17 wt%) as well. The contents of CaO strongly varies between 2.98 and 18.74 wt%, whereas F

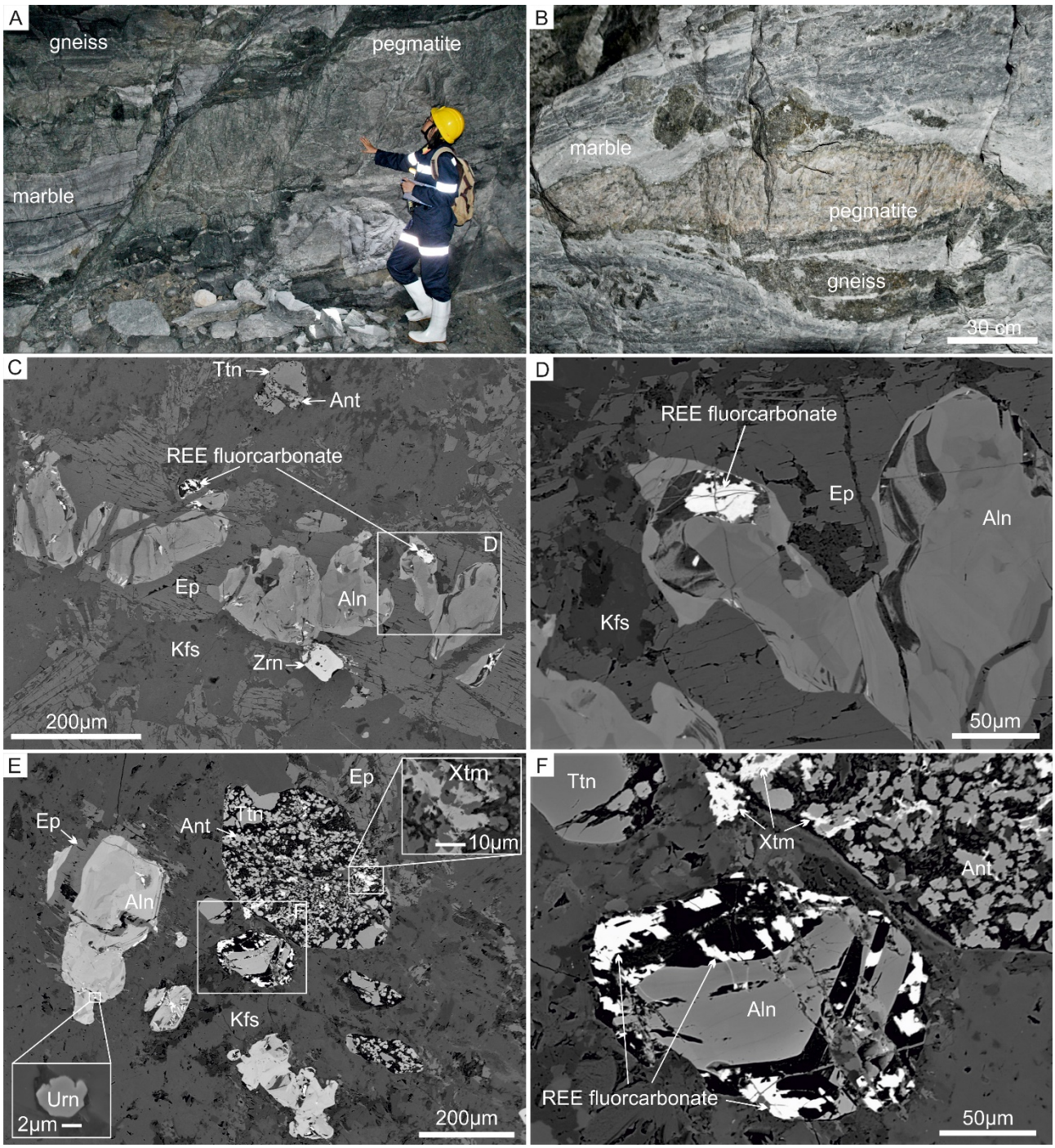

Figure 1. *A; B,* Macrophotographs of pegmatite outcrop, the Djurkovo mine, level 472; *C–F*, BSE images of occurrence and mineral relationships of the accessory minerals. Abb.: Kfs – K-feldspar; Ep – epidote; Aln – allanite; Ttn – titanite; Zrn – zircon; Ant – anatase; Xtm – xenotime; Urn – uraninite.

contents are relatively stable (5.57–7.19 wt%).

Because of the complex structure and composition of these phases, their natural ability to form intergrowths of several fluorcarbonates (Zeug et al. 2021), and their small size in the studied pegmatites, it was commonly impossible to assign the exact mineral species; some of their chemical compositions correspond to parisite-(Ce) and thorbastnäsite. Xenotime is present as irregular aggregates less than 20 µm in size, associated with leucoxene in the altered titanite. Its Y_2O_3 content reaches up to 41.9 wt%; it is accompanied by HREEs, such as Er (4.46 wt% Er_2O_3), Yb (4.44 wt% Yb_2O_3), and Dy (4.37 wt% Dy_2O_3). Uranium reaches 0.82 wt% UO_2. Thorite and uraninite occur as <5 µm large grains enclosed in titanite, allanite, and zircon. According to our observations, both allanite and titanite enclose grains of REE+Th fluorcarbonates and uraninite (~5 µm), whereas thorite and xenotime occur along with leucoxene in the altered titanite.

5 Concluding remarks

Deformed, boudinaged and folded pegmatites, often cut and displaced by faults, cross-cut the

metamorphic rocks hosting the Pb-Zn Djurkovo deposit, Central Rhodopes. The bodies are of varying thickness and position (concordant or oblique) towards the metamorphic foliation. Detailed petrographic and EMP study revealed the presence of accessory minerals such as allanite, titanite, apatite and zircon that usually accumulate significant amounts of incompatible elements such as REE+Y, Th and U. Late-stage hydrothermal alteration of the pegmatites led to partial or complete dissolution of the accessory minerals (*e.g.,* allanite, titanite), and extraction and reprecipitation of the incompatible elements (REE+Y, Th, U) as new phases – mainly fluorcarbonates and phosphates. These new minerals precipitated within the altered accessory crystals due to the presumable limited mobility of REE in fluids hampering any long-distance transport of these elements. As a rule, REE fluorcarbonates and uraninite formed mainly within the grains of the altered allanite, whereas xenotime and thorite precipitated within the altered titanite crystals.

The hydrothermal alteration of the REE-bearing accessory minerals (e.g., allanite, titanite, apatite, zircon) from the pegmatites gives a better insight on the trace elements extraction, redistribution and reprecipitation processes in the altered igneous rocks.

Acknowledgements

The study is financially supported by the Bulgarian National Science Fund KP-06-N34/4 project and complements ERA-MIN PEGMAT project KP-06-DO02/2.

References

Ballouard C, Massuyeau M, Elburg MA, Tappe S, Viljoen F, Brandenburg J-T (2020) The magmatic and magmatic-hydrothermal evolution of felsic igneous rocks as seen through Nb-Ta geochemical fractionation, with implications for the origins of rare-metal mineralizations. Earth Sci Rev 203, 103115, ISSN 0012-8252, https://doi.org/10.1016/j.earscirev.2020.103115

Buret Y, Kouzmanov K (2011) Polymetallic mineralization in the Laki mining district Southern Bulgaria: Paragenesis and fluid evolution. In: Abstract Volume 9th Swiss Geoscience Meeting. Zurich, 11–13 November 2011, Symposium 2: Mineralogy, Petrology, Geochemistry, 88–89

Buret Y, Kouzmanov K, Spikings R, Gerdjikov Y (2013) Timing of polymetallic Pb-Zn mineralisation in the Laki district, southern Bulgaria – constraints from 40Ar/39Ar dates. In: Abstract Volume 11 Swiss Geoscience Meeting. Lausanne, 15–16 November 2013, Symposium 2: Mineralogy, Petrology, Geochemistry, 49–50

Georgieva S, Vassileva R, Milenkov G, Stefanova E (2022) Major and trace element signature of epidote-group minerals in altered pegmatites from the Petrovitsa Pb-Zn deposit of the Madan ore region, Central Rhodopes, Bulgaria: Evidence of allanite/epidote transformation. Geol Carp 73(4): 365–380. https://doi.org/10.31577/GeolCarp.73.4.5

Linnen RL, Van Lichtervelde M, Cerný P (2012) Granitic pegmatites as sources of strategic metals. Elements 8: 275–280. https://doi.org/10.2113/gselements.8.4.275

Marchev P, Kaiser-Rohrmeier M, Heinrich C, Ovtcharova M, von Quadt A, Raicheva R (2005) Hydrothermal ore deposits related to post-orogenic extensional magmatism and core complex formation: The Rhodope Massif of Bulgaria and Greece. Ore Geol Rev 27: 53–89. https://doi.org/10.1016/j.oregeorev.2005.07.027

Vassileva RD, Grozdev V, Peytcheva I, von Quadt A, Salnikova E (2020) Andradite from Pb-Zn Djurkovo deposit, Central Rhodopes: chemical composition and U/Pb dating. Rev Bulg Geol Soc (Geosciences 2020) 81(3): 58–60

Zeug M, Nasdala L, Ende M et al (2021) The parisite–(Ce) enigma: challenges in the identification of fluorcarbonate minerals. Miner Petrol 115: 1–19. https://doi.org/10.1007/s00710-020-00723-x

Pegmatite REE-mineral association from the Kroushev Dol base metal deposit (south Bulgaria): mineral replacements and timing of formation

Rossitsa D. Vassileva[1], Sylvina Georgieva[1], Georgi Milenkov[1], Jan Cempírek[2], Radek Škoda[2], Elitsa Stefanova[1], Valentin Grozdev[1], Irena Peytcheva[1]
[1]Geological Institute, Bulgarian Academy of Sciences, Bulgaria
[2] Department of Geological Sciences, Masaryk University, Brno, Czech Republic

Abstract. The region of the Central Rhodopes, south Bulgaria, is known for large Pb-Zn deposits located in the Madan and Laki districts. The economic sulphide mineralization is hosted by the high-grade rocks of the Rhodope metamorphic complex. Mining operations revealed that pegmatite injections into the host gneisses, amphibolites and marbles represent a substantial part of the wall rocks in depth. Mineral composition of these dykes is represented by K-feldspar, plagioclases, and quartz as major constituents. In the pegmatites from the Kroushev Dol deposit (Madan district), REE-bearing mineralization includes accessory monazite, zircon, apatite, allanite, titanite, and thorite. Primary minerals of REE are monazite (LREE) and zircon (HREE); the REE were consequently redistributed among secondary apatite, allanite, thorite, and titanite. Common mineral breakdowns (e.g. oligoclase to albite; monazite to apatite; allanite to epidote; titanite to anatase) and replacement of the primary pegmatite minerals by the epidote-chlorite-carbonate association were caused by hydrothermal alteration by acid Pb-Zn ore-precipitating fluids. There seems to be no genetic link between the pegmatite emplacement and the economic galena-sphalerite accumulations and the U-Pb geochronometry on monazite, zircon and titanite proved that pegmatite formation (~40 Ma) significantly precedes the origin of the base metal mineralization (~30 Ma).

1 Introduction

The processes of crustal formation and granitic magmatism are responsible for accumulation of incompatible elements, including Th, U and rare-earth elements (REE). Owing to their chemical properties and geochemical behavior, they are seldom incorporated into major rock-forming minerals and preferably tend to form minerals in late stages of magma differentiation. REE-minerals frequently occur in pegmatites, which makes them potential sources for strategic metals and critical elements (e.g. Linnen et al. 2012).

Large pegmatite injections are part of wall rocks within the Pb-Zn deposits in Central Rhodopes, south Bulgaria. The Cenozoic (~30 Ma) base metal vein and metasomatic sulphide mineralization with economic importance is formed by hydrothermal fluid circulation/precipitation as open-space fillings or replacements in the host gneisses, marbles and amphibolites of the Rhodope metamorphic complex (Madan Unit). An ongoing study on the mineral and chemical composition of pegmatites exposed in the underground mine of Kroushev Dol revealed details on the abundance and diversity of REE accessory minerals (Fig. 1). This contribution describes Th- and U- bearing REE minerals from a selected pegmatite dyke on the 865 m.a.s.l. in the Kroushev Dol deposit, their mineral relationships, replacements, chemical composition, and U-Pb ages.

2 Results

2.1 Pegmatite mineralogy

The pegmatite is placed conformably in the host marble; it was studied in a profile across the body, perpendicular to the contacts. The main mineral composition comprises K-feldspar (Or_{83-96}), plagioclases (mostly oligoclase, $Ab_{66-73}An_{26-31}$) and quartz. Mineral relationships suggest that the observed albite (Ab_{91-98}) and adularia are later products. Albitization of primary plagioclase occurs as widespread alteration, preserving relics of oligoclase. Later adularia veinlets cut the matrix including albite (e.g. Fig. 1K), which corresponds to stages of intensive overprint by epidote-chlorite-carbonate alteration. Hydrothermal alteration affects the whole pegmatite volume but it is most intensively developed along the pegmatite contact with the host marbles and metasomatic ore mineralization.

Detailed petrographic study revealed that accessories have zonal distribution across the pegmatite. The inner pegmatite zone is characterized by association of monazite, zircon, allanite, apatite and thorite (Fig. 1 A-L), while in the areas proximal to the lithological contacts large titanite crystals prevail (Fig. 1 M-P).

The REE-minerals often form aggregates and/or accumulations in the pegmatite as seen by the optical and BSE observation. Most of the accessories (allanite, zircon, apatite, titanite; Fig. 1) generally form single well-shaped crystals within the feldspar-quartz matrix, apart from the monazite and thorite grains. They are both observed within the allanite crystals. Monazite appears as large subhedral relics (Fig.1 A-F), while thorite grains (below 10 μm) mostly form intergrowths with apatite (Fig. 1G, F), and/or are attached to microfractures in allanite volume (Fig.1I). Apatite occurs either as crystals and masses within allanite volume in close association with monazite/thorite (Fig. 1 A-H) or as aggregates (Fig. 1J) and single crystals often in assemblage with zircon (Fig. 1G, K). The latter is observed as long prismatic well-shaped crystals with fine oscillatory zoning (Fig. 1L) and without inherited cores (as seen by CL-microscopy). Most of the

aforementioned REE-minerals are observed as inclusions in allanite crystals (Fig. 1 A-I). The pegmatite periphery, especially along the contacts with marbles is characterized with Ca-rich mineralization and titanite occurrence (Fig. 1 M-P). The euhedral to subhedral crystals are large (more than 200 μm) and replaced on places by fine grained mineral mixture (leucoxene) dominated by anatase (proved by the X-Ray powder diffraction and Raman spectroscopy). Titanite closely associates with epidote-chlorite-carbonate alteration. Occasionally apatite completes the assemblage.

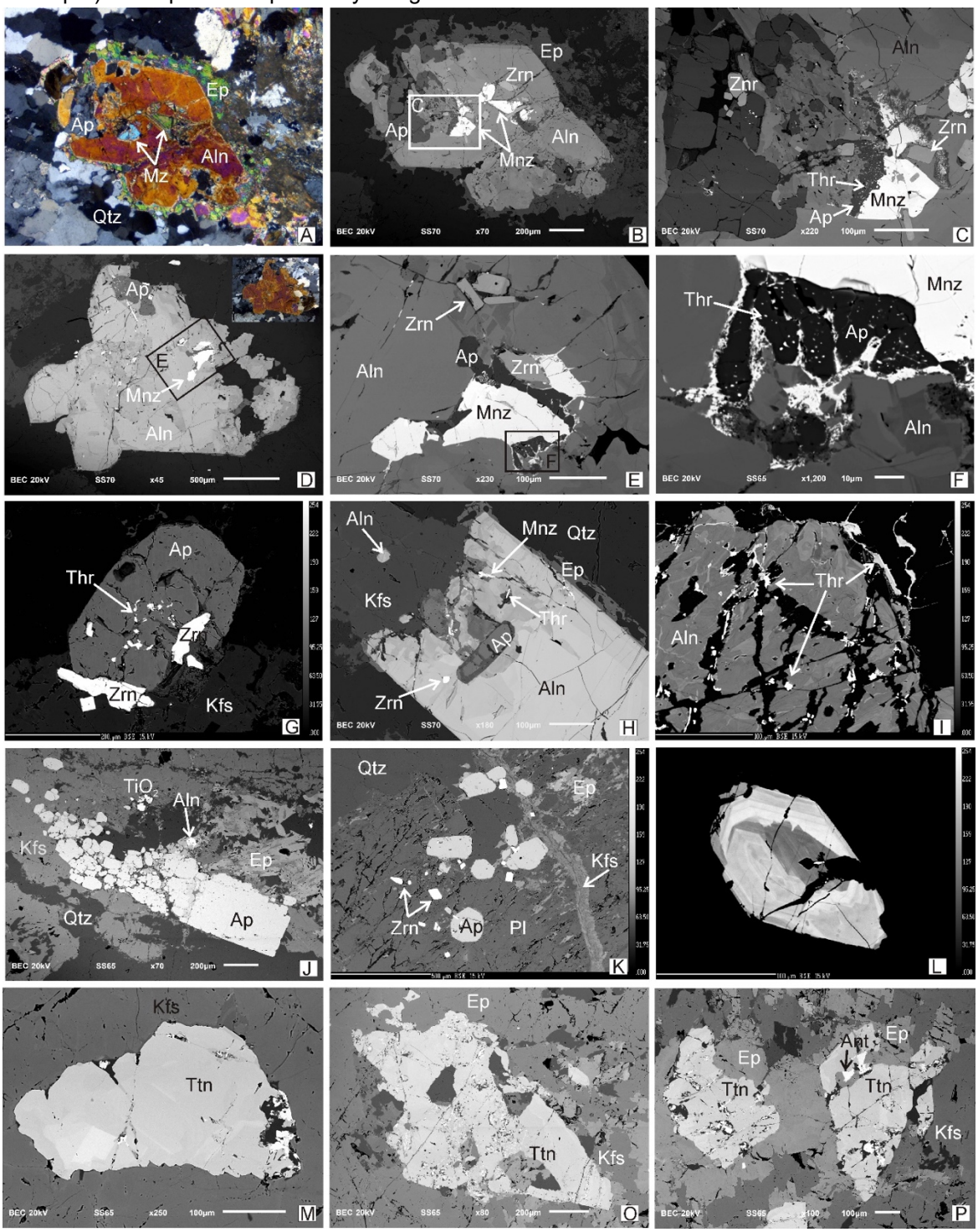

Figure 1. Mineral relationships and textures within the pegmatite-hosted REE association: (A) Epidote-overgrown allanite crystal with inclusions of monazite, zircon, apatite and thorite, PPL; (B) BSE image of crystal from A; (C) close view of the inner parts of allanite crystal, showing zircon and monazite grains and apatite-thorite intergrowths; (D) allanite crystal with apatite and monazite inclusions; (E) monazite relics, close view of (D); (F) thorite-apatite at monazite's expense in allanite crystal; (G) thorite grains and zircon crystals in apatite; (H) zircon and euhedral apatite in allanite; (I) thorite crack-fillings in inhomogeneous allanite; (J) apatite aggregate associating with later epidote; (K) zircon and apatite crystals in altered pegmatite, BSE; (L) oscillatory zoned zircon; (M) titanite in K-feldspar matrix; (O-P) large epidote-associated titanite crystals partly replaced by anatase. Abbreviations refer to: Ap – apatite, Aln – allanite, Ant – anatase, Cc – carbonate, Ep – epidote-clinozoisite, Qtz - quartz; Kfs - K-feldspar, Mnz – monazite, Pl - plagioclase, Thr – thorite, Tit – titanite, Zr - zircon

2.2 Compositional and geochemical features of REE-minerals

Determination of the chemical composition with electron probe microanalysis (EPMA) and laser ablation in inductively coupled plasma with mass spectrometry (LA-ICP-MS) revealed that the studied minerals concentrate large amounts of critical elements with potential importance. REE, U and Th are initially contained by monazite (LREE) and zircon (Hf, HREE) and consequently redistributed among the other accessory phases – allanite, apatite, thorite, and titanite.

Monazite is classified as monazite-(Ce) with significant La (La_2O_3 14.5-16.54 wt.%) and Nd incorporation (Nd_2O_3~9-10 wt.%). Lower, although notable contents of Y, Pr, Sm and Th were detected as major elements. The sum of REE varies between 476425 and 521923 ppm. Uranium content averages 2826 ppm. Chondrite-normalized pattern is characterized by extremely high values for the LREE, well pronounced negative Eu-anomaly and consecutive depletion towards HREE from Gd to Lu.

Apatite is characterized by F-content of ~3 wt.%. Significant Y incorporation (mostly ranging 1000-4000, reaching up to ~7000 ppm) is common for all measured crystals as well as trace amounts of Ga, Ge, and Sr. Certain compositional variations of the mineral depend on the mineral association and the co-existing REE phases and reflect on its geochemical signatures. Apatite crystals in assemblage with thorite and allanite (±monazite; Fig. 1A-F) have the highest values for all incorporated elements, compared to zircon-associated apatite single crystals (Fig. 1K) and apatite aggregate with epidote (Fig. 1J). Chondrite-normalized patterns of all apatites show negative Eu-anomaly, $LREE_{CN}$< $HREE_{CN}$, due to the concurrent growth with allanite and thorite.

Zircon composition has sufficient content of HREE, especially Yb (up to 2500 ppm) and Hf (0.9-1.78 wt.%). Significant incorporation of Th and U and their variation define the zonal pattern of the crystals. Fluorine amount of ~3500 ppm is steady in all measured compounds. Zr/Hf ratio is mostly ranging 40-42, while REE_{CN} are typical for the igneous rocks with positive Ce- and negative Eu-anomalies and enrichment in HREE.

Allanite to REE-bearing clinozoisite compositions show distinct chemical inhomogeneity (Fig. 1 B, D, H, I), which is defined generally by the variation of (REE+Th+Y)/Ca and to a less extend by Fe^{3+}/Al^{3+} ratios. Sufficient Ce- (up to 10 wt. % Ce_2O_3) and La-content (2-5 wt. % La_2O_3) substituting Ca are complemented by ~ 3 wt. % Nd_2O_3. Central parts of the crystals (around monazite relics; see Fig. 1 B, D) are enriched in Ce, while La increases towards the rims. Significant minor elements include Pr, Sm, Gd, Th and traces of Ga, Ge, and Y. REE_{CN}-pattern (plot by Milenkov et al 2023) resembles that of monazite but one order of magnitude lowered.

Titanite single crystals (Fig. 1M-P) reveal incorporation of Al, which defines the chemical inhomogeneity observed in BSE regime in some crystals (e.g. Fig. 1M). Characteristic trace element contents of V, Ni, Sn substitute for Ti^{4+} by means of polyvalent isomorphism. Yttrium, Nb, Zr and LREE, Th, U are present in significant amounts. Chondrite-normalised pattern of REE is characterised by the positive Eu anomaly (see plot by Milenkov et al 2023).

2.3 U-Pb geochronology

In-situ LA-ICP-MS U-Pb geochronology was applied on monazite, zircon and titanite. The monazite grains (Fig. 1B-F) were dated *in-situ* (n=17) and yielded lower intercept age of 40.8±2.6 Ma (MSWD=0.35; Fig. 2A). CL-observation on internal texture of zircon crystals revealed oscillatory magmatic growth zones without inherited cores that suggest magmatic origin (e.g. Fig. 1L). The defined zircon age (based on 14 measurements) is 40.0±2.1 Ma (MSWD=0.085; Fig. 2B). Titanite formation is estimated at 38.6±2.1 Ma (MSWD=1.07; n=20).

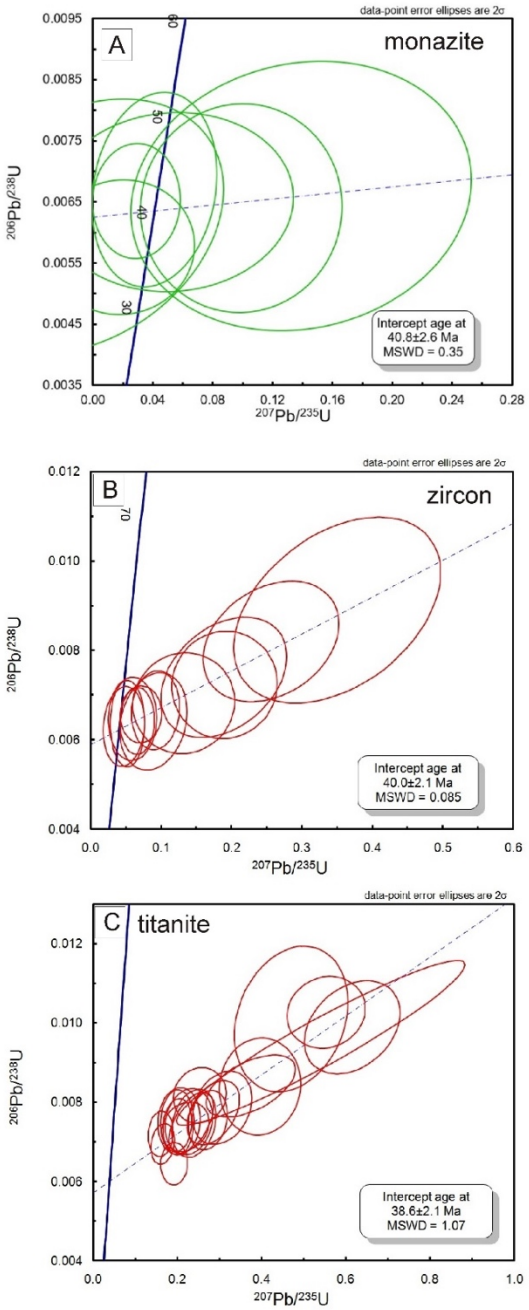

Figure 2. Concordia plots of monazite (A); zircon (B) and titanite (C)

2 Discussion

Mineral replacements

Despite the coexistence of several REE-bearing minerals, their relationships, chemical composition and U-Pb dating suggest continuous process of formation and phase transitions within the early REE-bearing minerals association. Considering their occurrence and morphology, monazite and zircon form in the earlier stages of pegmatite crystallization as proved also by the U-Pb ages. Initially, REE are partitioned between monazite (LREE) and zircon (HREE). The acid leaching of the host rocks (e.g. marbles) or host rock assimilation during pegmatite emplacement led to high initial Ca in the border zone (formation of titanite) and development of late-stage Ca-enriched fluid, which lowered significantly the monazite stability, while zircon remained stable. Dissolution and decomposition of the existing monazite caused redistribution of the incorporated elements. The released LREE (Ce, La) and P are fixed in newly-formed apatite and allanite (Fig. 1A-F). The transition from REE- to Ca-phosphate (monazite to apatite) was facilitated by the high Ca-content (Spear 2010) and strong partitioning of LREE to allanite. Liberated Th contributes to formation of thorite. Limited mobility of LREE from monazite in the fluid phase results in the observed close proximity of allanite. LREE-enrichment in allanite around the monazite grains and its chemical inhomogeneity indicate partial fractionation of La/Ce combined with high Ca content in fluid. On the other hand, apatite is depleted in LREE and shows increased HREE. Yttrium, instead of forming xenotime, is incorporated in apatite. A simplified expression of the monazite alteration suggested by Sato et al. (2014) is:monazite-(Ce) + Ca-rich fluid → allanite + apatite + thorite

After pegmatite solidification, later hydrothermal activity influenced partial replacement of allanite rims (Fig. 1A-B) by epidote-clinozoisite. Transformation within the epidote group minerals (allanite/clinozoisite; Armbruster et al 2006) is common for the studied pegmatites from the Madan Pb-Zn district (Georgieva et al., 2022).

Age of the pegmatite

Timing of the pegmatite emplacement was estimated by U-Pb geochronometry on monazite, zircon and titanite. As suggested by the mineral relationships the initial accessories were monazite and zircon evidenced also by the in-situ U-Pb LA-ICP-MS ages of 40.8±2.6 Ma and 40.0±2.1 Ma, respectively. Despite the slightly older monazite age, the results for both minerals are overlapping in their uncertainties. Pegmatite is injected into the high-grade rocks of the Rhodope metamorphic complex with Jurassic protolith age soon after the tectono-metamorphic regime switched from compressional to extensional. The late Alpine post-collisional history in the region is marked by partial melting and intrusion of granitic bodies at ~42 Ma (e.g. Smilyan pluton) and consequent migmatization, pegmatite and rhyolite dykes formation (Kaiser-Rohrmeier et al 2013; Ovtcharova et al. 2003; Hantsche et al. 2017; Milenkov et al 2022 and references therein). In the Madan region, these dykes predate the ore mineralization, which precipitated at ~ 30 Ma (Kaiser-Rohrmeier et al. 2004). The obtained titanite age is similar to the age of the titanites from pegmatites in the nearby Petrovitsa Pb-Zn deposit (Milenkov et al 2022).

Acknowledgements

The study is financially supported by the Bulgarian National Science Fund project KP-06-N34/4. Microprobe analyses at Masaryk University, Brno, were performed in cooperation within the ERA-MIN3 PEGMAT project from Bulgarian (KP-06-DO02/2) and Czech (TH79020002) grants.

References

Armbruster T, Bonazzi P, Akasaka M, Bermanec V, Chopin C,Giere R, Heuss-Assbichler S, Liebscher A, Menchetti S, PanGier´e R, Heuss-Assbichler S, Liebscher A, Menchetti S, Pan Y, Pasero M (2006) Recommended nomenclature of epidote-group minerals. European Journal of Mineralogy 18(5):551–567.

Georgieva S, Vassileva R, Milenkov G, Stefanova E (2022) Major and trace element signature of epidote-group minerals in altered pegmatites from the Petrovitsa Pb–Zn deposit of the Madan ore region, Central Rhodopes, Bulgaria: Evidence of allanite/epidote transformation. Geologica Carpathica, 73 (4): 365-380, https://doi.org/10.31577/GeolCarp.73.4.5

Hantsche AL, Kouzmanov K, Dini A, Vassileva R, Guillong M, von Quadt A, (2017) U-Pb age constraints on skarn formation in the Madan Pb-Zn district, Bulgaria: zircon evidence from Tertiary magmatism. 15th Swiss Geoscience Meeting, Abstract volume, 124–125.

Kaiser-Rohrmeier M, Handler R, von Quadt A, Heinrich C (2004) Hydrothermal Pb-Zn ore formation in the central Rhodopian dome, South Bulgaria: review and new time constraints from Ar-Ar geochronology. Swiss Bulletin of Mineralogy and Petrology 84 (1): 37–58.

Kaiser-Rohrmeier M, von Quadt A, Driesner T, Heinrich, CA,Handler R, Ovtcharova M, Ivanov Z, Petrov P, Sarov ST, Peytcheva I (2013) Post-orogenic extension and hydrothermal ore formation: high-precision geochronology of the central Rhodopian metamorphic core complex (Bulgaria-Greece). Econ Geol 108(4):691–718. https://doi.org/10.2113/econgeo.108.4.691

Linnen RL, Lichtervelde MV, Cerni P (2012) Granitic pegmatites as sources of strategic metals. Elements 8(4):275-280, DOI: 10.2113/gselements.8.4.275

Milenkov G, Vassileva R, Georgieva S, Grozdev V, Peytcheva I (2022) Trace-element signatures and U-Pb geochronology of magmatic and hydrothermal titanites from the Petrovitsa Pb-Zn deposit,Madan region, Central Rhodopes (Bulgaria).Geologica Balc51(2): 79–91.

Milenkov G, Vassileva RD, Georgieva S, Kouzmanov K, Cempírek J, Georgieva Y (2023) Comparative study of pegmatites from the Central Rhodopean Pb-Zn deposits (Bulgaria), this volume

Ovtcharova M, von Quadt A, Frank M, Kaiser-Rohrmeier M (2003) Triggering of hydrothermal ore mineralization in the Central Rhodopean core complex (Bulgaria) - insight from isotope and geochronological studies on Tertiary magmatism and migmatization. In: Eliopoulos D.G, (Ed.) *Mineral exploration and sustainable development*, 1: 367–370.

Sato K, Minakawa T, Kato T, Maki K, Iwano H, Hirata T, Hayashi S, Suzuki K (2014) Behavior of rare elements in Late Cretaceous pegmatites from Setouchi province, inner zone of southwest Japan. Journal of Mineralogical and Petrological Sciences 109: 28-33

Spear F S (2010) Monazite–allanite phase relations in metapelites. Chemical Geology 279: 55-62, doi:10.1016/j.chemgeo.2010.10.004

Comparison of the Beauvoir and Cínovec rare metal granite/greisen systems: Role of muscovitization on Li-Sn-W-Ta hydrothermal remobilization

Matthieu Harlaux, Olivier Blein, Blandine Gourcerol
BRGM – French Geological Survey, 45060 Orléans, France

Abstract. We provide a comparative review of greisenization in the Beauvoir (France) and Cínovec (Czech Republic/Germany) deposits, which are two of the world's best studied examples of peraluminous Li-Sn-Ta-W-mineralized granitic systems. While the Cínovec granite cupola is two-to-eight times less enriched in rare metals than Beauvoir, a Li-Sn-W greisen deposit was formed in the former but not in the latter. At Beauvoir, alteration of igneous lepidolite produced Sn-rich and Li-W-Ta-depleted greisen muscovite. In contrast, igneous and greisen zinnwaldite at Cínovec have similar contents of Li, Sn, W and Ta. Late replacement of zinnwaldite by muscovite in the Cínovec greisen is marked by enrichment in Sn and depletion in Li, W and Ta, similar to greisen muscovite from Beauvoir. We conclude that muscovitization, although associated with secondary Sn enrichment, is not essential for the formation of mineralized greisens, which are primarily controlled by the emplacement depth of magmas and the intensity of pervasive alteration.

1 Introduction

Rare metal granites (RMG) represent the most fractionated members of granitic suites and are characterized by significant enrichment in rare lithophile elements such as Li, Be, Sn, W, Cs, Ta and Nb (Černý et al. 2005; Linnen and Cuney 2005). While the magmatic evolution and the magmatic-hydrothermal transition of RMG systems have been extensively studied (Linnen and Cuney 2005; Ballouard et al. 2016; Breiter et al. 2017; Harlaux et al. 2017; Kaeter et al. 2018; Michaud and Pichavant 2020), the factors controlling metal remobilization and the formation of mineralized alteration zones around granitic plutons are much less understood.

Among metasomatic processes that affect granitic cupolas, greisenization is commonly associated with Sn-W and RMG deposits (Černý et al. 2005). This feldspar-destructive alteration results from high-temperature interactions between granitic rocks and acidic fluids, locally forming Li-Sn-W deposits (Černý et al. 2005; Breiter et al. 2017). Although greisenization has been investigated from mineralogical, geochemical, experimental and modelling standpoints (Halter et al. 1996, 1998; Breiter et al. 2017; Launay et al. 2019, 2023), it is still unclear why some RMG systems develop mineralized greisen deposits while other do not.

In this paper, we provide a comparative review of greisenization at Beauvoir (France) and Cínovec (Czech Republic/Germany), which are two well-studied examples of RMG in Europe (Gourcerol et al. 2019). The greisens in these two localities show major differences in terms of volume of altered rocks and metal enrichment. Comparing the Beauvoir and Cínovec deposits can provide, therefore, useful insights to better understand what controls the development of mineralized RMG-greisen systems.

2 Geological background

2.1 The Beauvoir RMG

The Beauvoir granite is located within the Echassières granitic complex in the NE part of the French Massif Central which belongs to the Moldanubian zone of the European Variscan belt. The Beauvoir granite was emplaced at ca. 315-310 Ma and is characterized by a strongly peraluminous S-type composition with a disseminated Sn-Li-Ta-Nb-Be mineralization (Cuney et al. 1992; Raimbault et al. 1995). The 900-m-long GPF-1 borehole drilled through the Beauvoir granite revealed a vertical zoning with three granitic units, which are from the upper to the lower (Cuney et al. 1992; Raimbault et al. 1995): (i) B1 unit (-100 to -450 m) corresponding to an albite-lepidolite-rich leucogranite containing globular quartz and rare anhedral perthitic K-feldspar; (ii) B2 unit (-450 to -750 m) consisting of a lepidolite-rich granular granite with idiomorphic quartz and low amounts of K-feldspar; and (iii) B3 unit (-750 to -880 m), which contains euhedral pink-colored K-feldspar and zinnwaldite. The abundance of accessory minerals (topaz, cassiterite, columbite-tantalite, microlite, and Li-Be phosphates) increases upward from the B3 to the B1 units, the latter being the most evolved (Cuney et al. 1992; Raimbault et al. 1995). The uppermost B1 unit exhibits greisen alteration consisting of a quartz-muscovite-topaz assemblage developed along fractures without significant mineralization (Monnier et al. 2020).

2.2 The Cínovec RMG

The Cínovec granite is located within the Krušné hory/Erzgebirge in the NW part of the Bohemian Massif which belongs to the Saxo-Thuringian zone of the European Variscan belt. The granite was emplaced at ca. 325-322 Ma into rhyolites of the Altenberg-Teplice caldera within a large volcanic-plutonic complex and is characterized by a moderately peraluminous A-type composition with enrichment in Li, Rb, Cs, Ta, Sn, W (Štemprok 2016; Breiter et al. 2017). Vertical zonation at Cínovec was documented by the 1600-m-long CS-1 borehole and consists of four major units, which are from top to bottom (Štemprok 2016; Breiter et al. 2017): (i) granite canopy (CnG; down to -260 m) composed of

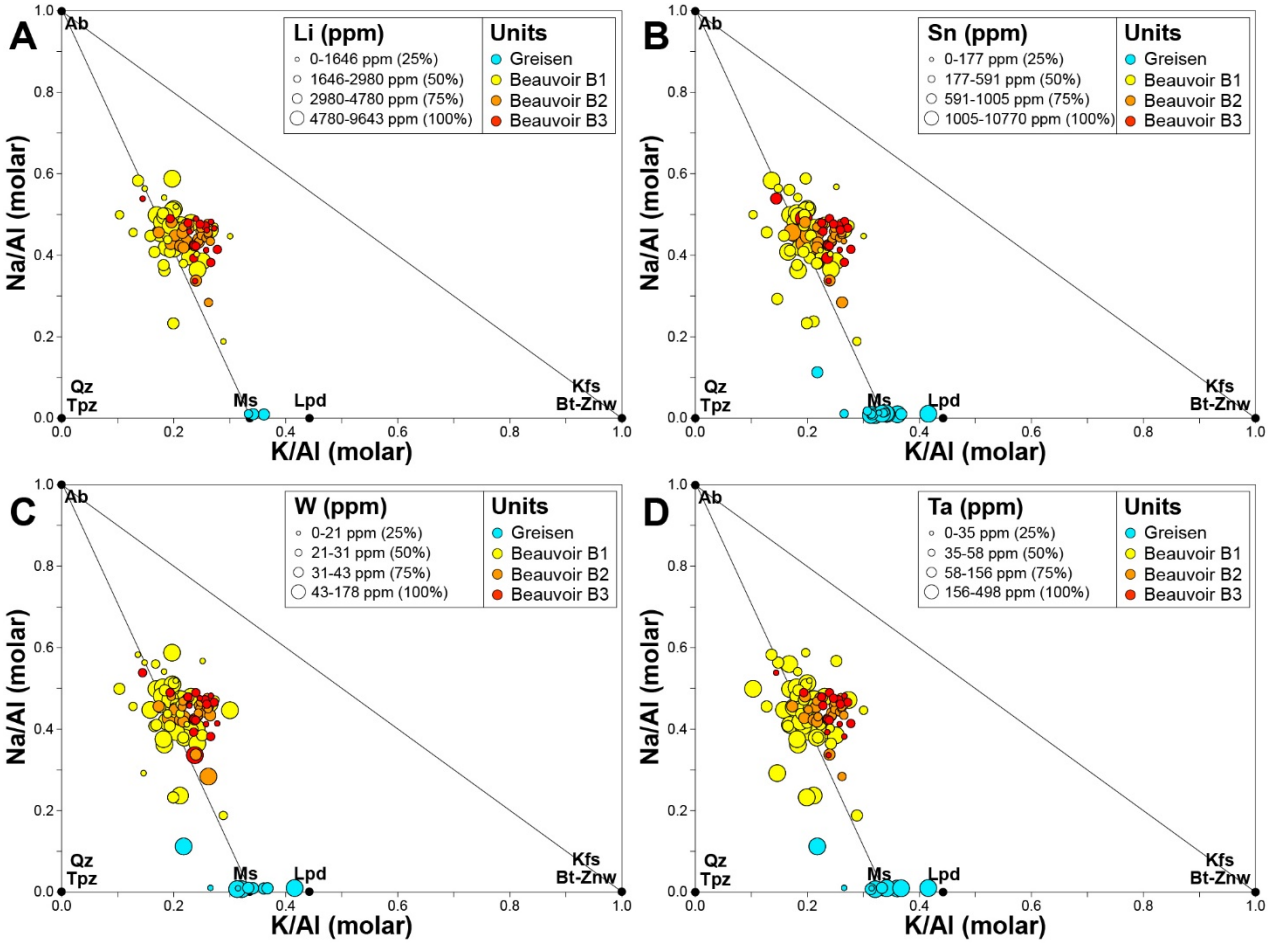

Figure 1. Bubbleplot diagrams of K/Al vs. Na/Al molar ratios for rock samples from Beauvoir illustrating the contents of Li, Sn, W, and Ta in granites and greisens. The bubble diameters correspond to quartile distribution (25%, 50%, 75%, 100%) of element concentrations. The node locations of common silicate minerals identified in these rocks are also plotted (Ab = albite, Bt = biotite, Kfs = K-feldspar, Lpd = lepidolite, Ms = muscovite, Qz = quartz, Tpz = topaz, Znw = zinnwaldite).

an equigranular fine-grained albite-zinnwaldite granite with subhedral albite, globular quartz, and rare K-feldspar; (ii) medium-grained porphyritic mica-free granite (MfG; -260 to -370 m), which contains subhedral quartz and anhedral K-feldspar and albite; (iii) fine- to medium-grained porphyritic albite-zinnwaldite granite (ZiG(m); -370 to -735 m) which shows evidence of commingling; and (iv) a lower suite of biotite granites (BtG; -735 to -1596 m) comprising fine-to-medium-grained porphyritic to coarse-grained equigranular facies with perthitic K-feldspar and subhedral plagioclase. Quartz–zinnwaldite greisens occur in the granite canopy, locally forming massive alteration zones. Disseminated mineralization in the greisen consists of irregularly distributed cassiterite, fluorite, topaz, columbite-tantalite, scheelite, wolframite and REE-F-carbonates (Breiter et al. 2017, 2019).

3 Results

3.1 Whole-rock compositions

Based on a compilation of whole-rock geochemical data from the Beauvoir and Cínovec RMG-greisen systems (Cuney et al. 1992; Raimbault et al. 1995; Dolejš and Štemprok 2001; Monecke et al. 2007; Štemprok 2016; Breiter et al. 2017; Müller et al. 2018), we compared the enrichment in Li, Sn, W and Ta related to greisenization. Data were plotted in the K/Al vs. Na/Al molar ratio diagram, which is convenient to identify alteration trends and related mineralogical changes (Davies and Whitehead 2010). Compared to the uppermost Beauvoir granite (B1 unit: avg Li = 4575 ppm; Sn = 1077 ppm; Ta = 179 ppm; W = 41 ppm), the quartz-muscovite greisens have moderate enrichment in Sn (avg = 1944 ppm; +81%) but no specific enrichment in Li (avg = 3403 ppm; -26%), Ta (avg = 236 ppm; +32%) and W (avg = 45 ppm; +9%; **Fig. 1**). In contrast, quartz-zinnwaldite greisens at Cínovec are moderately to strongly enriched in Li (avg = 4314 ppm; +292%), Sn (avg = 1126 ppm; +744%), W (avg = 491 ppm; +1884%) and Ta (avg = 78 ppm; +97%) compared to the uppermost granite (CnG unit: avg Li = 1100 ppm; Sn = 133 ppm; W = 25 ppm; Ta = 40 ppm; **Fig. 2**).

3.2 Mica compositions

To further investigate the evolution of Li, Sn, W and Ta contents during greisenization of RMG systems, we also compared the trace element concentrations of igneous and greisen micas from Beauvoir and

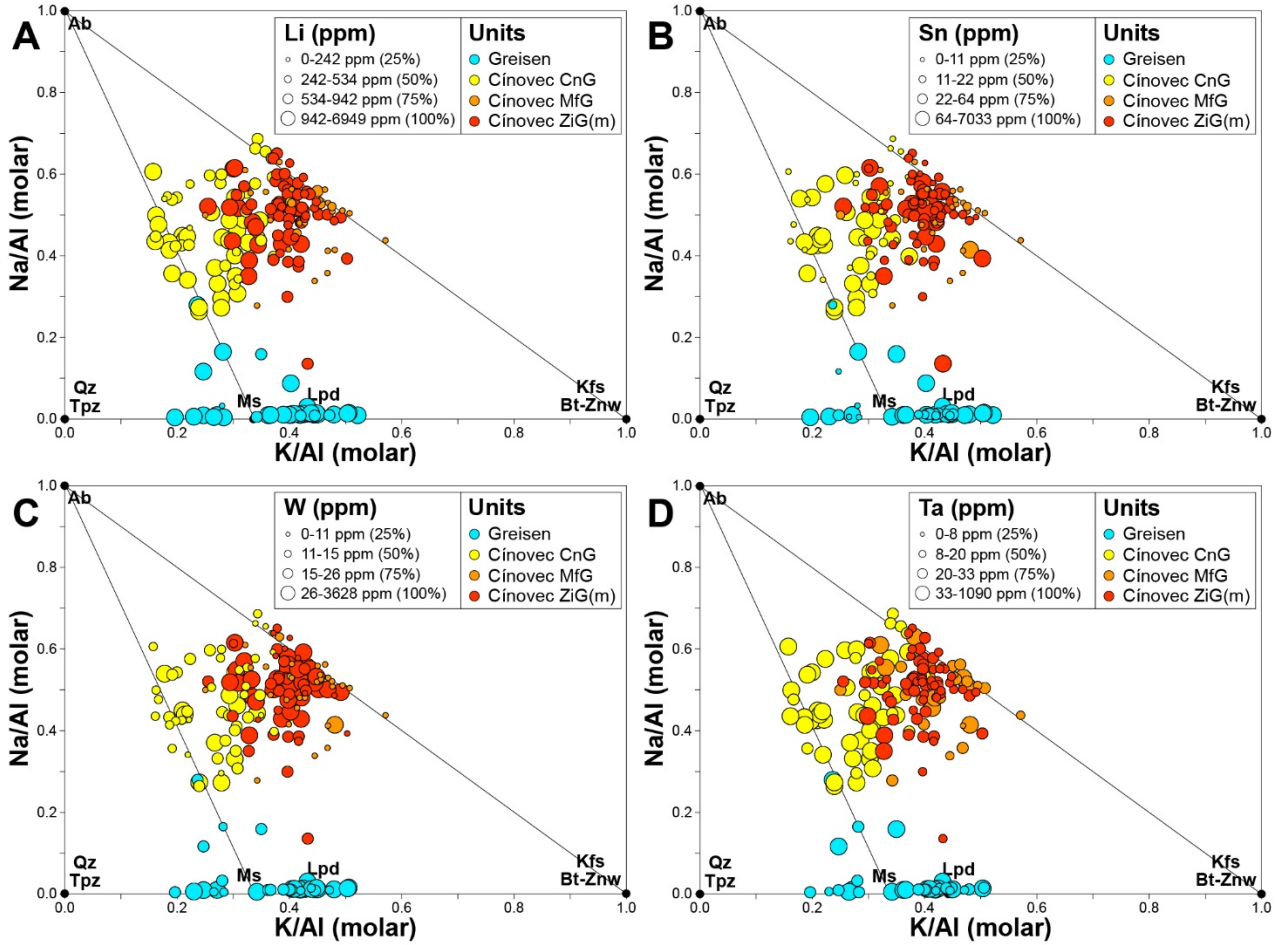

Figure 2. Bubbleplot diagrams of K/Al vs. Na/Al molar ratios for rock samples from Cínovec illustrating the contents of Li, Sn, W, and Ta in granites and greisens. The bubble diameters correspond to quartile distribution (25%, 50%, 75%, 100%) of element concentrations. The node locations of common silicate minerals identified in these rocks are also plotted (Ab = albite, Bt = biotite, Kfs = K-feldspar, Lpd = lepidolite, Ms = muscovite, Qz = quartz, Tpz = topaz, Znw = zinnwaldite).

Cínovec (Breiter et al. 2019; Monnier et al. 2022). At Beauvoir, greisen muscovite is strongly enriched in Sn (avg = 1173 ppm; +677%) but is significantly depleted in Li (avg = 648 ppm; -97%), W (avg = 2 ppm; -99%) and Ta (avg = 29 ppm; -52%) compared to igneous lepidolite from the B1 granite (avg Li = 25,127 ppm; Sn = 151 ppm; W = 246 ppm; Ta = 61 ppm; **Fig. 3A**). In contrast, greisen zinnwaldite from Cínovec has similar contents of Li (avg = 16,568 ppm), Sn (avg = 124 ppm), W (avg = 20 ppm) and Ta (avg = 19 ppm) compared to igneous zinnwaldite from the granite canopy (CnG unit: avg Li = 15,819 ppm; Sn = 122 ppm; W = 35 ppm; Ta = 40 ppm; **Fig. 3B**). However, late muscovite locally replacing zinnwaldite in the Cínovec greisen shows a marked enrichment in Sn (avg = 1287 ppm; +938%) and significant depletions in Li (avg = 3961 ppm; -76%), W (avg = 6 ppm; -70%) and Ta (avg = 17 ppm; -11%) relative to greisen zinnwaldite (**Fig. 3B**).

4 Discussion and conclusions

While the Cínovec RMG cupola is less enriched in rare metals than Beauvoir with two-to-eight times lower average contents of Li (1100 ppm vs. 4575 ppm), Sn (133 ppm vs. 1077 ppm), W (25 ppm vs.41 ppm) and Ta (40 ppm vs. 179 ppm), it is associated with a highly-mineralized Li-Sn-W greisen deposit. This difference of metal enrichment is recorded by the composition of micas, which are petrogenetic monitors of the evolution of RMG-greisen systems. At Beauvoir, alteration of Li-Sn-W-enriched igneous lepidolite produced Sn-rich and Li-W-Ta-depleted greisen muscovite, thus releasing Li, W and Ta in the hydrothermal fluid (Monnier et al. 2022). At Cínovec, there are no major changes of Li, Sn, W and Ta contents between igneous zinnwaldite and greisen zinnwaldite, the latter being interpreted to have fully re-equilibrated with the greisen-forming fluid (Breiter et al. 2019). Late alteration of zinnwaldite to muscovite in the Cínovec greisen is marked by a strong enrichment in Sn and depletion in Li, W and Ta, similar to greisen muscovite at Beauvoir. Therefore, muscovitization occurring in both RMG cupolas was not essential for the formation of mineralized greisens. Although it is associated with secondary Sn enrichment, muscovite alteration seems more an inhibitor of metal enrichment in greisens. The fact that massive mineralized greisens were formed at Cínovec but not at Beauvoir is likely related to different emplacement depths of magmas and volumes of

fluids released. Greisenization and veining at Cínovec were favored by hypabyssal emplacement (0.5-1.5 km) of the granitic magmas, thus causing widespread hydraulic fracturing and pervasive alteration of significant rock volumes (Štemprok 2016; Breiter et al. 2017). In contrast, the greater emplacement depth of the Beauvoir RMG (ca. 3-4 km) induced mostly fracture-related alteration, which may explain the lack of massive mineralized greisens (Cuney et al. 1992).

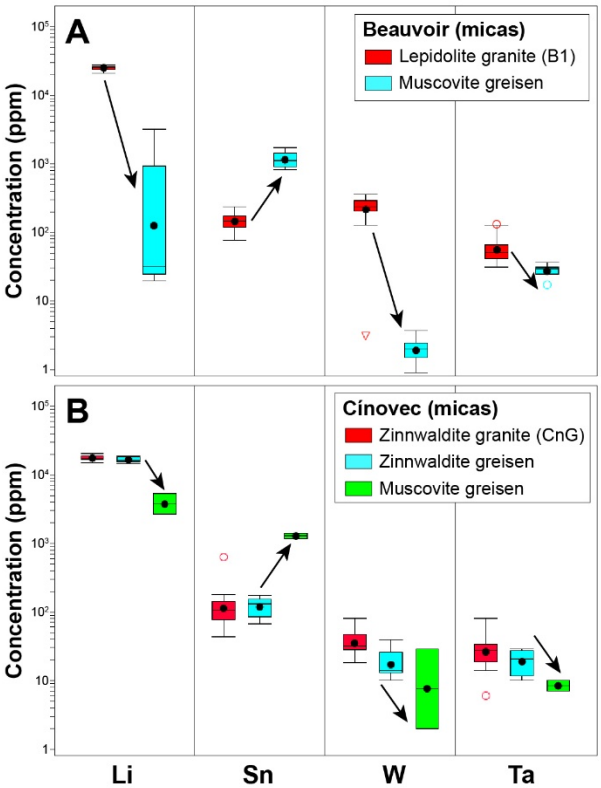

Figure 3. Box plots illustrating the evolution of Li, Sn, W and Ta contents in micas during greisenization of the granitic cupolas at Beauvoir (**A**) and Cínovec (**B**).

Acknowledgements

This project is supported by funds from the Horizon Europe research and innovation programme under Grant Agreement number 101057357, EIS – Exploration Information System (https://eis-he.eu).

References

Ballouard C, Poujol M, Boulvais P, Branquet Y, Tartèse R, Vigneresse JL (2016) Nb-Ta fractionation in peraluminous granites: A marker of the magmatic-hydrothermal transition. Geology 44:231-234.

Breiter K, Ďurišová J, Hrstka T, Korbelová Z, Vaňková MH, Galiová MV, Kanický V, Rambousek P, Knésl I, Dobeš P, Dosbaba M (2017) Assessment of magmatic vs. metasomatic processes in rare-metal granites: a case study of the Cínovec/Zinnwald Sn–W–Li deposit, Central Europe. Lithos 292:198-217.

Breiter K, Hložková M, Korbelová Z, Galiová MV (2019) Diversity of lithium mica compositions in mineralized granite–greisen system: Cínovec Li-Sn-W deposit, Erzgebirge. Ore Geol Rev 106:12-27.

Černý P, Blevin PL, Cuney M, London D (2005) Granite-related ore deposits. Econ Geol 100th:337–370.

Cuney M, Marignac C, Weisbrod A (1992) The Beauvoir topaz-lepidolite albite granite (Massif Central, France): The disseminated magmatic Sn-Li-Ta-Nb-Be mineralization. Econ Geol 87:1766-1794.

Davies JF, Whitehead RE (2010) Alkali/alumina molar ratio trends in altered granitoid rocks hosting porphyry and related deposits. Explor Min Geol 19:13-22.

Dolejš D, Štemprok M (2001) Magmatic and hydrothermal evolution of Li-F granites: Cínovec and Krásno intrusions, Krušné hory batholith, Czech Republic. Bull Czech Geol Surv 76:77-99.

Gourcerol B, Gloaguen E, Melleton J, Tuduri J, Galiegue X (2019) Re-assessing the European lithium resource potential – A review of hard-rock resources and metallogeny. Ore Geol Rev 109:494-519.

Halter WE, Williams-Jones AE, Kontak DJ (1996) The role of greisenization in cassiterite precipitation at the East Kemptville tin deposit, Nova Scotia. Econ Geol 91:368-385.

Halter WE, Williams-Jones AE, Kontak DJ (1998) Modeling fluid–rock interaction during greisenization at the East Kemptville tin deposit: implications for mineralization. Chem Geol 150:1-17.

Harlaux M, Mercadier J, Bonzi WME, Kremer V, Marignac C, Cuney M (2017) Geochemical signature of magmatic-hydrothermal fluids exsolved from the Beauvoir rare-metal granite (Massif Central, France): insights from LA-ICPMS analysis of primary fluid inclusions. Geofluids 2017:1–25.

Kaeter D, Barros R, Menuge JF, Chew DM (2018) The magmatic–hydrothermal transition in rare-element pegmatites from southeast Ireland: LA-ICP-MS chemical mapping of muscovite and columbite–tantalite. Geochim Cosmochim Acta 240:98-130.

Launay G, Sizaret S, Guillou-Frottier L, Fauguerolles C, Champallier R, Gloaguen E (2019) Dynamic permeability related to greisenization reactions in Sn-W ore deposits: Quantitative petrophysical and experimental evidence. Geofluids 2019:1-23.

Launay G, Branquet Y, Sizaret S, Guillou-Frottier L, Gloaguen E (2023) How greisenization could trigger the formation of large vein-and-greisen Sn-W deposits: a numerical investigation applied to the Panasqueira deposit. Ore Geol Rev 105299.

Linnen RL, Cuney M (2005) Granite-related rare-element deposits and experimental constraints on Ta–Nb–W–Sn–Zr–Hf mineralization. GAC Short Course Notes 17:45–68.

Michaud JAS, Pichavant M (2020) Magmatic fractionation and the magmatic-hydrothermal transition in rare metal granites: evidence from Argemela (Central Portugal). Geochim Cosmochim Ac 289:130-157.

Monecke T, Dulski P, Kempe U (2007) Origin of convex tetrads in rare earth element patterns of hydrothermally altered siliceous igneous rocks from the Zinnwald Sn–W deposit, Germany. Geochim Cosmochim Ac 71:335-353.

Monnier L, Salvi S, Jourdan V, Sall S, Bailly L, Melleton J, Béziat D (2020) Contrasting fluid behavior during two styles of greisen alteration leading to distinct wolframite mineralizations: The Echassières district (Massif Central, France). Ore Geol Rev 124:103648.

Monnier L, Salvi S, Melleton J, Lach P, Pochon A, Bailly L, Béziat D, De Parseval P (2022) Mica trace-element signatures: Highlighting superimposed W-Sn mineralizations and fluid sources. Chem Geol 600:120866.

Müller A, Herklotz G, Giegling H (2018) Chemistry of quartz related to the Zinnwald/Cínovec Sn-W-Li greisen-type deposit, Eastern Erzgebirge, Germany. J Geochem Explor 190:357-373.

Raimbault L, Cuney M, Azencott C, Duthou JL, Joron JL (1995) Geochemical evidence for a multistage magmatic genesis of Ta-Sn-Li mineralization in the granite at Beauvoir, French Massif Central. Econ Geol 90:548-576.

Štemprok M (2016) Drill hole CS-1 penetrating the Cínovec/Zinnwald granite cupola (Czech Republic): an A-type granite with important hydrothermal mineralization. J Geosci 61:395-423.

Dating and trace-element characterisation of Sn-W skarn-, greisen- and metamorphic vein-type occurrences from East-Greenland

Nynke Keulen, Benjamin Heredia, Sebastian Malkki, Tonny B. Thomsen, Diogo Rosa, David Whitehead
Geological Survey of Denmark and Greenland (GEUS), Øster Voldgade 10, 1350 Copenhagen, Denmark

Abstract. The traceability of Sn- and W-minerals to their deposit type (skarn, greisen or hydrothermal veins) was tested on rock samples and stream sediments from East Greenland. Scheelite and cassiterite grains from nine occurrences were analysed for their host rock mineral assemblage and geochemical fingerprint (trace elements and dates by laser-ablation inductively coupled plasma mass spectrometry). Samples from eight localities were collected from skarn, greisen or metamorphic vein occurrences, while the ninth consists of loose blocks transported by a glacier. The mineralogy of the samples was investigated with automated quantitative mineralogy (AQM) and trace elements of minerals from these outcrops were compared to trace element values for the same deposit types in literature. Furthermore, U/Pb-dating of the scheelite, cassiterite as well as zircon, apatite and rutile formed during the same mineralising events were estimated, to determine the timing of the mineralisation. AQM observations on the thin sections match well with trace element data, while new dates of the minerals reveal a more complex mineralisation history than previously known, with seemingly comprising at least three pulses during the Caledonian orogeny.

1 Introduction

Tin (Sn) and especially tungsten (W) occurrences in East Greenland were extensively studied by the exploration company Nordisk Mineselskab A/S from the late 1960s to early 1980s, sporadically followed up by investigations by GEUS and the Greenlandic Ministry of Mineral Resources (MMR) in the forty years afterwards, latest during the Summer 2022. Most of the occurrences are connected to the Caledonian orogeny in East-Greenland (Figure 1). Mineral occurrences are found in the uppermost Caledonian thrust sheet and in the passively overlying sediments of the Franz Joseph allochthon and are thought to be associated with the intrusion of Silurian and Devonian S-type granites (Higgins et al. 2004). Sn-mineralisation is observed as cassiterite, while W is found in scheelite. Mineralised rocks are found as skarn, greisen or metamorphic vein occurrences, depending on their host rock and the proximity to granites (Hallenstein & Pedersen, 1982).

Literature data reveal that different deposit types, like skarns, greisen, and metamorphic vein-type each have their own set of mineral trace element compositions (e.g., Wang et al. 2022, Sciuba et al. 2020 and many others). A good understanding of these properties can serve in assessing the potential for what deposit types are expected to be found upstream based on analysed stream sediment or till samples.

2 Geological setting

The occurrences can be divided into three major groups (Hallenstein & Pedersen, 1982, Strachan et al. 2001): 1) Skarn deposits related to the formation of thin granitic sheets in high-grade metamorphic sediments of the Krummedal sequence in the Hagar Bjerg thrust sheet. These are all scheelite occurrences; 2) Greisen deposits related to magmatic fluids and large granitic bodies intruding into the lower Eleonore Bay Supergroup of the Franz Joseph allochthon. Both cassiterite and scheelite occur; 3) In metamorphic quartz-scheelite veins, associated with antimony, arsenic, and copper found in bituminous limestone beds of the upper part of the Eleonore Bay Supergroup. Samples from nine different localities in East Greenland were investigated **(Figure 1**).

3 Analytical methods

3.1 Automated quantitative mineralogy (AQM)

Thin sections of samples were investigated with AQM to study the mineral assemblage formed during the mineralisation. AQM is a scanning electron microscope technique that combines back-scattered electron imaging with chemical analyses by energy dispersive spectroscopy in a mosaic with a small step-size (Keulen et al. 2020). Each analysis is interpreted as a mineral species and is coloured as a pixel in the false-coloured mineral map. Furthermore, cathodoluminescence (CL) imaging is performed to study growth zonations within scheelite and cassiterite.

3.2 LA-ICP-MS investigations

Laser-ablation inductively coupled plasma mass spectrometry (LA-ICP-MS) analyses were performed with two purposes: 1) to investigate the age constraints of mineralisation of scheelite, cassiterite together with other minerals formed at the same time, and 2) to characterise the deposit type by estimating the characteristic range of trace elements in its minerals. For this second purpose a database of literature data for cassiterite (K. Foltyn), scheelite and tourmaline was built.

To facilitate the matrix-matched cassiterite dating by LA-ICP:MS, a new standard was

developed, following a procedure described elsewhere at this conference (Thomsen et al.).

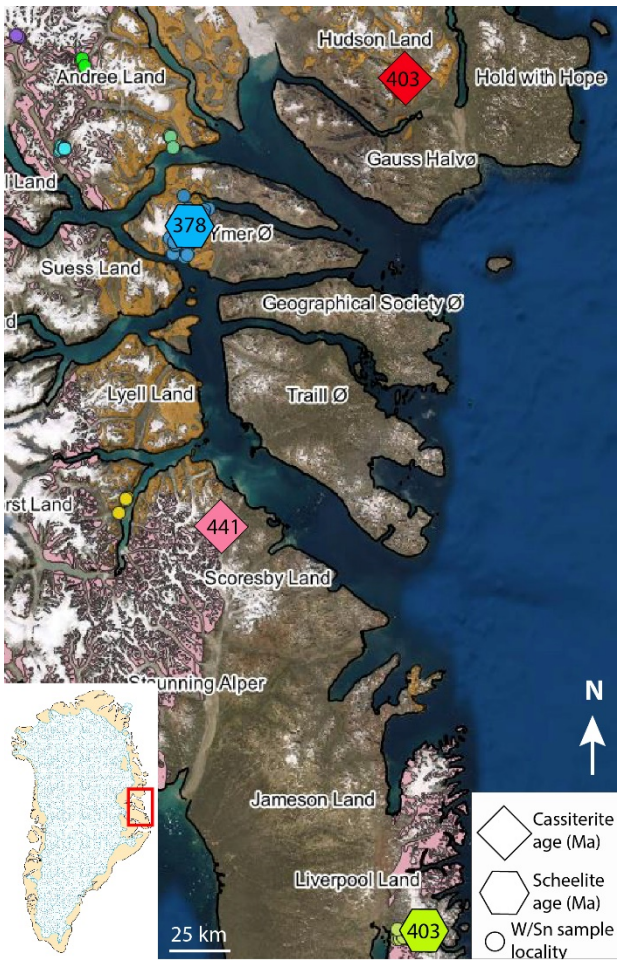

Figure 1. Map of East Greenland showing known scheelite and cassiterite localities. So far, the mineralisation dates of samples from Blokadedal (red), Margeries Dal (blue), Berserkerbræ (pink) and Kalkdal (green) have been determined. Data on other five occurrences will be shown during the conference.

4 Results

4.1 Field observations

Field observations in Blokadedal show the close association of a S-type granite and its alteration zones with tourmaline, fluorite, Y-La-allanite, yellowish-green mica minerals and quartz veins (Figure 2). Cassiterite is found in the alteration zone (greisen), while the more distal hydrothermal quartz veins host both scheelite and cassiterite.

4.2 Mineralogy

AQM observations confirm the three main settings with skarn, greisen and metamorphic vein occurrences, but also reveal differences in the mineral assemblages from the individual occurrences depending on the composition of the host rock and variations in the metasomatic fluids. The Blokadedal occurrence (**Figure 3A**) shows that cassiterite is present in three settings; associated with tourmaline, topaz and fluorite; with Li-bearing muscovite and biotite; or with muscovite and beryl.

The Margeries Dal occurrence (Figure 3B) shows quartz veins intruded in limestone, where scheelite precipitates. A range of different settings exists; scheelite occurs as veins, often coated with quartz or calcite, as dispersed grains in a matrix with quartz, dolomite, calcite, ±apatite, ±ankerite. Locally, scheelite is observed within siliciclastic sediments. The veined scheelite shows clear oscillatory zonation (**Figure 3B**). In the north-western part of the area, stibnite is deposited in quartz veins.

4.3 Dating of the mineralisation

ICP-MS analyses showed that the mineralisation of Sn and W did not occur in a single event but consisted of at least three different pulses likely between 441-378 Ma (**Figure 1**). This indicates that the mineralisation was triggered by local events, rather than a single regional event and that the timeslot with optimal conditions for melting and fractionation was longer than previously assumed.

4.4 Trace elements in scheelite and cassiterite

Comparison of the trace elements reveals that the scheelite occurrences from the study area compare well to literature trace element data and that the vein-type deposits, which were classified as the most tungsten-rich by Nordisk Mineselskab A/S can easily be distinguished from skarn-type scheelite (**Figure 4**).

5 Discussion

Formation of scheelite and cassiterite was possible during at least three stages in the history of the area: The first pulse at ca. 445-441 Ma was observed as the dates of cassiterite in Berserkerbræ. This age is not well understood, as it is older than the Caledonian S-type granites. Migmatisation was reported in the metasedimentary rocks of the Hagar Bjerg thrust sheets from 446 Ma onwards (Gilotti & McClelland 2008). This might have caused a local fractionated melt, resulting in enrichment in Sn (and W) and the formation of greisen with cassiterite.

Most S-type granites were emplaced near 425 Ma (Kalsbeek et al. 2008). S-type granites are typically the source of Sn and W in occurrences. McClelland and Gilotti (2003) define this period as the first stage of synorogenic extension, thus transporting heat to the Krummedal metasediments, which will likely promote partial melting and fractionation of Sn and W in the magma.

During the main pulse of mineralisation both scheelite and apatite from Kalkdal, as well as cassiterite and rutile from Blokadedal all give the same date (ca. 403 Ma), which is the possible age

of chemically evolved Devonian granites in area (Steenfelt 1982). AQM observations reveal that

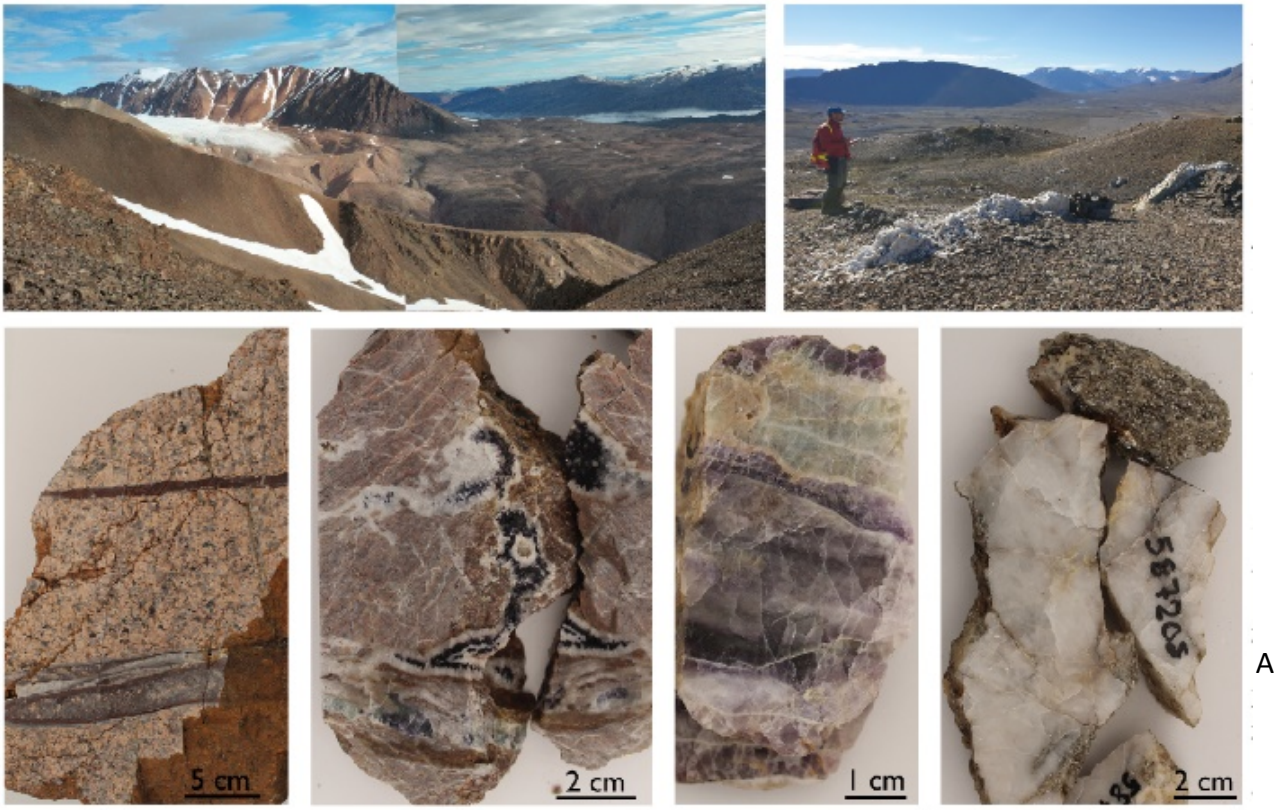

Figure 2 (above). Field observations from Blokadedal. Top row: Blokadedal with tin-bearing granite intrusion (pink, arrow). Sets of quartz-veins crosscut the Eleonore Bay Supergroup rocks. Bottom row: Altered granite samples with siliceous veins, including tourmaline (black), fluorite (green-purple) and brecciated rock. Quartz-veins with yellowish-green mica were previously correlated with enhanced W-Sn concentrations.

Figure 3 (below). A) Automated quantitative mineralogy (AQM) map of a cassiterite-bearing sample from Blokadedal. Cassiterite (red) is here associated with tourmaline and muscovite. **B**) AQM map and CL image of scheelite-bearing sample from Margeries Dal. Scheelite (dark blue) occurs as at least two generations of oscillatory hydrothermal veins that crosscut the altered bituminous limestone host-rock.

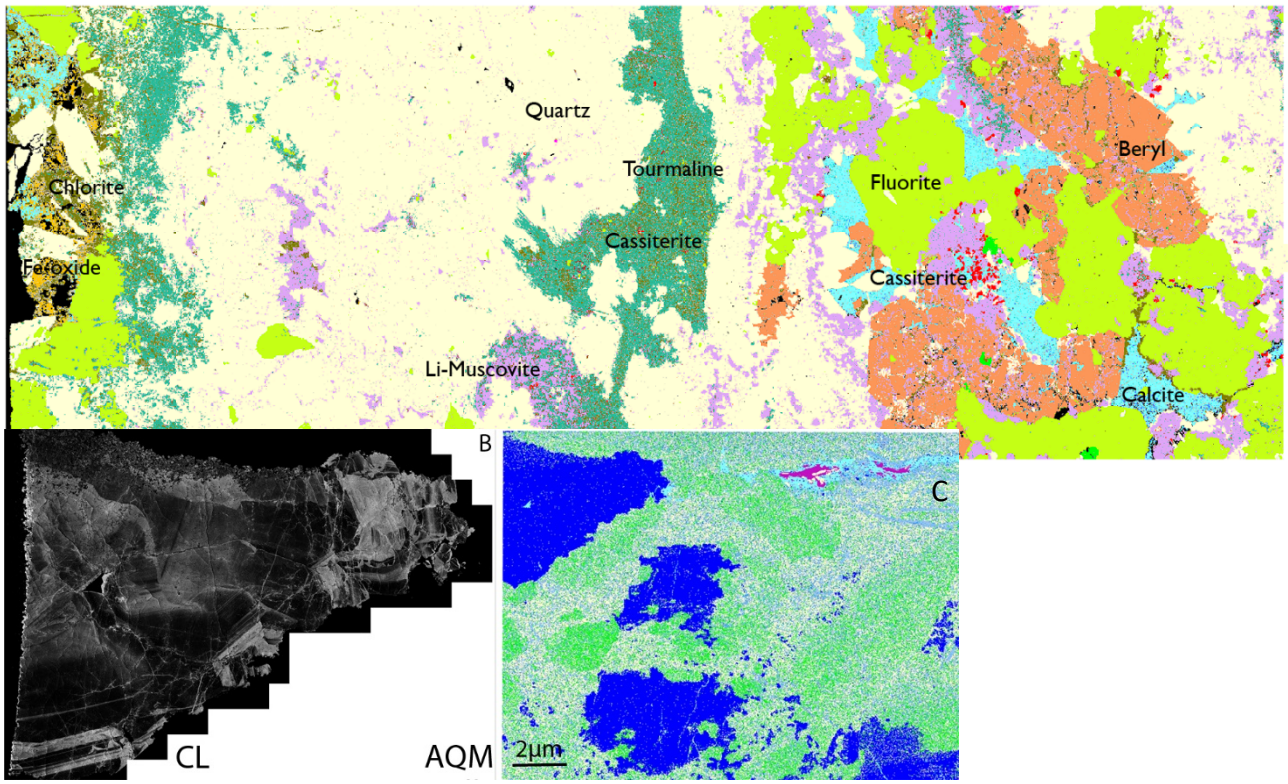

rutile and apatite grew as part of the mineralisation process and most likely not were present before the mineralisation. Therefore, it is likely that a renewed fractionation occurred, which produced granitic magma enriched in Sn and W. McClelland & Gilotti (2003) associated an age of 404 Ma with late orogenic extension and exhumation, which is a likely explanation for this renewed fractionation.

The last pulse of mineralisation is observed in the Margeries Dal area and is significantly younger (376 Ma). These, as well as other upper Eleonore Bay Supergroup scheelite occurrences, are not spatially associated with a granite, which is in agreement with the trace element signature in tourmaline and scheelite from the same occurrences.

Further integration of absolute dating and trace element compositions on the scheelite and cassiterite occurrences in the area will lead to a better understanding of the different mineralisation styles. Furthermore, the methodologies presented here act as a platform serving to improve our under-standing of the geological processes relevant for the formation of cassiterite and scheelite deposits in eastern Greenland.

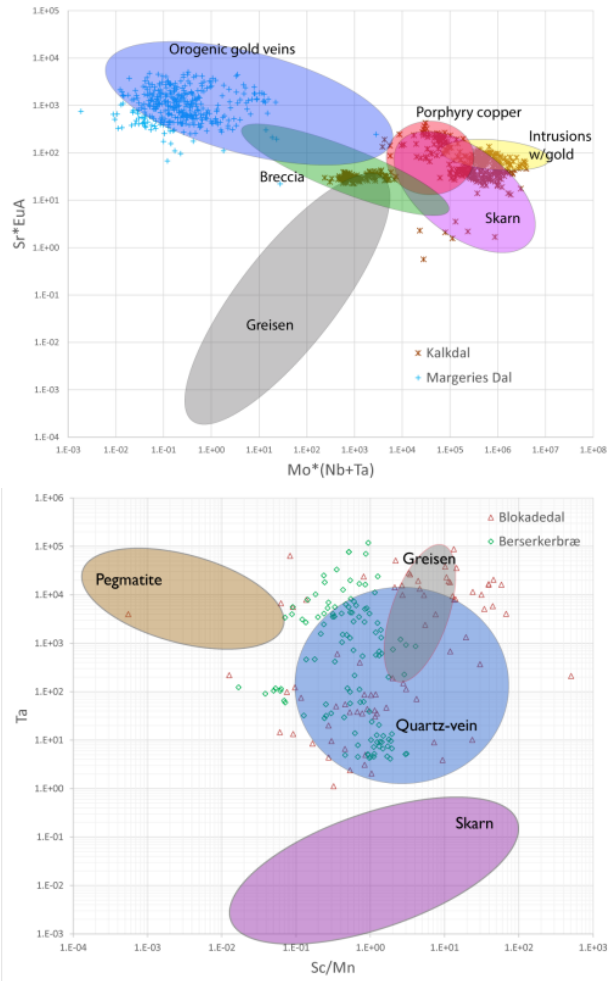

Figure 4. Trace element distribution for scheelite from Kalkdal and Margeries Dal and for cassiterite from Blokadedal and Berserkerbræ, compared to compositions reported in literature for different mineralisation types.

Acknowledgements

The project was financed by GEUS, EIT-RM project MinExTarget #109674 and the Greenlandic Ministry of Mineral Resources, Government of Greenland. Geologists from Nordisk Mineselskab A/S are thanked for collecting samples. M. Alaei and H. Vesturklett are thanked for laboratory assistance. K. Foltyn is thanked for collecting cassiterite trace element data from literature.

References

Gilotti JA & McClelland WC 2008 Geometry, kinematics, and timing of extensional faulting in the Greenlandic Caledonides – A synthesis. In: Higgins, AK, Gilotti, JA & Smith, MP (eds.). The Greenland Caledonides – evolution of the northeast margin of Laurentia. Geol Soc Am Mem 202:251-271

Hallenstein C & Pedersen J 1982 Study of Scheelite Mineralization in Central East Greenland. Nordisk Mineselskab A/S, 152pp. GEUS Dodex file report 20688

Higgins A, Elvevold S, Escher JC, Frederiksen KS, Gilotti JA, Henriksen N, Jepsen HF, Jones KA, Kalsbeek F, Kinny, PD, Leslie AG, Smith MP, Thrane K & Watt GR 2004 The foreland-propagating thrust architecture of the East Greenland Caledonides 72–75 N. J Geol Soc, London, 1661:1009-1026

Kalsbeek F, Higgins AK, Jepsen HF, Frei R & Nutman AP 2008 Granites and granites in the East Greenland Caledonides. In: Higgins AK, Gilotti JA & Smith MP (eds.). The Greenland Caledonides – evolution of the northeast margin of Laurentia. Geol Soc Am Mem 202: 227-249

Keulen N, Malkki SN, Graham S 2020 Automated Quantitative Mineralogy Applied to Metamorphic Rocks. Minerals 10:47, 29pp. DOI: 10.3390/min10010047

McClelland WC, Gilotti JA 2003 Late-stage extensional exhumation of high-pressure granulites in the Greenland Caledonides. Geology 31:259-262

Sciuba M., Beaudoin G., Grzela D. & Makvandi S. (2020) Trace element composition of scheelite in orogenic gold deposits. Mineral Dep 55:1149-1172

Steenfelt A. 1982 Uranium and selected trace elements in granites from the Caledonides of East Greenland. Mineral Mag 46:201-210

Strachan RA, Martin MW, Friderichsen, JD 2001 Evidence for contemporaneous yet contrasting styles of granite magmatism during extensional collapse of the northeast Greenland Caledonides. Tectonics 20:458-473

Wang C, Zhao K, Chen J & Ma X 2022 Examing fingerprint trace elements in cassiterite: Implications for primary tin deposit exploration. Ore Geol Rev 149: 105082, 13pp

Magmatic silica caps associated with intrusion-related ore deposits

Douglas Kirwin[1], Reimar Seltmann[2]
[1]Consultant Geologist, Bangkok, Thailand
[2]Natural History Museum, London, UK

Abstract. Magmatic silica caps comprising massive milky to cloudy mottled quartz have been observed in a number of cupolas associated with mineralized felsic intrusions. Furthermore, those silica-enriched zones may transition to an underlying comb quartz UST (Unidirectional Solidification Texture) horizon reflecting magma quench processes due to undercooling and oscillatory crystallization of excess silica during the magmatic to hydrothermal transition. Silica caps normally occur at the cupola contact with the host wall rocks and may vary considerably in terms of lateral extent and thickness from several meters to tens of meters. In many cases, they are well mineralized, particularly in highly evolved porphyry stocks hosting copper-gold-molybdenum mineralization. There are also many barren examples which at a district scale, represent pre-mineral magmatic accumulations, and as such, are vectors for adjacent fertile mineralized stocks. If the fluid pressures greatly exceed the lithostatic pressure once the silica cap has crystallized, then magmatic-hydrothermal breccias with clasts of "silica cap" quartz may form, either as carapace breccias or breccia pipes. Magmatic silica caps are not well documented in the literature, perhaps due to lack of recognition or destruction by overprinting late-magmatic or hydrothermal events.

1 Introduction

One of the first published records of a cupola-related silica cap is by Butler and Vanderwilt (1933) who, while working for the USGS at the Climax molybdenum deposit in Colorado, USA, mapped a 900 feet zone of massive fine-grained quartz in the White Tunnel and commented that it resembled quartzite. Brown (1939) reported on a prominent banded siliceous outcrop approximately 30 meters in diameter associated with a small monzonite plug in the Sedimentary Hills near Tucson, Arizona. The massive quartz was observed to be locally intergrown with coarse feldspar. This occurrence was later studied by Bennett (1957) who also alluded to the banded quartz outcrops. Another excellent example of a silica cap is that which occurs at the Sadisdorf tin deposit in the Erzgebirge district in Germany (Figure 1). Oelsner (1952-in German), referred to a "quarzglocke" located at the apex of a granitic tin-bearing greisen which was illustrated as a crescent-shaped cap in a mine cross section. A very prominent silica cap with underlying UST's at the Panasqueira tungsten mine in Portugal was described by Kelly and Rye (1979). The UST horizon was mentioned as "zebroid muscovite-quartz layers" (Figure 2). During the late 1970's, mine geologists working at the AMAX Climax and Henderson molybdenum deposits compiled extensive data about the silica caps, numerous UST and stockscheider horizons that were present in several of the highly mineralized cupolas.

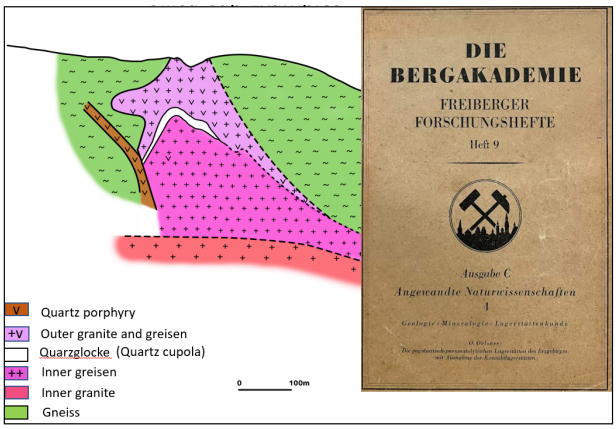

Figure 1. Cross section illustrating the silica cap at the Sadisdorf tin mine, Erzgebirge, Germany. (redrawn from Oelsner,1952)

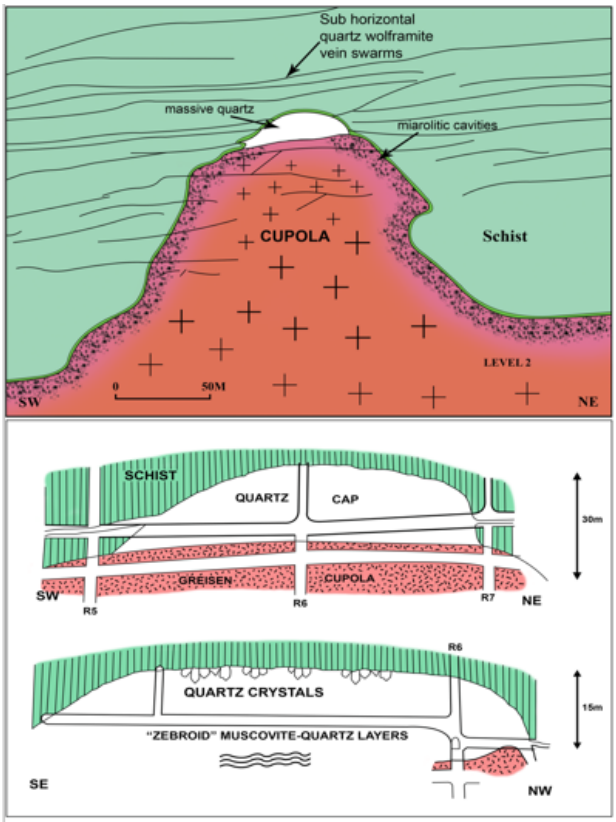

Figure 2. Schematic section illustrating the silica cap at the Panasqueira tungsten mine, Portugal (Kelly and Rye 1979).

A massive silica cap and underlying UST stockscheider zone at the Neo-Proterozoic alkali-

granite cupola at Jabal Umm Al Suqian in Saudi Arabia was studied by Bokhari et al. (1986). This important reference is the first record of very well-preserved cupola textures in Proterozoic intrusions. Another example of a cupola-related massive silica cap is the Max molybdenum deposit in British Columbia, Canada (Lawley 2009). Based on observations from numerous silica cap occurrences throughout Mongolia, Kirwin (2005) described examples from a variety of intrusion-related mineral systems, including the Oyu Tolgoi, Khongor, Tsagaan Survaga, Zun Mod, Bronze Fox porphyry copper-gold deposits, the Tsagaan Chuluut Au deposit, and Umnu Hutul tungsten deposits.

2 Silica caps associated with porphyry copper-gold-molybdenum deposits

During the exploration drilling conducted by Ivanhoe Mines Ltd, in 2002 at the Hugo Dummett deposit at Oyu Tolgoi in Mongolia, a thick zone of massive quartz with high grade gold and copper mineralization was intersected (Figure 3). This was termed the QV90 due to the presence of greater than 90% quartz and considered to be very high density stockwork veining (Khashgerel et al. 2006).

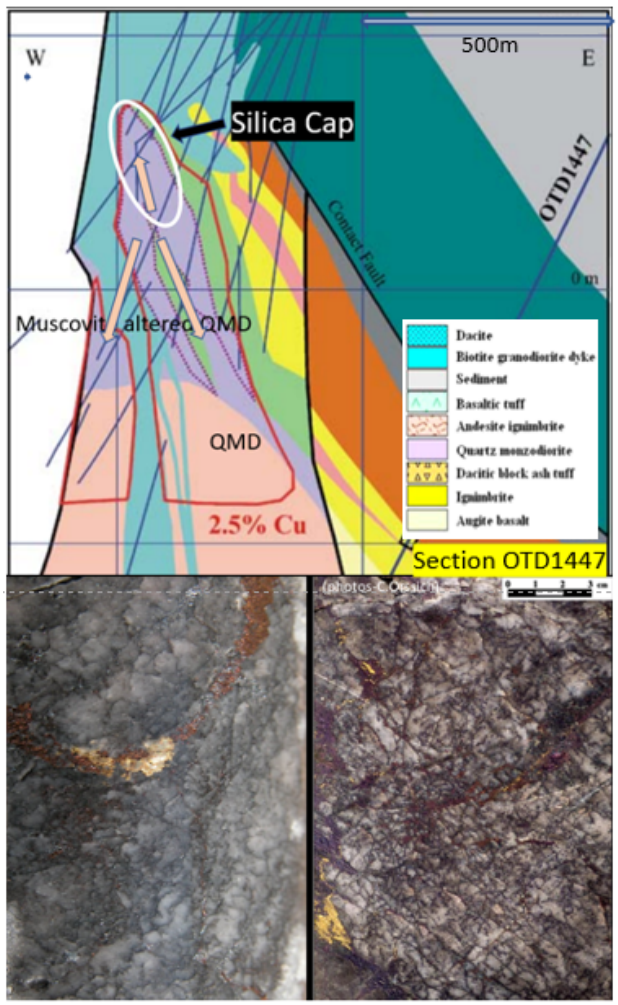

Figure 3. Drill section OTD1447 illustrating the massive high grade silica cap with fracture in fill comprising bornite and chalcopyrite, Oyu Tolgoi.

Closer observation of the QV90 core revealed that the uppermost part was comprised of cloudy and translucent quartz which has a distinctive mottled texture. The bornite and chalcopyrite mineralization was deposited during late-stage shattering of the silica cap. The QV90 zone has a vertical thickness of 10's of meters and occurs in a cupola of a quartz monzodiorite stock. Similar examples of porphyry-related mineralized silica caps are present at the Golpu deposit in Papua New Guinea, North Parkes and Briggs, Australia, Red Chris mine in British Columbia, Nabor porphyry at Basay in the Philippines, the Provost porphyry in Jamaica and Gajah Tidur at the Grasberg mine in Indonesia. Two interesting occurrences in southwest Arizona are located in the Saginaw and Sedimentary Hills, both of which transition downward into UST layers. The high silica zones in cupolas with underlying UST horizons at the Climax mine in Colorado could be interpretated to be examples associated with porphyry molybdenum mineralization. A much smaller "Climax-type" deposit is located at Mt. Unicorn in north-eastern Victoria, Australia where drilling by Dart Mining intersected a molybdenum-bearing massive silica zone, underlain by UST's and stockwork quartz veining (www.dartmiming.com.au). Another molybdenum bearing silica cap occurs at the Lana Corina copper-molybdenum deposit in Chile where drilling recently intersected 85 meters of 0.13% Mo in a massive quartz cupola at the top of a granodiorite stock (www.culpeominerals.com.au).

3 Silica caps associated with intrusion-related gold, tin, uranium, tungsten, REE fluorite mineralization

An intriguing silica cap associated with intrusion-related gold mineralization occurs at Tsagaan Chuluut in northeast Mongolia where a three-meter-thick layer of massive silica transitions into UST's layers with exceptionally large milky quartz crystals which C axis dimensions are greater than one meter. Numerous smaller silica caps outcrop within several square kilometers of extensive alluvial gold mine workings. Another very prominent silica cap 25 meters high and with a diameter of 75 meters known as "The Quartz Blow" is located near the town of Ravenswood in northeast Queensland, Australia. There are several current open pit and underground mines in the district which has produced in excess of 5M ozs Au. The silica cap (and numerous UST occurrences) is barren and represents the early magmatic component of systems which host breccia pipe (Mt Wright gold mine) and sheeted vein style gold mineralization (Nolans gold mine) post the magmatic hydrothermal transition. Other barren examples have been observed at Hada Sumu in the

vicinity of the Bilihe gold mine in Inner Mongolia, China.

Spectacular large silica caps are present at three uranium, fluorite and tin deposits in the Proterozoic Arabian Shield. The largest, located at Jabal Uum Al Suqian comprises at least 50MT of massive milky quartz which transitions into a five-meter-thick UST zone and underlying greisenized fine grained monzonitic stocks with abundant miarolitic cavities (Bokhari et al.1986). Very large individual mega quartz crystals (Figure 4) near the top of the cupola appear to have grown in a suspended silica melt during crystallization with a period of extreme volatile and fluid over pressuring.

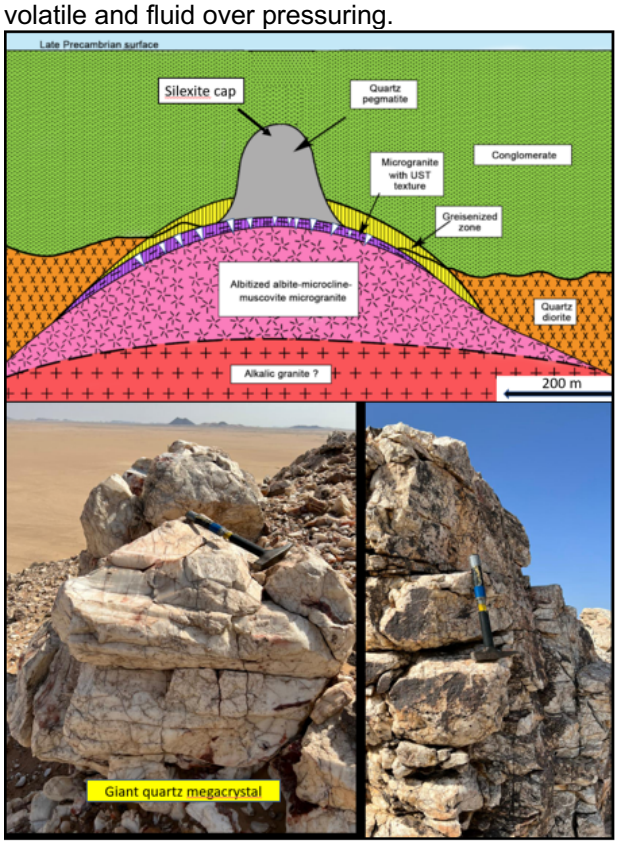

Figure 4. Geological section of the Jabal Umm Al Suqian silica cap and cupola (Bokhari et al.1986) and quartz mega crystal located near the apex of the silica cap.

A similar silica cap overlying a fluorine-rich magmatic pegmatite cupola is present at Jabal Ablah, Numerous euhedral mega quartz crystals may be observed at this locality. The Silsilah tin district in the northern part of the Arabian shield also features several prominent relatively small silica caps with underlying UST and stockscheider zones with large plumose feldspars. The Panasqueira tungsten mine in Portugal has a well-defined silica cap as described by Kelly and Rye (1979). Greisen-related tungsten-topaz deposit in the Torrington district, New South Wales, Australia feature magmatic silica caps (Lishmund 1974). A well-defined silica cap has been documented at the Knötell stock in the Krupna tungsten district in the Czech Republic (Eisenreich and Breiter 1993). The upper most part of the stock is composed of a coarse grained quartz rock (previously described as quartzite) with accessory molybdenum, fluorite and topaz. The contacts between coarse and fine grained quartz-rich rocks or greisens, are observed to be sharp. The Jabal Hamra silica cap in Saudi Arabia is a crescent-shaped stock 300 meters long by 100 meters wide, that averages over 6000 ppm combined REE (Jackson and Douch 1986).

4 Magmatic silica carapace breccias

Magmatic silica carapace breccias form at the contact of a silica cap and adjacent wall rocks where both rock types are clasts incorporated in a magmatic and or hydrothermal matrix. The breccia morphology reflects that of the host contact. A highly mineralized example occurs at the Maria copper-gold deposit in the Cananea district in Sonora, Mexico. A dome shaped quartz-sulphide breccia measuring 200 by 100 meters and 50 meters thick contains 1.6MT @ 6% Cu and 0.36% Mo (Wodzicki, 1992). Careful examination of the quartz clasts reveals micro-UST's with cloudy and translucent mottled textures. A smaller adjacent cupola has contact breccias with a tourmaline matrix. A detailed description of cupola carapace breccias is that by Klemm et al. (1997) from the Questa molybdenum mine in New Mexico. The Goat Hill breccia is located above and southward of the apex of an aplitic stock, which is considered to be the source for the mineralizing fluids. The association of high-Mo grade with the breccia bodies, and the volume and proximity of the breccias above intrusions, led to the interpretation that the mineralization was the result of direct volatile exsolution from shallow intrusions (Ross et al. 2002).

If continued over-pressuring is sufficient to allow escape of the mineralizing volatiles and fluids from the silica cap into the overlying wall rocks, then a breccia pipe would be initiated. This appears to have occurred at the Didipio gold-copper mine in the Philippines where a high-grade quartz clast breccia pipe (QBx) transitions at depth into a syenite cupola (Hermo et al. 2022). The clasts in the breccia are unmineralized and have wispy micro-UTS's, whereas the matrix contains very high copper and gold values. The silica cap formed during pre-mineral magmatic conditions was subsequently shattered during the magmatic to hydrothermal transition and became incorporated as clasts in the breccia ore body. Clasts with massive silica and UST's have been observed in the gold-bearing hydrothermal breccia at Kidston, Australia implying that a similar sequence of events took place there.

5 Conclusions

Silica caps associated with intrusion-related ore deposits are not well described in the literature. This may be due to lack of recognition and poor preservation during destructive processes related to the magmatic to hydrothermal transition. In some

examples they have been interpretated as large veins or silicified alteration zones. Magmatic silica caps occur in a variety of metallogenetic settings, and in particular, very high-grade zones in porphyry copper-gold and molybdenum deposits. There are numerous cases where unmineralized silica caps are present in mineralized districts, implying they formed prior to main-stage mineralization. Both scenarios are favourable exploration vectors for intrusion-related mineral deposits.

In many instances the massive silica displays a distinctive cloudy and translucent mottled texture with thin irregular wispy UST bands. Furthermore, massive silica caps frequently transition into underlying UST bands, most likely due to decreasing oscillating volatile and fluid over pressuring.

Acknowledgements

The authors wish to acknowledge the invaluable assistance provided Mr Nasir Jahdali, Dr Abdullah Nabhan. Mr Ghazi Kattu, Mr Mohammed Jehani and Mr Eid Marudah from the Saudi Geological Survey for arranging field trips to the silica cap localities in the Arabian Shield.

References

Bennett KC (1975) Geology and origin of the breccias in the Morenci-Metcalf district, Greenlee County, Arizona. MSc. Thesis, Univ of Arizona 181

Bokhari MM Jackson NI Oweidi K AL (1986) Geology and mineralization of the Jabal Umm Al Suqian albitized apogranite, southern Najd región, Kingdom of Saudi Arabia. J African Earth Sci 4 189-198.

Brown WH (1939) Tucson Mountains, an Arizona basin range. Bull Geol Soc Am 50 697-760.

Butler BS and Vanderwilt JW (1933) The Climax molybdenum deposit, Colorado. U.S.G.S. Bull 846-C,195-337.

Eisenreich M and Breiter K (1993). Krupka, deposit of Sn-W-Mo ores in the eastern Krušné Hory Mts. Bull Czech Geol Surv 68(3) 15-22 (in Czech).

Hermo MA Balangue-Tarriela MI Takashi R Gabor-Ratio JA
Frias S (2022) Mineralization styles and ore forming conditions of the quartz-fragment-rich breccia (QBX) at the Didipio alkalic porphyry Cu-Au deposit, Nueva Vizcaya, Philippines. Ore Geol Rev 124 21.

Jackson NJ and Douch CJ (1986) Jabal Hamra REE-mineralized silexite, Hijaz Region, Kingdom of Saudi Arabia. J African Earth Sci 4 269-274.

Kelly W and Rye R (1979) Geoologic, fluid inclusion and stable isotope studies of the tin-tungsten deposits of Panasqueira, Portugal. Econ Geol 74 1721-1822.

Khashgerel B Kavalieris I Hayashi, K (2008) Mineralogy, textures, and whole-rock geochemistry of advanced argillic alteration: Hugo Dummett porphyry Cu-Au deposit, Oyu Tolgoi mineral district, Mongolia. Miner Depos 43, 913-932.

Kirwin DJ (2005) Unidirectional solidification textures associated with intrusion-related Mongolian mineral deposits. In: Seltmann R. Gerel O and Kirwin D. (Eds.) 2005, Geodynamics and Metallogeny of Mongolia with a Special Emphasis on Copper and Gold Deposits, IAGOD Guidebook Series 11 63-84.

Klemm LM Petlke T Heinrich CA (2008) Fluid and source magma evolution of the Questa porphyry Mo deposit, New
Mexico, USA. Miner Depos 43 533-552

Lawley CM (2009) Age, geochemistry and fluid characteristics of the Max porphyry Mo deposit southeast British Columbia. MSc thesis Univ Alberta 177

Lishmund SR (1974). The Torrington silexite deposits. Geol Surv New South Wales. Quarterly Notes 17: 3–6.

Oelsner O (1952) Die pegmatitisch-pneumatolytischen lagerstätten des Erzgebirge mit Ausnahme der kontakpneumatolytschen Lagerstätten, Freiberg. Forsch Hft 41-80 (in German)

Ross P Jebrak M and Walker BM (2002) Discharge of hydrothermal fluids from a magma chamber and concomitant formation of a stratified breccia zone at the Questa porphyry molybdenum deposit, New Mexico. Econ Geol 97 1679-1698

Wodzicki WA (1992) The Maria deposit, Sonora, Mexico: A telescoped porphyry system. MSc thesis Univ California 49

Fluids involved in W-Be skarns from the Canadian Cordillera: example from the Cantung and Lened deposits, NWT, Canada

Hélène Legros[1], Vanessa Elongo[1], Oscar Laurent[2,3], Erin Adlakha[4], Hendrik Falck[5], Cyril Chelle-Michou[3], Pilar Lecumberri-Sanchez[1]
[1]Department of Earth and Atmospheric Sciences, University of Alberta, Edmonton, AB T6G 2E3, Canada
[2]CNRS, Géosciences Environnement Toulouse, Observatoire Midi-Pyrénées, 31400 Toulouse, France
[3]Institute of Geochemistry and Petrology, ETH Zurich, 8092 Zurich, Switzerland
[4]Department of Geology, Saint Mary's University, 923 Robie St., Halifax, NS B3H 3C3, Canada
[5]Northwest Territories Geological Survey, 5310 44 St., Yellowknife, NWT X1A 1K3, Canada

Abstract. The Lened and Cantung deposits are located in the Tombstone-Tungsten belt of the Canadian Cordillera, the only plutonic belt with world-class tungsten deposits in western North America. This study examines the boron and metal (including tungsten) concentrations of fluid inclusions hosted in several minerals from the Cantung and Lened W-(Be) deposits and discusses (i) the analytical challenges involved during fluid salinity calculations of B-rich fluids and (ii) the relationship between fluid chemistry and ore-forming processes of W-(Be) skarns. High Cs and Li of the fluid suggests a high degree of differentiation of a magmatic fluid source, while Sr and Ba show fluid–rock interaction with the surrounding limestone.

1 Introduction and context

Tungsten and beryllium-rich magmatic-hydrothermal systems are associated with highly differentiated peraluminous granites and are responsible for the precipitation of emerald and tungsten minerals (such as scheelite) in veins and skarns (Meinert et al. 2005).

Recent publications debate the potential mechanisms of tungsten precipitation in hydrothermal deposits, including depressurization of magmatic fluids (Korges et al. 2018), fluid-rock interaction (Lecumberri-Sanchez et al. 2017) and fluid cooling/mixing (Legros et al. 2019).

Also, high boron in these systems, indicated by extensive tourmalinization (Launay 2018) could be part of the decisive factors for enrichment.

The Cantung, and Lened W-(Be) skarn deposits are located at the border between the Northwest Territories and Yukon of Canada (Figure 1). These deposits are part of a large metallogenic belt that contains all major tungsten deposits in western North America (Elongo et al. 2020). Both deposits are associated with Middle to Late Cretaceous age quartz-monzogranites, and are interpreted to be the result of hydrothermal processes involving the local lower Palaeozoic carbonate rocks (Dick and Hodgson 1982). In both deposits, scheelite precipitated throughout the entire history of skarn evolution and subsequent hydrosilicate alteration but scheelite abundance peaked during the biotite-rich facies (Elongo et al. 2020).

This study aims at characterizing both the least-modified magmatic fluid and the chemical signature of the magmatic fluids modified by interaction with the limestone in the context of skarns, where very little data is currently published.

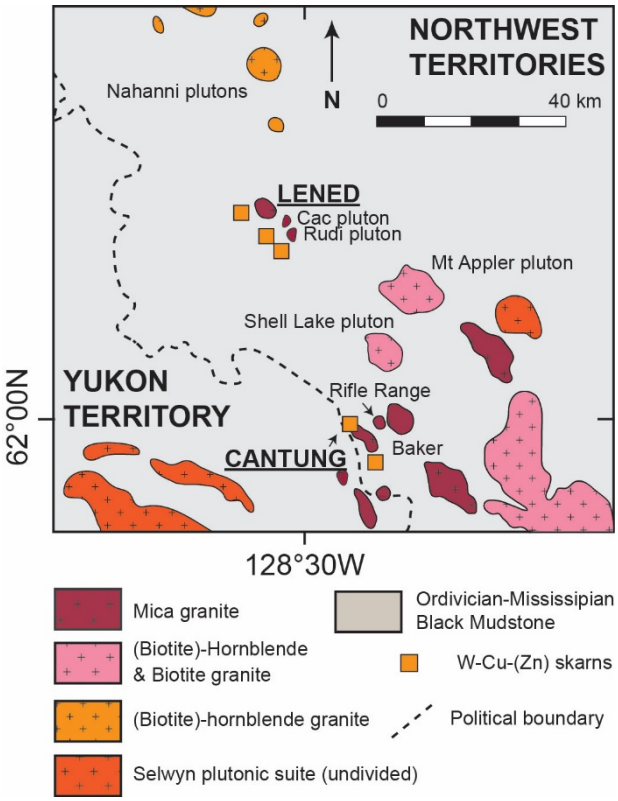

Figure 1. Local geological map showing the Lened and Cantung deposits (Legros et al. 2020, 2022)

2 Methods and results

A precise description of the mineralogical sequence was established prior to the fluid inclusion study for both Cantung and Lened deposits (Elongo et al. 2020)

The aqueous fluid inclusions have high CO_2-CH_4 and boron contents (Legros et al. 2020). At the Lened deposit, boron content is extremely high, as indicated by the presence of sassolite crystals (H_3BO_3) in fluid inclusions (Legros et al. 2022).

2.1 Boron concentration and salinity

In the case of the Lened deposit, the main components of the fluid system are H_2O–CO_2–$NaCl_{eq}$–H_3BO_3. Two methods currently exist to determine the salinity of fluids in the H_2O–$NaCl_{eq}$–H_3BO_3 system, closest system to our case study. The determination of salinity is especially crucial since it is often used as internal standard to process fluid inclusion trace element data acquired by LA-ICP-MS. The first method uses sassolite melting temperature measured by microthermometry (Peretyazhko et al. 2000) and the second method uses Raman peak intensities corresponding to the H_3BO_3 and H_2O species (Thomas 2002). The calculation of salinity ofr the Lened fluid inclusions in the H_2O-NaCl-H_3BO_3 system gives 3.5 to 5 wt. % $NaCl_{eq}$. Both methods also indicates that the fluid has 3 to 4 wt. % of H_3BO_3 (Legros et al. 2022). In our case, the calculation of salinity is not very precise and using $NaCl_{eq}$ as an internal standard would introduce a lot of uncertainty in the trace element data calculation. Moreover, a recent article suggested that, in a system where H_3BO_3 is almost the most dominant aqueous specie, using B as an internal standard would be more appropriate (Sirbescu et al. 2013). In our case, the boron content of the aqueous liquid phase is estimated to 0.5 wt. %.

2.2 Metal concentration

At Cantung, quartz veins with various mineralogical assemblages hosted in the granitic pluton and the overlying skarn host rocks were sampled. Trace element data of the fluids show relatively high concentrations of Li (40 to 474 ppm), Al (56 to 1003 ppm), As (36 to 490 ppm) and Cs (68 to 296 ppm); and lower concentrations of Rb (3.6 to 77 ppm), Sr (0.4 to 23 ppm), Sb (1 to 32 ppm), Ba (0.6 to 163 ppm), Mg (6.9 to 7.6 ppm) and other metals, such as Be (2.4 to 10.2 ppm), W (2.4 to 27 ppm) and Cu (5.1 to 73 ppm) (Legros et al. 2020, Figure 2).

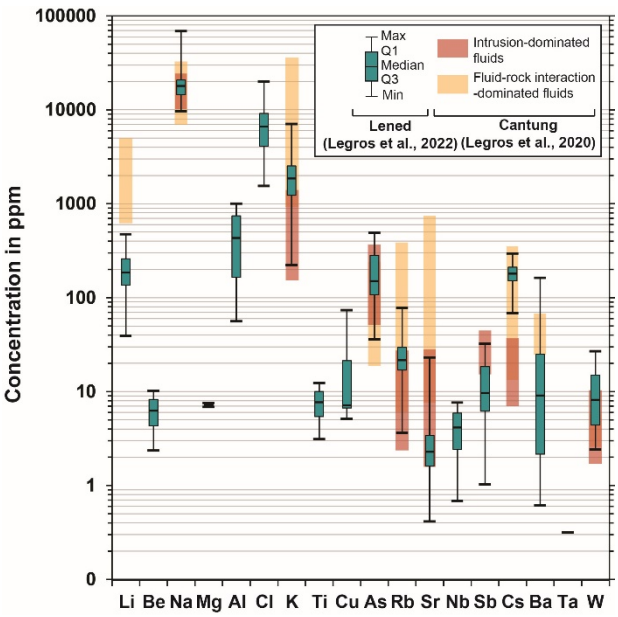

Figure 2. Trace element concentration measured in fluid inclusions from the Lened deposit, compared to the data acquired for the Cantung deposit (Legros et al. 2020, 2022)

At Lened, fluid inclusions in a single quartz vein systematically represented a boron-rich fluid. Using 0.5 wt. % B as an internal standard, the fluid inclusions had relatively high concentrations of Li (40 to 474 ppm), Al (56 to 1003 ppm), As (36 to 490 ppm) and Cs (68 to 296 ppm); and lower concentrations of Rb (3.6 to 77 ppm), Sr (0.4 to 23 ppm), Sb (1 to 32 ppm), Ba (0.6 to 163 ppm), Mg (6.9 to 7.6 ppm) and elements of economic interest, such as Be (2.4 to 10.2 ppm), W (2.4 to 27 ppm) and Cu (5.1 to 73 ppm) (Legros et al. 2022, Figure 2).

3 Discussion and conclusion

The high Cs and Li concentrations suggest a magmatic origin of the metals, while the moderate concentrations in Sr and Ba are indicative of fluid–rock interaction with the surrounding limestone during skarn formation (Figure 3).

High concentrations of B, K, Rb and Cs in the FIs, as well as the high salinity, indicate a high degree of fractionation of the magma, as often observed in these deposits (Korges et al. 2019; Pan et al. 2019).

The presence of sassolite (H_3BO_3) suggests that these fluids were highly acidic (Peretyazhko et al. 2000). The neutralization of the fluid through interaction with the surrounding limestone is the most probable trigger for scheelite precipitation.

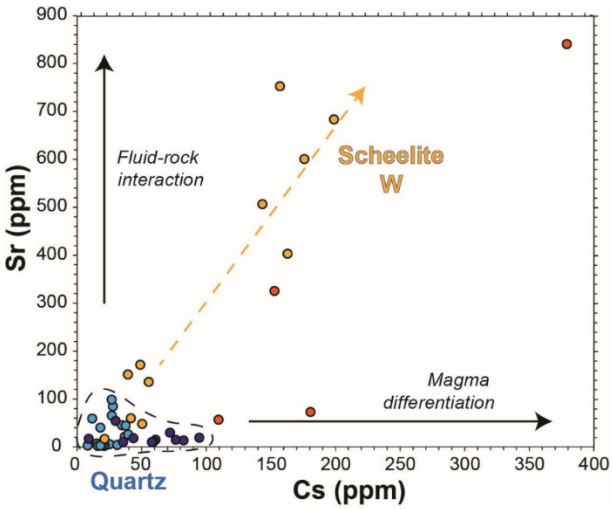

Figure 3. Binary diagram showing the influence of the two principal processes involved in Cantung fluid evolution (modified after Legros et al. 2020)

The presence of such high boron content in the magmatic fluid at Lened indicates a, potentially higher than usual, H_2O concentration in the magma (Peretyazhko 2010). More H_2O in the magma would imply a longer time to crystallize

and potentially a higher concentration in incompatible element when the fluid was exsolved.

Finally, identifying high boron concentration in the fluid as well as the potential occurrence of sassolite is essential to proper salinity calculation of the fluid (Legros et al. 2022).

Acknowledgements

This research was supported by NSERC and the Polar Continental Shelf Project. We would like to thank the executive team at the Cantung mine and the NWT Geological Survey for providing access and helping in the mine and the field. We are also grateful to Marie-Camille Caumon (GeoRessources lab, Nancy, France) for her help with the Raman method, Matthew Steele-McInnis for his help with the microthermometry equipment (University of Alberta, Canada).

References

Dick LA, Hodgson CJ (1982) The MacTung W-Cu(Zn) contact metasomatic and related deposits of the northeastern Canadian Cordillera. Econ Geol 77:845–867. https://doi.org/10.2113/gsecongeo.77.4.845

Elongo V, Lecumberri-Sanchez P, Legros H, et al (2020) Paragenetic constraints on the Cantung, Mactung and Lened tungsten skarn deposits, Canada: implications for grade distribution. Ore Geol Rev 125:

Korges M, Weis P, Lüders V, Laurent O (2018) Depressurization and boiling of a single magmatic fluid as a mechanism for tin-tungsten deposit formation. Geology 46:75–78. https://doi.org/https://doi.org/10.1130/G39601.1

Korges M, Weis P, Lüders V, Laurent O (2019) Sequential evolution of Sn–Zn–In mineralization at the skarn-hosted Hämmerlein deposit, Erzgebirge, Germany, from fluid inclusions in ore and gangue minerals. Miner Depos 1–16

Launay G (2018) Hydrodynamique des systèmes minéralisés péri-granitiques: étude du gisement à W-Sn-(Cu) de Panasqueira (Portugal)

Lecumberri-Sanchez P, Vieira R, Heinrich CA, et al (2017) Fluid-rock interaction is decisive for the formation of tungsten deposits. Geology 45:579–582. https://doi.org/https://doi.org/10.1130/G38974.1

Legros H, Elongo V, Laurent O, et al (2022) Formation of the Lened W-(Be) Skarn Deposit by Neutralization of a Magmatic Fluid—Evidence from H3BO3-Rich Fluids. Geosciences 12:236

Legros H, Lecumberri-Sanchez P, Elongo V, et al (2020) Fluid evolution of the Cantung tungsten skarn, Northwest Territories, Canada: differentiation and fluid-rock interaction. Ore Geol Rev 127C:103866. https://doi.org/10.1016/j.oregeorev.2020.103866

Legros H, Richard A, Tarantola A, et al (2019) Multiple fluids involved in granite-related W-Sn deposits from the world-class Jiangxi province (China). Chem Geol 508:92–115. https://doi.org/10.1016/j.chemgeo.2018.11.021

Meinert LD, Dipple GM, Nicolescu S (2005) World Skarn Deposits. One Hundredth Anniv. Vol. 0

Pan J-Y, Ni P, Wang R-C (2019) Comparison of fluid processes in coexisting wolframite and quartz from a giant vein-type tungsten deposit, South China: Insights from detailed petrography and LA-ICP-MS analysis of fluid inclusions. Am Mineral J Earth Planet Mater 104:1092–1116. https://doi.org/10.2138/am-2019-6958

Peretyazhko IS (2010) Genesis of mineralized cavities (miaroles) in granitic pegmatites and granites. Petrology 18:183–208

Peretyazhko IS, Prokof ev VY, Zagorskii VE, Smirnov SZ (2000) Role of Boric Acids in the Formation of Pegmatite and Hydrothermal Minerals: Petrologic Consequences of Sassolite (H~ 3BO~ 3) Discovery in Fluid Inclusions. Petrol C/C Petrol 8:214–237

Sirbescu M-LC, Krukowski EG, Schmidt C, et al (2013) Analysis of boron in fluid inclusions by microthermometry, laser ablation ICP-MS, and Raman spectroscopy: Application to the Cryo-Genie Pegmatite, San Diego County, California, USA. Chem Geol 342:138–150

Thomas R (2002) Determination of the H3BO3 concentration in fluid and melt inclusions in granite pegmatites by laser Raman microprobe spectroscopy. Am Mineral 87:56–68

Metallogeny of tin: From rocks to ore

Bernd Lehmann
Mineral Resources, Technische Universität Clausthal, 38678 Clausthal-Zellerfeld, Germany

Primary tin ore deposits are part of magmatic-hydrothermal systems invariably related to late leucocratic granite phases (tin granites/porphyries, pegmatites) of much larger - and often unexposed - felsic intrusions. Cassiterite (SnO_2) is the only tin mineral of economic significance. Due to its density (7.4 g/cm^3), hardness and chemical stability cassiterite may become dispersed by exogenic processes and then eventually form placer deposits within a few km from their primary source. Alluvial placer deposits were usually the starting point for tin mining, and have provided at least half of all tin mined historically.

The small-volume and late granitic phases in spatial, temporal and chemical relationship to tin ore deposits are highly evolved, i.e. near the low-pressure thermal minimum of the quartz-alkalifeldspar system with very few mafic components and very low Ti, Ca and Mg contents, but enrichment of incompatible trace elements, such as Sn, W, Ta, U, Li, Cs, Rb, Be, F, B. Systematic element distribution patterns in these granitic phases and their associated much larger multiphase granite systems suggest fractional crystallization as the main petrogenetic process controlling magmatic evolution and magmatic tin enrichment. This process can operate in granite melts of any origin, i.e. tin enrichment can be observed in I-, S- or A-type granites and their various tectonomagmatic environments. Oxidation state controls the bulk tin distribution coefficient, with low oxidation state favoring incompatible behavior of divalent tin in felsic systems, also mineralogically expressed by accessory ilmenite ($FeO{\cdot}TiO_2$) as opposed to accessory magnetite ($FeO{\cdot}Fe_2O_3$) in more oxidized melt systems where Sn^{4+} is dominant. This difference in the accessory mineralogy, and hence metallogenic potential (ilmenite- versus magnetite-series granites), can be easily detected in the field by a hand-held magnetic susceptibility meter.

The hydrothermal system is a continuation of the magmatic evolution trend and necessary consequence of the crystallization of a hydrous melt. The exsolved saline aqueous fluid phase, enriched in boron and/or fluorine plus a wide metal spectrum, can be accomodated and stored by the intergranular space in some crystallized melt portions, or accumulate in larger physical domains, accompanied by focused release of mechanical energy (brecciation, vein formation). The hydrothermal mobility of tin is largely as Sn^{2+}-chloride complexes; the precipitation of tin as cassiterite involves oxidation.

Tin typically characterizes the inner part of km-sized zoned hydrothermal systems with the chemical signature Sn-W-Cu-As-Bi in the inner part (greisen, vein/stockwork/breccia systems, skarn) and a broader halo with vein- or replacement-style Pb-Zn-Ag-Sb-Au-U mineralization. This zoning pattern may also occur telescoped on each other.

A particular feature of many tin systems is greisen alteration, i.e. texturally destructive coarse-grained quartz-muscovite alteration combined with fluorine, boron and lithium metasomatism. Such greisen alteration may affect the igneous rocks (endogreisen) or their country rocks (exogreisen) and is mineralogically expressed by topaz/fluorite, tourmaline and Li-rich mica, and the absence of feldspar. Cassiterite forms stout prismatic crystals at elevated temperature (400 $\pm$ 100°C), and acicular crystals (needle tin) at lower temperature. Tungsten is a common component of hydrothermal tin systems but often occurs spatially separated due to the different solubility control of wolframite ($[Fe,Mn]O{\cdot}WO_3$) compared to cassiterite, with the formation of scheelite ($CaO{\cdot}WO_3$) in Ca-rich country rocks.

Tin Deposition from Cooling Magmatic Fluids Revealed by Ion Probe Cassiterite Oxygen Isotope Analysis

Yang Li[1], Olivier Bachmann[2], Xian-Hua Li[3]
[1]School of Earth and Planetary Sciences, Peking University, Beijing, China
[2]Department of Earth Sciences, ETH Zürich, Zurich, Switzerland
[3]Institute of Geology and Geophysics, Chinese Academy of Sciences, Beijing, China

Abstract. The formation of tin deposits requires a mechanism to significantly reduce tin-solubility in fluids to deposit cassiterite, but the exact trigger of tin deposition is highly debated, and proposed mechanisms include mixing between magmatic fluids and surface water, cooling of magmatic fluids, and water-rock interaction. Here we push our understanding forward via the newly developed ion probe cassiterite oxygen isotope proxy (Li et al., 2022, 2022b and 2023). Using first-principle-calculation, we first show that the interpretation of cassiterite $\delta^{18}O$ is temperature insensitive, and an uncertainty of 100°C in temperature estimates only leads to a bias of 0.2 ‰ in calculated fluid-$\delta^{18}O$. We then developed a matrix-matched reference material-Yongde-CST and reached a analytical precision of <0.3 ‰ using large geometry ion probe. Ore-forming fluids from 9 tin-bearing deposits show a predominately magmatic affinity, with limited to no evidence of fluid mixing and/or water-rock interaction. Critically, cassiterite-quartz $\delta^{18}O$ thermometry indicates that cooling from pure magmatic fluid is an efficient driver for tin deposition.

1 The conceptual model of magmatic-hydrothermal ore systems

Magmatic-hydrothermal deposits are the primary source of Cu, Mo, Sn, W and other metals. Their formation is ultimately controlled by felsic magmatic reservoirs at depth. Upon extensive cooling and crystallization, metalliferous fluids will exsolve in magmatic reservoirs and then rise to shallow levels. The fluids then will experience cooling, phase separation, mixing with surface water, and variable degrees of water-rock interaction.

Oxygen is the major component of fluids and rocks; hence its isotope composition ($\delta^{18}O$) is one of the best studied proxies to decipher sources of fluids, and to trace fluid evolution, for which robust and precise analytical approaches are fundamental, and data interpretation without ambiguity is critical.

2 Cassiterite oxygen isotope analysis

A promising avenue to circumvent the aforementioned challenges is targeting cassiterite, the primary ore mineral of tin.

Using first-principle-calculation (Li et al. 2022a), we show that the interpretation of cassiterite-$\delta^{18}O$ is extremely insensitive to the accuracy of temperature estimates (Fig. 1), which is very different to other minerals such as quartz (Fig. 1). An uncertainty of 100-200 °C in temperature estimates only leads to a bias of 0.2-0.5 ‰ in calculated fluid-$\delta^{18}O$ (Fig. 1). This unique feature of cassiterite lifts the requirement of robust temperature-estimates, and we can always obtain fluid-$\delta^{18}O$ with high confidence even when the temperature is loosely constrained.

Before our study, cassiterite oxygen isotope analysis is only possible via gas source isotope ratio mass spectrometry. As a bulk analytical approach, it is time consuming and does not permit assess $\delta^{18}O$ zone by zone.

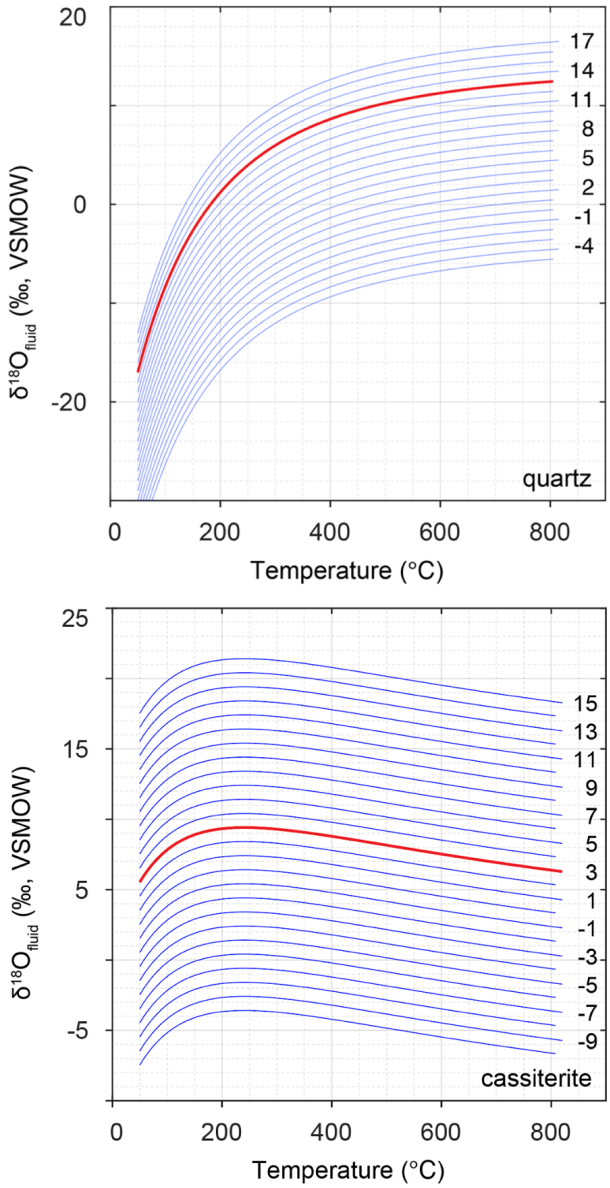

Figure 1. Oxygen isotope fractionation between mineral (top: quartz; bottom: cassiterite) and water as a function of temperature (Li et al. 2022a).

Our experiments show that cassiterite has no detectable crystallographic orientation effect and position effect at current analytical precision (i.e., 0.2-0.3 ‰). We then characterized Yongde-CST, the first matrix matched reference material for SIMS cassiterite oxygen isotope analysis with a recommended $\delta^{18}O$ of 1.36±0.16 ‰ (Li et al. 2022a), which is freely available and has been distributed to tens of laboratories worldwide already.

3 Coupling cassiterite and quartz oxygen isotopes provides tight constraints on both temperature and $\delta^{18}O$ of ore-forming fluids

When converting mineral-$\delta^{18}O$ to fluid-$\delta^{18}O$, quartz and cassiterite show dramatic differences in response to temperature (Fig. 1). This makes them an idea mineral pair for oxygen isotope thermometry (Li et al. 2022a).

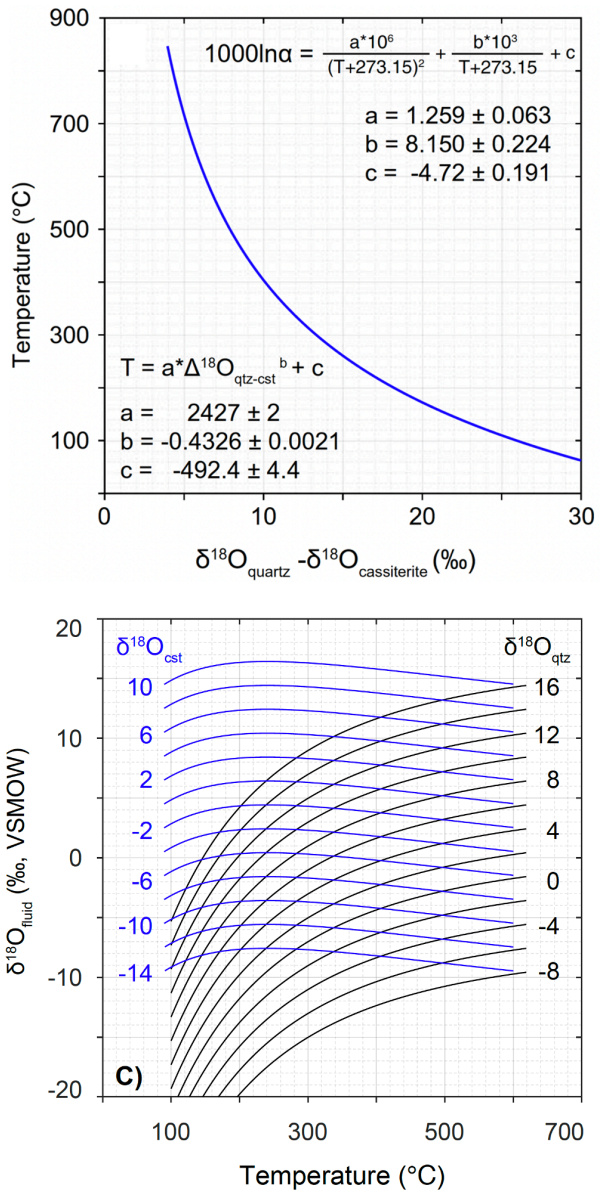

Figure 2. The $\delta^{18}O_{quartz\text{-}cassiterite}$ shows a strong dependence on temperature, hence using their oxygen isotope composition in tandem (bottom) could provide tight constrains on temperature and $\delta^{18}O$ of ore-forming fluids (Li et al. 2022a).

Current SIMS analysis has a precision of 0.2-0.3 ‰, this corresponds to an uncertainty of 10 °C for temperature obtained from quartz-cassiterite oxygen isotope thermometry. This approach also gives fluid-$\delta^{18}O$ at the same time (Fig. 2).

As a preliminary test to the newly developed SIMS cassiterite oxygen isotope analytical method, we have analyzed cassiterite grains from six deposits with different ages and geological backgrounds (Li et al. 2022a).

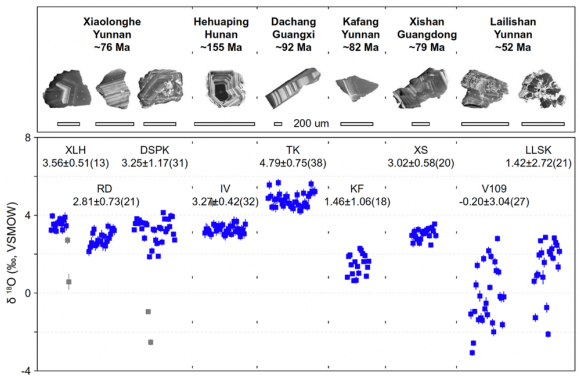

Figure 3. CL images and $\delta^{18}O$ of cassiterite grains from six deposit (Li et al. 2022a).

Fresh grains have a more clustered distribution in $\delta^{18}O$ between 2 ‰ and 4 ‰ and peak at 3.3 ‰, corresponding to fluid-$\delta^{18}O$ of 9.3 ‰ (Fig. 3). Grains with alteration show considerable variations in $\delta^{18}O$ between -3.1 ‰ and 2.9 ‰ (Fig. 3), both within and among grains (Li et al. 2022a).

The results highlight a magmatic affinity for ore-forming fluids in general, while the inter- and intra-deposit variations is likely jointly controlled by $\delta^{18}O$ of primary magma, and the degree of fluid mixing and/or water-rock interaction (Li et al. 2022a). This makes cassiterite $\delta^{18}O$ a promising proxy to investigate these processes.

4 Pulsed tin mineralization inferred from SIMS $\delta^{18}O$ mapping of a single cassiterite crystal

We further test whether cassiterite chemistry can be used to reveal the dynamics of ore formation. A zoned cassiterite grain from the Piaotang Sn-W deposit, Nanling, China, has been selected for SIMS $\delta^{18}O$ mapping and XRF elemental mapping (Li et al. 2022b).

Core and rim of the crystal have $\delta^{18}O$ of -2.1 ‰ and +2.4 ‰, respectively (Fig. 4). The $\delta^{18}O$ mapping mimics that of Fe-Nb-Ta contents, with high values occurring in the rim (Fig. 4). Low $\delta^{18}O$ of the first stage requires significant contribution of meteoric water (33 %), but the second (main) stage is dominated by magmatic fluids (>>90 %).

In line with the early stage tin-bearing veins being cut by the second, and main stage

mineralization, our results are best explained by a two-stage growth history. This case study demonstrates that cassiterite chemistry is a powerful tool to decode the dynamics of fluid evolution during tin mineralization (Li et al. 2022b).

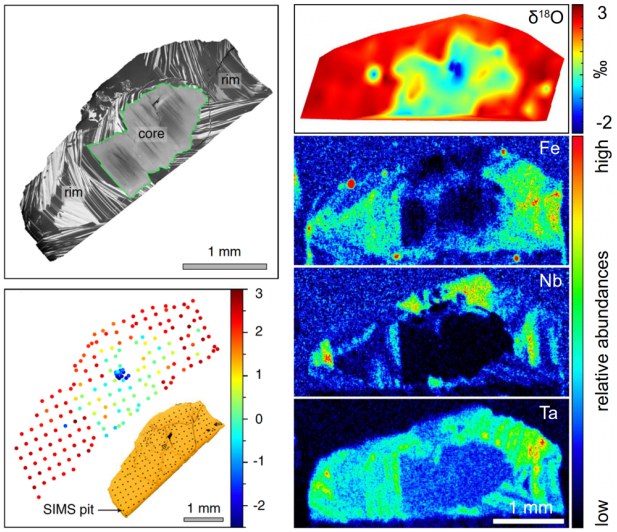

Figure 4. CL, $\delta^{18}O$ mapping and XRF elemental mapping of a single cassiterite grain from Piaotang (Li et al. 2022b).

5 Cooling, not mixing induced transient tin mineralization (~5,000 years) within a long-lived hydrothermal system (>250,000 years)

Quartz vein-type tin deposit is characterized by simply mineral assemblages and growth history, which is ideal to reconstruct fluid evolution. The euhedral nature and big grain sizes of quartz and cassiterite permit the realisation of high temporal resolution (core to rim analysis using SIMS).

Here we demonstrate the above scenario using paragenetically constrained cassiterite-quartz veins from the Weilasituo Sn deposit, inner Mongolia, China, as an example (Li et al. 2023).

5.1 Gradual Cooling during tin deposition without fluid mixing or water-rock interaction

At Weilasituo, textural evidence suggests that cassiterite precipitation started at the end of stage 1 quartz core (Q1-core) and ceased at the beginning of Q1-rim; hence Q1-core, Q1-mantle and Q1-rim are pre-, syn- and post-ore, respectively (Fig. 5). Q2 and Q3 are post-ore as well (Li et al. 2023).

Q1-core has a $\delta^{18}O$ of 11.4±0.4 ‰. Q1-mantle shows a rimward increase in $\delta^{18}O$ from 11.4 ‰ to 13.5 ‰, and co-precipitated cassiterite has a $\delta^{18}O$ of 3.6±0.4 ‰. Q1-rim has a $\delta^{18}O$ of 13.7±0.4 ‰ (Fig. 6). $\delta^{18}O$ of Q2 fluctuate between 12.7 ‰ and 15.3 ‰. $\delta^{18}O$ values of Q3 gradually decrease from 11.8 ‰ to 9.5 ‰ (Fig. 7).

The rimward increase of $\delta^{18}O$ for Q1-mantle and consistent $\delta^{18}O$ values for co-precipitated cassiterite suggest that Q1-mantle and cassiterite both were precipitated from fluids with a $\delta^{18}O$ of 8.6±0.4 ‰, with temperatures progressively decreasing from ~500 °C to ~390 °C ($\triangle$T=110 °C, Fig. 6). Hence tin mineralisation is triggered by cooling of pure magmatic fluids; mixing with external fluids and/or water-rock interaction are not evidenced (Li et al. 2023).

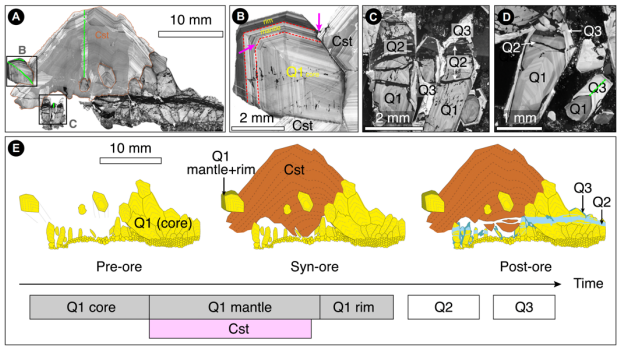

Figure 5. Paragenesis of quartz and cassiterite at Weilasituo, inner Mongolia, China (Li et al. 2023).

The rimward increase of $\delta^{18}O$ for Q1-mantle and consistent $\delta^{18}O$ values for co-precipitated cassiterite suggest that Q1-mantle and cassiterite both were precipitated from fluids with a $\delta^{18}O$ of 8.6±0.4 ‰, with temperatures progressively decreasing from ~500 °C to ~390 °C ($\triangle$T=110 °C, Fig. 6). Hence tin mineralisation is triggered by cooling of pure magmatic fluids; mixing with external fluids and/or water-rock interaction are not evidenced (Li et al. 2023).

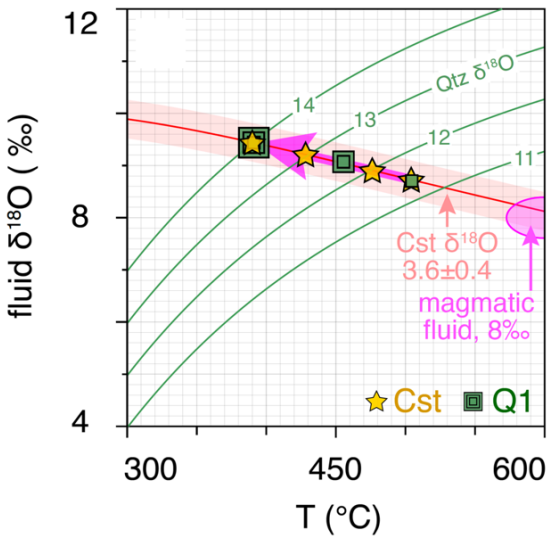

Figure 6. Quartz and cassiterite oxygen isotope thermometry tightly constrains the gradual cooling path during tin deposition at Weilasituo (Li et al. 2023).

After mineralization, as evidenced by the brittle fractures in Q1, Q2 marks the transition from lithostatic to hydrostatic conditions. Minor involvement of meteoric water occurred at this stage (Fig. 7). A further incursion of meteoric water was recorded by Q3 (Li et al. 2023).

5.2 Rapid (~5,000 years) tin mineralization within a long-lived (>250,000 years) system

Co-precipitation between quartz and cassiterite permits the application of quartz-cassiterite oxygen isotope thermometry, and a cooling history with high temporal resolution can be obtained when the euhedral quartz and cassiterite grains are analyzed by ion probe from core to rim. The timescales of this cooling history can be quantified using Al diffusion in quartz chronometry, which yields growth timescales (Fig. 7) of ~50 kyr, 2-10 kyr and 140-240 kyr for the core (pre-ore), mantle (syn-ore) and rim (post-ore) of Q1, respectively (Li et al. 2023).

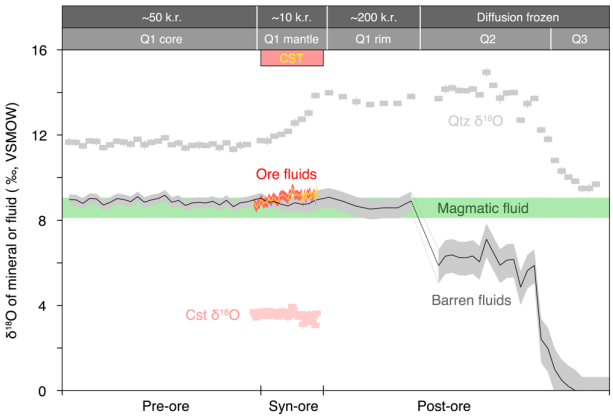

Figure 7. Oxygen isotope evolution of the Weilasituo hydrothermal system indicates pure magmatic fluids during tin mineralization, also shown is the timescales from quartz aluminum diffusion chronometry (Li et al. 2023).

The bulk tin at Weilasituo was deposited within ~5,000 years, within a much longer time window (>250,000) when only gangue minerals were formed. Hence only <5% of the hydrothermal system's lifetime was effective for mineralization (Li et al. 2023). This highlights that effective time needs to be considered in the future when studying ore-forming rates and efficiency.

The above advances highlight the importance of translating texture-controlled information into temporal patterns, which is readily applicable to other magmatic-hydrothermal systems.

Conclusion

Here we present a new proxy (cassiterite-quartz $\delta^{18}O$) which can decipher the temperature and $\delta^{18}O$ of ore-forming fluids with high confidence and high temporal resolution. The power and beauty of this new proxy has been demonstrated via a series of case studies, and indicates that tin-bearing fluid exsolution likely is pulsed, with cassiterite precipitation being driven by cooling, while fluid mixing and water-rock interaction are not evidenced in most cases.

Acknowledgements

We thank our colleagues for providing samples and supporting this research in various ways. Results presented here were summarized from our recent publications as listed at the end of this abstract, please check full papers for details. The Yongde-CST reference material is available to the community upon reasonable request. We are also open for collaborative research. We thank Prof. Mathias Burisch for detailed and informative review. We acknowledge support from National Natural Science Foundation of China (grant No. 42022022) and National Key Research and Development Program of China (2018YFA0702600).

References

Li Y, He S, Zhang R-Q, Bi X-W, Feng L-J, Tang G-Q, Wang W-Z, Huang F, Li X-H (2022a) Cassiterite oxygen isotopes in magmatic-hydrothermal systems: in situ microanalysis, fractionation factor, and applications. Mineralium Deposita 57:643-661. doi: 10.1007/s00126-021-01068-x.

Li Y, Zhang RQ, He S, Chiaradia M, Li XH (2022b) Pulsed exsolution of magmatic ore-forming fluids in tin-tungsten systems: a SIMS cassiterite oxygen isotope record. Mineralium Deposita 57:343-352. doi: 10.1007/s00126-022-01093-4.

Li Y, Pan J-Y, Wu L-G, He S, Bachmann O, Li X-H (2023) Transient tin mineralization from cooling of magmatic fluids in a long-lived system. Geology 51:305-309. doi: 10.1130/g50781.1.

In situ LA-ICP-MS U-Pb age of cassiterite from the Auxiliadora Sn-W vein type deposit, northwestern Spain

Iván Losada[1], Iñigo Borrajo[2], Joaquín E. Ruiz-Mora[3], Luis M. Rodriguez-Terente[4], John M. Hanchar[5], Fernando Tornos[2]
[1] University of Salamanca
[2] Instituto de Geociencias (IGEO, CSIC-UCM)
[3] Consultant. A Coruña
[4] Museum of Geology, University of Oviedo
[5] Department of Earth Sciences, Memorial University of Newfoundland

Abstract. The Auxiliadora deposit is a small mine located in the town of Noia, Galicia (northwestern Spain). Here, mineralization occurs in several quartz veins which crop out along the coast. This work is focused in the cassiterite mineralization which occurs intergrown with a micaceous selvage along the veins. The obtained U-Pb ages in cassiterite of 285.2 ± 2.4 Ma, corresponds to the last stage of the Hercynian orogenesis and is coeval with that obtained in other deposits in the area.

1 Introduction

Some of the most important Sn and W metallogenic districts in the world are found in the European Variscan belt. One of these districts is the Iberian massif (Spain and Portugal). Here, numerous Sn-W deposits occur in the northwesternmost region of Galicia, associated with the youngest Variscan magmatism at ca. 300 – 285 Ma (Borrajo et al. 2022; Losada et al. 2022). Several high grade mineralization like San Finx (Losada et al 2022), Santa Comba (Cuenin 1982), Fontao (Nesen 1979) and Penouta (Llorens et al. 2017) stand out, however there are dozens of small deposits that were mostly mined during the Second World War.

The Auxiliadora Sn-W vein type deposit is one of these small deposits, and it is part of a group of Sn-W mineralization located in the municipalities of Noia and Lousame (Ruiz Mora 1982). Among them, the San Finx, located 7 km to the southwest is the most important (figure 1).

In this study we present LA-ICP-MS U-Pb ages on cassiterite from the Auxiliadora deposit. This mineral is chemically and physically resistant, and its U-Pb isotopic composition is increasingly being used as a reliable geochronometer of the Sn mineralization event (e.g., Yuan et al. 2011; Carr et al. 2020).

2 History

The mining history in the area of Noia can be start in various concessions requested in the area of Santa Cristina de Barro (Noia), around the second half of the 19th century, with some prospecting work or mining in any case only testimonial.

At the end of 1937, the "Auxiliadora" concession was requested, covering practically the entire peninsula immediately to Noia with 30 hectares.

During the 1940s, due to the extremely high prices of tungsten and the good tin market, work was carried out clandestinely throughout the area, without mechanization or hardly technical supervision. In 1945, a hundred of workers produced between 40 and 50 kg per day of cassiterite concentrates. The ore was sent for magnetic separation to the facilities of a mine that dredged the sediments of the ria and that was located a few hundred meters to the north. The mining of the numerous veins outcropping on the coast was completely superficial, being more important than the underground mine, equipped with two shafts of 20 meters each. Another part of the mined deposit was the alluvium or coastal maritime sediments, which supported the bulk of the activity due to its ease of exploitation, and from which cassiterite, wolframite, scheelite and rutile concentrates were obtained. The mine worked during the Second World War and another 5 years in the following decade. The production obtained is difficult to assess, but perhaps it was around 60 t of cassiterite in total and about 20 t of wolframite during the years 1943-1944. Around 1956 the mine was closed.

3 Geological setting

Auxiliadora is located on the Barro peninsula (Figure 1), in the town of Noia. The best outcrops are found at Abruñeiras-Punta da Cruz beach.

The host rock is mainly the Borneiro orthogneiss, from the Malpica Tui high-pressure, low-temperature unit (Llana Fúnez 2020). It is a coarse-grained, heterogeneously deformed rock with a granodioritic composition. In an area of ca 15 km surrounding the mine, syn-late to post-variscan granites crop out.

The deposit is composed of dozens of quartz veins with irregular thickness between 1 mm and 5 cm. The veins trend 090-120/80 NE. They develop a muscovite-rich selvage with cassiterite at the contact with the host rock (Figure 2). The quartz infilling is absent in the narrow zones of the veins where they are composed mainly of muscovite. Other minerals present are wolframite, scheelite, chalcopyrite and pyrite.

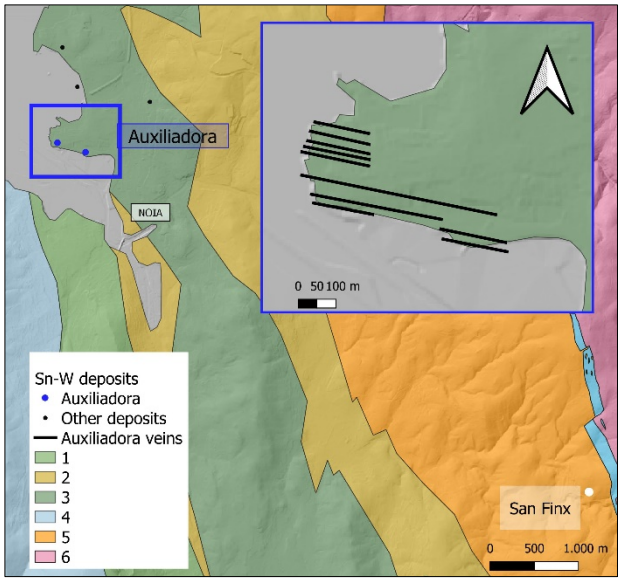

Figure 1 Simplify Geological map of the area near the town of Noia. (1) Malpica Tui unit – Peralcaline ortogneiss (2) Malpica Tui unit – Beo paragneiss (3) Malpica Tui unit – Borneiro ortogneiss (4) early granodiorite (5) schist domain (6) Monte Freito granite. Modified from Llana Fúnez (2000) and Ruiz Mora (1982).

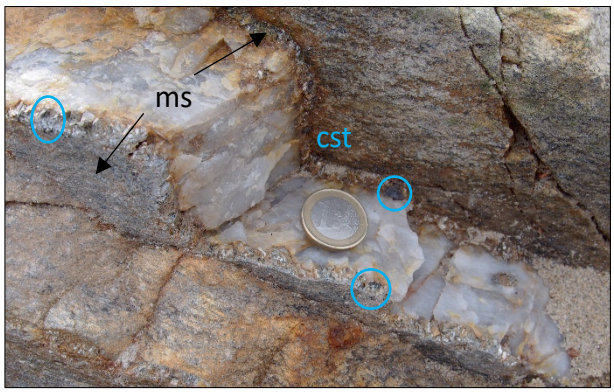

Figure 2. Quartz vein with muscovite (ms) and cassiterite (cst, darkest mineral) on the selvages. Abruñeiras beach.

4 Cassiterite geochemistry

The observed crystals (Figure 3) are formed by combinations of the prism {100} and the tetragonal dipyramids {111} and to a lesser extent {101}, agreeing with frequent habits in this type of deposits, already described by Murciego et al. (1986).

Cassiterite crystals are black and completely opaque, which may be due to impurities of metallic elements (Fe, Ti, Mn, Nb and Ta). Of the mentioned elements, electron microprobe analyses show significant titanium contents as an outstanding impurity, greater than 1% wt. of TiO_2, in most of the analyses.

Figure 3 Cassiterite crystal on quartz from the Abruñeiras beach.

One epoxy mount of cassiterite crystals were examined by cathodoluminescence to reveal internal structures and zoning before EPMA and LA-ICPMS analysis at Memorial University of Newfoundland.

Point analyses and quantitative X-ray maps were acquired on a JEOL JXA 8230 electron EPMA with a W filament and five wavelength dispersive spectrometers (WDS). Operation conditions for the point analysis were a electron beam current of 20 nA, a spot diameter of 3 µm, and an accelerating voltage of 15 kV. The count time was 30 seconds, with off-peak (background) count times of 15 seconds. For X-ray map, an accelerating voltage of 15 kV, sample current of 250 nA, and a pixel dwell time of 150 ms were used.

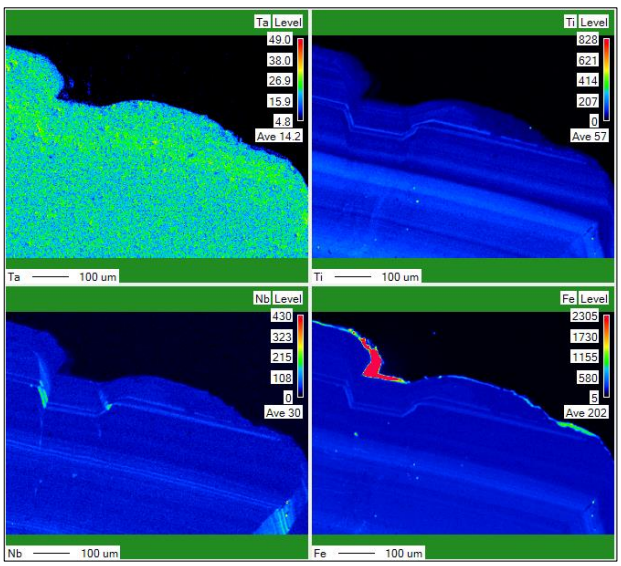

Figure 4. X-ray maps of cassiterite showing Ta, Ti, Nb and Fe distribution.

In Figure 4, the trace elements in a cassiterite crystal are shown. A homogeneous distribution of Ta is observed throughout the section of the crystal, while the distribution of traces of Ti, Nb and Fe are located in certain growth intervals of the cassiterite, being evident by the zoning that can be observed in the images of the mentioned elements.

In view of the represented values, only the Ti impurities are significant, mainly during the initial stages of formation. The elements Nb, Fe and Ti replace Sn in the cassiterite structure. The studied sample displays homogeneous and very low Ta values.

5 Geochronology

5.1 Methods

Large (> 5 mm) grains of cassiterite were easily separated by handpicking and mounted in an epoxy disc. Samples were carefully checked under a binocular microscope and areas free of cracks or inclusions were selected for U-Pb dating by using optical microscopy and BSE images.

LA-ICP-MS U-Pb analysis of cassiterite was performed at the Micro Analysis Facility (MAF) of the Memorial University of Newfoundland, St, John's, Canada by using a Thermo Finnigan Element XR high-resolution. The U-Pb analysis were collected during a single session in November 2022. The spot size diameter was of 110 µm. The conditions were set at an energy density of 4 J/cm^2 and a pulse frequency of 10 Hz. Yankee cassiterite was used as the primary standard (Carr et al. 2020).

5.2 Results

Seventeen analyses in different grains from Auxiliadora cassiterite sample yielded a lower intercept age in the Tera-Wasserburg diagram of 285.2 ± 2.4 Ma (2σ, MSWD = 0.25). The initial $^{207}Pb/^{206}Pb$ ratios were anchored following the two stages Pb model from Stacey and Kramers (1975). The same analysis gave a ^{207}Pb corrected weighted average $^{206}Pb/^{238}U$ age of 285.9 ± 1.2 Ma (MSWD = 0.87). This age is in good agreement with the obtained U-Pb Tera-Wasserburg intercept. Approximated U and Th concentrations range between 662 ppm and 18 ppm for U and 0.47 ppm and 0.03 ppm for Th in the studied sample. Crystal zoning has no effect on the U, Th and Pb concentrations and the U-Pb dating.

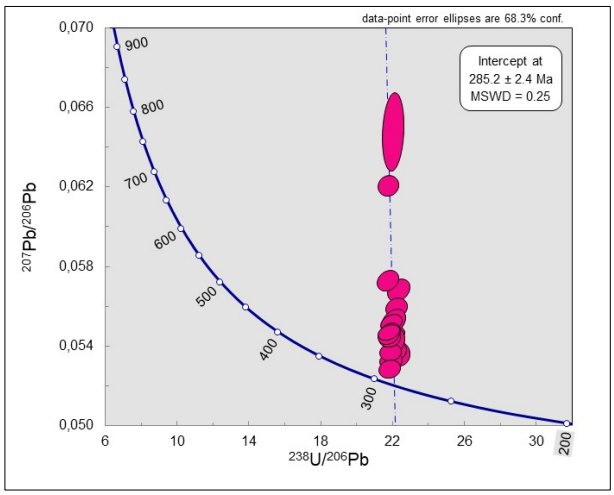

Figure 5. Tera-Wasserburg diagram of Auxiliadora cassiterite.

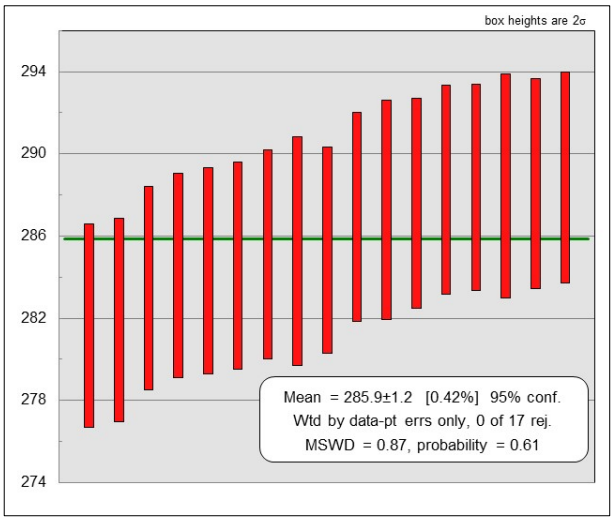

Figure 6. ^{207}Pb corrected weighted average $^{206}Pb/^{238}U$ age of Auxiliadora cassiterite.

5 Conclusions

The age obtained on the cassiterite from the Auxiliadora deposit is 285.2 + 2.4 Ma and is coeval with that obtained on the mica (287.75 ± 1.03 Ma) and apatite (281.7 ± 6.3 Ma) from the San Finx mine, 7 km to the southeast (Losada et al. 2022). This supports a single W-Sn hydrothermal event probably related with the emplacement of post-Variscan granites in the region.

Acknowledgements

This research has been conducted within the iTarg3T (Innovative targeting & processing of W-Sn-Ta-Li ores: towards EU´s self-supply) project and has received funding by the EIT Raw Materials of the European Union´s Horizon 2020 research and innovation programme under Grant Agreement Nº 18036.

Thanks to Xoel, Diego and Marcos Chouza, and Cristina M. for their invaluable help in the search and sampling of the veins.

Thanks to Matthieu Harlaux for his constructive comments which improve the manuscript.

References

Borrajo I, Tornos F, Stein, HJ (2022) Re-Os evidence for diachronous W-Sn mineralization in Iberia (Spain and Portugal). In: Advances in Magmatic Mineral Systems, Magmatic and Hydrothermal Deposits Related to Felsic Rocks. 16th SGA Biennial Meeting 1:37-40.

Carr PA, Zink S, Bennett VC, Norman MD, Amelin Y, Blevin PL (2020) A new method for U-Pb geochronology of cassiterite by ID-TIMS applied to the Mole Granite polymetallic system, eastern Australia. Chem Geol 539:119539.

Cuenin O (1982) Interpretation des lèvres geologiques dans la mine de Santa-Comba Galice Espagne. Dissertation, University of Nancy.

Llana-Fúnez, S. (2000) La estructura de la unidad Malpica Tui (Cordillera Varisca en Iberia). Dissertation, University of Oviedo.

Llorens-González T, García-Polonio F, Lopez-Moro F, Fernández-Fernández A, Sanz-Contreras J, Moro-Benito M (2017) Tin-tantalum-niobium mineralization in the Penouta deposit (NW Spain): Textural features and mineral chemistry to unravel the genesis and evolution of cassiterite and columbite group minerals in a peraluminous system Tin-tantalum-niobium mineralization. Ore Geol Rev 81:79-95.

Losada I, Borrajo I, Tornos F, Hanchar J (2022) Geochronology of San Finx Sn-W vein type deposit, northwestern Spain. In: Advances in Magmatic Mineral Systems, Magmatic and Hydrothermal Deposits Related to Felsic Rocks. 16th SGA Biennial Meeting 1:208–211.

Murciego A; Martín Pozas JM, García Sánchez A (1986) Parámetros cristalinos de casiteritas de yacimientos españoles. Boletín de la Sociedad Española de Mineralogía 9:217-224.

Nesen G (1979) Une mineralization étain-tungstène liée à un complexe granitique annulaire à endogranite et stockscheider en Galice (mine de Fontao, Espagne). Comptes Rendus 288:787-790.

Ruiz Mora JE (1982) Mineralizaciones estannovolframiferas en Noia y Lousame. Estudio previo. Cadernos do Laboratorio Xeolóxico de Laxe 3:595-624.

Stacey J, Kramers J (1975) Approximation of terrestrial lead isotope evolution by a two-stage model. Earth Planet Sci Lett 26:207–221.

Yuan S, Peng J, Hao S, Li H, Geng J, Zhang D (2011) In situ LA-MC-ICP-MS and ID-TIMS U–Pb geochronology of cassiterite in the giant Furong tin deposit, Hunan Province, South China: New constraints on the timing of tin–polymetallic mineralization. Ore Geol Rev 43:235-242.

U-Pb Zircon Geochronology of the San Rafael Sn(-Cu) Deposit San Rafael (Peru): Sources of Magmas and Magmatic Evolution

Sava Markovic[1], Lorenzo Tavazzani[1], Dawid Szymanowski[1], Kalin Kouzmanov[2], Cyril Chelle-Michou[1]
[1]Institute of Geochemistry and Petrology, Swiss Federal Institute of Technology (ETH Zurich), Zurich 8092, Switzerland
[2]Department of Earth Sciences, University of Geneva, Geneva 1205, Switzerland

Abstract. The steadily rising demand for Sn metal imposes a need to better understand the factors controlling the distribution and size of granite-related Sn deposits. In this contribution, we employ in situ and high-precision U-Pb zircon geochronology, tools commonly applied to porphyry systems, to study the evolution of the magmatic system associated with the San Rafael Sn(-Cu) deposit in southern Peru. The intrusive complex at San Rafael comprises a suite of roughly coeval, reduced peraluminous (S-type) granitic intrusions, and subordinate lamprophyres. The age-spectra of xenocrystic zircon suggest that the oxidized redbeds of the Middle Triassic Mitu Group may had potentially represented the predominant source for the reduced Sn-mineralizing granitic magmas at San Rafael, a hypothesis that is challenged by the very contrasting oxidation states of the two rock units. Our preliminary dataset of high-precision U-Pb zircon dates for three intrusions suggests that the intrusive complex at San Rafael was constructed over timescales of ~400 kyr, between ~24.41–24.02 Ma.

1 Introduction

Granite-related magmatic-hydrothermal deposits provide a significant share of Sn required to meet the societal needs (e.g., Cerny et al. 2005). The rising demand for Sn necessitates a better understanding of the factors controlling the spatial distribution and sizes of these deposits, which could aid their more efficient discovery. U-Pb zircon geochronology has proven to be a powerful tool for studying the evolution of mineralizing magmatic-hydrothermal systems (e.g., Large et al. 2021). In particular, studies focusing on porphyry Cu-Au(-Mo) deposits showed great success in disentangling fine temporal relationships between different mineralizing intrusions, and even tentatively suggested that the size of these mineralized systems may be gauged during early exploration stages based on the quantified duration of magmatic activity (Chelle-Michou et al. 2017; Chelle-Michou and Rottier 2021). Nonetheless, this approach is yet to be applied to granite-related Sn systems, and this work presents a pioneering study. In this contribution, we present in situ (LA-ICP-MS) and preliminary high-precision (ID-TIMS) zircon U-Pb dates of intrusives from the San Rafael Sn(-Cu) deposit (Peru) with the aim of better understanding the sources and timescales of evolution of Sn mineralizing magmas.

2 Deposit Geology

The granite-related Sn(-Cu) San Rafael deposit of southern Peru represents one of world's largest crustal anomalies of Sn, with over 1 Mt of contained Sn metal at an average grade of ~2% (Harlaux et al., 2020). San Rafael belongs to the northernmost Central Andean Sn-W(-Ag) metallogenic province, and is located in the Cordillera de Carabaya of Eastern Cordillera (Figure 1; e.g., Clark et al. 1983). The Sn ore cassiterite (SnO_2) is mined underground at San Rafael, and provides for ~12% of world's Sn supply (Minsur 2022). The cassiterite is hosted by NW-SE-striking, quartz-cassiterite-sulphide-chlorite veins and associated hydrothermal breccias that extend vertically over 1.2 km, from within the intrusive complex up into the thermally metamorphosed cover (Kontak and Clark 2002).

The stratigraphy of the broader Cordillera de Carabaya is represented by 1) unexposed Precambrian metamorphic rocks, 2) Ordovician–Devonian metaclastics of the San José, Sandia, and Ananea Formations, 3) Late Paleozoic metasandstones and carbonates of the Carboniferous Ambo and Tarma Groups, and Permian Copacabana Group, 4) Middle Triassic sequence of red sandstones and intercalated volcanics of the Mitu Group, and 5) Cretaceous sandstones and carbonates of the Cotacucho Group (Laubacher 1978; Reitsma 2012).

The precursor magmatism to Sn mineralization at San Rafael comprises a suite of texturally variable, feldspar-biotite-cordierite-bearing, reduced, peraluminous (S-type) granitoids, and subordinate lamprophyres. Six distinct rock types have been mapped at San Rafael, including: 1) a megacrystic granite, 2) a fine-grained granite, 3) a medium-grained granite, 4) a tourmaline-bearing leucogranite, 5) a porphyritic granite, and 6) two lamprophyre dykes (Harlaux et al. 2021). Ubiquitous macroscopic textures of mingling and mixing between highly evolved granitic, and mafic magmas (e.g., mutual co-magmatic enclaves with lobate boundaries, and dismembered dykes) imply roughly coeval crystallization/emplacement of these units, the age of which was quantified by previous U-Pb zircon and monazite geochronology

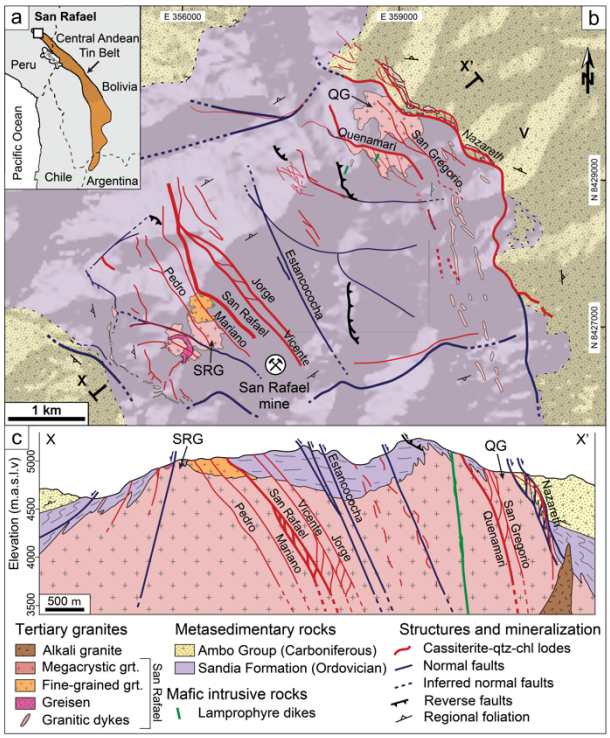

Figure 1. **a** Location of the Sn-Cu deposit San Rafael within the Central Andean tin belt of Eastern Cordillera (southeast Peru; modified after Mlynarczyk et al. 2003). **b** Geological map of the immediate area and **c** longitudinal cross-section of San Rafael (modified after Harlaux et al. 2021). SRG–San Rafael granite, QG-Quenamari granite. to ~24 Ma (Kontak and Clark 2002; Harlaux et al. 2021).

3 Methodology

Zircon crystals were separated from the magmatic rocks, thermally annealed (Mattinson 2005), and embedded in epoxy mounts. Cathodoluminescence (CL) images of the internal texture of zircon were acquired on a JEOL JSM-6390 LA scanning electron microscope (SEM) equipped with a Deben Centaurus panchromatic CL detector.

In situ isotopic U-Pb analyses were carried out using a S155-LR ASI Resolution Excimer laser ablation system coupled with a Thermo Scientific Element-XR sector-field (SF)-ICP-MS at ETH Zurich. Zircon grains showing a relatively homogeneous CL texture and no inheritance based on the results of in situ dating were selected for high-precision geochronology using isotope dilution-thermal ionization mass spectrometry (ID-TIMS). The selected grains were chemically abraded, washed in multiple cycles in HCl and HNO_3, spiked with the ET(2)535 tracer solution, and dissolved. U and Pb were separated from the matrix elements in solution by HCl-based ion-chromatography. Isotopic ratios of U and Pb were measured on a Thermo TRITON Plus TIMS instrument.

4 Results and discussion

4.1 CL images, and age-spectra of xenocrystic zircon

Zircon from different intrusions at San Rafael were classified into bright, intermediate, and dark according to their CL tone, and deformed, oscillatory, sector-zoned, and plane based on their CL texture. Notably, dark oscillatory rims, rich in U (1 000–5 000 ppm, and up to 15 000 ppm) are characteristic for zircon from all samples. Apart from this, no systematic features have been observed in zircon CL texture across different samples. Out of a total of 233 zircon grains dated in situ, 27% contained a xenocrystic component (i.e., core or whole zircon xenocryst), indicating a substantial crustal component in the makeup of San Rafael magmas.

U-Pb analyses of xenocrystic zircon display two major peaks, of Permian/Triassic and Cambrian/Ordovician age, and fewer points plotting within Proterozoic age-range (Figure 2). Our results are largely consistent with those of Harlaux et al. (2021), who identified the same major peaks, but did not observe the Proterozoic zircon population. The age spectra of our analyses reproduce well those obtained for the oxidized, red sandstones of the Middle Triassic Mitu Group (Harlaux et al. 2021), suggesting that this unit statistically represents the most likely predominant protolith for the reduced S-type granitic magmas at San Rafael. The Mitu Group consists of a volcano-sedimentary rift sequence deposited in a phase of Permo-Triassic magmatism in the Eastern Cordillera, in association with the break-up of Pangea (Reitsma 2012; Spikings et al. 2016). Nonetheless, the Mitu Group being a direct source of the reducing granitic magmas of San Rafael is not consistent with the differing oxidation states of the two, and would require an intermediate reduction step to produce the S-type magma compositions. Alternatively, the chemically more suitable (i.e., reduced) protoliths (e.g., finer-grained Proterozoic/Cambrian units) may be underrepresented or missing in the age-spectra due to the equally unlikely absence or extreme partial melting conditions (fluid absent, >925 °C) and complete dissolution of zircon in the source (Mintrone et al. 2020).

4.2 Oligocene magmatic evolution of San Rafael

Preliminary high-precision ^{230}Th-corrected ^{206}Pb/^{238}U zircon dates for the megacrystic, medium-grained, and fine-grained granite at San Rafael are presented in Figure 3. The distribution of individual zircon dates from the three units records magmatic crystallization on time-scales of ~400 kyr, from ~24.41–24.02 Ma. The megacrystic and fine-

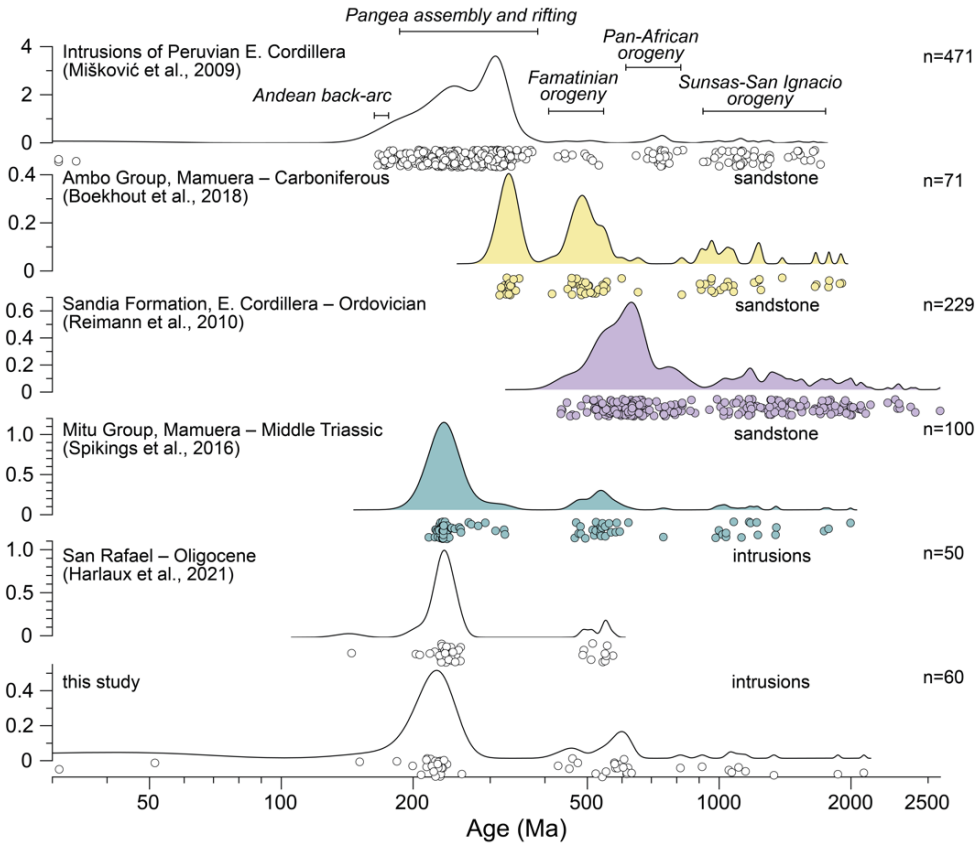

Figure 2. Comparison of U-Pb probability density distributions for xenocrystic zircon from San Rafael, and zircon of proximal sedimentary units and regional intrusions of the Peruvian Eastern Cordillera.

grained granites display a continuous date distribution, whereas the distribution of zircon dates from the medium-grained granite is strongly bimodal. Megacrystic and medium-grained granites record the first phase of magmatic crystallization, which started ~24.35 Ma. The youngest interval of the magmatic history is recorded by the younger population of zircon dates from the medium-grained granite, which fall in the range between ~24.08–24.02 Ma. Zircons from the fine-grained granite, as well as the younger zircons of the megacrystic granite, record crystallization from 24.30 to 24.18 Ma, intermediate between the two age groups of the medium-grained granite.

The spread of our ID-TIMS zircon dates overlaps within uncertainty with the in situ weighted-mean dates of the same units by Harlaux et al. (2021), and is somewhat younger than the single crystal ID-TIMS zircon (24.7 ± 0.2 Ma) and monazite (24.6 ± 0.2 Ma) ages of Kontak and Clark (2002). Our zircon dates of the megacrystic and fine-grained granites are consistent with their coeval emplacement implied from their field relationships. To the contrary, the younger zircon distribution in the medium-grained porphyry granite records magmatic crystallization >100 kyr after the cooling of the previous two units.

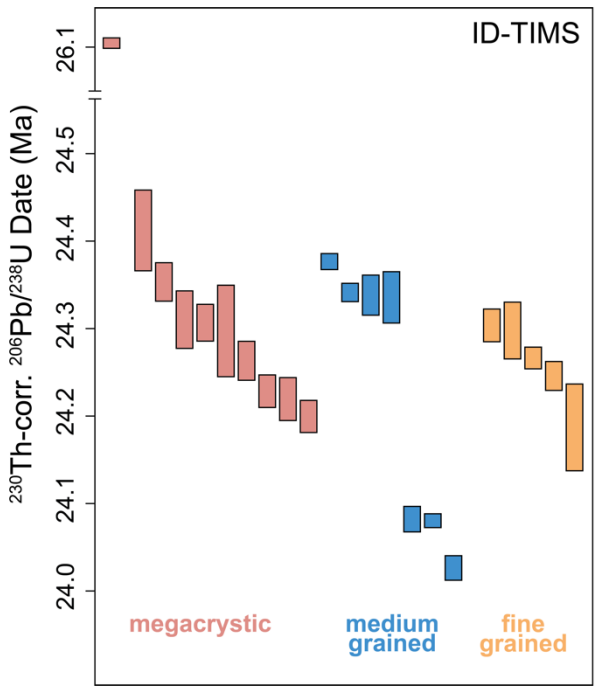

Figure 3. High-precision U-Pb dates of zircon from the megacrystic, medium-grained, and fine-grained granite at San Rafael.

5 Conclusions

This contribution presents preliminary results of in situ and high-precision zircon U-Pb geochronology from intrusions of the Sn(-Cu) magmatic-hydrothermal deposit San Rafael (Peru). Zircons from different intrusions contain a high proportion of xenocrystic components, and appear in bright, intermediate, and dark cathodoluminescence CL tones, and deformed, oscillatory, sector-zoned, and plane textures. The age-spectra of xenocrystic zircon from San Rafael is most akin to that of the regional oxidized redbeds of the Middle Triassic Mitu Group. However, considering the Mitu group as a protolith for the reduced granitic magmas at San Rafael is challenged by the very contrasted oxidation states between the two rock units. The preliminary dataset of high-precision U-Pb zircon dates for different intrusions suggest that the intrusive complex at San Rafael was assembled in several pulses over a timescale of ~400 kyr, between ~24.41–24.06 Ma.

Acknowledgements

The authors acknowledge the generous funding received through the ETH Zurich Research Grant. We also thank the geological team of Minsur S.A. for their logistical support and assistance, and collaborators L. Torró, M. Harlaux, and K. Kouzmanov for field guidance, providing the first samples from San Rafael, and motivating discussions.

References

Cerny P, Blevin P, L, Cuney M, London D (2005) Granite-related ore deposits. Society of Economic Geologists 100:337-370.

Chelle-Michou C, Rottier B, Caricchi L, Simpson G (2017) Tempo of magma degassing and the genesis of porphyry copper deposits. Sci Rep-Uk 7:1-12. doi: ARTN 40566
10.1038/srep40566.

Chelle-Michou C, Rottier B (2021) Transcrustal Magmatic Controls on the Size of Porphyry Cu Systems: State of Knowledge and Open Questions Tectonomagmatic Influences on Metallogeny and Hydrothermal Ore Deposits: A Tribute to Jeremy P Richards (Volume I). pp 87-100.

Clark AH, Palma VV, Archibald DA, Farrar E, Arenas F. MJ, Robertson RCR (1983) Occurence and Age of Tin Mineralization in the Cordillera Oriental, Southern Peru. Econ Geol 78:514-520.

Harlaux M, Kouzmanov K, Gialli S, Clark AH, Laurent O, Corthay G, Flores EP, Dini A, Chauvet A, Ulianov A, Chiaradia M, Menzies A, Durand GV, Kalinaj M, Fontbote L (2021) The upper Oligocene San Rafael intrusive complex (Eastern Cordillera, southeast Peru), host of the largest-known high-grade tin deposit. Lithos 400. doi: ARTN 10640910.1016/j.lithos.2021.106409.

Kontak DJ, Clark AH (2002) Genesis of the giant, bonanza San Rafael Lode tin deposit, Peru: Origin and significance of pervasive alteration. Econ Geol Bull Soc 97:1741-1777. doi: Doi 10.2113/97.8.1741.

Large SJE, Buret Y, Wotzlaw JF, Karakas O, Guillong M, von Quadt A, Heinrich CA (2021) Copper-mineralised porphyries sample the evolution of a large-volume silicic magma reservoir from rapid assembly to solidification. Earth Planet Sc Lett 563:1-12. doi: ARTN 11687710.1016/j.epsl.2021.116877.

Laubacher G (1978) Estudio geologico de la region norte del Lago Titicaca. Instituto Geologia y Mineria, Peru.

Mattinson JM (2005) Zircon U-Pb chemical abrasion ("CA-TIMS") method: Combined annealing and multi-step partial dissolution analysis for improved precision and accuracy of zircon ages. Chem Geol 220:47-66. doi: 10.1016/j.chemgeo.2005.03.011.

Minsur (2022) Responsible Minerals Assurance Process–Due Diligence Report.

Mintrone M, Galli A, Laurent O, Chelle-Michou C, Schmidt MW (2020) Quantifying frozen melt in crustal rocks: A new melt-o-meter based on zircon rim volumes. Chem Geol 551:119755.

Reitsma MJ (2012) Reconstructing the Late Paleozoic:Early Mesozoic plutonic and sedimentary record of south-east Peru: Orphaned back-arcs along the western margin of Gondwana. PhD thesis, University of Geneva, Switzerland, pp 246.

Spikings R, Reitsma MJ, Boekhout F, Miskovic A, Ulianov A, Chiaradia M, Gerdes A, Schaltegger U (2016) Characterisation of Triassic rifting in Peru and implications for the early disassembly of western Pangaea. Gondwana Res 35:124-143. doi: 10.1016/j.gr.2016.02.008.

Critical minerals in Climax-type magmatic-hydrothermal systems

Celestine N. Mercer[1], Mario Guzman[1], Albert H. Hofstra[1], Joshua M. Rosera[2]
[1]U.S. Geological Survey, Denver, CO, USA
[2]U.S. Geological Survey, Reston, VA, USA

Abstract. Today's global economy is challenged to meet the growing demand for commodities used in existing and emerging advanced technologies. Critical minerals are commodities found in a wide variety of ore deposits that are vital to the economic or national security of individual nations that are vulnerable to supply disruption. The U.S. Geological Survey is striving to advance understanding of critical mineral resources by employing a Mineral Systems approach. Climax-type systems are one of 17 mineral systems currently under investigation. The aim of this work is to inventory and assess knowledge gaps on the abundance of 50 critical minerals in Climax-type systems. Here we synthesize geochemical data from ore concentrates, ore, waste, and minerals together with information on production from, and resources in, ore deposits. The goal of this work is to estimate the amount of critical minerals present in processed mine waste and unmined resources, discuss those that could potentially be recovered in the future, and identify important future areas of research.

1 Distribution of Climax-type magmatic-hydrothermal systems

Climax-type magmatic-hydrothermal systems occur in post-subduction, continental rift settings with thick cratonic crust and are associated with hydrous, fluorine-rich bimodal magmatism (Sinclair, 1995; Ludington and Plumlee, 2009; Rosera et al., 2022). Most well-known Climax-type magmatic-hydrothermal systems are located in western North America, although in recent years several significant Climax-type systems have been recognized in the East Qinling-Dabie orogenic belt of China (Shapinggou, Nannihu-Sandaozhuang, Donggou, Yechangping and Yongping-Shizito; Zeng et al., 2013; Audétat and Li, 2017). The North American systems typically range in age from early Eocene (as old as ~51 Ma, Big Ben, MT) to Pliocene (as young as ~5 Ma, Silver Creek, CO). With few exceptions, these systems are products of bimodal magmatism involving hydrous, fluorine-rich, highly evolved (i.e., rare metal) granites and topaz rhyolites (dominantly A-type or "ferroan"; Frost and Frost, 2011; commonly ~77 wt% SiO_2, >300 ppm Rb, >80 ppm Y+Nb) and contemporaneous hydrous mafic intrusions (trachybasalt to trachyandesitic) that appear to be unique to melting Proterozoic lithosphere during the transition from Laramide shortening to continental extension and subsequent rifting (White et al., 1981; Ludington and Plumlee, 2009; Audétat and Lee, 2017; Rosera et al., 2021).

Exsolution of supercritical magmatic fluids derived from a series of felsic intrusions, perhaps supplemented by fluid components sparged from mafic intrusions (e.g; Hattori and Keith, 2001; Hofstra et al., 2014b; Audétat and Li, 2017), drive formation of a variety of ore deposits as they ascend, boil, react with country rocks, mix with groundwater, and vent to the surface. The broad spectrum of deposit types results from the considerable thermal and chemical gradients that extend from the deep plutonic root zones to the surface fumarolic portions of the system. The nature of host rocks and preexisting structures do not exert a strong control on root zone and porphyry deposits because focusing is dominated by magma emplacement and hydrofracturing processes, while peripheral and shallow deposits are localized by permeable rocks and dilatant structures.

2 Anatomy, deposits, and commodities from root zone to vapour phase

Climax-type systems contain a wide variety of important ore deposit types, including plutonic root-zone deposits (pegmatite, greisen), porphyry stock and peripheral deposits (porphyry, skarn, polymetallic sulfide vein, distal disseminated), lithocap zone deposits (epithermal, lithocap), and volcanogenic and vapor phase deposits (Fig. 1). Principal commodities include beryllium (Be), fluorite (CaF_2), aluminum (Al), potash (K_2SO_4), copper (Cu), zinc (Zn), yttrium (Y), niobium (Nb), molybdenum (Mo), silver (Ag), tin (Sn), tungsten (W), gold (Au), lead (Pb), and uranium (U). While some of these primary commodities are classified as critical minerals, an assortment of other critical minerals may be found in Climax-type systems in elevated concentrations, including antimony (Sb), arsenic (As), bismuth (Bi), gallium (Ga), germanium (Ge), indium (In), lithium (Li), magnesium (Mg), niobium (Nb), rhenium (Re), and tantalum (Ta). Some of these critical minerals have been historically produced while others are potential byproducts. It should be noted that only rarely do individual systems exhibit all of the possible deposit types and coevolved intrusions are frequently barren (e.g., Audétat, 2019).

Predominant ore minerals in Climax-type systems include alunite, bertrandite, cassiterite, chalcopyrite, fluorite, galena, molybdenite, scheelite, sphalerite, uraninite, and wolframite. However, a wide variety of minerals occur in the spectrum of deposit types generated by Climax-type systems and many contain critical minerals.

3 Data sources

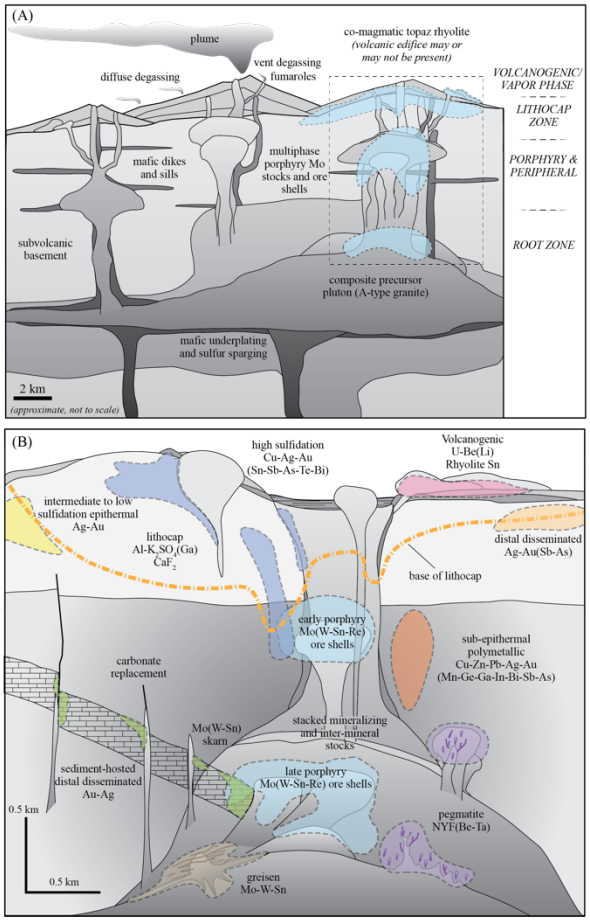

Figure 1. Schematic model for Climax-type magmatic-hydrothermal systems from root zone to vapor phase. (A) Mid- to upper crustal polybaric magma reservoirs, mafic intrusions, multiphase porphyry Mo stocks, and volcanic edifices, which may or may not be present. Climax-type system zones of mineralization are shown in blue, including the root zone, porphyry and peripheral zone, lithocap zone, and vapor phase zone. Horizontal scale is approximate, vertical aspect is exaggerated. Dashed box shows approximate inset shown in part B. Modified after Mercer et al. (2015). (B) Anatomy of Climax-type ore deposits within the magmatic-hydrothermal system. Modified after Launay et al (2021), Richards and Mumin (2013), Sillitoe (2010), and Seedorff and Enaudi (2004). Scale is approximate.

Mineral site information for this report was acquired primarily from the USMIN Mineral Deposit Database, the Keith Long Significant Deposit Database (Long et al., 1998), the Giant Porphyry-Related Camps of the World-A Database (v.2.7; Mutschler et al., 2000), and USGS deposit models (Climax-type porphyry: Ludington and Plumlee, 2009; Volcanogenic U: Breit et al. 2011; Volcanogenic Be: Foley et al., 2012). This was supplemented with site information from the USGS Mineral Resource Data System that were cross referenced using additional authoritative sources. Climax-type mineral sites ranging from occurrences to prospects to well-characterized deposits are documented in this report, but for the purpose of quantifying critical minerals this work focuses on significant known deposits.

Existing whole rock geochemical data on mineralized and altered rock samples were compiled from several sources including the National Geochemical Database on Ore Deposits: Legacy Data (Granitto et al., 2021), the Global Geochemical Database for Critical Minerals in Archived Mine Samples (Granitto et al., 2020), and additional published data.

166 new whole rock multi-element data were acquired from available mineralized and altered rock samples and ore concentrates compiled in the National Geochemical Database on Ore Deposits: New Data (Granitto et al., in prep.). 57 archived samples with older geochemical analyses were reanalyzed for more modern and complete geochemical profiles, while 79 samples were newly collected from research collections, university collections, and personal collections in an effort to expand the number of deposits for which multi-element geochemical information exists.

Geochemical data were evaluated relative to their abundance in upper crust using box plots, where a box of length equal to the interquartile range is divided at the median of the data. Whiskers extend to the furthest data point within 1.5 times the interquartile range beyond the edge of the box, and outliers beyond the whiskers are represented with circles. Median values of each element were interpreted to be more representative than mean values given the skewed nature of the datasets.

4 Critical mineral enrichments

The deepest root-zone levels of Climax-type systems reside near the top of A-type granitic plutons where fluids and metals are derived from a subjacent magmatic reservoir. This zone lies beneath the porphyry ore zone, and while no two systems are alike, some may mineralize niobium-yttrium-fluorine (NYF) pegmatites or Mo-W-Sn(-Bi) greisen (i.e., muscovite ±topaz ±fluorite ±tourmaline) and vein deposits (Fig. 1). Ore samples from this realm (e.g., Sweet Home, Mt. Antero, CO) have anomalous median concentrations >100x crustal value of Be, Bi, Cd, In, Re, Sb, and Te (in addition to Cu, Mo, Pb, and Zn).

Extending from the pluton roof lies the porphyry stock Mo(W-Sn) realm and a variety of deposits may develop peripherally away from this zone, including proximal and distal skarn, sub-epithermal polymetallic vein, and distal disseminated deposits (Fig. 1). Climax-type systems are best known for their massive porphyry Mo deposits (e.g., Climax, Henderson, CO; Questa, NM, Fig. 2) with median concentrations >10x crustal value of Cd, Re, Se, and Te (in addition to primary commodities Mo and W). Porphyry molybdenite (MoS_2) concentrates (Mt Hope, NV; Climax, Henderson, CO) are enriched >1000x crustal value in Cd, Re, and Te; wolframite (WO_4) concentrates (Climax, CO) >1000x crustal

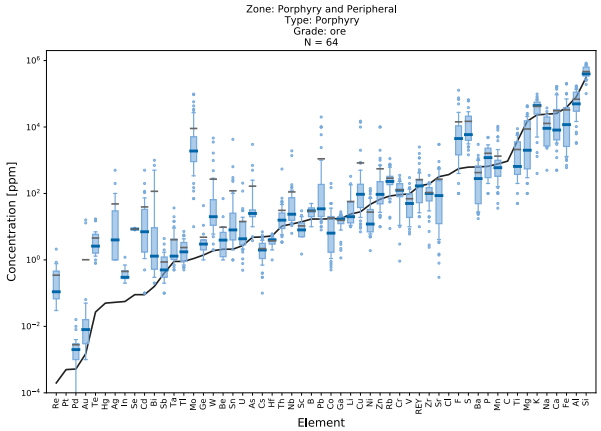

Figure 2. Box plot of elemental abundance in ore samples from porphyry Mo deposits relative to upper crustal abundance (black line). Median shown with bold blue line.

value in Re; monazite ($REE(PO_4)$) concentrates (Climax, CO) >1000x crustal value in Bi, Cd, Mo, Nb, Sn, Ta, U, and W; and pyrite (FeS_2) concentrates (Climax, CO) >1000x crustal value in In. Polymetallic vein and replacement ore samples (e.g., Climax, Henderson, Mt. Emmons, Sunnyside, CO; Victorio, NM; Deer Trail, UT, Fig. 3) have anomalous median concentrations >100x crustal value of As, Au, Bi, In, Sb, Se, and Te (in addition to Pb and Zn) and >1000x crustal value of Cd and Re. Above and commonly overprinting the porphyry realm lies the lithocap environment (Fig. 1). This zone is eroded away at most well known Climax-type porphyry Mo deposits but has been identified in porphyry Mo deposit systems in New Mexico, Utah, and Colorado (Hofstra et al., 2014a). Much of the lithocap zone may be barren, but some portions contain significant alunite, from which potash (K_2SO_4) and alumina (Al2O3) have been historically produced, kaolinite ($Al_2Si_2O_5(OH)_4$), and fluorite (CaF_2) (e.g., Alunite Ridge, UT) while some areas locally host a variety of intermediate- and high-sulfidation epithermal deposits and polymetallic vein and replacement deposits. This realm is an indicator of Mo and other system-related resources at depth (Mercer et al., 2022). Intermediate- and high-

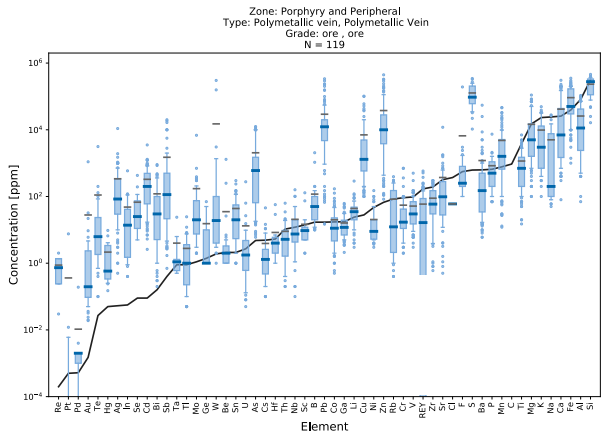

Figure 3. Box plot of elemental abundance in ore samples from polymetallic vein and replacement deposits relative to upper crustal abundance (black line). Median value shown with bold blue line.

sulfidation epithermal deposits (e.g., Red Mountain, CO) have anomalous median concentrations >100x crustal value in Bi, In, Se, and Sn (in addition to Cu, Pb, and Zn) with >1000x crustal value of As, Cd, Sb, and Te.

At the top of the volcanic pile (e.g., topaz rhyolite flows, domes, tuffs) lies the volcanogenic and vapor phase zone, the shallowest lithological expression of Climax-type systems (Fig. 1). Here mineralization occurs post-eruptively when fluids (e.g., hydrothermal fluids driven by magmatic heat, fluids expelled from devitrification of volcanic glass, meteoric water, volcanic lakes) leach and react with vitric felsic volcanic rocks, remobilizing and concentrating critical elements. Important resources of Be and U form in this realm (Breit and Hall, 2011; Foley et al., 2012). The world's largest volcanogenic Be deposit (Spor Mountain, UT) contains anomalous median concentrations >10x crustal value of Bi, Cd, Li, and Ta (in addition to Pb, Sn, W, and Zn) and >100x crustal value of Be, F, In, and U.

5 Critical mineral estimates based on primary commodity ratios

Median ratios of critical minerals to primary commodities may be used along with existing commodity grade, tonnage, or assessed endowments to estimate potential critical mineral grade, tonnage, or endowment values. Current geochemical and commodity grade/tonnage data on many Climax-type ore deposits are sparse, which presently limits the utility of this approach.

Preliminary calculations for the median porphyry molybdenite ore concentrates returns ratios with Mo including Cd/Mo = 0.0011, Re/Mo = 0.000012, Te/Mo = 0.00009 with notable ratios of Bi/Mo = 0.000097, REE/Mo = 0.000098, and Sn/Mo = 0.00006. Porphyry wolframite ore concentrates yield ratios with W including Re/W = 0.000006, Nb/W = 0.009, REE/W = 0.0011, Sn/W = 0.0014, and Ta/W = 0.0005. Porphyry monazite ore returns ratios with REE of Bi/REE = 0.2, Nb/REE = 5.0, Sn/REE = 13, Ta/REE = 0.94, U/REE = 1.3, Cd/REE = 0.02, and Sc/REE = 0.08. Molybdenite ore ratios suggest potential endowment of the Climax-Sweet Home ore deposit with 144 tonnes Te (298% of 2022 U.S. imports for consumption), 155 tonnes Bi (5% of 2022 U.S. imports for consumption), 157 tonnes REM (1.6% of 2022 U.S. imports for consumption), and 96 tonnes Sn (0.2% of 2022 U.S. imports for consumption).

Initial calculations for median beryllium ore concentrations returns significant ratios with Be of Ce/Be = 1.004, Li/Be = 2.149, Zn/Be = 2.819, Cs/Be = 0.583, Nb/Be = 0.883, Y/Be = 0.811, and Zr/Be = 0.816. These ratios suggest the potential existence at the Spor Mountain mine of 15,261 tonnes Ce (no consumption data available, but

~3,000% current U.S. stockpile), 32,665 tonnes Li (960% of 2022 U.S. imports for consumption), 42,849 tonnes Zn (6000% of 2022 U.S. imports for consumption), 13,422 tonnes Nb (150% of 2022 U.S. imports for consumption), 12,327 tonnes Y (1500% of 2022 U.S. imports for consumption), and 12,403 tonnes Zr (47% of of 2022 U.S. imports for consumption).

6 Conclusions and future areas of research

Climax-type systems are indeed an important past, current, and future source of critical minerals. Despite considerable knowledge and data on Climax-type magmatic hydrothermal systems, there are considerable gaps in existing geochemical datasets on the abundance of critical minerals, especially in whole rock data from root zone, lithocap, volcanogenic and vapour phase deposits. Existing high-spatial resolution, multi-element geochemical analyses of ore and gangue are rare and we highlight this as an area for future research as well.

These data are preliminary or provisional and are subject to revision. They are being provided to meet the need for timely best science. These data have not received final approval by the U.S. Geological Survey (USGS) and are provided on the condition that neither the USGS nor the U.S. Government shall be held liable for any damages resulting from the authorized or unauthorized use of the data.

Acknowledgements

We thank M. Granitto, D. Schmidt and R. Khoury for help compiling literature data and sample processing. We also thank C.M. Mercer for programming expertise.

References

Audétat A and Li W (2017) The genesis of Climax-type porphyry Mo deposits—Insights from fluid inclusions and melt inclusions. Ore Geol Rev 88:436–460.

Audétat A (2019) The Metal Content of Magmatic-Hydrothermal Fluids and Its Relationship to Mineralization Potential. Econ Geol 114:1033–1056.

Breit GN and Hall SM (2011) Deposit model for volcanogenic uranium deposits. USGS OFR 2011–1255:1-5.

Foley NK, Hofstra AH, Lindsey DA, Seal RRII, Jaskula B, Piatak NM (2012) Occurrence model for volcanogenic beryllium deposits, Chap. F of Mineral deposit models for resource assessment. USGS SIR 2010–5070–F:1-43.

Frost CD and Frost BR (2010) On Ferroan (A-type) Granitoids: their Compositional Variability and Modes of Origin. J Petro 52:39–53.

Granitto M, Wang B, Shew NB, Karl SM, Labay KA, Werdon MB, Seitz SS, Hoppe JE (2019) Alaska geochemical database version 3.0 (AGDB3)—including "best value" data compilations for rock, sediment, soil, mineral, and concentrate sample media. USGS Data Series 1117. https://doi.org/ 10.3133/ds1117.

Granitto M, Emsbo P, Hofstra AH, Orkild-Norton AR, Bennett MM, Azain JS, Koenig AE, Karl NA (2020) Global Geochemical Database for Critical Minerals in Archived Mine Samples: U.S. Geological Survey data release, https://doi.org/10.5066/P9Z3XL6D.

Granitto M, Schmidt DE, Karl NA, Khoury RM (2021) National Geochemical Database on Ore Deposits: Legacy data. USGS Data Release, https://doi.org/10.5066/P944U7S5.

Hattori KXI and Keith J (2001) Contribution of mafic melt to porphyry copper mineralization: evidence from Mount Pinatubo, Philippines, and Bingham Canyon, Utah, USA. Miner Deposita 36:799–806.

Hofstra, A. H., Cosca, M.A., and Rockwell, B.W. (2014a) Advanced argillic lithocaps above Climax-type Mo porphyries? Evidence from porphyry clusters in New Mexico, Utah, and Colorado: SEG Annual Meeting, Keystone, CO, 1 pg.

Hofstra AH, Landis GP, Rye RO (2014b) Magmatic Steam Alunite Veins: The Epithermal Expression of UST Layers in Porphyry Intrusions? Pan-American Current Research on Fluid Inclusions (PACROFI-XII) 21-22.

Long KR, DeYoung JHJr, Ludington SD (1998) Database of Significant Deposits of Gold, Silver, Copper, Lead, and Zinc in the United States. USGS OFR 98-206a-b:33.

Ludington S and Plumlee GS (2009) Climax-type porphyry molybdenum deposits. USGS OFR 2009–1215:16.

Launay G, Sizaret S, Lach P, Melleton J, Gloaguen E, Poujol M (2021) Genetic relationship between greisenization and Sn-W mineralizations in vein and greisen deposits: Insights from the Panasqueira deposit (Portugal). Bul Soc Géolog France 192:1-29.

Mercer CN, Hofstra AH, Todorov TI, Roberge J, Burgisser A, Adams DT, Cosca M (2015) Pre-Eruptive Conditions of the Hideaway Park Topaz Rhyolite: Insights into Metal Source and Evolution of Magma Parental to the Henderson Porphyry Molybdenum Deposit, Colorado. J Petrol 56-4:645–679.

Mercer CM, Cosca MA, Hofstra AH, Premo WR, Rye RO, Landis GP (2022) $^{40}Ar/^{39}Ar$ Geochronology of Magmatic-Steam Alunite from Alunite Ridge and Deer Trail Mountain, Marysvale Volcanic Field, Utah: Timing and Duration of Miocene Hydrothermal Activity Associated with Concealed Intrusions. Minerals 12:1533.

Mutschler FE, Ludington S, Bookstrom AA (2000) Giant porphyry-related camps of the world – A database, USGS OFR 99-556 Version 2.7, https://pubs.usgs.gov/of/1999/of99-556/.

Richards JP and Mumin AH (2013) Magmatic-hydrothermal processes within an evolving Earth: Iron oxide-copper-gold and porphyry Cu ± Mo ± Au deposits. Geol 41:767–770.

Rosera JM, Gaynor SP, Coleman DS (2021) Spatio-Temporal Shifts in Magmatism and Mineralization in Northern Colorado Beginning in the Late Eocene. Econ Geol 116-4:987–1010.

Rosera JM, Frazer R, Mills R, Jacob K, Gaynor, S, Coleman D, Farmer L (2022) Fluorine-Rich Mafic Lower Crust In The Southern Rocky Mountains: The Role Of Pre-Enrichment In Generating Fluorine Rich Silicic Magmas And Porphyry Mo Deposits. Am Min DOI: https://doi.org/10.2138/am-2022-8503

Seedorff E and Einaudi MT (2004) Henderson porphyry molybdenum system, Colorado: I. Sequence and abundance of hydrothermal mineral assemblages, flow paths of evolving fluids, and evolutionary style. Econ Geol 99:3–37.

Sillitoe RH (2010) Porphyry Copper Systems. Econ Geol 105:3–41.

Sinclair WD (1995) Porphyry Mo (Climax-type), Selected British Columbia mineral deposit profiles Volume 1. Metallics and coal, Lefebure DV and Ray GE, eds. British Columbia Ministry of Energy of Employment and Investment Open File 1995–20:105–108.

White WH, Bookstrom AA, Kamilli RJ, Ganster MW, Smith RP, Ranta DE, Steininger RC (1981) Character and origin of Climax-type molybdenum deposits. Econ Geol 75th Anniv Vol:270–316.

Zeng Q, Liu J, Qin K, Fan H, Chu (2013) Types, characteristics, and time–space distribution of molybdenum deposits in China. Internat Geol Rev 55:1311–1358.

Comparative study of pegmatites from the Central Rhodopean Pb-Zn deposits (Bulgaria)

Georgi Milenkov[1], Rossitsa D. Vassileva[1], Sylvina Georgieva[1], Kalin Kouzmanov[2], Jan Cempírek[3], Yana Georgieva[4]
[1]Geological Institute, Bulgarian Academy of Sciences, Sofia, Bulgaria
[2]Department of Earth sciences, University of Geneva, Geneva, Switzerland
[3]Department of Geological Sciences, Masaryk University, Brno, Czech Republic
[4]Sofia University "St. Kliment Ohridski", Sofia, Bulgaria

Abstract. Pegmatites are one of the main sources of some critical elements required for the 'green transition'. This specific lithology is commonly observed as a host rock for polymetallic mineralization in Pb-Zn deposits from the Central Rhodopes in Bulgaria. The main pegmatite-forming minerals are feldspar, quartz and mica. Allanite, titanite, zircon, monazite and apatite are commonly observed as accessory minerals. Despite no genetic relation between the Pb-Zn mineralization and the pegmatites, the latter are altered by the ore-forming fluids in these deposits. The hydrothermal alteration resulted in redistribution of various components to new minerals phases such as thorite, bastnäsite, parisite, xenotime, REE-bearing clinozoisite and others.
We studied pegmatites from four different deposits located in two districts - Madan (Petrovitsa and Krushev Dol deposits) and Laki (Djurkovo and Govedarnika deposits). Macroscopically, the pegmatites from the different localities do not vary much; however, their geochemical signatures (e.g., feldspars, allanite and titanite compositions) differ significantly. Proximity to the hydrothermal fluid source, structural control, metamorphic grade, and deformation were essential factors that influenced the geochemistry of the pegmatite minerals.

1 Introduction

Pegmatite geochemistry, origin and economic potential have been vastly studied in the past decades. The traditional usage of pegmatites for ceramics shifted towards their importance as a major source for rare and critical elements needed for the "green transition" (Li, Be, Cs, Ta, Nb, U, REE). To properly define pegmatite exploration strategies and evaluate their economic potential, mineralogical and geochemical studies of pegmatites are essential as they allow recognition of their genetic mechanisms and identification of potential ore minerals.

Abundant pegmatite dykes are observed in some of the Pb-Zn deposits in the Central Rhodopes, Southern Bulgaria (Figure 1). New data on the mineralogical and geochemical characteristics, geochronology, and general mineral zonation were recently reported (Georgieva et al. 2022; Milenkov et al. 2022). In this study we compile and compare recent and newly obtained geochemical data of major and accessory minerals of pegmatites from four Pb-Zn deposits, two in the Madan district (Petrovitsa and Krushev Dol) and two in the Laki district (Djurkovo and Govedarnika).

2 Geological setting

The region is part of the Alpine-Balkan-Carpathian-Dinaride province in south-eastern Europe. The studied deposits are currently underground mining operations. Despite their affiliation to two different ore districts (Laki and Madan; Figure 1B), the ore bodies are hosted by the rocks of the Madan lithotectonic unit. The unit belongs to the Middle Allochtone of the Rhodope Metamorphic Complex (Jahn-Awe et al. 2012) and is composed of biotite gneisses, amphibolites and marbles. In both Laki and Madan areas, the Pb-Zn deposition is controlled by NNW- (Madan) or NNE-trending (Laki) transtensional fault systems; the ores are mainly present in quartz-sulphide veins and metasomatic skarn bodies hosted by the high-grade metamorphic rocks.

At ~42 Ma, magmatism related to post-collisional extensional tectonics began locally by the intrusion of the Smilyan granite, shifting towards extension-related rhyolite dykes and ignimbrite deposit emplacement (Smolyan Basin) at ~31 Ma (Kaiser-Rohrmeier et al. 2013). Skarn formation and sulfide mineralization in the Madan ore district was constrained between 31.41±0.39 Ma (U-Pb dating on zircon in pre-ore rhyolite; Hantsche et al. 2017) and 29.95±0.23 Ma (Ar-Ar dating on hydrothermal sericite; Kaiser-Rohrmeier et al. 2004). The origin of the Pb-Zn mineralization is still under debate.

Formation of the studied pegmatite dikes pre-dates timing of the hydrothermal and skarnification processes; ages of pegmatite formation range from 50 to 40 Ma (Milenkov et al. 2022).

3 Local geology

All studied pegmatites in the Madan unit share the same main characteristics. The pegmatites are commonly observed as layer-like bodies concordant to the main metamorphic foliation (Figure 1C, D, E). Most of the studied pegmatites underwent several stages of ductile and brittle deformation, causing their sigmoidal shape with several groups of fractures (Figure 1C and D). Their thickness varies between 0.1 and 5 m. Sometimes pegmatite injections crosscut the other host rocks.

Besides the observed deformation, the pegmatites also underwent later hydrothermal alteration. Its intensity is stronger towards the lithological contacts with other rocks from the metamorphic sequence. The boundary between

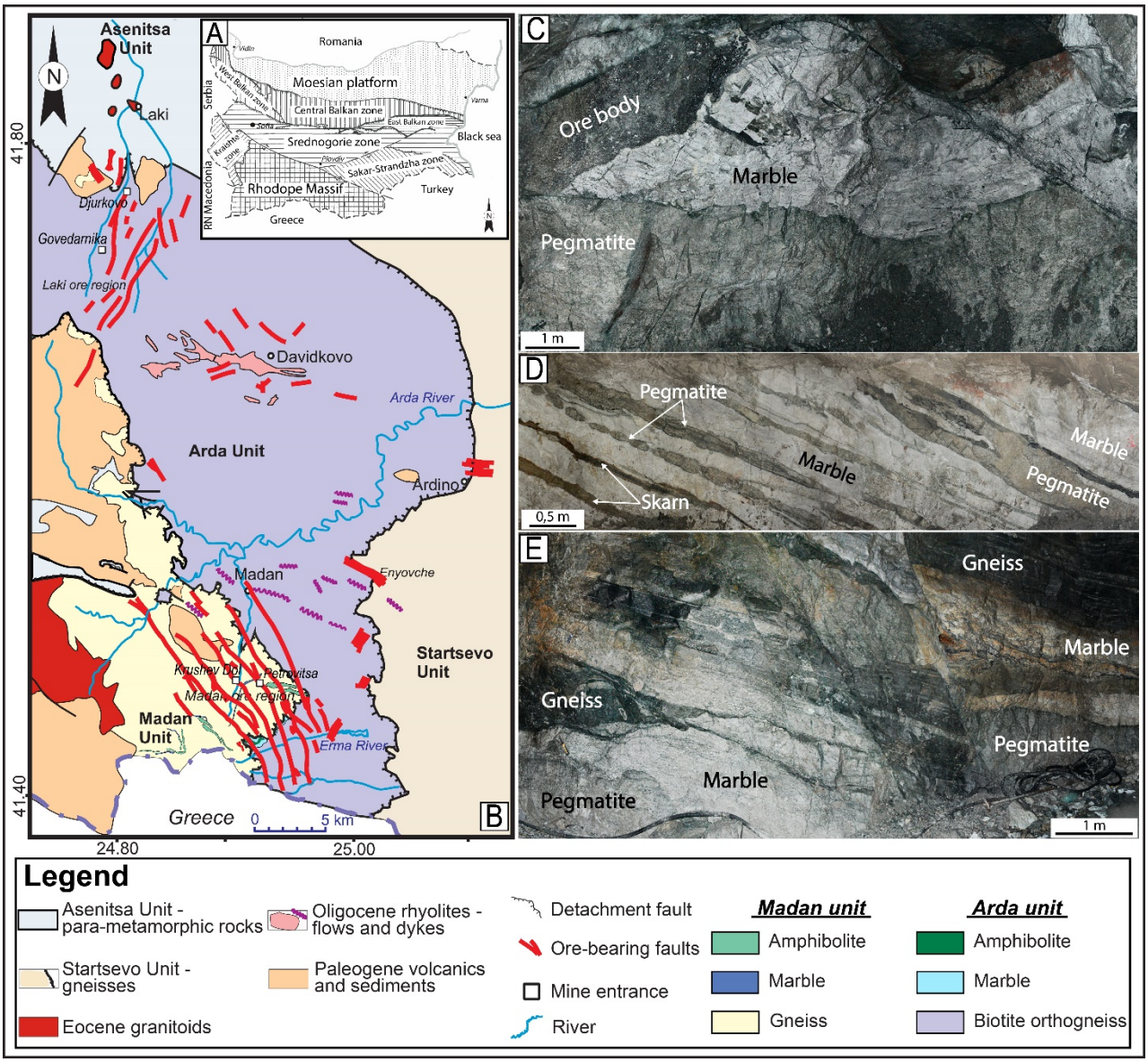

Figure 1. A) Tectonic map of Bulgaria; B) Geological map of the Central Rhodopes and the main ore districts and deposits (Vassileva et al. 2009); Pegmatite outcrops in C) Petrovitsa, D) Govedarnika, and E) Djurkovo deposits.

pegmatites and marbles favours precipitation of anorthite at the expense of the other feldspars. Epidote-chlorite-adularia-(±hematite) and sericite-carbonate are other very typical hydrothermal associations.

The primary mineral assemblage consists of K-feldspar, plagioclase, quartz and micas, while titanite, allanite, zircon, apatite and monazite are the main accessories (Milenkov et al. 2022). Alteration minerals such as albite, epidote, chlorite, clinopyroxene, sericite, kaolinite, rutile, adularia and calcite replace the primary pegmatite minerals. Based on the genetic classification of Ivanov (1991), the studied pegmatites belong to the Rare-Element class, corresponding to Niobium-Yttrium-Fluorine (NYF) family according to Černý and Ercit (2005).

4 Results

Feldspars are the most abundant pegmatite-forming minerals, followed by quartz. Based on petrography study either plagioclase prevail over K-feldspar or vice versa. Mica appears sporadically within the bodies. Feldspar composition is highly variable (Figure 2A). K-feldspar (orthoclase) is typical for all localities, while the Ca-plagioclase (anorthite) is observed only at Petrovitsa. Orthoclase, oligoclase, albite and andesine compositions are the most common feldspars within both Madan and Laki districts.

Allanite–REE-rich clinozoisite and titanite are the most widespread accessory minerals in the pegmatites. Their size highly varies between 5 μm and 1.5 mm, the shape is subhedral to anhedral. Patchy zonation rarely occurs in titanite but is characteristic for allanite. The sum of REE, Th and Y contents shows that most of the allanites suffered hydrothermal alteration and are partly transformed to REE-rich clinozoisite (Figure 2B). The most preserved allanites come from Krushev Dol, while in Petrovitsa the analyses show mainly clinozoisites. The Govedarnika deposit shows a mixed pattern.

Recently, Milenkov et al. (2022) distinguished magmatic and hydrothermal titanite (with ages of formation ~50 Ma and ~40 Ma, respectively) in the pegmatite from the Petrovitsa deposit. Geochemical (EPMA and LA-ICP-MS) data of titanites from Petrovitsa, Krushev Dol and Govedarnika show variable concentrations of critical elements (Figure 2C). The two titanite generations from Petrovitsa show differences in minor and trace element behavior. Compared to the magmatic type (Titanite 1) with relatively uniformly high contents of all elements, the hydrothermal type (Titanite 2) is depleted in V, Ga, Sr, Hf, Th, and REE, and has generally higher but more variable contents of Y, Nb, Ta and U. The sum of REE is twice higher in the magmatic titanites. Samples from Krushev Dol show the highest concentrations of most of the studied elements. In contrary, most of the lowest contents are present in titanite crystals at Govedarnika.

Chondrite-normalized REE patterns from both allanite and titanite are shown in Figure 2D.

The Petrovitsa magmatic titanite (Titanite 1) has a narrow spread of Σ(REE) with light rare-earth elements (LREE)-enriched pattern whereas the Petrovitsa Titanite 2 and the analyses from Krushev Dol show the opposite trend - wider Σ(REE) spread and flat to heavy rare-earth elements (HREE)-enriched pattern. The pattern of titanites from Govedarnika deposit is flatten but the REE concentrations are very low. Negative Eu anomaly is observed in both titanites from Petrovitsa whereas those from Krushev Dol and Govedarnika show a positive one. The REE_{CN} patterns of allanite from the three studied deposits are strongly LREE-enriched with negative Eu anomaly and minor differences in pattern slope; the highest La_{CN}/Lu_{CN} is present in allanite from Krushev Dol whereas the lowest in allanite from Govedarnika (Figure 2D).

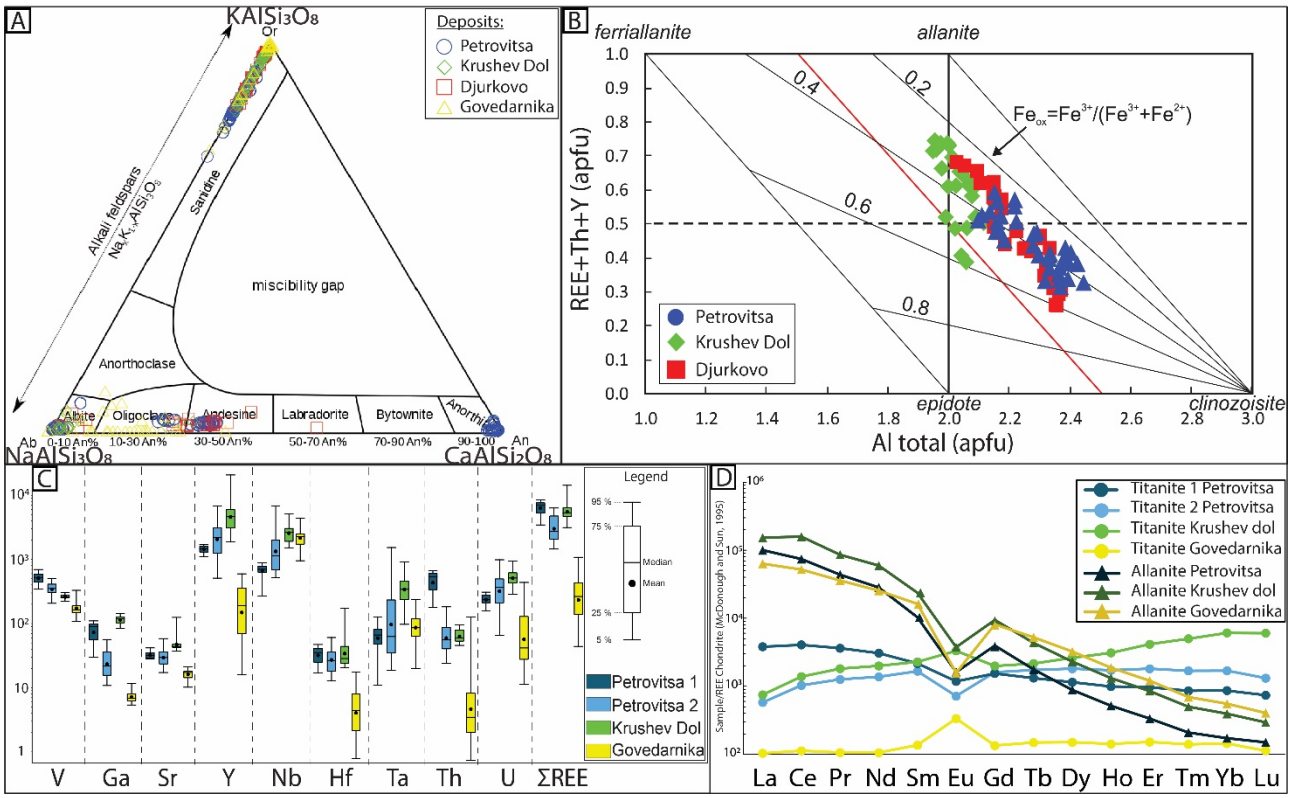

Figure 2. Comparison between the concentrations of studied minerals from different deposits: A) Feldspar compositions in apfu (atoms per formula unit); B) Composition of epidote-group minerals represented on the classification diagram REE+Th+Y vs. Al (Petrík et al. 1995); C) Minor and trace-element concentrations within the titanites in ppm; D) Chondrite-normalized REE patterns.

5 Discussion and conclusions

Macroscopically, the studied pegmatite bodies from the Madan and Laki outcrops do not show significant differences. They are all very similar in terms of size, shape and position relative to host rocks and structures. However, geochemical signatures of their main and accessory minerals vary significantly among the different localities. The differences mainly arise from the influence of the Ca-rich (epidote-forming) alteration.

Titanite from pegmatites in the Petrovitsa deposit occurs in magmatic (Titanite 1) and hydrothermal (Titanite 2) generations distinguished by their Th/U and LREE/HREE ratios, sum of REE, Eu-anomaly, and age of formation (Milenkov et al. 2022). The new titanite data from the Krushev Dol and Govedarnika deposits allow comparison of titanite geochemistry in pegmatites from the three deposits. Almost all the studied titanite crystals from Govedarnika have very low contents of trace elements. In addition, the Th/U ratio below 0.3 and positive Eu anomaly

are indicative of a metamorphic origin for the studied mineral (Scibiorski et al. 2019). In contrast, titanite from Krushev Dol shows very high minor and trace element contents and REE patterns similar to those of Titanite 2. Other features (Th/U ratio, HREE>LREE, positive Eu anomaly) also indicate more hydrothermal influence rather than magmatic (Milenkov et al. 2022), but a possible mixture of both as an overlapping process can be considered as well.

Composition of the epidote-supergroup minerals (allanite-clinozoisite) varies among and within the individual localities. According to the recommended nomenclature of epidote-group minerals by Armbruster et al. (2006), the approved chemical criterion to assign minerals to the allanite subgroup is REE + Th + U > 0.5 apfu. This condition is fulfilled by most of the analyses from Krushev Dol with minor REE-rich epidote only. Compositions from Petrovitsa mostly represent only REE-rich clinozoisite whereas values from Djurkovo fall both in allanite and REE-rich clinozoisite fields. This indicates the advanced hydrothermal alteration on the pegmatites in Petrovitsa. At all localities, the influx of multiphase hydrothermal events partly or entirely transformed allanite to REE-rich epidote-clinozoisite, causing remobilization of REE in secondary minerals (Georgieva et al. 2022). The interaction between allanite and oxidized fluids caused considerable REE leaching from the mineral. The presumable limited mobility of these elements in fluids prevents their significant transport, therefore they are incorporated in closely crystalized epidote-clinozoisite. Besides allanite and titanite, also thorite, REE-fluorcarbonates, apatite, monazite and zircon from the studied pegmatite localities concentrate REE.

Pegmatite bodies located in the Middle Allochtone of the Rhodopean metamorphic complex show different geochemical characteristics mainly controlled by the hydrothermal alterations overprinting them. The bodies in the Petrovitsa deposit (Madan district) are the most altered, which may support the work of Hantsche et al. (2021) suggesting that the magmatic source for the Pb-Zn mineralization is closest exactly to this deposit. As the pegmatite bodies pre-date formation of the Pb-Zn mineralization, the hydrothermal fluids had a significant influence on them. The other deposit from the Madan district, Krushev Dol, features less alterations in pegmatite, which may indicate lower interaction between fluids and pegmatites and/or more distal magmatic source. The pegmatite bodies located in Govedarnika deposit (Laki district) have experienced high metamorphism and deformation, and it can be assumed that they have been metamorphosed. The major element compositions in minerals from Djurkovo (Laki district) are intermediate between the other studied deposits. Further analysis on this deposit will be obtained in order to clarify its origin, stages of alteration and deformation.

Acknowledgements

The study is financially supported by the Bulgarian National Science Fund: projects KP-06-N34/4 and KP-06-DO02/2. Part of the EPMA results are financed by the ERA-MIN3 PEGMAT project.

References

Armbruster T, Bonazzi P, Akasaka M, Bermanec V, Chopin C, Giere R, Heuss-Assbichler S, Liebscher A, Menchetti S, Pan Gier´e R, Heuss-Assbichler S, Liebscher A, Menchetti S, Pan Y, Pasero M (2006) Recommended nomenclature of epidote-group minerals. European Journal of Mineralogy 18(5):551–567.

Černý P, Ercit TS (2005) The classification of granitic pegmatites revisited. Can. Mineral. 43: 2005–2026.

Georgieva S, Vassileva R, Milenkov G, Stefanova E (2022) Major and trace element signature of epidote-group minerals in altered pegmatites from the Petrovitsa Pb-Zn deposit of the Madan ore region, Central Rhodopes, Bulgaria: Evidence of allanite/epidote transformation. Geologica Carp 73(4): 365–380.

Hantsche AL, Kouzmanov K, Dini A, Vassileva R, Guillong M, von Quadt A, (2017) U-Pb age constraints on skarn formation in the Madan Pb-Zn district, Bulgaria: zircon evidence from Tertiary magmatism. 15th Swiss Geoscience Meeting, Abstract volume, 124–125.

Hantsche AL, Kouzmanov K, Milenkov G, Vassileva RD, Vezzoni S, Dini A, Sheldrake T, Laurent O, Guillong M (2021) Metasomatism and cyclic skarn growth along lithological contacts: physical and geochemical evidence from a distal Pb-Zn skarn. Lithos 400-401 (3): 106408.

Ivanov I (1991) Granite Pegmatites in Bulgaria. Publishing House of the Bulgarian Academy of Sciences, Sofia. (In Bulgarian with English abstract), 204 p.

Jahn-Awe S, Pleuger J, Frei D, Georgiev N, Froitzheim N, Nagel T (2012) Time constraints for low-angle shear zones in the Central Rhodopes (Bulgaria) and their significance for the exhumation of high-pressure rocks. International Journal of Earth Sciences 101, 1971–2004.

Kaiser-Rohrmeier M, von Quadt A, Driesner T, Heinrich, CA, Handler R, Ovtcharova M, Ivanov Z, Petrov P, Sarov ST, Peytcheva I (2013) Post-orogenic extension and hydrothermal ore formation: high-precision geochronology of the central Rhodopian metamorphic core complex (Bulgaria-Greece). Econ Geol 108(4):691–718.

Kaiser-Rohrmeier M, Handler R, von Quadt A, Heinrich C (2004) Hydrothermal Pb-Zn ore formation in the central Rhodopian dome, South Bulgaria: review and new time constraints from Ar-Ar geochronology. Swiss Bulletin of Mineralogy and Petrology 84 (1): 37–58.

Milenkov G, Vassileva R, Georgieva S, Grozdev V, Peytcheva I (2022) Trace-element signatures and U-Pb geochronology of magmatic and hydrothermal titanites from the Petrovitsa Pb-Zn deposit, Madan region, Central Rhodopes (Bulgaria). Geologica Balc 51(2): 79–91.

Petrík I, Broska I, Lipka J, Siman P (1995) Granitoid Allanite-(Ce): Substitution Relations, Redox Conditions and REE Distributions (On an Example Of I-Type Granitoids, Western Carpathians, Slovakia). Geologica Carpathica 46, 79–94.

Scibiorski E, Kirkland CL, Kemp AIS, Tohver E, Evans NJ (2019) Trace elements in titanite: A potential tool to constrain polygenetic growth processes and timing. Chem Geol 509: 1–19.

Vassileva RD, Atanassova R, Bonev IK (2009) A review of the morphological varieties of the ore bodies in the Madan Pb-Zn deposits, Central Rhodopes, Bulgaria. Geochem Mineral Petrol 47:31-49.

Regional rock geochemistry of granites and elvans in SW England: delineation of composite intrusions and Sn-Li potential

Charles J. Moon[1,3], Beth Simons[2,3] , Nick P. J. Harper[4], Frederick A. Jackson[5], Robin K. Shail[3] and Chris M. Yeomans[5]

[1]Moon Geology, Rose Cottage, Calstock,,Cornwall, UK cjm@moongeology.co.uk
[2]Park an Fenten, St Agnes, Cornwall
[3]Camborne School of Mines, University of Exeter, Penryn, Cornwall
[4]Deep Digital Cornwall, Camborne School of Mines, University of Exeter, Penryn, Cornwall
[5]Cornish Lithium Ltd, Tremough Innovation Centre, Penryn, Cornwall

Abstract. Comprehensive major and trace element suites were determined on elvans from SW England. Results were combined with F, B and Cl on previously reported non-mineralised granite samples in a search for vectors to mineralisation. PCA and machine learning confirmed the classification of granites into 5 groups mainly based on trace elements. Lithium enrichment in granites (and potential) is strongly correlated with F, both in G4/5 groups (Li-mica, topaz) as well as, more weakly, in G2 (muscovite) granites, which host greisen Sn-W deposits. There is also correlation of F with W and Ta, in G4/5 although only disseminated Sn-W mineralisation is known. Boron is enriched in G2 and G5 but most strongly in G4. There is no enrichment of background granites in Sn.

The elvans are related to both G1/G2 and G4/G5 granites, based largely on Nb/Zr ratios, although Ni and REE indicate intrusion of some may have been driven by lamprophyres. Several of the G1/G2 ungreisened elvans are strongly enriched in Sn. In contrast some G4/G5 elvans (ongonites) are enriched in Li-Ta-Sn-F and are geochemically similar to aplite/ pegmatites. The chemistry of elvans is proposed to indicate the location of subsurface mineralising processes, and hence potential.

1 Introduction

Granites are known to host and be genetically linked to the formation of tin and lithium deposits in SW England (Alderton 1993). Elvan (quartz-porphyry/ rhyolite) dykes (1-10 m thick, up to 2 km long) are closely linked, spatially and temporally to Sn-base metal veins but are slightly younger than comparable granites. The composite nature and detailed systematic geochemistry are less well known for both granites and elvans

This study details an extension of earlier studies of the 75 background granites that established components using XRF/ ICP geochemistry and textures (Simons et al 2016, 2017) by analysing their samples for F, Cl and B as well as collecting and determining trace and major elements for 151 elvan samples. This latter study is the first comprehensive geochemical study of the elvans. It builds on earlier elvan studies notably of Henley 1972 and Antipin et al. 2002.

2 Analytical Methods

The granite samples of Simons et al. were originally analysed by a combination of XRF and 4 acid ICP-MS. These have been further analyzed for F, Cl and B by ion chromatography and ICP-MS by ALS in Ireland and Vancouver. Elvan samples were mainly analysed for majors and trace elements at ALS by a combination of fusion ICP-ES/MS as well as 4 acid and aqua regia ICP-MS; F was determined by fusion ion chromatography.

3 Granites

Early Permian granites were intruded into Devonian and Carboniferous sediments. They were subdivided into 5 groups (G1-G5) based on their textures and major as well as trace element chemistries by Simons et al 2016. These correspond to older (c. 290-282 Ma) and younger granites of the geochronological studies of Chen et al. (1993) and Chesley et al. (1993).

Mineralisation consists of vein Sn-W-Cu, sheeted- vein Sn-W and later crosscutting Pb-Zn-F veins. Sn-Cu veins are often zoned or telescoped. The timing of emplacement of Sn-Cu veins has been much debated but appear slightly later than G2 granites with crosscutting Cu-rich veins younger than Sn veins in the same area. Lithium targets are bulk mineable Li-enriched micas, mainly zinnwaldite, and limited petalite or amblygonite in aplites and pegmatites. Current hard rock Li targets are all in G4/5 granites.

This study shows lithium enrichment in granites is strongly correlated with F both in the G4/5 granites (Li-mica, tourmaline/ topaz) as well as more weakly in G2 (muscovite) granites (Figure1). The latter are the main host to greisen Sn-W deposits. Enrichment of F in the G4/5 correlates with distinct Ta and weak W enrichment but not Sn. Boron is enriched in G2 and G5 granites but most strongly in the G4 granites, reflecting their mappable tourmaline. Disseminated Sn-W mineralisation is known from G4/5 granites. Chlorine is low in G1-G2 granites as well as greisens but high in G3-G5 granites.

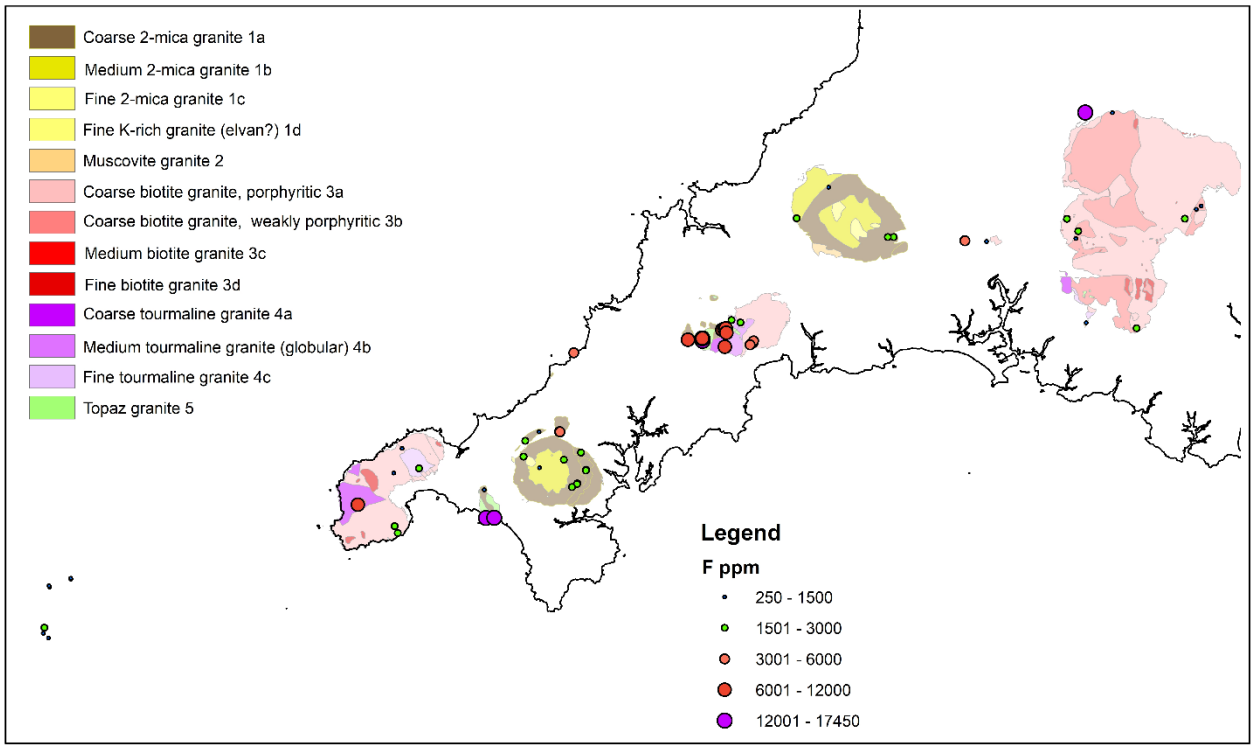

Figure 1. Fluorine in granites, n=75

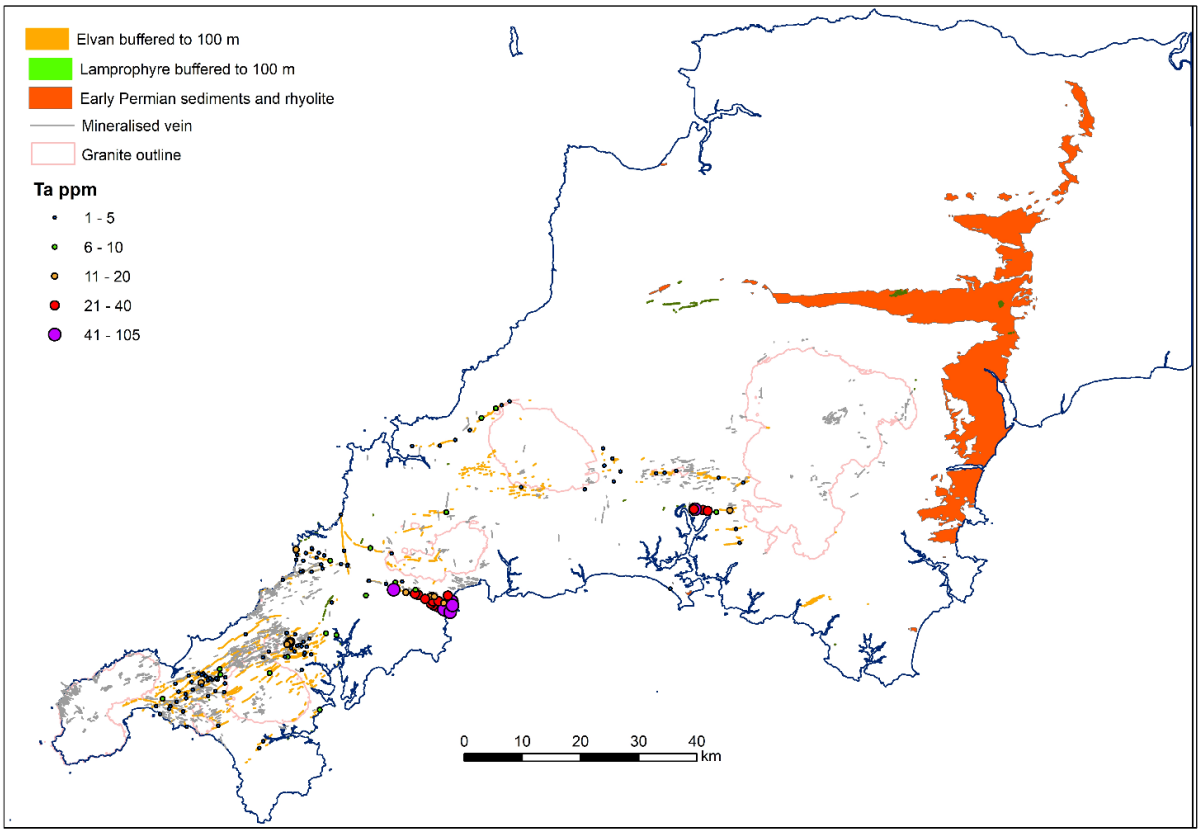

Figure 2. Tantalum in elvans, fusion ICP-MS, n=151.

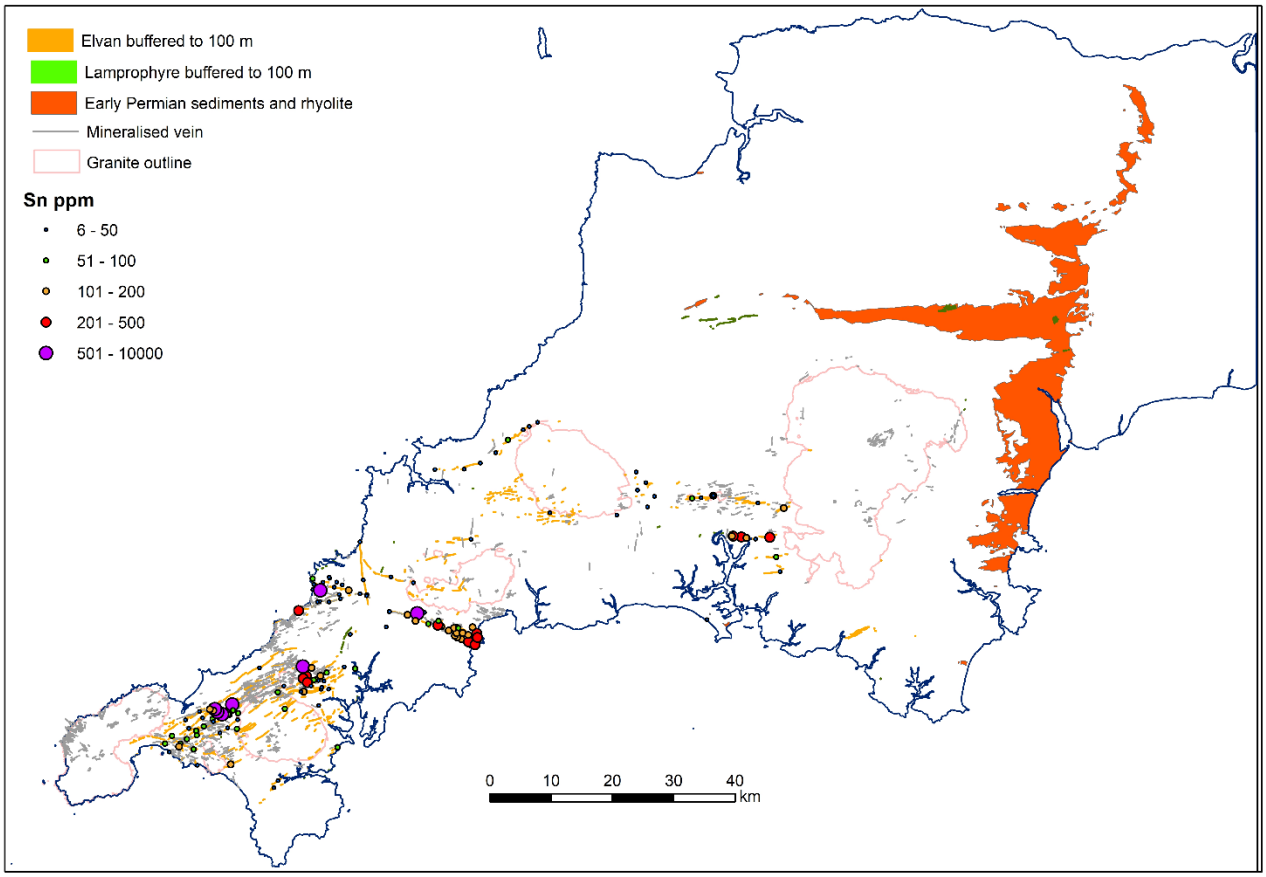

Figure 3. Tin in elvans, fusion ICP-MS. N=151. Top cut at 10000 ppm Sn

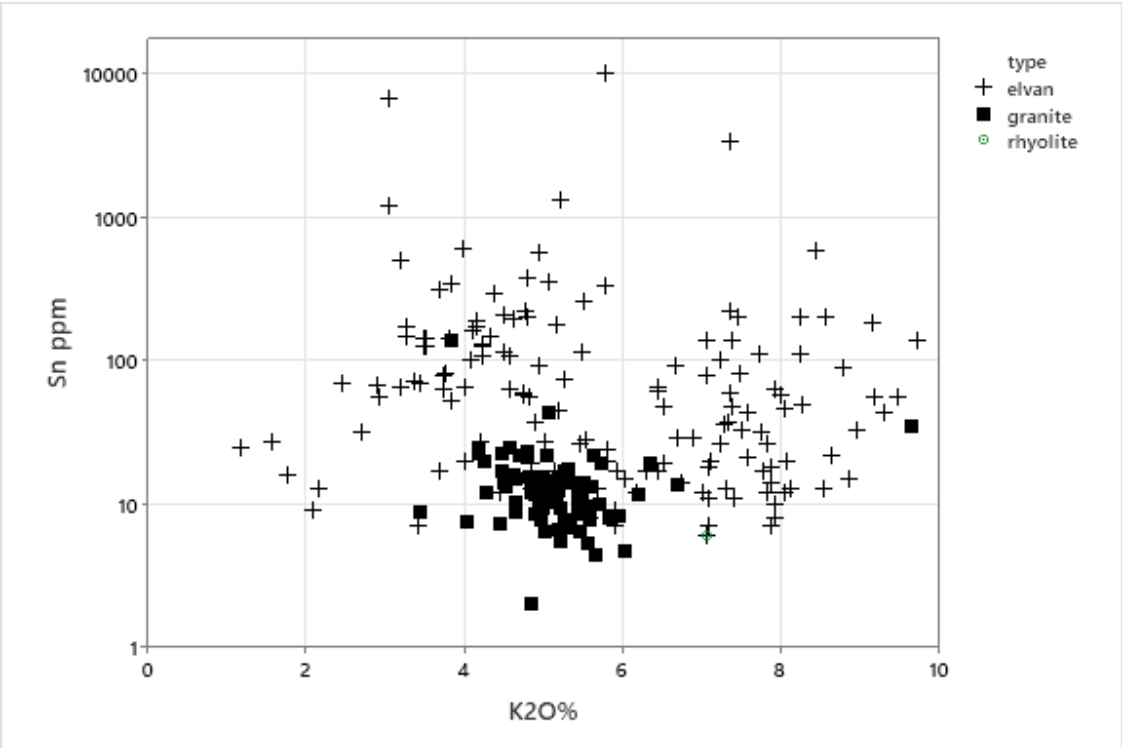

Figure 4. Scattergram Sn ppm vs K_2O%. Note distinct bimodal K_2O distribution.

The granite dataset has been subject to multivariate (Principal Component Analysis/ Clustering) and machine learning analysis. This confirms the classification of Simons et al is robust and allows more detailed discrimination of individual samples. Determination of F, B and Cl aids trace element determination in this classification and improves that based on Nb/Zr used by Manning et al. 1996

Multi-element rock geochemistry locates distinct areas of Li enrichment for further work. However, there is no background enrichment in Sn and no obvious vector to Sn-bearing veins.

4 Elvans

The origin of the elvan dykes of Cornwall and Devon has been an enigma with very little work in the last 40 years due to aleration. They are clearly closely related to granite intrusions, cutting all but the latest granites, and even more closely related to mineralization (Goode 1973). The limited published analyses suggest enrichment in K_2O and derivation from G1/G2 granites (Stone 1968; Hall 1970; Henley1972).

In several areas elvans are spatially related with lamprophyres, notably near St Kew, where lamprophyre fragments are contained in elvans. What is not clear is whether lamprophyres have driven elvan intrusion or used the same structures. Lamprophyric input can be recognized through high MgO, Ni and REE in elvans. Elvans in a number of cases are also intruded in the same locations as high Zr acid intrusives of projected Devonian age. An example is the Kingsand area where intrusive elvans cut red beds and are close to interbedded rhyolite.

Plots of Nb/Zr show affinity with both G1/3, G2 and G4/5 granites of Simons et al 2016. The high Nb elvans are chemically similar to ongonites (high level F-rich intrusives) of the Trans-Baikal and Mongolia (Antipin et al. 2002; Dostal et al. 2015) and are the first reports in the UK. These ongonitic elvans are significantly enriched in Li, F, Ta, (Figure 2) resembling the Meldon Aplite in chemistry, and in Sn. Tin is also particularly enriched in low-Li elvans in the area west of Camborne where some elvans are tourmaline-rich (Figure 3).

Enrichment in K_2O (Figure 4) has been cited as essential. This study reveals it is district specific. Cationic plots after Charoy (1984), indicate sericitization probably occurs as overprints.

Variation in chemistry suggests that within districts, individual elvans were intruded over time but with differing sources. Intrusion is controlled by NW-SE faults indicating these structures tapped magmas or hydrothermal systems at depth and may reveal the location of major hydrothermal activity.

Acknowledgements

Deep Digital Cornwall funded granite F, Cl and B analyses to Moon Geology. Cornish Lithium Ltd funded much of the elvan study and Chris Harker is thanked for support. Sharon Uren at CSM analysed early samples for Ben Thompson and Luke Holroyd in MSc studies of elvans.

References

Alderton DHM (1993) Mineralization associated with the Cornubian granite batholith In: Pattrick RAD, Polya DA (eds) Mineralization in the Biritsh Isles. Chapman & Hall, pp.270-354.

Antipin VS, Halls C, Mitichkin MA, Scott P, Kuznetsov AN (2002) Elvans of Cornwall (*England*) and Southern Siberia as Subvolvanic Counterparts of Subalkalic Rare Metal Granites. Russian Geology and Geophysics 43:847-857.

Charoy B (1984) A Discussion of the Paper by Ball and Basham Petrogenesis of the Bosworgey Granitic Cusp in the SW England Tin Province and Its Implications for Ore Mineral Genesis Mineral Deposita 19: 318-319

Chen Y, Clark AH, Farrar E, Wasteneys HAHP, Hodgson MJ, Bromley AV (1993) Diachronous and independent histories of plutonism and mineralization in the Cornubian Batholith, southwest England. Journal of the Geological Society, London 150:1183-1191.

Chesley JT, Halliday AN, Snee LW, Mezger K, Shepherd TJ, Scrivener RC (1993) Thermochronology of the Cornubian Batholith in southwest England: implication for pluton emplacement and protracted hydrothermal mineralisation. Geochimica et Cosmochimica Acta 57:1817-1835.

Dostal J, Kontak DJ, Gerel O, Gregory Shellnutt J, Fayek M (2015) Cretaceous ongonites (topaz-bearing albite-rich microleucogranites) from Ongon Khairkhan, Central Mongolia: Products of extreme magmatic fractionation and pervasive metasomatic fluid: Rock interaction. Lithos 236-237:173-189. doi: 10.1016/j.lithos.2015.08.003.

Goode AJJ (1973) The mode of intrusion of the Cornish elvans. IGS Report 73/7 Her Majesty's Stationery Office, London, 8pp.

Hall A (1970) The composition of Cornish quartz-porphyry("elvan") dykes. Proceedings of the Ussher Society 2:205-208.

Henley S (1972) Petrogenesis of Quartz Porphyry Dykes in South-West England. Nature 235:95-96.

Manning DAC, Hill PI, Howe JH (1996) Primary lithological variation in the kaolinized St Austell Granite, Cornwall, England. Journal of the Geological Society 153:827-838. doi: 10.1144/gsjgs.153.6.0827.

Simons B, Shail RK, Andersen JCO (2016) The petrogenesis of the Early Permian Variscan granites of the Cornubian Batholith: Lower plate post-collisional peraluminous magmatism in the Rhenohercynian Zone of SW England. Lithos 260:76-94. doi: 10.1016/j.lithos.2016.05.010.

Simons B, Andersen JCØ, Shail RK, Jenner FE (2017) Fractionation of Li, Be, Ga, Nb, Ta, In, Sn, Sb, W and Bi in the peraluminous Early Permian Variscan granites of the Cornubian Batholith: Precursor processes to magmatic-hydrothermal mineralisation. Lithos 278-281:491-512. doi: 10.1016/j.lithos.2017.02.007.

Stone M (1968) A study of the Praa Sands elvan and its bearing on the origin of elvans. Proceedings of the Ussher Society 2:37-43.

Scheelite in the Panasqueira tungsten deposit. An example of host rock control in tungstate composition.

Fernando Noronha[1], Filipe Pinto[2], Jorge Ferreira[3]
[1]ICT-Porto Pole – Faculdade de Ciências Univ. Porto. Portugal
[2]Beralt Tin and Wolfram Portugal AS. Panasqueira. Portugal
[3]LNEG- UCTM-LAB Amieira. Portugal

Abstract Previous studies have shown that in the tungsten deposits of the Iberian Massif, the deposition of wolframite $(Fe,Mn)WO_4$ is related with modified aquo-carbonic fluids resulting from the fluid-rock interaction.
In the case of the Panasqueira deposit, the tungstate exploited is wolframite and the surrounding rocks are schists of Late Ediacaran to Early Cambrian age. The interaction of primary magmatic fluids with the surrounding schists produced modified fluids enriched in Fe and Mn necessary for wolframite deposition. This study focuses the mineral assemblage present in a vein under exploration at level 1, L1D23R6AW30, in the Barroca Grande sector. In this vein, in addition to wolframite, there is also scheelite present, a rare mineral in Panasqueira deposit. It should be noted that unlike all the veins with wolframite, this one, with scheelite, cuts a basic rock, intrusive in the schists. Scheelite is later than wolframite and occurs associated with ferromagnesian chlorites and ferromagnesian carbonates. We consider that there was a lithological control in the deposition of scheelite and that the Ca, necessary for the deposition of scheelite, resulted from the fluid-rock interaction between hydrothermal fluids and the pre-existing basic rock hosting the vein.

1 Introduction

The most important W deposits in the Iberian Peninsula, in terms of W concentrate production, are located in the Central Iberian Zone (CIZ) of the Iberian Massif. This zone forms the spine of the Iberian Variscan unit, and it is characterized by the occurrence of a very thick autochthonous formation the “Schist-Greywacke Complex” (SGC) pre-Ordovician in age (Thadeu 1951).
The Panasqueira W (Sn-Cu) deposit, located in Central Portugal, is the largest quartz-vein type deposit in the Iberian Peninsula. Wolframite is the main ore being cassiterite and chalcopyrite by-products. The production in 2021 was 908 T of wolframite, 78 T of cassiterite and 839 T of chalcopyrite concentrates per month.
This study analyses the mineralogy present in a vein recently explored in level 1 (L1D23R6AW30) in the Barroca Grande sector, where scheelite, a rare mineral in Panasqueira, is found. The occurrence of scheelite, also at level 1, (L1D23R5AW14), was reported in 1978 by Décio Thadeu, in a personal communication to Kelly and Rye (1979, pp. 1758). However, it was not the subject of any description in the works followed. It should be noted that in both cases the veins cut a pre-ore basic rock dyke.

2 Geology and mineralogy

The Panasqueira district is flanked to the Northeast by the Serra da Estrela granite pluton of Variscan age. Country rocks underlying the Panasqueira district consist of folded metasedimentary sequences, regionally metamorphosed to low grade (chlorite-sericite) during the Variscan orogeny. These sequences are mainly composed of a several thousand metre thick lower marine flyschoid series of schist and greywackes from SGC.
The schists are cut by N-S, NE-SW and NNE-SSW faults. Pre-ore and post-ore veins of intrusive basic rocks are quite frequent and cut the SGC. These rocks occur often very weathered and there are few geochemical and petrographic studies that allow the classification of these basic rocks (Thadeu 1951, 1977).
The evidence of acid magmatism only occurs at depth through a greisen dome, that corresponds to the upper part of the Panasqueira granite intrusion found in the deeper levels of the underground mine workings (Kelly and Rye 1979). The results from a recent intensive drilling campaign confirm the shallow underlying batholith composed of several granite facies (Marignac et al. 2020; Breiter et al. 2023).
The Panasqueira deposit consists of a dense swarm of sub-horizontal quartz-veins which host the wolframite mineralization. The ore-bearing veins occupy flat sets of open joints. Individual veins are from 5 to 100 cm thick (averaging 30 cm). They have a dip of about $8\text{-}10^0$ SW and frequently exhibit a structure resulting from different phases of infilling related to reopening events.
In a pioneering work Kelly and Rye (1979) described a deposition sequence with different deposition stages separated by periods of fracture and reopening episodes. Wolframite and cassiterite belongs to a first stage of mineralization, the “oxide silicate stage” (OSS), followed by the second main stage "the main sulphide stage" (MSS) (arsenopyrite, pyrite, pyrrhotite, sphalerite, chalcopyrite, stannite), and third stage “pyrrhotite alteration stage” (PAS) (pyrite, marcassite chalcopyrite, galena, Pb-Bi-Ag sulphosalts and siderite). A latter stage characterised by chlorite and a widespread carbonates deposition was also considered (LCS).
However, it should be noted that the mineralogy and mineral deposition sequence of Panasqueira are extremely complex, not only due to its great extension and, the longevity of fluid circulation systems but also to the fact the exploration of the deposit has been active for over a century. So it is practically impossible to present a complete

paragenetic picture in order to represent the entire history of the deposit.

Thus, the paragenetic sequence and mineral assemblage characteristic of each stage, proposed by Kelly and Rye (1979), were complemented by several authors namely Wimmers (1985), studying in detail the sulphides of the MSS stage and Lourenço (2002) defining three different types of mineralization, a W-Sn-Cu main mineralization, a Pb-(Zn) mineralization associated with N-S and NE-SW faults and a Sn-Cu mineralization in late fractures.

More recently, Martins et al. (2020) and Mateus et al. (2020) defined three stages roughly comparable to OSS, MSS and LCS stages of Kelly and Rye (1979) and consider a intermediary stage that marks the transition from MSS to LCS characterized by a magmatic-hydrothermal rejuvenation of the mineralizing system. Cathelineau et al. (2022) also consider OSS, MSS and LCS, but they excluded cassiterite from the OSS and consider a sub-stage characterized by the occurrence of rutile, topaz and cassiterite and a fourth stage, previous to LCS with minerals represented in previous stages, but present in geodes.

The study of the fluids associated with the main stages of mineralization led to the conclusion that the mineralizing fluids contemporary with the wolframite deposition (OSS) were aquo-carbonic (H_2O-CO_2-CH_4-N_2-NaCl) and that the fluids associated with MSS were aqueous, with a low volatile phase density and with a progressive enrichment in H_2O and CH_4 content (Kelly and Rye 1979; Bussink et al. 1984; Polya 1989; Noronha et al. 1992, Lourenço 2002 and Cathelineau et al. 2022). Later fluids from LCS were predominantly aqueous and saline of the H_2O-NaCl-($CaCl_2$) type (Lourenço, 2002).

As for the origin of the fluids, they were considered magmatic by several authors (Kelly and Rye 1979; Bussink et al. 1984; Lecumberri et al. 2017) while other pointed to the fundamental role of modified aquo-carbonic fluids in the genesis of W mineralization (Polya, 1989; Noronha et al. 1992; Cathelineau et al. 2022).

3 Methodology

Samples from the vein and from the basic rock were taken for laboratory work. They were analyzed using optical microscopy, scanning electron microscope with energy dispersive X-ray spectroscopy (SEM-EDS) and MRFX analysis.

Petrographic analysis of polished thin-sections was performed at the Faculty of Sciences of the University of Porto (FCUP), Portugal, using a stereomicroscope Zeiss Stemi SV11 Apo coupled with a Sony Cyber-Shot DSC-S75 digital camera and using a Leica DM LSP polarizing microscope, with transmitted and reflected light, coupled with a Leica camera with LAS EZ software 2.0.0.

SEM-EDS analyses were performed at the Materials Centre of the University of Porto (CEMUP), Portugal, using an FEI Quanta 400 FEG-ESEM/EDAX Genesis X4M instrument. The SEM was operated at 15 kV in high-vacuum mode, manual aperture, 5 µm beam spot size.

MRFX map analysis were carried out at the UCTM-LAB from LNEG Amieira Porto using Bruker M4 TORNADO® operating at 50kV - 600 µA - 20 µm -40 ms (pixel time),

The abbreviations used to identify the different mineral phases followed the nomenclature proposed in Whitney and Evans (2010).

4 Results and Discussion

The basic rock has a greenish-black appearance and medium to fine granularity. The petrographic study revealed a very metasomatized rock that is currently essentially formed by titanium-altered pyroxene (Ti confirmed by SEM-EDS), olivine (generally serpentinized), hornblende, actinolite, plagioclase, metallic minerals (titanomagnetite, pyrite and sphalerite), chlorite, sphene, minerals from the epidote group, apatite, biotite, leucoxene and calcite were also observed. SEM-EDS maps reveal that the whole-rock composition (in Atm%) is Fe (2.84 to 3.07), Al (4.27 to 6.00), Ca (2.67 to 5.40), C (7.67 to 8.97), Mg (1.49 to 2.82) , Na (1.69 to 1.96), Ti (0.50 to 0.86), K (0.13 to 0.16) and P (0.12 to 0.35).

The mineralized vein with an average thickness 10cm, (Figure 1A) was observed in the mine under UV-light which allowed the identification of scheelite in the central zone and the apatite in contact with the host basic rock (Figure 1B). Along the vein contacts, with the basic rock, fine selvages (1 cm) of muscovite were observed, both in the hanging wall and in the footwall, associated with apatite, small subhedral crystals of wolframite, and some arsenopyrite. In the center of the vein white quartz crystals, occurs together with some sphalerite, scheelite and abundant chlorite and carbonates.

Figure 2 shows MRFX mapping carried out in one of the collected samples where we find all the minerals observed in the vein and which allows a better visualization of the relationship between them.

Wolframite, occurs in small crystals, associated with muscovite, apatite and arsenopyrite. It is black in color and under the microscope sometimes shows dark red internal reflections. It should be noted that the crystals show variations in composition, but it is not possible to define zones characterized by enrichment in Fe or Mn. SEM-EDS semiquantitative analyzes reveal that it has an average ferberitic composition (16.6 to 18.1 Atm % Fe, 15 to 3.1 Atm % Mn and 22.5 to 24.8% W).

Scheelite occurs in crystals, which can reach 3 cm, surrounded by chlorite and siderite, making it difficult to establish its place in the deposition sequence. However, it predates calcite. SEM-EDS semi-quantitative analyzes reveal an average composition of 31.9 to 38.6% Atm% W and 21.2 to 21.7 Atm% Ca.

Chlorite occurs in dark green masses infilling the spaces between the quartz crystals which, in turn, are surrounded by a thin layer of latter muscovite. It is latter than wolframite and associated minerals

(muscovite, apatite, arsenopyrite and muscovite) sphalerite and scheelite and before Fe-Mg-Mn carbonates, dolomite and calcite (Figure 2). Under the microscope, chlorite reveals a strong pleochroism between green and yellow and a birefringence in which it exhibits anomalous blue colors. SEM-EDS semiquantitative analyzes reveal that it is a chlorite rich in Fe and Mg (11.6 to 12.6 Atm % of Fe and 6.4 to 6.9 Atm % of Mg).

After the chlorite, a yellowish carbonate in small crystals occurs that are brownish under the microscope (Figure 3). When in masses it integrates fine grains of pyrite, calcite and dolomite. SEM-EDS semiquantitative analyzes reveal that it is a Fe-Mg-Mn carbonate (16.9 to 19.5 Atm % Fe, 9.0 to 10.9 Atm % Mg and 2.5 to 3.2 Atm % of Mn) ("magnesian siderite").

Calcite and dolomite were the last minerals to be deposited in the vein.

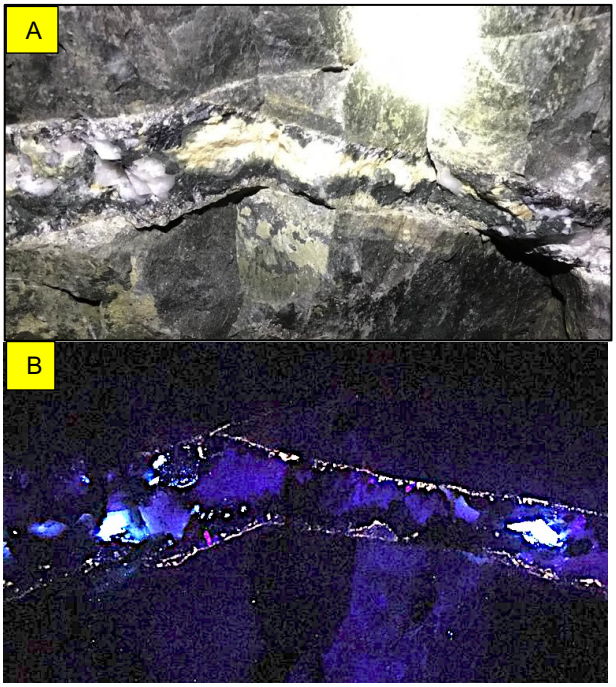

Figure 1. A **-** Subhorizontal vein mineralized with scheelite and wolframite; B – The same vein illuminated with ultraviolet light with scheelite (white) in the center and apatite (yellow) in the selvages.

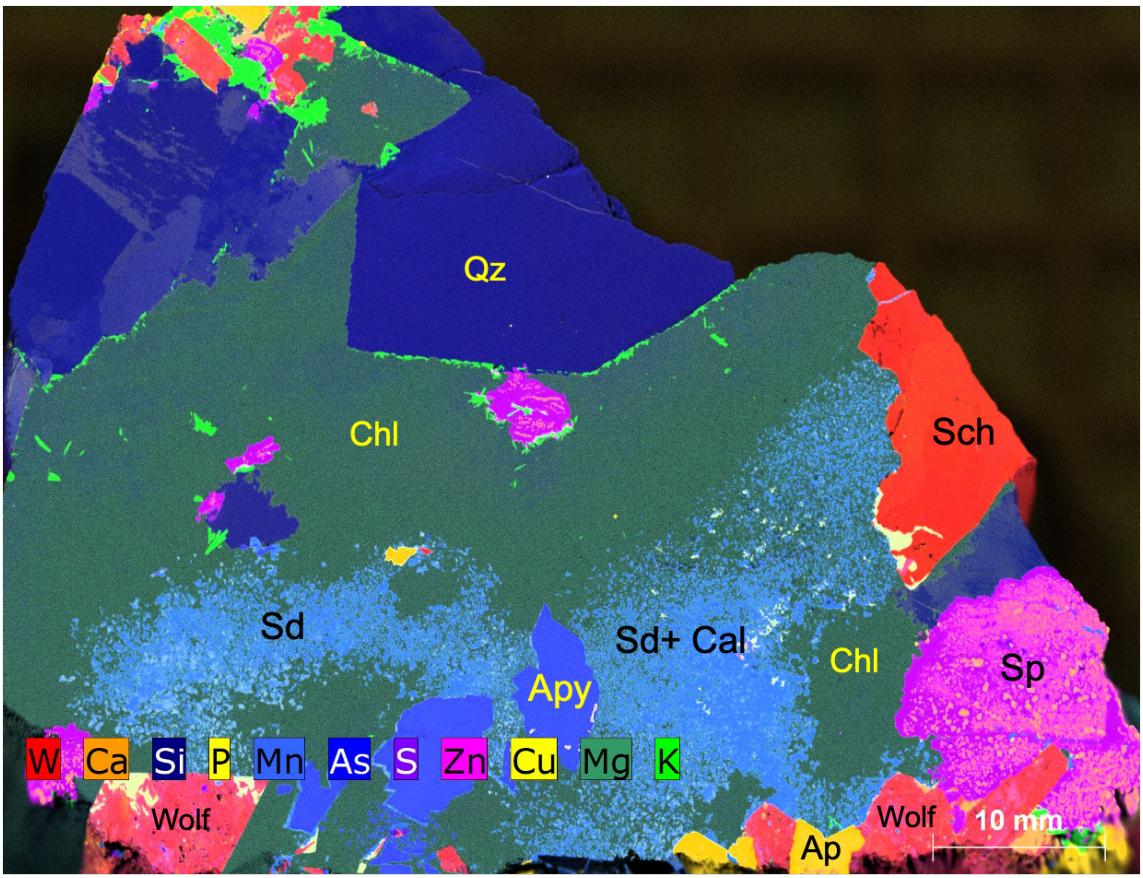

Figure 2- MRFX map from the collected sample. (Qz-quartz; Sch-scheelite; Wolf-wolframite; Chl-chlorite; Sd- "magnesian siderite"; Sp-sphalerite; Apy-arsenopyrite; Ap-apatite; Cal-calcite; Muscovite (light green)). Minerals are represented by colors that do not exactly correspond to the grid proposed for each chemical element but result from the combination of these colors. For example, scheelite (W+Ca) corresponds to a brighter red than wolframite (W+Mn+Fe).

The occurrence of chlorite was first reported by Kelly and Rye (1979). Mateus et al (2020) consider three generations of chlorite: chlorite I, the earliest and occurring at the end of the OSS; chlorite II that occurs at the end of what they consider the "rejuvenation event"; and a chlorite III already associated with a late hydrothermal activity related to the filling of fault zones.
In our study the fine-grained chlorite that occurs in masses in the vein, considering its relationship with wolframite and sphalerite and with “magnesian siderite”, corresponds to chlorite II from Mateus et al (2020). The estimated temperatures using the geothermometer of Bourdelle et al. (2013) indicate an event between 200 and 250°C corresponding to Fe, Mg-chlorite crystallization.

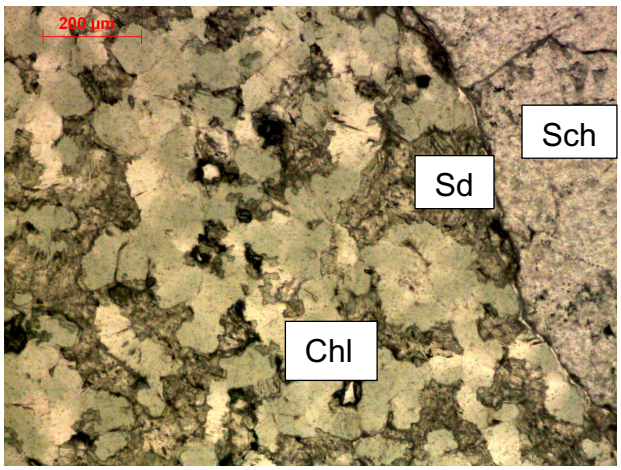

Figure 3- Scheelite (Sch) associated with chlorite (Chl) and “magnesian siderite” (Sd). Plolarized light (N//)

Lecumberri et al. (2017) demonstrated quantitatively that the Panasqueira ferberite deposited from a W bearing primary fluid that interacted with the surrounding schists contributed with the iron necessary to precipitate ferberite ($FeWO_4$). The absence of Ca in the schists does not allow the precipitation of scheelite ($CaWO_4$) which will only be deposited if the Ca-bearing fluids necessary for its deposition are supplied to the fluids carrying W.

5 Conclusions

We consider that there was a lithological control in the deposition of scheelite in the studied vein and that the Ca necessary resulted from the fluid-rock interaction between a hydrothermal fluid and the pre-existing basic rock hosting the vein.
Since chlorite and siderite are magnesiferous, we also consider that the basic rock, by interaction with the hydrothermal fluid, was the source of Fe and Mg necessary for the formation of these later minerals.

Acknowledgements

Thanks to Beralt Tin and Wolfram (Portugal, S.A.), for the realization of this work. Thanks to Prof. M.R. Machado Leite for the use of MRFX from UCTM-LAB at LNEG. This work is supported by FCT-.IP., projects UIDB/04683/2020 and UIDP/04683/2020. The comments by anonymous reviewers were appreciated.

References

Bourdelle, F., Parra, T., Chopin, C. and Beyssac, O. (2013) A new chlorite geothermometer for diagenetic to low-grade metamorphic conditions. Contributions to Mineralogy and Petrology, 165, 723–735.
Breiter K, Ďurišová J, Korbelová Z, Galiová V, Hložková M. (2023) Granite Pluton at the Panasqueira Tungsten Deposit, Portugal: Genetic Implications as Revealed from New Geochemical Data. Minerals, 13, 163 ,1-35.
Bussink R, Kreulen R & Jong A, (1984). Gas analyses, fluid inclusions and stable isotopes of the Panasqueira tungsten-tin deposits, Portugal. Bull. Minéral.,107:703-713.
Cathelineau M, Boiron M C, Marignac C, Doura M, Dejean M, Carocci E, Truche L, Pinto F (2020). High pressure and temperatures during the early stages of tungsten deposition at Panasqueira revealed by fluid inclusions in topaz. Ore Geology Reviews 126, 10374, pp 17.
Kelly WC, Rye RO (1979) Geologic, fluid inclusions and stable isotope studies of the tin-tungsten deposits of Panasqueira, Portugal. Econ. Geol. 74:1721-1822.
Lecumberri-Sanchez P, Vieira R, Heinrich CA, Pinto F, Wälle, M (2017) Fluid-rock interaction is decisive for the formation of tungsten deposits. Geology 45, 579–582.
Lourenço A, (2002) Paleofluidos e mineralizações assocadas às fases tardias da Orogenia Hercínica. Unpupblished Thesis. Porto Univ., pp. 303.
Marignac C, Cuney M, Cathelineau M, Lecomte A, Carocci E, Pinto F, (2020). The Panasqueira rare metal granite suites and their involvement in the genesis of the world-class Panasqueira W-Sn-Cu vein deposit: a petrographic, mineralogical and geochemical study. Minerals 10, 562
Martins I, Mateus A, Figueiras J, Rodrigues P, Pinto F (2020). Thermal evolution of the W-Sn(-Cu) Panasqueira ore system (Portugal): Insights from pyrite-pyrrhotite and arsenopyrite geothermometers. Comunicações Geológicas 107, Especial II, 69-74
Mateus A, Figueras J, Martins I, Rodrigues PC, Pinto F (2020). Relative abundance and compositional variation of silicates, oxides and phosphates in the W-Sn-rich lodes of the Panasqueira Mine (Portugal): implications for the ore-forming process. Minerals 10, 551.
Noronha F, Doria A, Dubessy J, Charoy B (1992) Characterization and timing of the different types of fluids present in the barren and ore-veins of the W-Sn deposit of Panasqueira, Central Portugal. Mineral. Deposita, 27:72-79.
Polya D (1989) Chemistry of the main-stage ore-forming fluids of the Panasqueira W-Cu(Ag)-Sn Deposit, Portugal: Implications for models of ore genesis. Econ. Geol., 84: 1134-1152.
Thadeu D (1951) Geologia do couto mineiro da Panasqueira. Comun. Serv. Geol. Portg. 32:5-64
Thadeu D (1977) Hercynian paragenetic units of the Portuguese part of the Hesperic Massif. Bol. Soc. Geol. Portg. 20:247-276.
Wimmers D (1985) Silver minerals of Panasqueira, Portugal: A new occurrence of Te-bearing canfieldite. Mineral.Mag. 49, 745–748.
Whitney DL, Evans BW (2010) Abbreviations for names of rock-forming minerals. Am Mineral, 2010, 95, 185-187.

Ore-forming events at the W-rich Santa Comba deposit, NW Spain

Candela Pita[1], Fernando Tornos[1], Iñigo Borrajo[1], Lluis Boixet [3], Elena Crespo[2]
[1] Geosciences Institute (IGEO, CSIC-UCM), Madrid, Spain.
[2]Complutense University of Madrid (UCM), Madrid, Spain.
[3]Rafaella Resources, Brisbane, Queensland, Australia

Abstract. The NW of the Iberian Peninsula is known to have abundant W-Sn deposits associated with peraluminous Variscan granites. The Santa Comba deposit is one of them but despite being commonly known as a quartz vein swarm with W mineralization it also contains a large disseminated mineralization hosted by a porphyritic intrusion. The mineralization is zoned around and related to an epizonal, zoned intrusive complex that includes several units whose relationships fit the Exogranite-Stockscheider-Endogranite model. Disseminated ore is enriched in wolframite but from a certain depth becomes enriched in scheelite. Our findings show that in Santa Comba there are four events of tungsten mineralization associated with three different ore-forming events with different compositions and ore-trapping mechanisms.

1 Introduction

The Santa Comba mine is located in NW Spain and is one of the largest tungsten deposits of Iberia. Aside from the historically mined vein swarm mineralization, the hosting granite has disseminated W-Sn mineralization. This mineralization is found in the youngest magmatic intrusion (endogranite) of several units that define an epizonal, zoned poly-intrusive complex of late Variscan age.

Although the relationships between the units that comprise this magmatic complex fit the Exogranite-Stockscheider-Endogranite model proposed by Nesen (1979), Santa Comba is a rather unique and poorly studied type of deposit. The disseminated mineralization seems to be related to zones of pervasive high-temperature hydrothermal alteration and stockwork-like systems, sometimes sharing features with porphyry-like deposits.

Mineralogy includes both hubnerite ($MnWO_3$) and ferberite ($FeWO_3$); they usually form zoned crystals and are commonly associated with scheelite ($CaWO_4$). Disseminated scheelite becomes increasingly important with depth but is also present concentrated in veins. The relationship between the two tungsten ores has genetic implications since scheelite and wolframite have different compositions and precipitate under different T-P-X conditions.

In this study, we explore the nature and implications of the tungsten-bearing assemblages to gain a better understanding of the ore-forming events.

2 Geology of Santa Comba

2.1 Geological setting

The Santa Comba mine is about 45 km northwest of Santiago de Compostela, Galicia, Spain. The deposit is within the Iberian Massif, in the westernmost section of the Variscan Orogen (Martínez Catalán et al. 1990). Here, a Neoproterozoic to Early Paleozoic Terrane (Central Iberian Zone) is overthrusted by rocks with oceanic affinities that belong to the Allochthonous Terrain of Galicia-Trás-os-Montes (Fig. 1).

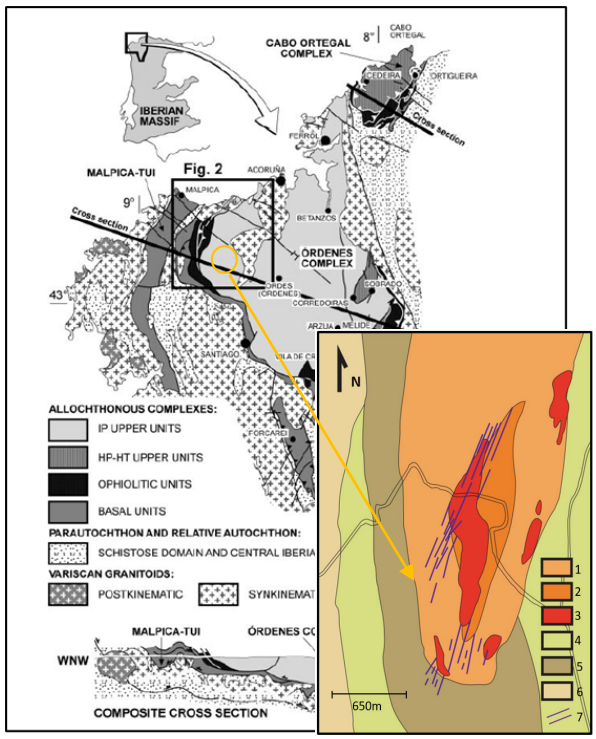

Figure 1. To the left: Map and geological section showing the three Allochthonous Complexes mentioned and their location within the Iberian Massif (modified from Abati et al. 2003). To the right: Geological map of Santa Comba (modified from Borrajo et al. 2022). 1-2: exogranite; 3: endogranite; 4: Órdenes Complex; 5: orthogneisses; 6: schists; 7: quartz veins with Sn-W.

The area includes widespread peraluminous magmatism associated with crustal thickening and later orogenic collapse related to the collision of Gondwana and Laurasia, between 330-285 My ago (Gutiérrez-Alonso et al. 2011). The mineralization and the hosting intrusion are located in a pull-apart structure formed on a major N-S dextral shear zone that bounds the contact between both Terranes.

2.2 Geology of the mineralization

The Santa Comba Plutonic Complex includes four different lithologies, all of them showing a penetrative N-S magmatic foliation. There are two

barren external units. The outer intrusion is a two-mica porphyritic granite with abundant biotite whereas the inner unit is somewhat similar but muscovite is the more prominent mica.
The youngest and most internal unit of the complex is a leucocratic equigranular granite (endogranite) with pervasive hydrothermal alteration. Apart from the absence of biotite, its most distinctive feature is the presence of a "stockscheider" that shapes the contact between the endogranite and the muscovite-rich exogranite. Nesen (1979) described this rock as consisting primarily of large, up to 10 cm long, crystals of perthitic alkaline feldspar that grow inwards to the youngest intrusion. These structures are spatially related to an alternating tourmaline-rich and albite-rich banding and probably limit a cooling carapace of the endogranite.
Due to the presence of abundant tourmaline along large areas of the endogranite, Cuenin (1982) also differentiated between common endogranite (rich in muscovite) and tourmaline-rich endogranite. In general, foliation in the tourmaline-rich facies is more diffuse.

2.3 The hydrothermal alteration of the endogranite

The endogranite shows a pervasive hydrothermal alteration that includes an early albitization of oligoclase followed by a potassic alteration with the growth of K-feldspar + muscovite and a later quartz + muscovite (phyllic) alteration. Quartz is the only residual magmatic phase; early quartz occurs as large (3-4 mm) subhedral grains with evidence of brittle-ductile deformation. Later hydrothermal quartz occurs as significantly smaller anhedral grains intergrown with muscovite. There are also two generations of muscovite. Early muscovite crystals are large and deformed while the younger muscovite grains related to the phyllic alteration are much smaller, replacing K-feldspar or intergrown with quartz.

The endogranite also includes large but scarce pods of greisen alteration of uncertain chronology. It is a coarse-grained rock including muscovite, tourmaline, quartz, and sometimes topaz. This evolution suggests that exsolved fluids accumulated below the carapace were in equilibrium with the host granite leading to potassic alteration; later cooling would drop the pH and form the phyllic alteration.

3 The mineralization

Wolframite, scheelite, and cassiterite occur both disseminated in the leucogranite and in later hydrothermal veins. The disseminated mineralization includes mm-sized, randomly located, anhedral to subhedral grains of wolframite I with less abundant cassiterite. They seem to be related to the most tourmaline-rich facies of the endogranite. Disseminated wolframite has a H/F ratio of ca. 52 and is usually associated with low-Mo scheelite (scheelite I), which becomes the predominant phase at greater depths. Both wolframite I and scheelite I can be rimmed by a micron-thick layer of wolframite II (Fig. 2).
Crosscutting the endogranite, the exogranite and the host metamorphic rocks there is an N-S trending swam of quartz veins with coarse-grained wolframite II which has a more hubneritic composition, H/F= 63 (Table 1). They are accompanied by cassiterite and only have small selvages of muscovite. Wolframite shows a widespread replacement by late, also Mo-poor, scheelite II along grain edges and cracks (Fig. 2). In the veins, scheelite II is also associated with a late hydrothermal event as large, undeformed anhedral crystals intergrown with quartz, white mica, chlorite, and sulfides (arsenopyrite, pyrite, base metal sulfides), and gold (Fig. 3). These veins are channelized along extensional brittle structures related to late NE-SW shearing.

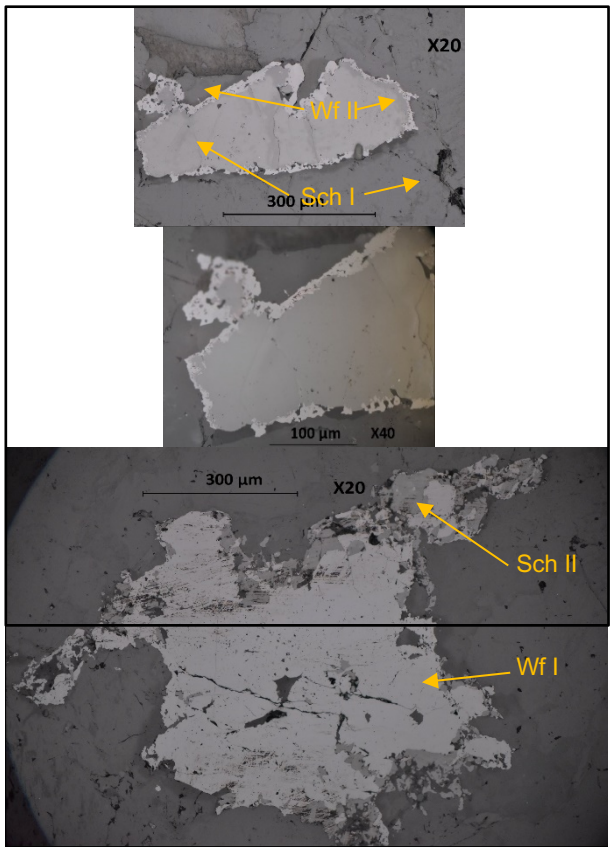

Figure 2. Microphotographs of two different wolframite-scheelite grains in the altered endogranite.

Of major interest is the presence of scheelite I, which is the dominant tungsten-bearing phase at depth in the disseminated ore and is coated by wolframite II or occurs as small inclusions in wolframite I and II. Scheelite I shows signs of deformation such as undulant extinction and fractures and hosts at least two generations of fluid inclusions (Fig. 3).

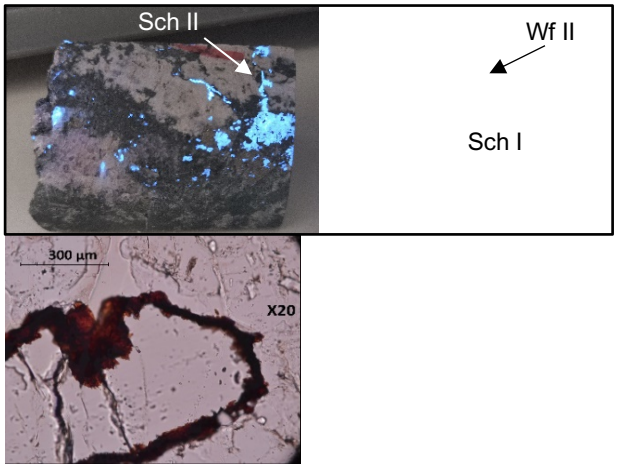

Figure 3. Scheelite-rich mineralization in the disseminated ore. Left: massive scheelite II replacing wolframite I (blue under UV light, sample 10 cm long). Right: Grain of scheelite I with an edge of wolframite II.

The temporal evolution of wolframite with an increase in the hubnerite endmember can be interpreted as related to an increase in the Mn/Fe ratio of the fluid during the later stages of the magmatic-hydrothermal evolution, matching the results of Borrajo et al. (2022). The ferberite/hubnerite ratio in the mineralization is controlled by the Fe/Mn ratio of the fluid, the K_D, and the temperature of precipitation.

	Stg 1		Stg 2	Stg 3
Element	Wf I	Sch I	Wf II	Sch II
FeO	13.34	0.02	8.29	0.17
MnO	11.77	0.00	16.13	0.15
MgO	0.00	0.00	0.00	0.00
CaO	0.02	21.09	0.15	21.27
Na_2O	0.00	0.00	0.00	0.00
K_2O	0.00	0.00	0.00	0.00
TiO_2	0.01	0.00	0.00	0.00
NiO	0.00	0.00	0.00	0.02
Nb_2O_5	0.77	0.00	0.02	0.00
MoO_3	0.07	0.02	0.03	0.05
Ta_2O_5	0.16	0.00	0.00	0.05
PbO	0.00	0.00	0.00	0.00
WO_3	72.89	77.98	74.01	78.09
SnO_2	0.02	0.00	0.02	0.00
Total	99.03	99.11	98.64	99.79

Table 1. Average compositions (wt.%) of the different generations of scheelite (Sch) and wolframite (Wf).

4 Discussion

Mineralization at Santa Comba can be grouped into three ore-forming events. Scheelite I and wolframite I would co-precipitate during the First Stage as disseminated mineralization while wolframite II would represent the Second Stage and scheelite II the Third Stage (Fig 4).

We interpret the First Stage as the precipitation of tungsten during granite replacement due to metasomatic alteration. This is done by the reaction of ascending fluids with an already consolidated carapace. The reactions involved in this process would be similar to the ones described by Pollard and Taylor (1986) but on a much larger scale (Fig. 5). The first hydrothermal fluids reacting with the endogranite cupola would induce the replacement of biotite by muscovite in the endogranite following the reaction

$$3KFe_3AlSi_3O_{10}(OH)_2 + 20HCl \rightarrow KAl_3Si_3O_{10}(OH)_2 + 6SiO_2 + 9FeCl_2 + 2KCl + 12H_2O$$

An increase in aFe^{2+}/aH^{+2} due to the destruction of biotite would promote the early precipitation of ferberite. Deeper replacement of magmatic oligoclase by albite following the reaction

$$Na_{0.8}Ca_{0.2}Al_{1.2}Si_{2.8}O_8 + 0.4Na^+ + 0.8H_4\ SiO_4 \rightarrow 1.2NaAlSi_3O_8 + 0.2Ca^{2+} + 1.6H_2\ O$$

And then the replacement of oligoclase by K-feldspar

$$Na_{0.8}Ca_{0.2}Al_{1.2}Si_{2.8}O_8 + 0.2H_4SiO_4 + 0.8H^+ + K^+ \rightarrow KAlSi_3O_8 + 0.8Na^+ + 0.2Ca^{2+} + 0.2Al^{3+} + 0.8H_2O$$

would increase aCa^{2+}/aH^{+2}, promoting the precipitation of scheelite I since, as Wood and Samson (2000) describe, the Ca/Fe ratio of a solution in equilibrium with both scheelite and ferberite decreases strongly with increasing temperature, meaning that the field of stability of scheelite expands with increasing temperature.

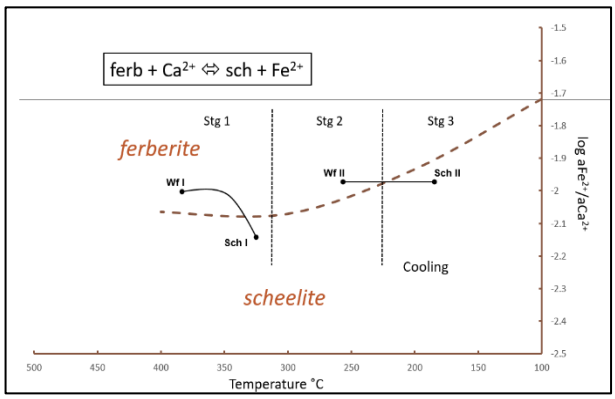

Figure 4. log aFe^{2+}/aCa^{2+} against temperature calculated from thermodynamic data of Dick (2019).

During late-hydrothermal stages, the entrance of fluids with increased Mn/Fe and Mn/Ca ratios would stabilize more Mn-rich wolframite II at the expense of scheelite and ferberite. This is consistent with the fact that evolving magmatic-hydrothermal fluids are gradually enriched in Mn due to the early precipitation of Fe-Ca-rich phases, stabilizing Mn-

bearing minerals in the very late assemblages (Burt 1977). Minor wolframite II would precipitate as hubneritic rims in both, wolframite I and scheelite I but become the main ore in the vein system. The Third stage would precipitate at lower temperatures, where scheelite is the dominant tungsten-bearing phase for a wide range of aFe^{2+}/aCa^{2+} ratios (Fig. 4).

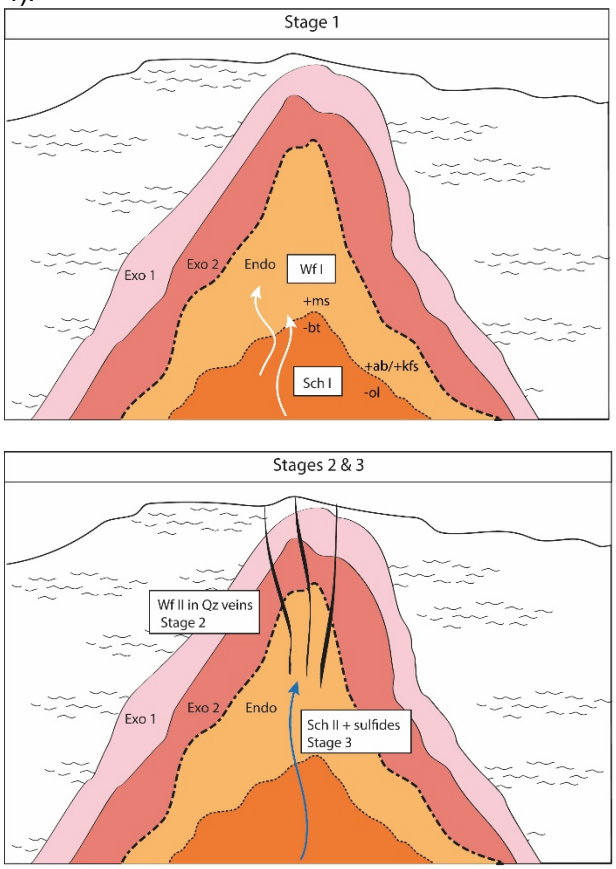

Figure 5. Diagram depicting the evolution of the endogranite during the different mineralization stages.

5 Conclusions

This preliminary study on the mineralogy of the disseminated W-Sn ore at Santa Comba suggests that hydrothermal alteration played a major role in the precipitation of tungsten-bearing minerals. Probably, the ultimate reason for the precipitation of ferberite, hubnerite, or scheelite is the availability and competition between Fe, Mn, and Ca in an evolving system. Limited availability of Fe in peraluminous granitoids, especially if hydrothermally altered, expands dramatically the stability fields of scheelite and hubnerite. In extreme cases, scheelite can be the early phase to precipitate instead the more common presence of ferberite in other more Fe-rich systems.

Acknowledgments

This study was conducted within the EIS (Exploration Information System) project of Horizon Europe (contract 101057357). This study would not have been possible without a training scholarship granted by Rafaella Resources. We would like to thank César Casquet and Pedro Granda for their support and advice.

References

Abati J, Arenas R, Martínez-Catalán JR, Díaz-García F (2003) Anticlockwise P-T path of granulites from the Monte Castelo Gabbro (Órdenes Complex, NW Spain): J Petrol 44:305-327.

Borrajo I, Tornos F, Boixet L (2022). Porphyry-like magmatic-hydrothermal W-(Sn) mineralization: Fontao and Santa Comba deposits (northwestern Spain). 22nd Biennial SGA Meeting Abstract volume.

Burt DM (1977). Mineralogy and petrology of skarn deposits. Rend Soc It Min e Pet 33:859–873.

Cuenin O (1982) Interpretation des lèvres geologiques dans la mine de Santa-Comba Galice Espagne. Disertation, University of Nancy.

Dick JM (2019) CHNOSZ: Thermodynamic calculations and diagrams for geochemistry. Front Earth Sci 7:108.

Gutiérrez-Alonso G, Fernández-Suárez J, Jeffries TE, Johnston ST, Pastor-Galán D, Murphy JB, Gonzalo JC (2011) Diachronous. post-orogenic magmatism within a developing orocline in Iberia, European Variscides. Tectonics: 30:1-17.

Martínez-Catalán JR (1990) A non-cylindrical model for the northwest Iberian allochthonous terranes and their equivalents in the Hercynian belt of Western Europe. Tectonophysics 179: 253-272.

Nesen G (1979) Les endogranites a stockscheider de Fontao et Santa Comba, Galice Espagne: un nouveau modele de gisement Sn-W en Galice. In: VI Reunión sobre la geología del NW de la Península Ibérica Oviedo 1979.

Pollard PJ, Taylor RG (1986) Progressive evolution of alteration and tin mineralization; controls by interstitial permeability and fracture-related tapping of magmatic fluid reservoirs in tin granites. Econ Geol; 81: 1795–1800.

Wood SA, Samson I (2000). The Hydrothermal Geochemistry of Tungsten in Granitoid Environments: I. Relative Solubilities of Ferberite and Scheelite as a Function of T, P, pH, and mNaCl. Econ Geol. 95: 143-182.

Major and trace element composition of the Lithium-rich Tuff from the Macusani Volcanic Field, Puno, Peru

Johan S. Ramírez-Briones[1], Lisard Torró[1], Lorenzo Tavazzani[2], Loïs Monnier[3], Oscar Laurent[3], Mariana K. Segovia-More[1], Mercy K. Sanandres-Flores[1], Jean Vallance[1], Cyril Chelle-Michou[2], Stefano Salvi[3], Patrice Baby[1,3]
[1]Geological Engineering Program, Faculty of Sciences and Engineering, Pontifical Catholic University of Peru, Peru
[2] Department of Earth Sciences, ETH Zürich, Switzerland
[3]GET-UMR CNRS/IRD/Univ. Paul Sabatier, Toulouse, France

Abstract. A major Li resource has been announced in the Falchani Lithium Project, Macusani Volcanic Field, Puno, Peru. The main Li host is the so-called Lithium-rich Tuff, in which Li values are mostly between 3,000 and 4,000 ppm. Major element compositions of Lithium-rich Tuff samples are consistent with alkali and silica leaching during feldspar hydrolysis and formation of clay (Ca-Mg-smectite in the most pervasively altered samples, and kaolinite) and zeolite minerals during hydrothermal alteration by acidic, reduced fluids rich in complexing agents such as F. The general composition of the Lithium-rich Tuff differs from that of previously reported ash-flow tuffs in the Macusani Volcanic Field. Rather, it approximates the composition of highly evolved peraluminous obsidian glasses known as 'macusanite'.

1 Introduction

The volcanogenic lithium Falchani Lithium Project hosts 60.9 Mt indicated resources grading 2,954 ppm Li and 260.1 Mt inferred resources grading 2,706 ppm Li (https://americanlithiumcorp.com/falchani-lithium-project). It is located 750 km to the northeast of the so-called *Lithium Triangle of the Andes* (López Steinmetz and Salvi 2021) (Fig. 1), which contains more than 50% of the global Li resources. The mineralization at Falchani is hosted by pyroclastic horizons of the Macusani Volcanic Field (MVF), chiefly in a unit referred to as Lithium-rich Tuff in which Li attains contents higher than 4,000 ppm (Nupen 2019). These tuffs, deposited in a lacustrine environment (Nupen 2019), are variably altered to clays and zeolites (Segovia-More et al. 2023). In this abstract, we discuss the magmatic provenance and post-depositional alteration of the Lithium-rich Tuff from a geochemical perspective.

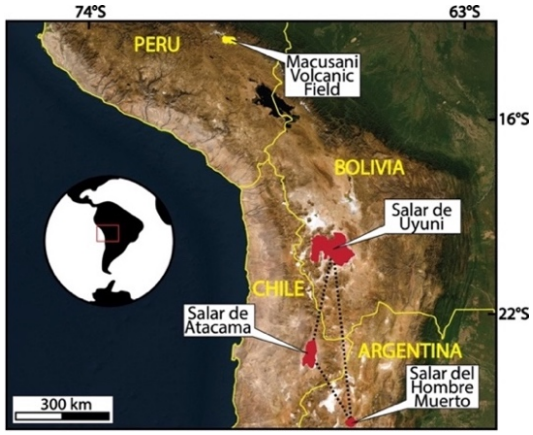

Figure 1. Location of the Macusani Volcanic Field (Peru) and the *Lithium Triangle of the Andes.*

2 Geological setting

The MVF is the northernmost Oligocene-Miocene volcanic field in the NW-trending Macusani Structural Zone (Perez et al. 2016) (formerly known as the Precordillera de Carabaya; Sandeman et al. 1997) of the southern Peruvian Eastern Cordillera. These volcanic fields rest on sialic Paleozoic basement, Triassic syn-rift continental deposits and intra-plate alkaline basalts (Mitu Group) and, to a lesser extent, pre-Oligocene marine siliciclastic rocks (Perez et al. 2016). Tertiary extrusive rocks in the Macusani Structural Zone were grouped by Sandeman et al. (1997) into the Crucero Supergroup, which exhibits two petrologically and temporally distinct suites: i) late Oligocene–early Miocene S-type rhyodacites and rhyolites, high-K calc-alkaline basalts, and shoshonites of the Picotani Group; and ii) mid- to late-Miocene, strongly peraluminous, S-type rhyolites of the Quenamari Group.

The Macusani Formation, the youngest unit of the Quenamari Group of Sandeman et al. (1997), is amply exposed in the MVF. It encompasses 250 to 450-m-thick unwelded, poorly stratified, crystal-rich, rhyolitic pyroclastic flows of ash- and lapilli-sized fragments and unusual accessory mineral phases such as sillimanite, andalusite, muscovite, and tourmaline (Cheilletz et al. 1992). Two volcanic eruptive events were dated by Cheilletz et al. (1992) at 10 $\pm$ 1 (Lower member) and 7 $\pm$ 1 Ma (Upper member). López (1996) has proposed the subdivision of the Macusani Formation (in full synonymy with 'Quenamari Formation') into 3 members: the Chacacuniza Member (equivalent to

the Lower member of Cheilletz et al. 1992), the Sapanuta Member, and the Yapamayo Member. The Lithium-rich Tuff described in the Falchani Lithium Project is stratigraphically correlated with the Sapanuta Member (Nupen 2019).

Noteworthy, the MVF first caught the interest of the geoscientific community in the 1920s due to the discovery of 'macusanite', a rhyolitic glass extremely enriched in incompatible lithophile elements (e.g., up to 3,717 ppm Li) and with an exotic mineralogy including andalusite and sillimanite phenocrysts. It was interpreted as a rare case of extreme fractionation of felsic peraluminous magmas (Pichavant et al. 1987). Its extrusion was coeval with the deposition of the Macusani Formation between ca. 8 and 4 Ma (Cheilletz et al. 1992; Pichavant et al. 1987; Poupeau et al. 1993).

3 Methodology

Twelve Lithium-rich Tuff samples from outcrops and three drill holes in Falchani Lithium Project were analyzed. Major and trace element contents were measured on fused lithium tetraborate beads. Major element compositions were determined by X-ray fluorescence (XRF) using a Bruker-S8 Tiger at PUCP, Peru. Trace elements were analyzed by laser ablation-inductively coupled plasma-mass spectrometry (LA-ICP-MS) using a 193-nm ArF Excimer laser with an ELAN 6100 DRC quadrupole mass spectrometer, at ETH in Zurich, Switzerland.

4 Results

The major composition of Lithium-rich Tuff samples comprises SiO_2 (60.4-73.9 wt.%), Al_2O_3 (14.0-20.1 wt.%), K_2O (1.3-6.8 wt.%), and Na_2O (1.3-4.6 wt.%; Fig. 2). Other elements found in minor amounts (TiO_2, FeO, MnO, MgO, CaO, and P_2O_5) add to 1.2 wt.%, on average. LOI values are higher in smectite-dominant (8.2-13.5 wt.%) samples than in kaolinite-dominant (2.0-4.4 %) samples (Fig. 2). In the TAS diagram, most samples plot in the rhyolite field (Fig. 3). However, a positive covariance between K_2O+Na_2O and SiO_2 (r = 0.8) is observed, indicating progressive depletion in alkalis and silica toward the samples most pervasively altered to smectite and zeolite. TiO_2 contents remain nearly constant and show positive correlation with Al_2O_3 (r = 0.8) reflecting residual enrichment (Fig. 4).

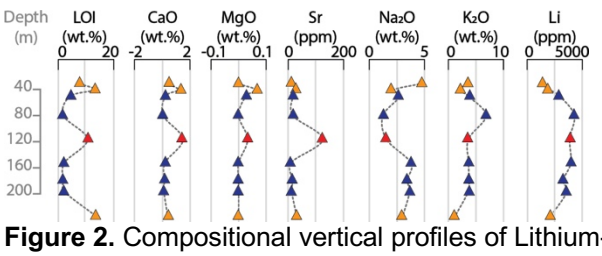

Figure 2. Compositional vertical profiles of Lithium-rich Tuff drill-hole samples. Symbols as in Fig. 3.

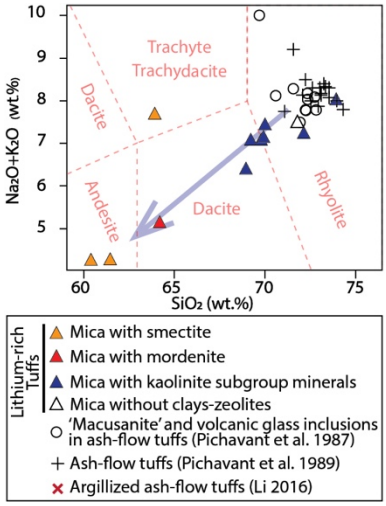

Figure 3. Na_2O+K_2O vs SiO_2 (TAS) plot of Lithium-rich Tuff samples, ash-flow tuffs, and 'macusanite'. Mineralogical groups of Lithium-rich Tuff after Segovia-More et al. (2023).

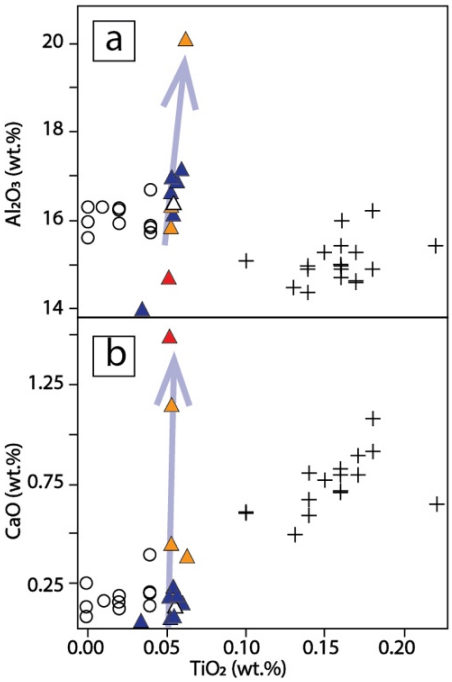

Figure 4. (a) TiO_2 vs Al_2O_3 plot and (b) TiO_2 vs CaO plot of volcanic rocks from the MVF. Symbols as in Fig. 3.

The abundances of most trace elements analyzed are normally <100 ppm. However, the contents of Cs (210-8,993 ppm), Rb (540-2,177 ppm), Sn (175-274 ppm), and Be (54-271 ppm) are conspicuously high. Total rare earth element contents (ΣREE) are in the range of 12.3 to 21.6 ppm, and of Y, in the range of 4.3 to 48.1 ppm. Chondrite-normalized (CN) REY (lanthanides + Y) patterns display negative slopes and systematic strong negative Eu anomalies $((Eu/Eu^*)_{CN}$ = 0.1-0.2; Fig. 5). Two samples exhibit a differential strong positive anomaly of Y.

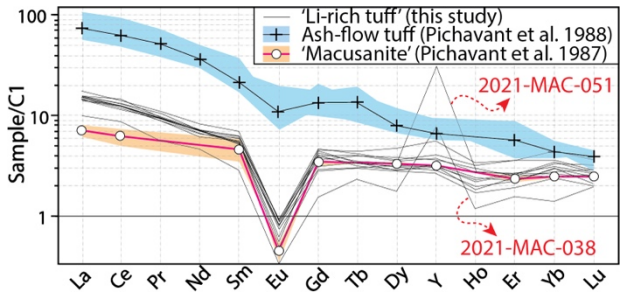

Figure 5. Chondrite-normalized REY patterns (C1 values after McDonough and Sun 1995) of Lithium-rich Tuff samples. Average (line) and upper and lower (shaded colors) values for 'macusanite' and ash-flow tuffs are shown.

5 Discussion

5.1 Magmatic source rocks

All Lithium-rich Tuff samples (except 2021-MAC-038 and 2021-MAC-051), 'macusanite' (data from Pichavant et al. 1987), and ash-flow tuffs (data from Pichavant et al. 1988) from the MVF plot in the field of strongly peraluminous (1.5-3.1 aluminum-saturation index) igneous rocks in the Zr-Al_2O_3-TiO_2 ternary diagram (Fig. 6).

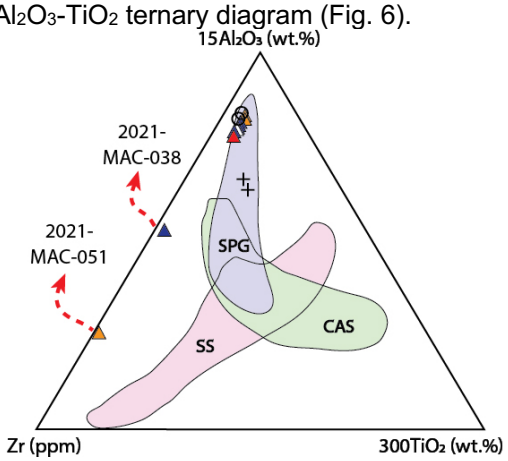

Figure 6. Composition of Lithium-rich Tuff samples, ash-flow tuffs (Pichavant et al. 1988), and 'macusanite' (Pichavant et al. 1987) in the provenance discrimination plot for weathered rocks after García et al. (1994). Symbols as in Fig. 3. Key: SPG: strongly peraluminous granite; CAS: calc-alkaline igneous suites; SS: shales and sandstones.

In general, Lithium-rich Tuff samples are closer in composition to 'macusanite' than to ash-flow tuffs except for enrichment in Be Cu, Zr, Mo, Cs, and TiO_2, and a strong depletion in V, Tl, and Pb (Fig. 7). Likewise, Lithium-rich Tuff samples generally show similar CN REY patterns as 'macusanite' except for slightly higher La/Sm values (Fig. 5). In contrast, ash-flow tuffs yield higher ΣREE, $(La/Sm)_{CN}$, and $(Sm/Yb)_{CN}$, and much lower Eu negative anomalies relative to Lithium-rich Tuff samples.

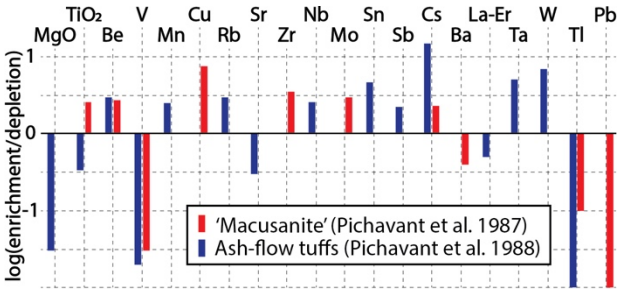

Figure 7. Enrichment/depletion patterns of average values for selected elements in Lithium-rich Tuff samples compared to ash-flow tuffs and 'macusanite'.

The fact that the Lithium-rich Tuff samples are compositionally more akin to 'macusanite' than to previously reported ash-flow tuffs could reflect a major component of highly evolved volcanic glass (equivalent or similar to 'macusanite') in this unit, previous to its alteration. Noteworthy, Torró et al. (2023) have described contrasting compositions for micas (zinnwaldite and lepidolite) hosted in the 'Li-rich tuff' relative to micas in other pyroclastic and intrusive rocks from the MVF, suggesting crystallization from a more evolved rhyolitic magma.

5.2 Geological controls on the composition of the Lithium-rich Tuff

The observed K_2O+Na_2O and SiO_2 depletion (Fig. 3) and CaO and Al_2O_3 enrichment (Fig. 4) trends in Lithium-rich Tuff samples connect the compositions of smectite-rich and kaolinite-rich tuffs and are consistent with alkali and silica leaching during feldspar hydrolysis under acidic conditions and clay formation. Higher LOI, CaO, and MgO contents accord well with a predominance of Ca(-Mg)-smectite in the most pervasively altered samples (Fig. 2). Li (2016) also documented widespread argillic alteration in ash-flow tuffs from the eastern sector of the MVF characterized by the crystallization of Ca-smectite and illite, the latter with exceptionally high F contents (7.8-8.7 wt.%). Lower $(Ce/Ce^*)_{CN}$ in Lithium-rich Tuff samples compared to the altered samples analyzed by Li (2016) (Fig. 8a) suggests alteration under more reducing conditions in the former. On the other hand, the strong positive correlation between Sr and Cs (r = 0.99) and the distinctively high contents of these two elements in the sample 2021-MAC-053 are consistent with Cs^+ and Sr^{2+} being selectively adsorbed by zeolites such as mordenite (e.g., Munthali et al. 2015).

CHARAC (i.e., CHArge-and-RAdius-Controlled; Bau 1996) behavior in geochemical systems means that elements partition is controlled by ion's charges and radii and that isovalent elements with similar radii retain their respective chondritic ratios. In the Y/Ho vs Zr/Hf diagram shown in Figure 8b, most samples plot in a narrow area outside the CHARAC field and display similar compositions as the autometasomatized topaz-zinnwaldite, alkali-

feldspar Eibenstock granite in Germany. There is a subtle compositional trend from the least altered (i.e., those with mica without clays or zeolites) through kaolinite-dominant to smectite-dominant Lithium-rich Tuff samples toward the field of hydrothermal vein fluorite (Fig. 8b). This suggests sub-solidus metasomatic reactions with fluids enriched in a variety of ligands (e.g., B, F), leading to fractionation between geochemical twin pairs – i.e., non-CHARAC behavior – due to selective molecular complexation (Bau 1996). For example, F-complexes are more stable for Y than Ho and hence would explain the higher Y/Ho in most Lithium-rich Tuff samples relative to CHARAC. Also, Zr/Hf ratios <~25 in peraluminous granites are often interpreted to reflect sub-solidus hydrothermal alteration by F-rich, acidic, reduced fluids of magmatic origin (Ballouard et al. 2016).

Finally, the samples 2021-MAC-038 and 2021-MAC-051 stand as outliers in most compositional diagrams (Figs. 6, 8). The sample 2021-MAC-038 has a relatively low LOI value (2 wt.%) and yields the lowest contents of high-field strength elements and ΣREE (Fig. 5). Since the stability of $[REE(F)_2]^-$ complexes increases from La to Lu, the observed higher $(La/Sm)_{CN}$ in this sample may reflect REE leaching by fluids distinctively enriched in F. Further, the anomalously high Zr and Y (up to 714 and 48 ppm, respectively) contents, and super-CHARAC Zr/Hf and Y/Ho ratios (up to 315 and 41, respectively; Fig. 8) in both 2021-MAC-038 and 2021-MAC-051 suggest strong metasomatic enrichment by F-rich fluids under neutral to alkaline pH (see Inguaggiato et al. 2015), in contrast to the acidic alteration conditions constrained for the rest of the Lithium-rich Tuff samples.

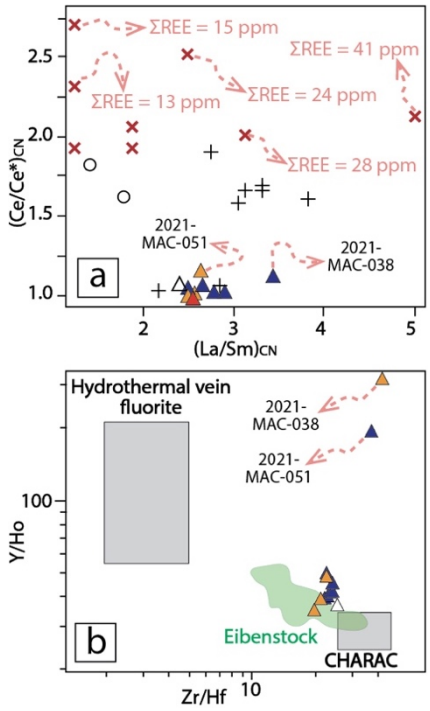

Figure 8. Trace element ratio bivariant plots of Lithium-rich Tuff, ash-flow tuffs, and 'macusanite'. (a) $(La/Sm)_{CN}$ vs $(Ce/Ce^*)_{CN}$ plot. (b) Zr/Hf vs Y/Ho plot showing fields of Eibenstock granite after Bau (1996). Symbols as in Fig. 3.

6 Conclusions

The composition of Lithium-rich Tuff samples from the MVF indicates derivation from a strongly peraluminous rhyolitic magma. Incompatible trace element compositions and CN REY patterns of Lithium-rich Tuff samples are more similar to those of 'macusanite' than to previously reported ash-flow tuffs from the MVF suggesting a higher proportion of 'macusanite'-like glass in the tuff previous to its alteration. Major element compositions reflect alkali and silica leaching during feldspar hydrolysis under acidic conditions and the formation of secondary clays (Ca-Mg-smectite in the most pervasively altered samples, and kaolinite) and zeolites. Incompatible trace element composition indicates post-depositional, metasomatic reactions with hydrothermal fluids enriched in complexing agents such as F.

Acknowledgements

We want to thank the geologists from Macusani Yellowcake for the help and hospitality during sampling tasks. This research work was supported by the Peruvian PROCIENCIA-FONDECYT project 1122-2020 E041-2020-01-01.

References

Bau M (1996) Controls on the fractionation of isovalent trace elements in magmatic and aqueous systems: evidence from Y/Ho, Zr/Hf and lanthanide tetrad effect. Contrib Mineral Petrol 123:323-333.

Ballouard C, Poujol M, Boulvais P, Branquet Y, Tartèse R, Vigneresse JL (2016) Nb-Ta fractionation in peraluminous granites: A marker of the magmatic-hydrothermal transition. Geology 44:231–234.

Cheilletz A, Clark AH, Farrar E, Arroyo Pauca G, Pichavant M, Sandeman HA (1992) Volcano-stratigraphy and $^{40}Ar/^{39}Ar$ geochronology of the Macusani ignimbrite field: monitor of the Miocene geodynamic evolution of the Andes of southeast Peru. Tectonophysics 205:307–327.

Garcia D, Fonteilles M, Moutte J (1994) Sedimentary fractionations between Al, Ti, and Zr and the genesis of strongly peraluminous granites. J Geol 102:411–422.

Inguaggiato C, Censi P, Zuddas P, Londono JM, Chacon Z, Alzate D, Brusca L, D'Alessandro W (2015) Geochemistry of REE, Zr and Hf in a wide range of pH and water composition: The Nevado del Ruiz volcano-hydrothermal system (Colombia). Chem Geol 417:125–133.

Li V (2016) The uranium mineralization of the Macusani District, southeast Peru: Mineralogy, geochemistry, geochronology and ore-genetic model. Doctoral dissertation, Queen's University. Canada.

López JC (1996) Geología del cuadrángulo de Nuñoa. Hoja 29-u. Instituto Geológico, Minero y Metalúrgico, pp 1-171.

López Steinmetz RL, Salvi S (2021) Brine grades in Andean salars: When basin size matters. A review of the Lithium Triangle. Earth Sci Rev 217:103615.

McDonough WF, Sun SS (1995) Composition of the Earth. Chem Geol 120:223-253.

Munthali NW, Johan E, Aono H, Matsue N (2015) Cs^+ and Sr^{2+} adsorption selectivity of zeolites in relation to radioactive decontamination. J Asian Ceram Soc 3:245–250.

Nupen S (2019) Mineral resource estimates for the Falchani Lithium Project in the Puno District of Peru - under the guidelines of national instrument 43-101. The Mineral Corporation, Bryanston, pp 1-72.

Perez ND, Horton BK, Carlotto V (2016) Structural inheritance and selective reactivation in the central Andes: Cenozoic deformation guided by pre-Andean structures in southern Peru. Tectonophysics 671:264–280.

Pichavant M, Valencia Herrera J, Boulmier S, Briqueu L, Joron JL, Juteau M, Marin L, Michard A, Sheppard AMF, Treuil M, Vernet M (1987) The Macusani glasses, SE Peru: evidence of chemical fractionation in peraluminous magmas. In: Mysen BO (ed) Magmatic processes, physicochemical principles. Geochem Soc Special Publ 1:359–373.

Pichavant M, Kontak DJ, Briqueu L, Valencia Herrera J, Clark AH (1988) The Miocene-Pliocene Macusani Volcanics, SE Peru - II. Geochemistry and origin of a felsic peraluminous magma. Contrib Mineral Petrol 100:325–338.

Poupeau G, Labrin E, Sabil N, Bigazzi G, Arroyo G, Vatin-Pérignon N (1993) Fission-track dating of 15 macusanite glass pebbles from the Macusani volcanic field (SE Peru). Nucl Tracks Radiat Meas 21:499–506.

Sandeman HA, Clark AH, Farrar E, Arroyo-Pauca G (1997) Lithostratigraphy, petrology and ^{40}Ar-^{39}Ar geochronology of the Crucero Supergroup, Puno Department, SE Peru. J South Am Earth Sci 10:223–245.

Segovia-More MK, Torró L, Villanova-de-Benavent C, Ramírez-Briones J, Vallance J, Monnier L, Laurent O, Salvi S, Baby P, Proenza JA, Nieto F (2023). Mineralogy of 'lithium-rich tuffs' from the Macusani Volcanic Field, Puno, Peru. This volume.

Torró L, Villanova-de-Benavent C, Monnier L, Laurent O, Segovia-More MK, Sanandres-Flores M, Ramírez-Briones J, Vallance J, Salvi S, Baby P, Proenza JA, Nieto F (2023) Lithium-bearing micas in tuffs from the Macusani Volcanic Field, Puno, Peru. This volume.

High-temperature meteoric water incursion in the Beauvoir rare-metal granite: insights from apatite

Océane Rocher[1], Julien Mercadier[1], Antonin Richard[1], Christophe Ballouard[1], Loïs Monnier[2], Oscar Laurent[2], Nordine Bouden[3], Johan Villeneuve[3], Patrick Fullenwarth[4]
[1] Université de Lorraine, CNRS, GeoRessources, Vandœuvre-lès-Nancy, France
[2] Université de Toulouse, CNRS, IRD, UPS, CNES, Géosciences Environnement Toulouse (GET), Toulouse, France
[3] Université de Lorraine, CNRS, Centre de Recherche Pétrographique et Géochimiques, Vandœuvre-lès-Nancy, France
[4] Imerys Ceramics France - Kaolins de Beauvoir, Echassières, France

Abstract. Magmatic and hydrothermal apatite generations of the Beauvoir rare-metal (Li-Ta-Nb-Sn-Be) granite (Massif Central, France) were investigated through textural observations, in-situ major elements (EPMA) and oxygen isotopic (SIMS) compositions in order to trace the origin(s) of fluids having affected the intrusion as well as their geochemical evolution. Magmatic apatite shows relatively low $\delta^{18}O$ values (~4-8 ‰) corresponding to $\delta^{18}O_{melt}$ values of ~5-10 ‰ at 550°C, i.e., lower than expected for typical peraluminous granitic melts. This could be explained either by percolation into the magma of meteoric water, or by isotopic re-equilibration of magmatic apatite during subsolidus interaction with external fluids at ~450-400°C. Furthermore, cathodoluminescence imaging reveals complex textures for hydrothermal apatite highlighting their partial recrystallisation and chemical modification with the evolution of fluid chemistry. The wide range of $\delta^{18}O$ values (-9 to +13‰) and Mn contents of hydrothermal apatite suggest a progressive mixing of reduced magmatic and oxidized meteoric fluids during metasomatism. Moreover, an interaction of greisen-related fluids with micaschist country-rocks is evidenced by relatively high $\delta^{18}O$ values and S concentration in one apatite generation. Our results support protracted oxidized meteoric fluid incursions in the Beauvoir granite, possibly from supra- to sub-solidus conditions, which may have significantly affected metal deposition processes.

1 Introduction

The Beauvoir granite (French Massif Central-FMC) is characterised by disseminated Sn-Li-Ta-Nb-Be mineralisation and represents one of the best examples worldwide of peraluminous high-phosphorus rare-metal granite (PHP-RMG; Cuney et al. 1992). Its mineralogical and geochemical evolution is closely linked to the hydrothermal system active from its crystallisation to its exhumation (Merceron et al. 1992; Cuney et al. 1992; Monnier et al. 2019). Previous fluid inclusion studies have shown the complex fluid circulations that affected the granite, in particular the mixing dynamics of magmatic and external fluids (Aïssa et al. 1987; Monnier et al. 2020), as well as hydrothermal mobility of rare metals during the magmatic-hydrothermal transition (Harlaux et al. 2017). As apatite [$Ca_5(PO_4)_3(F,OH,Cl)$] is a common accessory mineral throughout the intrusion and occurs as several generations associated to the major fluid circulation episodes, we use its geochemistry and oxygen isotope composition to trace the origin of hydrothermal fluids in the Beauvoir granite and their geochemical evolution.

2 Geological setting

The Echassières granitic complex of the northern FMC was emplaced within the internal zone of the European Variscan belt during its late-orogenic Carboniferous evolution. The complex consists of three granitic units that intruded the autochthonous micaschists of the Sioule metamorphic series: (i) the oldest La Bosse granite, concealed at depth and presumed to be at the origin of a quartz-wolframite vein system, the La Bosse stockwork; (ii) the Colettes granite, a cordierite-bearing two-mica granite; and (iii) the Beauvoir granite, an highly-evolved albite-lepidolite-topaz leucogranite hosting disseminated Sn-Li-Ta-Nb-Be mineralisation and characterised by the presence of three distinct magmatic facies (from top to bottom: B1, B2 and B3; Cuney et al. 1992).

The Beauvoir granite was emplaced at ca. 310-315 Ma (Cheilletz et al. 1992; Melleton et al. 2015) and has a complex magmatic-hydrothermal history. The intrusion, as well as the surrounding rocks, have been affected by several fluid circulation episodes, the two majors being (i) a greisenisation episode possibly triggered by the exsolution of magmatic fluids from the melt and having progressively mixed with external fluids and (ii) the late development of sub-vertical quartz veins, fluorite and low-temperature phosphate precipitation, and widespread kaolinisation (Merceron et al. 1992; Monnier et al. 2019). Greisen alteration has been particularly intense at the apical part of the Beauvoir granite but is also encountered at depth, especially at the transition zones between the three facies. It consists in the replacement of igneous minerals, essentially feldspar, by a quartz-muscovite assemblage, which is commonly associated with the precipitation of other secondary minerals, such as apatite and topaz.

3 Material and methods

Eleven samples taken from the historic drillhole GPF1 were studied. They are representative of the different generations of apatite occurring within the Beauvoir intrusion. Here, we focus on magmatic apatite encountered in the B2 and B3 facies, as

well as the distinct hydrothermal apatite generations observed in the B3 facies. The mineralogy and textural relationships were investigated using backscattered electron (BSE) and cathodoluminescence (CL) imaging, and major and minor element compositions were obtained using a Cameca SX100 electron microprobe (EMP) at GeoRessources. Oxygen isotopic composition was measured in the vicinity of EMP spots at the Centre de Recherches Pétrographiques et Géochimiques (CRPG) using a Cameca IMS 1280HR ion microprobe (SIMS). The analytical conditions were similar to those used by Decrée et al. (2020).

4 Results

4.1 Petrography

Although magmatic apatite was only described by Cuney et al. (1992) within the B2 and B3 facies, it seems to be present throughout the entire intrusive complex. Its colour varies from green to blue and it forms anhedral to sub-euhedral grains co-crystallising with magmatic topaz (Fig. 1a). It also commonly contains zircon inclusions, especially in the B2 facies. As expected for peraluminous granites, apatite shows a Mn^{2+}-activated yellow-greenish CL signal (Kempe and Götze 2002). It is characterized by a magmatic oscillatory zonation, evolving from a dark greenish to yellowish colour in the core to a relatively brighter rim, whereas altered areas have the brightest emission (Fig. 1a).

Petrographic observations revealed the existence of three hydrothermal apatite generations in the B3 facies (Fig. 2): (1) early hydrothermal, (2) greisen- and (3) late greisen-related apatite.

Early hydrothermal apatite (1) has been found in association with topaz, quartz and cassiterite within a vein (Fig. 1b). It shows a complex CL texture with dark primary areas replaced by brighter zones.

Greisen alteration is associated with a heterogeneous apatite population (2-3). *Greisen-related apatite (2)* locally forms anhedral crystals co-crystallising with a quartz-muscovite assemblage and is found as replacement of magmatic minerals such as feldspar, lepidolite or amblygonite (Fig. 1c). It has also been observed in greisen veins or greisenised zones as sub-euhedral to euhedral crystals associated with quartz ± muscovite. Wolframite has been identified in two samples and seems related to greisen alteration and apatite crystallisation. Greisen-related apatite (2) CL signature is characterised by a more greenish colour than magmatic apatite. Finally, a *late greisen-related apatite type (3)* was identified as replacement of other phosphate minerals, potentially the Ca-Be phosphate herderite, in a greisenised area from the B3 facies. It differs from greisen-related apatite (2) by a distinctive orange CL signature (Fig. 1d).

4.2 Major elements content

Magmatic and early hydrothermal (1) apatite are F-rich (3.9- 5.5 wt% and 1.9- 3.7 wt% respectively) and are, thus, fluorapatite, whereas the greisen-related apatite population (2-3) shows heterogeneous F content ranging from 1.0 to 5.2 wt% (i.e., hydroxy- to fluoro-apatite). Mn content strongly vary between apatite generations from less than 0.25 wt% in late greisen-related apatite (3) up to ~4.6 wt% in magmatic apatite.

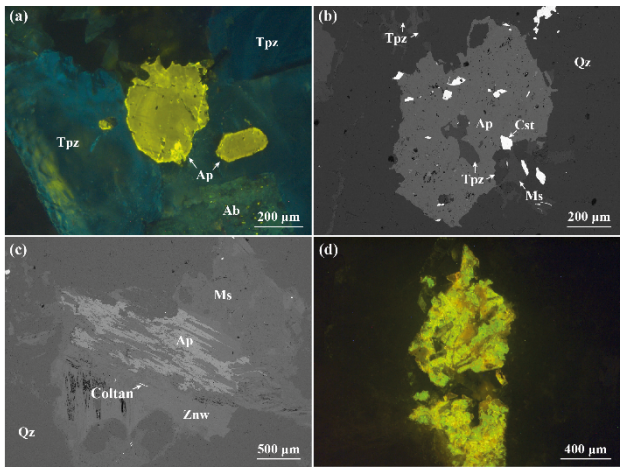

Figure 1. (a) CL image of magmatic apatite in the B2 facies; (b) BSE image of early hydrothermal apatite (1); (c) BSE image of greisen-related hydrothermal apatite (2) replacing igneous zinnwaldite (a Li-Fe-mica); (d) CL image of late greisen-related hydrothermal apatite (3). (Ab: albite, Ap: apatite, Cst: cassiterite, Ms: muscovite, Qz: quartz, Coltan: columbo-tantalite, Tpz: topaz, Znw: zinnwaldite)

4.3 Oxygen isotopic composition

The O isotopic compositions ($\delta^{18}O$) of magmatic apatite from the B2 and B3 facies range from 3.9 to 6.7 ‰ and 6.0 to 8.9 ‰, respectively. Hydrothermal apatite generations of the B3 facies show a wide range of $\delta^{18}O$ values, lying between 4.0 and 7.5 ‰ for early hydrothermal apatite (1), -8.8 and +12.6 ‰ for greisen-related apatite (2), and -7.5 and +9.2 ‰ for late greisen-related apatite (3).

5 Discussion

5.1 Incursion of meteoric water at the magmatic stage?

Oxygen isotopic composition of the melt can be estimated from $\delta^{18}O$ data obtained for magmatic apatite using the crystal-melt temperature-dependent fractionation factor of Zhao and Zheng (2003) for rhyolitic melt (Fig. 2). $\delta^{18}O_{melt}$ values calculated for a crystallisation temperature of 550°C (Cuney et al. 1992; Pichavant 2022) range from 5.0 to 8.2 ‰ and 6.4 to 10.6 ‰ for the B2 and B3 units, respectively. Such values are significantly lower than the bulk rock $\delta^{18}O$

compositions of other variscan peraluminous granites, typically above 11 ‰ when their magmatic signature is preserved (Fig. 2; Bernard-Griffiths et al. 1985; Turpin et al. 1990; Tartèse and Boulvais 2010; Ballouard et al. 2017). The ^{18}O depletion of the melt could be explained by the exchange and interaction with meteoric water at high temperatures (Taylor 1968). Previous bulk-rock or mineral O isotope studies of the Beauvoir granite have already suggested the percolation into the magma of meteoric water having previously circulated within the host micaschists (Fouillac and Rossi 1991). They observed a decrease in $\delta^{18}O$ from the deepest B3 to shallowest B1 units, interpreted as reflecting an intensification of the interactions with surface-derived waters at the apical part of the intrusion. The decrease in $\delta^{18}O$ of magmatic apatite from the B2 to B3 units is also consistent with such phenomenon (Fig. 2).

The incursion of oxidizing meteoric water in the Beauvoir granite at the magmatic stage could have key implications regarding the crystallization kinetics of ore minerals; notably, because the solubility of redox sensitive element-bearing phases such as cassiterite (SnO_2) is expected to decrease drastically in granitic melt with increasing oxygen fugacity (fO_2) (Bhalla et al. 2005; Pichavant 2022).

Such interaction at suprasolidus conditions has however been questioned by Cuney et al. (1992), on the basis of fluid inclusion data, textural observations indicating a possible re-equilibration of igneous minerals and the evidence of disequilibrium in $\delta^{18}O$ data. They proposed that the interaction of the granite with external fluids occurred at lower temperatures (450 to 400°C), resulting in the isotopic re-equilibration of igneous minerals.

From the in-situ data presented here, it is difficult to favour any of these two hypotheses, yet; as magmatic apatite grains show little alteration on CL images, an isotopic re-equilibration at hydrothermal stage cannot be confirmed. Future study of fluid inclusions trapped into apatite crystals will probably provide key information to explain their relatively low $\delta^{18}O$ values.

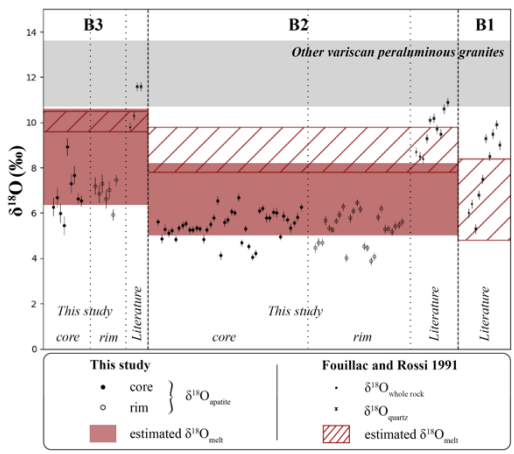

Figure 2. $\delta^{18}O$ data of magmatic apatite from the B2 and B3 facies (this study), of quartz and whole rock (Fouillac and Rossi 1991) and recalculated $\delta^{18}O$ of the melts in equilibrium using Zhao and Zheng (2003) fractionation factors and a crystallisation temperature of 550°C (Cuney et al. 1992; Pichavant 2022).

5.2 Sub-solidus evolution of the hydrothermal system

As shown for magmatic apatite, oxygen isotopic composition of the parent fluid can be estimated from $\delta^{18}O$ data of hydrothermal apatite through correction of the temperature-dependent fractionation (Fig. 3; Zheng 1996). Temperatures used derive from fluid inclusion studies. Early hydrothermal apatite (1) is presumed to have crystallised from magmatic fluids exsolved from the melts. These fluids were observed in fluid inclusions in the B1 facies and are characterised by homogenization temperatures (T_H) ranging from 370 to > 600°C (L1- and L2-fluids described by Aïssa et al. 1987 and Harlaux et al. 2017). Greisenising fluids inferred to be at the origin of hydrothermal apatite (2) resulted from the mixing between magmatic and external fluids and have been trapped into fluid inclusions of various petrographic properties and characterised by a wide range of T_H (400-190°C; Monnier et al. 2020). The petrographic heterogeneity of the greisen-related apatite population (2-3) could reflect the evolution of the magmatic-hydrothermal system over time. The late greisen-related apatite (3) could thus have crystallised from cooler greisenising fluids.

An overall decrease in $\delta^{18}O_{fluid}$ values is observed from early hydrothermal apatite (1) (3.4 to 8.0 ‰) to greisen-related (2) and late greisen-related apatite (3) (-13.9 to +12.0 ‰ and -12.6 to +8.6 ‰ respectively; Fig. 4a). This could be explained by the progressive mixing of magmatic fluids with ^{18}O-depleted external fluids which had already been outlined through the study of fluid inclusions (Aïssa et al. 1987). Negative values obtained for greisenising fluids, down to -13.9 ‰ for apatite crystallisation temperature ranging from 200 to 400°C, are characteristic of a meteoric origin.

We also observe a significant decrease in Mn concentrations of apatite, from more than 4.0 wt% for magmatic apatite to < 0.25 wt% for late greisen-related apatite (3). Mn content in apatite is dependent on magma or fluid compositions and fO_2 (Belousova et al. 2002 and references therein). Apatite preferentially incorporates Mn^{2+} over Mn^{3+} and Mn^{4+} as it directly substitutes for Ca^{2+} (Belousova et al. 2002). As previously suggested for other granite-related hydrothermal deposits from the Variscan belt (e.g., Ballouard et al. 2018), the progressive decrease of Mn content in apatite over time could thus be explained by fO_2 increase in the magmatic-hydrothermal system due to the progressive mixing with meteoric water. This is

consistent with the rough correlation between apatite Mn content and $\delta^{18}O$ values (Fig. 3).

The late greisen-related apatite generation (3) is characterised by the lowest Mn concentrations (< 0.25 wt%; Fig. 3b) and is also relatively enriched in S and Na (up to ~1.4 wt% and 1.1 wt% respectively). The strong correlation observed between S and Na content of the Beauvoir granite apatite (not shown) most likely results from the substitution scheme (SO_4^{2-} + Na^+ = PO_4^{3-} + Ca^{2+}; Pan et al. 2002). The enrichment in S could be related to a protracted circulation of the greisenising fluids within the micaschists, also leading to the isotopic equilibration of the fluids with the micaschists, explaining the relatively high $\delta^{18}O$ values obtained for this apatite type.

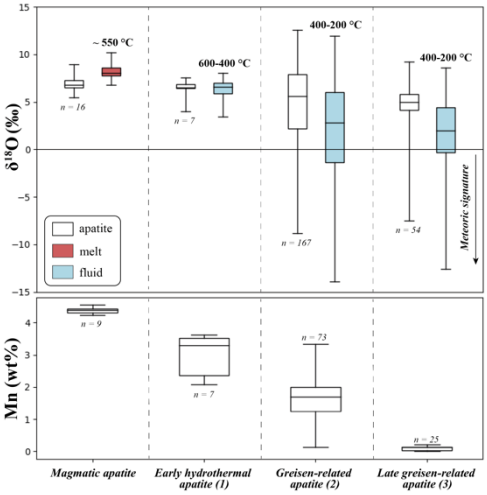

Figure 3. (a) $\delta^{18}O$ data of apatite generations from the B3 facies and recalculated $\delta^{18}O$ for the parent melt or fluid using Zhao and Zheng (2003) and Zheng (1996) equations; (b) Mn concentrations of apatite crystals.

6 Conclusion

O isotopic and major elements compositions of the distinct apatite generations identified in the Beauvoir granite suggest an early incursion of meteoric water in the hydrothermal system, possibly at the magmatic stage, as well as the progressive increase in fO_2 leading to an overall decrease in apatite Mn content. Constraining the timing of meteoric fluid incursion in the Beauvoir magmatic-hydrothermal system is crucial, as it might have major implications regarding the crystallisation mechanism of rare metal-bearing minerals in granitic magmas.

Acknowledgements

We would like to acknowledge Imerys, the LabEx RESSOURCES 21 [ANR-10-LABX-21-01] and the CNRS-INSU through its TelluS-SYSTER program for providing financial support to this study.

References

Aïssa M, Weisbrod A, Marignac C (1987) Caractéristiques chimiques et thermodynamiques des circulations hydrothermales du site d'Échassières. GPF 2-3:335-350.

Ballouard C, Poujol M, Boulvais P et al (2017) Magmatic and hydrothermal behavior of uranium in syntectonic leucogranites: The uranium mineralization associated with the Hercynian Guérande granite (Armorican Massif, France). Ore Geol Rev 80:309-331.

Ballouard C, Poujol M, Mercadier J et al (2018) Uranium metallogenesis of the peraluminous leucogranite from the Pontivy-Rostrenen magmatic complex (French Armorican Variscan belt): the result of long-term oxidized hydrothermal alteration during strike-slip deformation. Miner Depos 53:601-628.

Bhalla P, Holtz F, Linnen RL, Behrens H (2005) Solubility of cassiterite in evolved granitic melts: effect of T, fO2, and additional volatiles. Lithos 80:387-400.

Belousova EA, Griffin WL, O'Reilly SY, Fisher NI (2002) Apatite as an indicator mineral for mineral exploration: trace-element compositions and their relationship to host rock type. J Geochem Explor 76:45-69.

Bernard-Griffiths J, Peucat JJ, Sheppard S and Vidal P (1985) Petrogenesis of Hercynian leucogranites from the southern Armorican Massif: contribution of REE and isotopic (Sr, Nd, Pb and O) geochemical data to the study of source r ock characteristics and ages. Earth & Planet Sci Lett 74:235-250.

Cheilletz A, Archibald DA, Cuney M, Charoy B (1992) $^{40}Ar/^{39}Ar$ ages of the Beauvoir topaze-lepidolite leucogranite and the Chedeville sodolithic pegmatite (North French Massif Central). Petrologic and geodynamic signification. C R de Acad Sci Serie 2 315:329-336.

Cuney M, Marignac C, Weisbrod A (1992) The Beauvoir topaz-lepidolite albite granite (Massif Central, France); the disseminated magmatic Sn-Li-Ta-Nb-Be mineralization. Econ Geol 87:1766-1794.

Decrée S, Cawthorn G, Deloule E et al (2020) Unravelling the processes controlling apatite formation in the Phalaborwa Complex (South Africa) based on combined cathodoluminescence, LA-ICPMS and in-situ O and Sr isotope analyses. Contr Mineral Petrol 175:1-31.

Fouillac A, Rossi P (1991). Near-solidus delta18O depletion in a Ta-Nb-bearing albite granite; the Beauvoir Granite, France. Econ Geol 86:1704-1720.

Harlaux M, Mercadier J, Bonzi WME et al (2017) Geochemical signature of magmatic-hydrothermal fluids exsolved from the Beauvoir rare-metal granite (Massif Central, France): Insights from LA-ICPMS analysis of primary fluid inclusions. Geofluids 2017.

Kempe U and Gotze J (2002) Cathodoluminescence (CL) behaviour and crystal chemistry of apatite from rare-metal deposits. Mineral Mag 66:151-172.

Melleton J, Gloaguen E and Frei D (2015) Rare-elements (Li–Be–Ta–Sn–Nb) magmatism in the European Variscan belt, a review. Proceedings of the 13th Biennial SGA Meeting 2:24-27.

Merceron T, Vieillard P, Fouillac AM, Meunier A (1992) Hydrothermal alterations in the Echassieres granitic cupola (Massif Central, France). Contr Mineral Petrol 112:279-292.

Monnier L, Salvi S, Melleton J, et al (2019) Multiple generations of wolframite mineralization in the Echassières district (Massif Central, France). Min 9:637.

Monnier L, Salvi S, Jourdan V et al (2020) Contrasting fluid behavior during two styles of greisen alteration leading to distinct wolframite mineralizations: The Echassières district (Massif Central, France). Ore Geol Rev 124.

Pan Y, Fleet ME (2002) Compositions of the apatite-group minerals: substitution mechanisms and controlling factors. Rev in mineral and geochem 48:13-49.

Pichavant M (2022) Experimental crystallization of the Beauvoir granite as a model for the evolution of Variscan rare metal magmas. J Petrol 63.

Tartèse R and Boulvais P (2010) Differentiation of peraluminous leucogranites "en route" to the surface. Lithos 114:353-368.

Taylor HP (1968) The oxygen isotope geochemistry of igneous rocks. Contr Mineral Petrol 19:1-71.

Turpin L, Cuney M, Friedrich M et al (1990) Meta-igneous origin of Hercynian peraluminous granites in NW French Massif Central: implications for crustal history reconstructions. Contr Mineral Petrol 104:163-172.

Zhao ZF and Zheng YF (2003) Calculation of oxygen isotope fractionation in magmatic rocks. Chem Geol 193:59-80.

Zheng YF (1996) Oxygen isotope fractionations involving apatites: Application to paleotemperature determination. Chem Geol 127:177-187.

High-resolution mineralogy of Lithium-rich Tuff from the Macusani Volcanic Field, Puno, Peru

Mariana K. Segovia-More[1], Lisard Torró[1], Cristina Villanova-de-Benavent[2], Johan Ramírez-Briones[1], Jean Vallance[1], Loïs Monnier[3], Oscar Laurent[3], Stefano Salvi[3], Patrice Baby[1,3], Joaquín A. Proenza[2], Fernando Nieto[4]
[1]Geological Engineering Program, Faculty of Sciences and Engineering, Pontifical Catholic University of Peru, Peru
[2]Departament de Mineralogia, Petrologia i Geologia Aplicada, Facultat de Ciències de la Terra, Universitat de Barcelona, Spain
[3]Géosciences Environnement Toulouse, CNRS/IRD/CNES/Univ. Paul Sabatier, Toulouse, France
[4]Departamento de Mineralogía y Petrología and IACT, Universidad de Granada-CSIC, Spain

Abstract. With Li contents ranging as high as ~2,000 to 4,000 ppm, the so-called Lithium-rich Tuff in the Macusani Volcanic Field hosts the main lithium resource in the recently discovered Falchani Project in south-eastern Peru. These tuffs comprise quartz, plagioclase (albite), K-feldspar (sanidine), trioctahedral micas (zinnwaldite + lepidolite), kaolinite ± halloysite, and dioctahedral smectites, in addition to cristobalite and mordenite in a few samples. The highest Li contents (3,000-4,200 ppm Li) are found in the central portion of the Lithium-rich Tuff sequence, which is characterized by micas + kaolinite subgroup minerals ± mordenite. In the upper and lower domains of the tuff sequence, Li contents reach values of 2,000 ppm and the mineralogy is dominated by micas + dioctahedral smectite ± kaolinite ± halloysite. Lithium is contained mostly in zinnwaldite and lepidolite, and probably also adsorbed onto, or in interlayer positions in clay minerals.

1 Introduction

Lithium is a critical raw material for the development of eco-efficient energy technologies. Examples include Li-ion batteries for electric vehicles, much needed to promote the transition from fossil fuels to renewable energy sources in order to achieve EU's 2025 carbon neutrality goal (IRENA 2019; European Commission 2020). Finding new conventional (e.g., granitic pegmatites, salars) and non-conventional (e.g., volcanogenic, oilfield brines) Li resources is thus essential to cover the ever-growing demand for this metal (Bowell et al. 2020; Jowitt et al. 2021; Graham et al. 2021).

In November 2017, the discovery of a major lithium resource in the Falchani Lithium Project in the central area of the Macusani Volcanic Field, located in the Eastern Cordillera of the Andes (Puno Department) in south-eastern Peru, was announced by Macusani Yellowcake S.A.C., the Peruvian subsidiary of American Lithium Corp. As of 2023, indicated resources amount to 0.39 Mt Li_2O while inferred are 1.52 Mt Li_2O (https://americanlithiumcorp.com/ falchani-lithium-project). Lithium mineralization occurs in Neogene breccias and tuffs. Out of these, the main lithium resource, and the highest grades – mostly between 2,000 and 4,000 ppm Li – are found in the so-called Lithium-rich Tuff (The Mineral Corporation 2019).

In spite of the economic importance of this tuff, a detailed mineralogical characterization is not available to this day. In this abstract, we present new mineralogical data, with an emphasis on clay minerals, in order to discuss the mineralogical expression of lithium in the Lithium-rich Tuff and a classification of the Falchani deposit.

2 Geological setting

The unit referred to as Lithium-rich Tuff by companies exploring in south-eastern Peru belongs to the Macusani Volcanic Field (Fig. 1), a sequence of volcanic and volcano-sedimentary units mostly exposed in the Quenamari Meseta plateau, at an altitude of 4,400 m a.s.l., and is part of the Neogene ignimbrite centers of the Central Andes. The Macusani Volcanic Field is located between the Cordillera de Carabaya and the central Andean backthrust belt, and belongs to the Macusani Structural Zone (Perez et al. 2016), previously known as the Precordillera de Carabaya (Sandeman et al. 1997). It relates to tectonic shortening/crustal thickening and contemporaneous lithospheric removal/thinning (Salisbury et al. 2011; Göğüş et al. 2022).

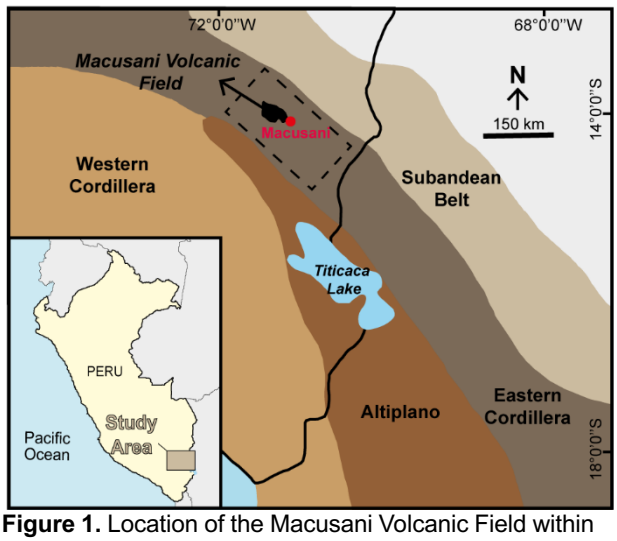

Figure 1. Location of the Macusani Volcanic Field within the geomorphotectonic map of the Central Andes.

Late Oligocene to late Miocene volcano-sedimentary sequences exposed in the Macusani Volcanic Field were grouped by Sandeman et al. (1997) under the Crucero Supergroup and subdivided into the Quenamari and Picotani groups. Rhyolitic ash-flow tuffs of the late Miocene (6.8 – 10.5 Ma) Macusani Formation, in which the

studied Lithium-rich Tuff is found, are part of the Quenamari Group. The Macusani Formation comprises whitish-grey, poorly consolidated, lapilli-crystal tuffs mineralogically consisting of quartz, sanidine, plagioclase, sillimanite, andalusite, muscovite, biotite, and tourmaline (Sandeman et al. 1997). Geochemically, they are characterized by felsic and highly peraluminous signatures, with 71.5-75 wt% SiO_2, high Al_2O_3 (normative corundum >2%), and high alkalis, with an enrichment in lithophile trace elements (e.g., Li, Be, Cs, Nb; Pichavant et al. 1988). López (1996) renamed the Macusani Formation as Quenamari Formation and proposed its subdivision, from bottom to top, into the Chacacuniza, Sapanuta and Yapamayo members. In the Falchani Project, rocks of the Sapanuta Member, including the Lithium-rich Tuff, are widely exposed (The Mineral Corporation 2019).

3 Analytical methods

Thirty-two representative samples of Lithium−rich Tuff were analysed by powder XRD using a Bruker D8 Discover diffractometer in Bragg-Brentano θ/2θ geometry of 240 mm radius, at the Centro de Caracterización de Materiales of the Pontifical Catholic University of Peru (CAM−PUCP). Seventeen mica- and clay-rich samples, eleven of which from drill core, were analysed by XRD on oriented mounts using the same equipment and setup as for powdered samples, in air dried, ethylene glycol-saturated (ETG), and heated (at 400 °C to 550 °C) preparations. Three samples were studied using a Quanta 650 FEI scanning electron microscope (SEM) equipped with an EDAX−Octane Pro Energy Dispersive Spectrometry (EDS) microanalysis system at CAM−PUCP. Three more samples were studied by Transmission Electron Microscopy (TEM), using powder specimens deposited onto formvard-covered Cu grids, to determine the mineral composition by Analytical Electron Microscopy (AEM) in the Thalos microscope of the CIC of the University of Granada, calibrated with natural standards.

4 Results

Powder XRD results show that the tuffs are mainly composed of quartz, plagioclase (probably albite), K-feldspar (probably sanidine), and mica (zinnwaldite and lepidolite; see Torró et al. 2023), with variable proportions of clay minerals (kaolinite subgroup minerals and smectites), mordenite, and cristobalite. The tuff samples can be grouped into four categories according to their prevalent mineralogy: i) mica with no zeolite nor clay minerals, ii) mica with kaolinite subgroup minerals (Fig. 2a), iii) mica with smectite (Fig. 2b), and iv) mica with mordenite.

According to oriented-mount XRD data, the clay mineral peaks with $d_{(001)}$ spacing of 12 to 15.1 Å correspond to smectite. The $d_{(001)}$ spacing expands with ETG to 16.6 to 17 Å, and contracts to ~10 Å with oven-dried treatment at 400°C and 550°C. Moreover, the clay presenting peaks with $d_{(001)}$ spacing of 7.1 to 7.2 Å at 2θ~12.3° for air dried samples corresponds to kaolinite subgroup minerals. ETG and 400° heat treatments have no effect on the diffractogram of this mineral, but the $d_{(001)}$ spacing peak was destroyed by heat treatment at 550°, which is consistent with the aforementioned subgroup.

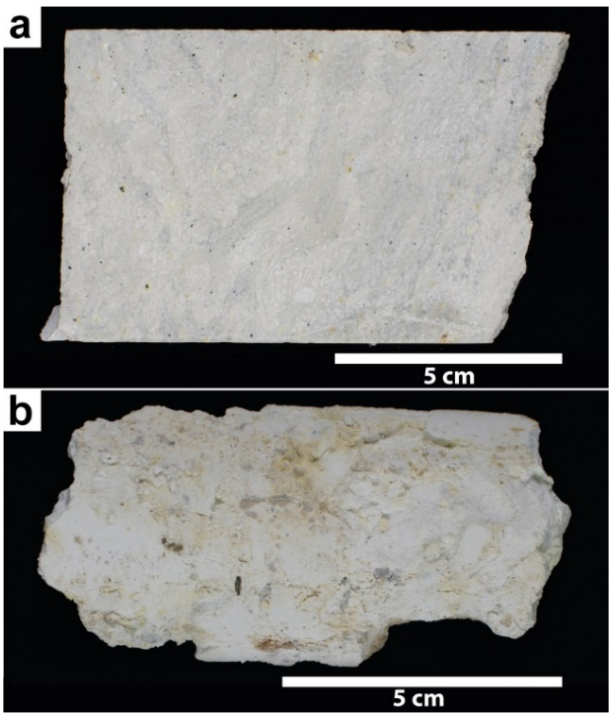

Figure 2. Lithium-rich Tuff samples from the Macusani Volcanic Field. a) 2021-MAC-040: mica (scattered black grains) with kaolinite subgroup minerals. b) 2021-MAC-051: mica with smectite.

In Figure 3, the diffractograms obtained from powder XRD analysis of drill-core samples are ordered according to their relative depth, with their corresponding lithium contents. A vertical mineral

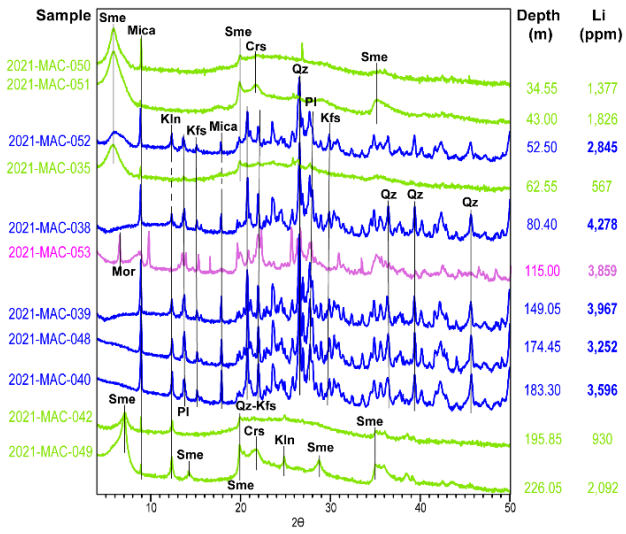

Figure 3. Drill core samples classified according to the prevalent mineralogy (color) and ordered according to their relative depth. Key: plagioclase (Pl), mica (Mica), quartz (Qz), K-feldspar (Kfs), kaolinite (Kln), smectite (Sme), cristobalite (Crs), and mordenite (Mor).

zoning comprising three main domains is observed. The upper domain presents Li contents in the range of 567 to 1,826 ppm and is dominantly composed of smectite and micas. The central domain has the highest Li contents – ranging from 2,845 to 4,278 ppm – and is dominated by micas and kaolinite. Finally, the lower domain presents Li contents between 930 and 2,092 ppm and the mineralogy consists predominantly of smectite, micas ± kaolinite.

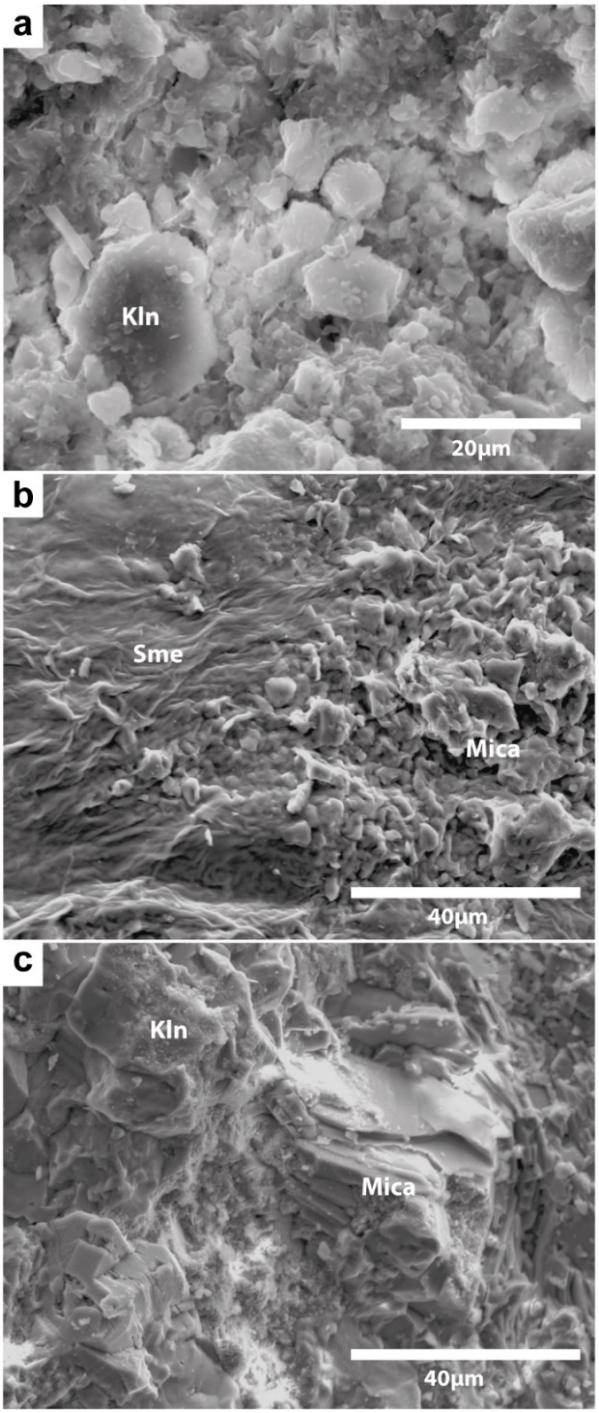

Figure 4. Secondary-electron SEM images of samples from the Lithium-rich Tuff. a) Pseudohexagonal plates of kaolinite with sheet-like masses probably corresponding to mordenite. b) Hybrid morphologies of tightly interwoven flakes characteristic of smectite and areas with scalloped edges of micas. c) Flaky grain of mica and kaolinite aggregates.

Secondary-electron SEM images of samples 2021-MAC-026, 2021-MAC-035, and 2021-MAC-039 show the morphologies of clay minerals, micas, and zeolites. In sample 2021-MAC-026, small plates of variable thicknesses are observed, most probably corresponding to kaolinite subgroup minerals, according to their pseudohexagonal morphology (Fig. 4a). In addition, some grains yield high contents of O and Si in EDS spectra, compatible with the zeolite mordenite. In sample 2021-MAC-035, tightly interwoven and wavy flakes with curved-edges are distinctive of smectite (see Keller et al. 1986), whereas mica grains show scalloped edges (Fig. 4b). SEM-EDS analyses in smectite reveal relatively high contents of Si and Al and minor proportions of Mg, Ca, and Na. Finally, in sample 2021-MAC-039, a flaky grain of mica and kaolinite subgroup minerals are observed (Fig. 4c).

The TEM study shows that the fine fraction of samples 2021-MAC-049 and 2021-MAC-050 is majorly composed of smectite (Fig. 5a) showing dioctahedral characteristics in the electron diffractions (Fig. 5b), and chemical compositions with the octahedral population approaching 2 atoms per formula unit (apfu). Iron and Mg contents are low, with some analyses showing a slight octahedral deficit. Interlayer occupancy is deficient and composed of small quantities of Na, K, and Ca. The fine fraction of sample 2021-MAC-038 contains predominantly mica and kaolinite subgroup minerals. Mica consists mostly of Si, Al, and K, with very scarce Mg and Fe, and its composition can be approximated to that of 'lepidolite'. Assumption of the normal values of Li for this type of mica brings the octahedral occupancy to values in the range of 3 apfu (see also Torró et al. 2023).

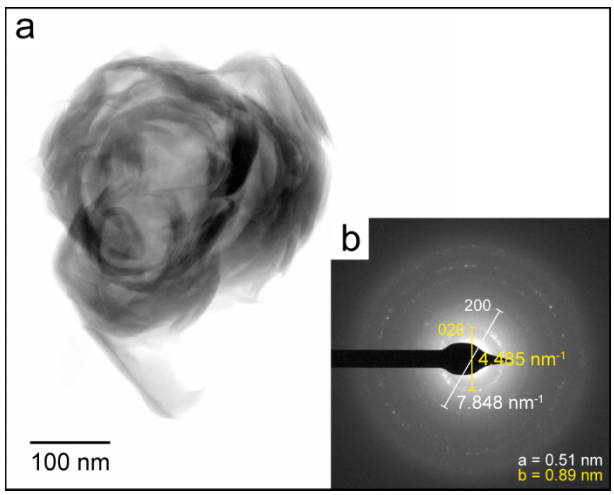

Figure 5. a) TEM image showing a flower-shaped smectite aggregate with curved morphologies. b) Electron diffraction pattern showing the crystal

parameters (a = 5.1 Å, b = 8.9 Å) indicative of dioctahedral smectite.

5 Discussion

A close correlation between lithium mineralization and pyroclastic units would ascribe the Falchani Lithium Project in the Macusani Volcanic Field to the volcanogenic lithium deposit type. Volcanogenic deposits stand as 'non-conventional' Li resources – in front of 'conventional' LCT pegmatites and hydromorphic ('salar') deposits (Bowell et al. 2020). Enrichment in lithium to economic grades in volcanogenic deposits is considered to result from the interaction of pre-existing volcanic rocks enriched in lithium and atmospheric or hydrothermal fluids in rhyolitic calderas, triggering the deposition of secondary, Li-rich minerals (Benson et al. 2017; Bowell et al. 2020).

Volcanogenic lithium deposits are subdivided into clay, ion-clay, and jadarite subtypes depending on the nature of prevalent lithium-bearing phases (Bowell et al. 2020). From a mineralogical point of view, the best studied volcanogenic lithium deposits are those in the McDermitt Caldera in Nevada (USA). Castor and Henry (2020) concluded that, in the Thacker Pass deposit of the McDermitt Caldera, lithium occurs in hectorite (Li-smectite), in an illitic clay that is chemically similar to tainiolite, and in a mixed-layer smectite-illite clay. These authors reported a vertical mineral zonation consisting of i) illitic clays in the lower sedimentary section (~ 3,000 ppm Li), ii) a transitional zone with mixed smectite-illite (tainiolite?) clays (~ 2,000 ppm Li), and iii) an overlying upper sedimentary section dominated by hectorite (< 2,000 ppm Li).

Based on the XRD, SEM-EDS, and TEM data presented here, the mineralogy of the Lithium-rich Tuff unit in the Macusani Volcanic Field consists of quartz, plagioclase, K-feldspar, trioctahedral micas, mordenite, cristobalite, and clay minerals (kaolinite ± halloysite and dioctahedral smectite). The trioctahedral micas correspond to zinnwaldite and lepidolite and are interpreted as igneous in origin (see textural and compositional details in Torró et al. 2023). No other lithium-bearing minerals have been identified in the studied samples. However, preliminary metallurgical tests on Lithium-rich Tuff from the Falchani Lithium Project reported by The Mineral Corporation (2019) describe Li recovery as high as 90 % by leaching with sulfuric acid at 90-95°C, thus suggesting that Li may also occur adsorbed or in interlayer positions in smectite and/or kaolinite subgroup minerals. Our ongoing mineralogical work on samples from the Falchani Lithium Project will help assess the contribution of relict (i.e., zinnwaldite-lepidolite) and secondary (i.e., smectite, kaolinite subgroup minerals) phases to the bulk lithium resource and refine the classification of the deposit.

Acknowledgements

We wish to thank the geologists from Macusani Yellowcake for their help and hospitality during fieldwork. This research work was financed by the Peruvian PROCIENCIA-FONDECYT project 1122-2020 E041-2020-01-01, and logistically supported by the 2021 SGR 00239 project of the Agència de Gestió d'Ajuts Universitaris i de Recerca de Catalunya.

References

Benson TR, Coble MA, Rytuba JJ, Mahood GA (2017) Lithium enrichment in intracontinental rhyolite magmas leads to Li deposits in caldera basins. Nat Commun 8:270.

Bowell RJ, Lagos L, de los Hoyos CR, Declercq J (2020) Classification and characteristics of natural lithium resources. Elements 16:259–264.

Castor SB, Henry CD (2020) Lithium-rich claystone in the McDermitt Caldera, Nevada, USA: geologic, mineralogical, and geochemical characteristics and possible origin. Minerals 10:1-39.

European Commission (2020) Study on the EU's list of Critical Raw Materials. European Commission, Brussels, Belgium, 158 p.

Göğüş OH, Sundell K, Uluocak EŞ, Saylor J, Uğurcan Ç (2022) Rapid surface uplift and crustal flow in the Central Andes (southern Peru) controlled by lithospheric drip dynamics. Sci Rep 12:5500.

Graham JD, Rupp JA, Brungard E (2021) Lithium in the green energy transition: the Quest for both sustainability and security. Sustainability 13:11274.

IRENA (2019) Global energy transformation: a roadmap to 2050. Abu Dhabi, 52 p.

Jowitt SM, McNulty BA (2021) Battery and energy metals: future drivers of the minerals industry? SEG Discovery 127:11-18.

Keller WD, Reynolds RC, Inoue A (1986) Morphology of clay minerals in the smectite-to-illite conversion series by scanning electron microscopy. Clays Clay Miner 34:187-197.

López JC (1996) Geología del cuadrángulo de Nuñoa. Hoja 29-u. Instituto Geológico, Minero y Metalúrgico, 171p

Pichavant M, Kontak DJ, Briqueu L, Valencia Herrera J, Clark AH (1988) The Miocene-Pliocene Macusani Volcanics, SE Peru - II. Geochemistry and origin of a felsic peraluminous magma. Control Mineral Petrol 100:325–338.

Salisbury MJ, Jicha BR, de Silva SL, Singer BS, Jiménez NC, Ort MH (2011) $^{40}Ar/^{39}Ar$ chronostratigraphy of Altiplano-Puna volcanic complex ignimbrites reveals the development of a major magmatic province. GSA Bulletin 123:821-840

Sandeman HA, Clark AH, Farrar E, Arroyo-Pauca G (1997) Lithostratigraphy, petrology and ^{40}Ar-^{39}Ar geochronology of the Crucero Supergroup, Puno Department, SE Peru. J South Am Earth Sci 10:223–245

The Mineral Corporation (2019) Mineral Resource Estimates for the Falchani Lithium Project in the Puno District of Peru. Bryanston, pp 1-72.

Torró L, Villanova-de-Benavent C, Monnier L, Laurent O, Segovia-More MK, Sanandres-Flores M, Ramírez-Briones J, Vallance J, Salvi S, Baby P, Proenza JA, Nieto F (2023) Lithium-bearing micas in the 'lithium-rich tuff' from the Macusani Volcanic Field, Puno, Peru. This volume.

Characteristics of productive and barren Jecheon adakitic intrusions in the Hwanggangri mineralized district, Republic of Korea

Jieun Seo[1], Seon Gyu Choi[1], Gi Eun Shin[1], Young Jae Lee[1]
[1]T Department of Earth and Environmental Sciences, Korea University, Korea

Abstract. The Hwanggangri mineralized district (HMD) in South Korea contains a variety of mineral deposit types. The Jurassic Jecheon and Songhaksan granodiorite in the Hwanggangri district have similar adakitic geochemical characteristics in major and trace element variation and REE patterns, but they have different petrology and mineralogy. The Jecheon granodiorite is classified as coarse-grained hornblende-biotite granodiorite with observed hornblende, greenish brown colored biotite, and sphene with
mafic microgranular enclave (MME) by mingling and mixing. It has oxidized I-type, magnetite-series characteristics with higher magnetic susceptibility values of 3.60–13.04x10^{-3} SI and Mg#. On the other hand, the Songhaksan granodiorite is S-type medium-grained two mica granodiorite having lower magnetic susceptibility values of 0.01–0.05x10^{-3} SI and Mg#. Therefore, the Jecheon (southwest) and Songhaksan (northeast) granodiorites were originated different source material because they have different magnetic susceptibility, mineralogy, and mineral chemistry. In addition, there are two types of MME in Jecheon granodiorite, which were formed in the process of mixing with two veins. The Jecheon granodiorite in the southwest is barren, while the Songhaksan granodiorite in the northwest is a productive igneous rock that formed the Dongmyeong Skarn type W deposit.

1 Introduction

The Hwanggangri mineralized district (HMD) is located on the boundary of the Okcheon metamorphic belt and the Taebaeksan Basin (Fig. 1). The HMD contains a number of Jurassic and Cretaceous intrusive rocks. The HMD contains a variety type of mineral deposits (porphyry, skarn, carbonate replacement, and fissure–filling vein types). W–Mo deposits are one of the major types of metal ores in South Korea, and they are widely distributed and closely related to Jurassic–Cretaceous magmatism (Shimazaki et al, 1987; Park et al. 1988a,b; So et al. 1991; Lee at al. 2022). The W–Mo deposits have variable ratios of the constituent metals because of the variety of fluids derived from different emplacement depths of magmas during the Jurassic and Cretaceous (Choi et al. 2007). The HMD is a representative area of major metals and fluorite mineralization in South Korea, and it stretches from south of the Jecheon intrusion to the northern part of the Weolaksan intrusion. Numerous Mo–W–Cu–Pb–Zn–Au–Ag polymetallic deposits occur in this area, and there are many fluorite deposits among the intrusion bodies (Hwang 2002). Most of the deposits are related Late Cretaceous intrusions and shown the age of mineralization is Late Cretaceous (96.5–76.2 Ma) including Geumseong, Jungbo, Kwangsin, and Geumsil mines, with the exception of the Dongmyeong deposit, which is 176.6±5 Ma (Choi et al. 1993). These deposits are hosted in limestones/dolomitic limestones of the Joseon Supergroup. The Dongmyeong tungsten skarn deposit formed in the contact area between the Joseon Supergroup (Paleozoic limestone) and the Jecheon intrusion (Jurassic granitoids). Uniquely, the Jecheon intrusion related to the Dongmyeong deposit appears to be a single intrusive body, however, the northeastern and southeastern part of body show different geochemical characteristics. In this study, we described the petrology, mineralogy, and geochemistry of Jecheon Jurassic intrusions in the HMD that are associated with barren or productive deposits and described the mixing/mingling features within Jecheon intrusion.

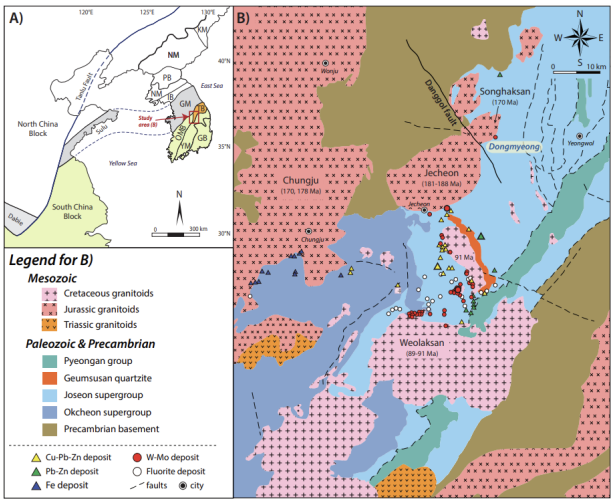

Figure 1. A) Simplified geological map of the Korean Peninsula, B) Geological map of the Hwanggangri mineralized district (HMD), showing the location of various types of deposits (modified from Lee et al. 2022). Abbreviations: KM = Kwanmobong massif, NM = Nangrim massif, PB = Pyeongnam basin, IB = Imjingang belt, GM = Gyeonggi massif, OMB = Okcheon metamorphic belt, TB = Taebaeksan basin, YM = Yeongnam massif, GB = Gyeongsang basin.

2 Geological background

The Korean Peninsula is located on the northeastern Asia plate, and it is made up of three Precambrian massifs (Nangrim, Gyeonggi, and Yeongnam), three Phanerozoic basins (Pyeongnam, Taebaeksan, and Gyeongsang), and two metamorphic belts (Imjingang and

Okcheon) (Fig. 1A). The study area includes the boundary between the Okcheon metamorphic belt and Taebaeksan Basin. The Joseon Supergroup within the Taebaeksan Basin consists mainly of Cambrian–Ordovician sedimentary rocks (Fig. 1B; Chough 2013). The Carboniferous–Lower Triassic clastic sedimentary units of the Pyeongan Supergroup overlie unconformably the Cambrian–Ordovician carbonate sequences of the Joseon Supergroup, and they have been intruded by Mesozoic igneous rocks. Jurassic and Cretaceous igneous intrusive rocks are widespread in both the Okcheon metamorphic belt and the Taebaeksan Basin, and in particular it is the Late Cretaceous (90–70 Ma) igneous rocks that are associated with mineralization (Sagong et al. 2005; Choi et al. 2005). The Mesozoic intrusions show a trimodal age distribution are reported by several researchers (Jwa 1988; Chough et al. 2000), which may be related to the Songrim disturbance in the Triassic (248–210 Ma), the Daebo orogeny in the Jurassic (200–155 Ma), and the Bulguksa of Magmatism in the Cretaceous–Early Tertiary (110–50 Ma).

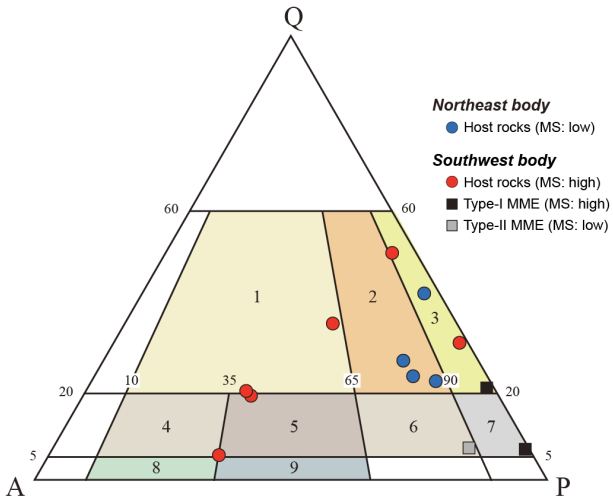

Figure 2. QAP rock classification scheme for the studied plutonic rocks based on the modal composition: 1, granite; 2, granodiorite; 3, tonalite; 4, quartz syenite; 5, quartz monzonite; 6, quartz monzodiorite; 7, diorite; 8, syenite; 9, monzonite (IUGS classification of the igneous rocks).

The Jecheon intrusion appears to be a single intrusive body, but the northeast (Songhaksan granodiorite) and southwest (granotoids) parts are divided by the Danggol Fault (Fig. 1B). The Jecheon intrusion was emplaced at 3.8kbar depth (Cho and Kwon 1994) and consists of megacrysts of K-feldspar, porphyritic texture biotite granite and coarse-grained biotite granodiorite (Jin et al., 1992). It has characteristics of magnetite-series, I-type, and adakitic granitoid (Ishihara et al. 2005). The Jecheon intrusion yields SHRIMP U-Pb ages of 181-188 Ma (Zhai et al. 2016). MME observed within the Jecheon intrusion body have SHRIMP U-Pb ages of 178.9 and 184.2 Ma. MME intruded at a similar period with the Jecheon intrusion. The ages of the Songhaksan intrusion are reported as SHRIMP U-Pb age of 170 ± 2 Ma (Zhai et al. 2016). The emplacement depth of Jecheon granodiorite estimated by hornblende geobarometery is 3.8kbar and it has been reported to have been emplaced at deeper depths (Cho and Kwon, 1994).

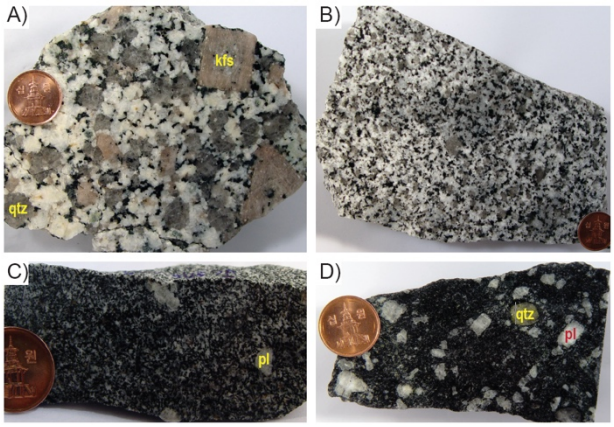

Figure 3. Photographs of hand specimens of Jurassic intrusions in the HMD. A) Southwestern part of Jecheon intrusion, which shown euhedral pinkish K-feldspar megacrysts and mafic minerals, B) Northeastern part of Jecheon intrusion, C) Type-I MME within the southwestern part of Jecheon intrusion, D) Type-II MME within the southwestern part of Jecheon intrusion.

The Jecheon intrusion is composed of granodiorite and micro mafic enclaves (MME), which are interpreted as evidence of mingling and mixing. The Jecheon granotoids show slightly heterogeneous grain size and mineralogy and show a common granodiorite to granite composition (Fig. 2). The mineralogy of the Jecheon granodiorite is dominated by plagioclase, quartz, alkali feldspar and mafic minerals of hornblende and biotite with minor amounts of sphene implying granodiorite formed in an oxidized environment. The Jecheon granodiorites are commonly coarse grained (5 to 10mm) with mega crystals of alkali feldspar (Fig. 3A). Mega crystals of alkali feldspar formed by mingling and mixing. Mafic minerals are observed around these alkali feldspar phenocrysts. Biotite showing greenish brown pleochroism is not altered and it suggests the Jecheon granodiorite formed in an oxidized environment. MME within the Jecheon granodiorite is divided into two types according to the difference in magnetic susceptibility (MS) (Fig. 3C, D). While, the Songhaksan granodiorite has medium grained texture with 2 to 5mm grain size (Fig. 3B). The mineralogy is dominated by quartz, plagioclase, alkali feldspar, mafic minerals and the percentage of alkali feldspar is lower than the Jecheon granodiorite. Plagioclase showing porphyritic texture forms well zoned crystals and most feldspars are strongly altered to sericite. The volume percentage of mafic minerals of 7 to 10% is similar to the Jecheon granodiorite. Biotite showing reddish brown pleochroism suggests that the Songhaksan granodiorite formed in a reduced environment and some biotite is altered to chlorite. Primary muscovite formed in magma and

secondary muscovite by alteration ranging from 1 to 2 %.

3 Methodology

Whole rock major, trace, and rare earth element (REE) concentrations in the intrusions and enclaves were determined using inductively coupled plasma atomic emission spectrometry (FUS-ICP-AES; Termo JarrelAsh ENVIRO II) and inductively coupled plasma mass spectrometry (FUS-ICP/MS; Perkin Elmer Optima 3000) at Activation Laboratories Ltd., Canada. Ferrous iron was determined by a gravimetric method (TITR).

Electron microprobe analyses of the minerals in the Jecheon adakitic intrusions, non-adakitic intrusions, and enclaves were performed using a JEOL JXA-8600 SX microprobe at Korea University, Seoul, South Korea. Accelerating voltage, beam current, probe diameter, and livetime were 15.0 kV, 3.0 nA, 3 μm, and 100s, respectively.

4 Results

The samples of the southwestern part of Jecheon intrusions (Jecheon granodiorite, MME) and northeastern part of Jecheon intrusions (Songhaksan granodiorites) were shown different magnetic susceptibility (MS). The Jecheon granodiorite have 3.60 to 13.04x10^{-3} SI of high MS. The MS of Songhaksan granodiorite shows low values ranging from 0.01 to 0.05x10^{-3} SI. According to Ishihara et al. (1990), the Jecheon granodiorite is magnetite series with high MS while the Songhaksan granodiorite consists of ilmenite series showing lower than 3x10^{-3} SI. The samples of MME show 0.58 to 1.51 and 3.42 to 15.71x10^{-3} SI divided into two groups and it implies that different magmas occurring mixing and mingling intruded.

The Jecheon granodiorite has low SiO_2 (66.47–70.68 wt. %), and high TiO_2 (0.38–0.53 wt. %), Al_2O_3 (13.47–16.30 wt. %), $Fe_2O_3^{tot}$ (3.03–4.17 wt. %), MgO (1.03–1.58 wt. %), CaO (2.67–4.61 wt. %), and P_2O_5 (0.13–0.17 wt. %). MME is characterized by lowest SiO_2 (50.17–53.74 wt. %) among the studied granitoids and high TiO_2 (0.89–1.21 wt. %), Al_2O_3 (14.90–18.17 wt. %), $Fe_2O_3^{tot}$ (7.80–12. 14 wt. %), MgO (3.20–5.99 wt. %), CaO (7.27–8.63 wt. %), and P_2O_5 (0.27–0.52 wt. %), but has low K_2O (1.45–2.46 wt. %) and Na_2O (3.34–4.51 wt. %). The Songhaksan granodiorite has low SiO_2 (66.51–68.42 wt. %) and high TiO_2 (0.58–0.72 wt. %), Al_2O_3 (15.49–16.43 wt. %), $Fe_2O_3^{tot}$ (3.37–4.01 wt. %), MgO (1.05–1.30 wt. %), CaO (3.31–3.93 wt. %), and P_2O_5 (0.17–0.22 wt. %) whereas contains low K_2O (2.85–3.57 wt. %) and Na_2O (3.42–3.66 wt. %). It seems that the Jecheon and Songhaksan granodiorites show similar major element distributions.

The Jecheon and Songhaksan granodiorite have similar geochemical characteristics of Rb, Zr, Y, Nb, and V contents. The Jecheon granodiorite and MME have contents of Ba (291–1189; 200–644 ppm), Sr (316–570; 259–787 ppm), respectively and show wide ranges of Ba and Sr contents compared to the Songhaksan granodiorite contents of Ba (848–1240 ppm) and Sr (503–535 ppm). These chemical properties correspond to adakitic properties. (Fig. 4A,B).

The total contents of rare earth elements of Jecheon granodiorite, MME, and Songhaksan granodiorites are 107.32–176.56 ppm, 163.63–262.36 ppm, and 146.67–189.47 ppm, respectively. These granitoids are mostly enriched in light rare earth elements (LREE) and depleted in high rare earth elements (HREE). The Jecheon granodiorite, MME, and Songhaksan granodiorite have no Eu anomaly and high (La/Yb)N values of 21.20–24.20, 6.20–17.59, and 27.66–53.82, respectively (Fig 4C, D,E,F). These features of high (La/Yb)N suggest that the Jurassic granitoids are associated with adakite.

Two types of dykes and two types of MME are observed in the Jecheon intrusion, which is the result of the mixing/mingling processes of granodiorite and mafic dykes.

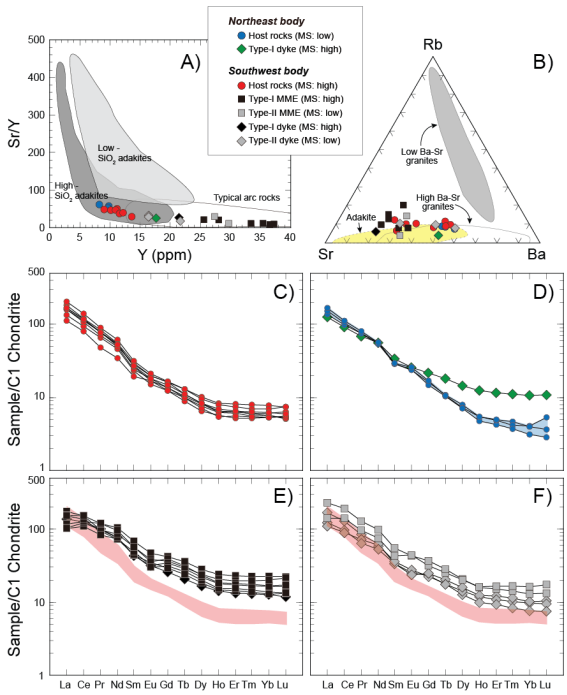

Figure 4. Geochemical characteristics of the Jecheon intrusions. A) Sr/Y versus Y diagram (modified after Defant and Drummond, 1990; Martin et al., 2005; He et al., 2012). B) Rb-Sr-Ba ternary diagram for high and low Ba-Sr granite fields (after Tarney and Jones, 1994). C) Chondrite-normalized rare earth element (REE) patterns for the southwestern part of Jecheon intrusion (granitoids) (Sun and McDonough, 1989). D) the northeastern part of Jecheon intrusion (granitoids and mafic dykes). E) the southwestern part of Jecheon intrusion (MMEs). F) the southwestern part of Jecheon intrusion (mafic dykes).

5 Conclusions

The Jecheon and Songhaksan granodiorites were reported as one granite mass (Ishihara et al., 2000;

Shibata et al., 1983) while Jin et al. (1992) reported that the Jecheon and Songhaksan granodiorites are bounded by a fault. The differences between the Jecheon and Songhaksan granodiorites are as follows. In magnetic susceptibility values, the Jecheon granodiorite is magnetite series with more 3 x 10-3 SI while the Songhaksan granodiorite consists of ilmenite series with relatively lower magnetic susceptibility values. The Jecheon granodiorite is classified as I-type granitoids of coarse-grained hornblende-biotite granodiorite with mega crystal of K-feldspars whereas the Songhaksan granodiorite shows S-type granitoids of medium grained two mica granodiorite with muscovite. The sphene and greenish brown colored biotite implying formed in oxidized environment are observed in the Jecheon granodiorite. On the other hand, the Songhaksan granodiorite has reddish brown pleochroism biotite and it suggests that the Songhaksan granodiorite formed in reduced environment. In this study, it suggests that they were derived from magma that originated from a different source with different magnetic susceptibility values, grain size, and mineralogy.

The Jecheon granodiorite and MME have a wide range of K_2O contents with similar SiO_2 contents and have characteristics of calc-alkaline series to high-K calc-alkaline series due to mingling and mixing, but the Songhaksan granodiorite is high-K calc-alkaline series (Rickwood 1989).

The Jurassic W skarn type Dongmyeong deposit (176.5 Ma) is related to the Songhaksan granodiorite located on the northern side of the Hwanggangri district. The Songhaksan granodiorite is metaluminous to peraluminous S-type granitoids and has less evolved geochemical features of Rb/Sr ratio and Eu/Eu* values. The Dongmyeong deposit has no greisen alteration and fluorite. The Jecheon granodiorite, MME, Songhaksan granodiorite have high Nb/Ta values of 7.07–12.38, 8.11–15.98, and 11.63–13.80, respectively and have features of less evolution in diagrams for fractionation in peraluminous granites.

The Jecheon hornblende-biotite granodiorite, which shows high magnetic susceptibility values (magnetite series) and greenish pleochroic biotite, is not associated with W deposits. While, the Songhaksan granodiorite with lower magnetic susceptibility values of $0.01–0.05x10^{-3}$ SI is identified as ilmenite series and S-type granite, is associated with W deposits.

Acknowledgements

This research was supported by Basic Science Research Program through the National Research Foundation of Korea (NRF) funded by the Ministry of Education (NRF-2022R1I1A1A01071269).

References

Cho DL, Kwon ST (1994) Hornblende geobarometry of the Mesozoic granitoids in South Korea and the evolution of crustal thickness. Jour. Geol. Soc. Korea 30:41-61.

Cho SG, Park JW, Seo J, Shin JK, Kim NH, Yoo IK, Ahn YH (2007) Hidden Porphyry-Related Ore Potential of the Geumseong Mo Deposit and Its Genetic Environment. Econ. Environ. Geol. 40:1-14.

Choi SG, Ryu IC, Pak SJ, Wee SM, Kim CS, Park ME (2005) Cretaceous epithermal gold-silver mineralization and geodynamic environment, Korea. Ore geol. Rev. 26:115-135.

Choi SH, So CS, Shelton KL, Kim SJ (1993) Mineralogy and geochemistry of the Dongmyeong tungsten mine, Korea. Journal of Southeast Asian Earth Sciences 8:349-358.

Chough SK (2013) Geology and sedimentology of the Korean peninsula. Elsevier, London, 363.

Chough SK, Kwon ST, Ree JH, Choi DK (2000) Tectonic and sedimentary evolution of the Korean peninsula: a review and new review, Earth-Science Rev. 52:175-235.

Defant MJ, Drummond MS (1990) Derivation of some modern arc magmas by melting of young subducted lithosphere. Nature 347:662-665.

He H, Zhaochong Z, Timothy K, Dongyang Z, Tong H (2012) Geochronology and geochemistry of the Chuanwulu complex in the South Tkanshan, western Xinjiang, NW China: Implications for petrogenesis and Phanerozoic continental growth. Lithos 140-141: 66-85.

Hwan, J (2002) Geochemistry of groundwater in limestone and granite of Hwanggangri fluorite mineralized area. J. Korea Earth Sci. Soc. 23 486-493.

Ishihara S, Jin MS, Terashima S (2005) Mo-related adakitic granitoids from non-island-arc setting: Jecheon pluton of South Korea. Resource Geol. 55:385-396.

Jin MS, Kim SJ, Shin SC, Choo SH, Chi SJ (1992) Thermal history of the Jecheon granite pluton in the Ogcheon fold belt, South Korea. Jour. Petrol. Soc. Korea 1:49-57.

Jwa Y.J (1988) Temporal, spatial and geochemical discriminations of granitoids in South Korea. Res. Geol. 48:273-284.

Lee JH, Seo J, Choi SG, Oh CW, Lee YJ (2022) Different characteristics of barren and W–Mo–productive Cretaceous granites in the Hwanggangri mineralized district, South Korea. Ore Geology Reviews 141:104645.

Lee KS, Chang HW, Park KH (1998) Neoproterozoic bimodal volcanism in the central Ogcheon belt, Korea: age and tectonic implication. Precambrian Res. 89:47-57.

Mutch EJF, BlundyJ.D, Tattich BC, Cooper FJ, Brooker RA (2016) An experimental study of amphibole stability in low-pressure granitic magmas and a revised Al-in-Hornblende geobarometer. Contributions to Mineralogy and Petrology 171:1–27.

Park HI, Chang HW, Jin MS (1988a) K–Ar ages of mineral deposits in the Taebag mountain district. J. the Korean Inst. of Mining Geol. 21:57-67.

Park HI, Chang HW, Jin MS (1988b) K–Ar ages of mineral deposits in the Gyeonggi massif. J. the Korean Inst. of Mining Geol. 21: 263-275.

Rickwood PC (1989) Boundary lines within petrologic diagrams which use oxides of major and minor elements. Lithos 22:247-263.

Sagong H, Kwon ST, Ree J.H (2005) Mesozoic episodic magmatism in South Korea and its tectonic implication. Tectonics, 24:1-18.

Schmidt MV (1992) Amphibole composition in tonalite as a function of pressure: an experimental calibration of the Al-in-hornblende barometer. Contributions to Mineralogy and Petrology 110:304-310.

Shimazaki H, Shibata K, Uchiumi S, Lee MS, Kaneda H (1987) K–Ar ages of some W–Mo deposits and their bearing on metallogeny of South Korea. Mining Geol. 37: 395-401.

So CS, Shelton KL, Chi SJ, Yun ST (1991) Geochemical studies of the Gyeongchang W-Mo mine, Republic of Korea: Progressive meteoric water inundation of A magmatic hydrothermal system. Econ. Environ. Geol. 86: 750-767.

Tarney J, Jones CE (1994) Trace element geochemistry of orogenic igneous rocks and crustal growth models. Journal of the Geological Society of London 151: 855-868.

Zhai MG, Zhang YB, Zhang XH, Wu FY, Peng P, Li QL, Hou QL, Li TS, Zhao L (2016) Renewed profile of the Mesozoic magmatism in Korean Peninsula: Regional correlation and broader implication for cratonic destruction in the North China craton. Science China Earth Sciences 59:2355-2388.

Structural features tied to mineral deposits deformed by shear zones

Stanislav Jacko[1], Roman Farkašovský[1], Julián Kondela[1], Alexander D. Thiessen[1]
[1]Department of Geosciences, Faculty BERG, Technical University of Košice, Slovakia

Abstract. The argentiferous Strieborna vein of the Rožňava ore field (ROF) is closely connected with Transgemeric shear zone (TGSZ) evolution. Spatial geometry of the vein segments is the product of four boudin evolution stages: (1) pre-deformed, (2) initial, (3) boudin forming and (4) boudin differentiation stage controlled by vertical mineralization allocation. During the Cretaceous transpressional events, the vein was segmented into five morphologically individual symmetrical – assymetric bodies with different mass value of chemical elements. Results of the Strieborna vein sulphosalt spatial analysis confirm their vertical zonation. Sb and Ag contents show a tendency for decreasing concentrations with depth, while Bi contents increase with depth and preserves boudin evolution stages created at different rheological environments. Rheological contrast between the boudin body and the surrounding rocks creates different boudin shapes. The higher the contrast, the higher the asymmetry. The economically most prospective elements are concentrated in the asymmetric boudins tension shadows (low pressure areas).

1 Introduction

Vein-type deposits overprinted by later shearing around the world, are not commonly economically mined. Sparse resources, structural reworking, mineralization heterogeneity and exploration costs moved the shear zone deposits outside of economic interest. However, some visibly sheared and boudinaged gold (Baker et al. 2002; Smith et al. 2013; Martins et al. 2016) or iron deposits (Roache 2004; Rajabzadeh and Rasti 2017) are profitably mined. Structural research and understanding of the shear zones in the economically potential areas may affect the mining exploration. Research may also as increase the quality and quantity of raw materials in the heterogenic structural space. The Strieborna vein represents a significant, and recently one of the most valuable ROF ore vein bodies situated at the TGSZ. The vein occurs within two rheologically different Early Paleozoic rock sequences controlled by a competence contrast, i.e. in between brittle-deformed meta-pyroclastics underlying the vein, and ductile-deformed phyllites forming the vein`s hanging wall. The Strieborna vein shows a record of multiple epigenetic hydrothermal processes (Sasvári and Maťo 1998; Hurai et al. 2002). This study focuses on the Strieborna vein boudinage development at rheologically contrasting parent rocks. It aims to identify boudin formation continuity based on the analysis of boudin geometry, the structural pattern of the boudin bodies, and also to check temporal and spatial evolution of ore phases throughout the vein boudinage deformation.

2 Geological Setting

The Rožňava ore filed is located in the Gemeric belt (the Gemeric Superunit cf. Plašienka 1999; Bezák et al. 2009) of the Western Carpathians (Figure 1). It is the southernmost unit of the Western Carpathians (Andrusov 1968) formed in the south edge of Variscan orogeny. Structurally, the Gemeric belt consists of southwardly dipped nappe sheets evolved initially from Variscan fold structures (Rozložník 1976; Grecula et al. 1995). Broadly preserved cleavage sets transposing the basement rocks primary foliation belong partly to Variscan structural remnants (Grecula et al. 1995; Faryad 1995; Lexa et al. 2003), or to the Alpine shortening results (Maluski et al. 1993; Dallmeyer et al. 1994) as they occur in both Late Paleozoic and Mesozoic cover formations (Jacko and Sasvári 1990; Plašienka 1999; Németh 2002). Also, regionally significant shear zones of NE-SW and NW-SE directions cutting either basement or Mesozoic formations belong to the Alpine origin.

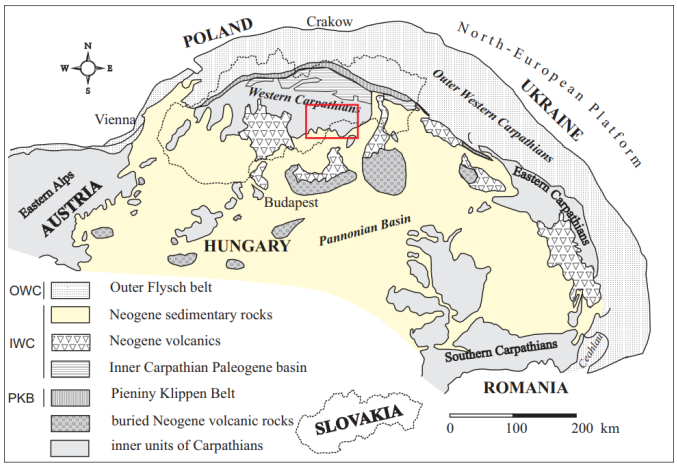

Figure 1. Location of the study area at the Western Carpathians.

Early Paleozoic volcano-sedimentary, a low-grade metamorphic suite of the Gelnica Group itself is divided into three formations (Vlachovo, Bystrý potok, Drnava; Bajaník et al. 1983; Vozárová and Ivanička 1996). Only the last of them is present in the ROF area. During Variscan and Alpine regional metamorphism, the Gelnica Group sequence was metamorphosed under lower greenschist P-T conditions to variously colored phyllites, metasandstone/

metagreywackes, crystalline limestones and metavolcanic rocks (Faryad 1991, 1995; Vozárová 1993).

3 Methodology

The structural analysis of the Strieborna vein was realized at the surface as well as underground. The Strieborna vein itself was systematically surveyed at five underground mining levels. Geological structures were also correlated with controlling audio-frequency magnetotelluric sources at higher spectral band (~1 Hz to 80 kHz) signals. Boudins geometrical classification is based on Ramsay and Huber (1987), Hammer and Passchier (1991), Goscombe and Passchier (2003), Goscombe et al. (2004), Rodrigues et al. (2016) and extended by parameters described by Samanta et al. (2017). We compared surface structural research with the ore vein mineralization distribution and structural pattern of the Strieborna vein ore body.

4 Results and discussion

4.1 Structure and lithology

The Drnava Formation rock sequences (Figure 2) show NE-SW direction and generally moderate SE inclination of the structural planes. They were deformed by the Transgemeric shear zone (TGSZ) of the strike same direction in the studied area. The ROF rock suites, including mineralized veins, were incorporated into the TGSZ structural pattern.

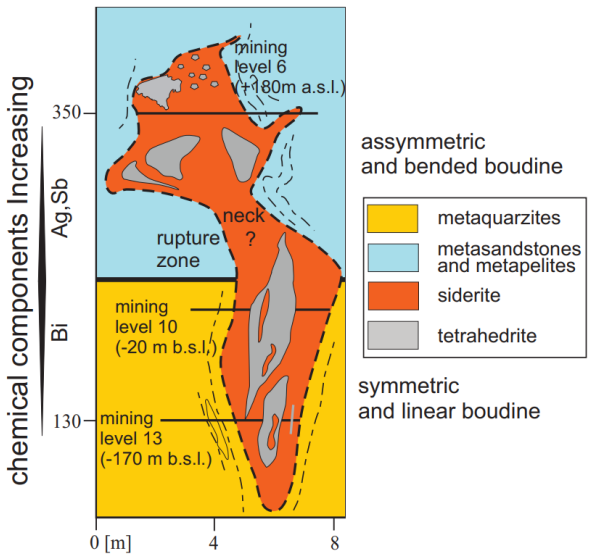

Figure 2. Vertical scheme illustrates dependence between vein boudin morphology and surrounding rocks rheology. Distribution of chemical compositions relates to successive mineralization process of tetrahedrite and sulphosalts as well as boudin formation.

Ore veins of the ROF area were developed within metapsammitic rocks of the Drnava Formation that are irregularly intercalated by dark metapelites with tiny conglomeratic and carbonate layers (Figure 2). All mentioned rocks are metamorphosed at greenschist facies conditions (Faryad 1991, 1995; Vozárová 1993).

4.2 Cleavage and folds

A typical feature of the Gelnica Group rocks is a steep cleavage set that relates to area shortening. Early Cretaceous tectonometamorphic processes (deformation stage AD1 sensu Németh et al. 1997) formed an asymmetric positive fan structure across the entire length of the Gemer belt (Lexa et al. 2003). A progressive structural evolution, caused by shear strain, successively transposed Alpine folds into a position parallel to the curved structure of the Gemeric belt. Consequently, fold axes orientation varies between SW–NE and SSW–NNE, depending on their position in the above-mentioned bent structure. An average fold amplitude at the shear zone varies from 0.5 to 2.0 meters. The fold axial cleavage planes are frequently injected by hydrothermal quartz veins. They are well-identified in the adjacent fold limbs, mainly at rheological boundaries between slates and hydrothermal quartz filling.

4.3 Boudins

Nicely preserved Strieborna vein boudins occupy a depth interval between the 6th and 10th mining levels, forming five boudin bodies. Their length varies from several tens to more than 100 m. They originated along two dislocation sets filled by mylonites of meter to decimeter wide thicknesses. Structural data indicate that the process of the Strieborna vein boudinage is closely related to the strike-slip activity of the mentioned fault sets. The Strieborna vein and the Čučma stibnite vein recline at the same NNE–SSV fault structure and they contain the same mineral associations of the quartz–sulphidic phase (Grecula et al. 1995; Sasvári and Maťo 1998; Mikuš et al. 2018). They probably underwent a similar hydrothermal evolution during the final steps of vein formation. The brittle–ductile mylonitic shear zone up to 1 m thick runs near the Strieborna vein at 6th mining level, parallel to foliation in the metapelitic rocks. The dark phyllites enclose lenses of white hydrothermal quartz with variable lengths and visible signs of shear deformation. They are segmented by shear bands, or they form boudins, asymmetric objects, and remnants of isoclinal folds. The minor veins can be also deformed by shear bands or folded.

Based on the kinematics (sensu Goscombe et al. 2004), the minor boudins can be divided into two types: boudins, the origins of which relate to tension deformation (Figure 3), and those that are segmented by shear movement (Figure 4). According to the boudin geometry, they can be divided into three main categories. Asymmetric shear band boudins have boudin blocks separated by shear planes. The boudin blocks are formed mainly by siderite, less by quartz.

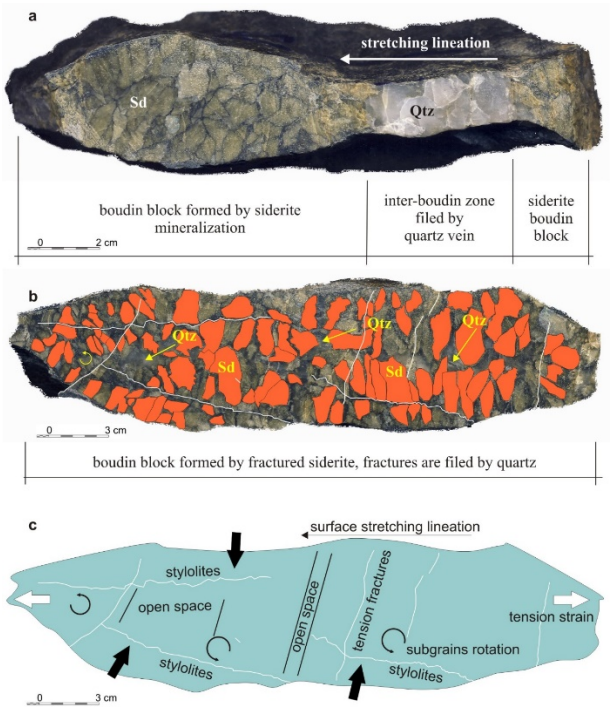

Figure 3. Structural geometry of symmetric torn boudins. a – Position of younger extensional quartz into siderite. b –Cleveage planes and siderite tensile fractures filed by younger hydrothermal quartz. c – Tensile boudin internal structure composed of several structure elements, i.e. responded paleostress marked by stylolites and tension fractures. Boudinal stretching also allowed subgrains rotation into paleostress free boudin segments.

The inter-boudin zone is filled by quartz or by surrounding metapelitic rock. In some cases, the terminal parts of the shear band boudin blocks were dragged in the direction of the boudin separation and form drawn boudins. The boudin blocks of the symmetric torn boudins are always formed by siderite, and inter-boudin zones are filled with quartz The siderite in the boudin blocks is brittlely deformed. Single grains are separated from each other, or they are fractured along their cleavage planes. The open space among the separated parts of the siderite grains is filled with quartz. Various microstructural markers were observed in torn boudins, these were previously unknown in the ROF area. Pressure markers like tapered stylolite teeth and stylolitic joint surfaces indicate a maximal compressive stress oriented perpendicularly to the foliation. The minor siderite veins deformed as a brittle material set in the more ductile metapelites. The foliation planes of the surrounding metapelites are bent around the boudin structures (Figure 4).

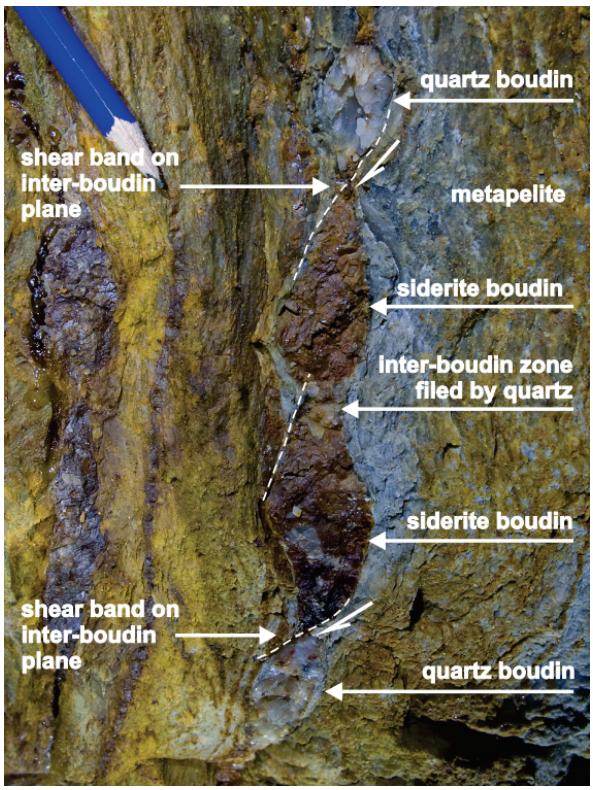

Figure 4. Asymmetric shear bands distribution at an inter-boudin plane filled by brown siderite and light quartz. Lens-like distribution of sideritic and quartzose boudins, divided by shear band inter-boudin planes resulting from shear deformation of relatively much more thickened ductile phyllite surrounding.

3 Conclusion

The Strieborna vein deformations were evidently related to the sinistral brittle–ductile shearing along the Transgemeric shear zone (TGSZ). Five boudin bodies, several tens to more than 100 m in length, were present between 6th and 10th mining levels of the vein. They were created at two regional dislocation sets of NNE–SSW and NE–SW directions. Both spatially corresponded to the principal Alpine structures of the Rožňava mining area and show slightly to moderately inclined strike-slip kinematics.

Boudins of sample dimensions provide valuable information about the successive evolution of shear zone deformation, kinematics, and internal geometry as well as the precipitation of individual vein associations.

The oldest demonstrable Strieborna vein boudinage stage was the post-quartz–siderite one, which tied to consecutive deformations. The presence of siderite grains rotated in the direction of the stretching lineation and diagonally oriented stylolitic patterns seam to follow successive deformations of the TGSZ.

The rheological contrast between the boudin body and the surrounding rocks creates different boudin shapes. The higher the contrast, the higher the asymmetry. The economically most

prospective elements are concentrated in the asymmetric boudins tension shadows (low pressure areas).

References

Andrusov D (1968) Grundriss der Tektonik der Nördlichen Karpaten. Slovak Academy of Sciences, Bratislava, pp 1–188

Bajaník Š, Hanzel V, Ivanička J, Mello J, Pristaš J, Reichwalder P, Snopko L, Vozár J, Vozárová A (1983) Explanation to geological map of the Slovenské Rudohorie Mts. –eastern part. Dionýz Štúr Geological Institute, Bratislava, pp 1–223 (in Slovak)

Baker DEL, Seccombe PK, Collins WJ (2002) Structural history and timing of gold mineralization in the northern East Strelley Belt, Pilbara Craton, Western Australia. Econ Geol 97: 775–785

Bezák V , Biely A, Broska I, Bóna J, Buček S, Elečko M, Filo I, Fordinal K, Gazdačko Ľ, Grecula P, Hraško Ľ, Ivanička J, Jacko S sen., Jacko S jun., Janočko J, Kaličiak M, Kobulský J, Kohút M, Konečný V, Kováčik M, Lexa J, Madaras J, Maglay J, Mello J, Nagy Z, Németh Z, Olšavský M, Plašienka D, Polák M, Potfaj M, Pristaš J, Siman P, Šimon L, Teták F, Vozárová A, Vozár J, Žec B (2009) Explanations to the general geological map of Slovak Republic, scale 1: 500 000. Geol Surv Slov Rep, Bratislava, pp 1–534 (in Slovak with English summary)

Dallmeyer RD, Neubauer F, Fritz H, Mocanu V (1994) Pre-Variscan, Variscan and Alpine tectonothermal evolution within the southern Carpathians, Romania: evidence from 40Ar–39Ar hornblende and muscovite ages. J Czech Geol Soc 39: 18–19

Faryad SW (1991) Metamorphism of the Early Paleozoic sedimentary rocks in the Gemericum. Miner Slov 23: 315–324

Faryad SW (1995) Determination of P–T metamorphism conditions in the Early Paleozoic Gemericum rock sequences. Miner Slov 27: 9–19

Goscombe B, Passchier CW (2003) Asymmetric boudins as shear sense indicators – an assessment from field data. J Struct Geol 25: 575–589

Goscombe B, Passchier CW, Hand M (2004) Boudinage classification: end-member boudin types and modified boudin structures. J Struct Geol 26: 739–763

Grecula P, Abonyi A, Abonyiová M, Antaš J, Bartalský B, Bartalský J, Dianiška I, Drnzík E, Ďuďa R, Gargulák M, Gazdačko Ľ, Hudáček J, Kobulský J, Lörincz L, Macko J, Návesňák D, Németh Z, Novotný L, Radvanec M, Rojkovič I, Rozložník L, Rozložník O, Varček C, Zlocha J (1995) Mineral deposits of the Slovak ore Mountains, Vol. 1., Geocomplex, Bratislava, pp 1–834

Hanmer, S, Passchier C (1991) Shear-Sense Indicators: A Review. Geological Survey of Canada Papers 90-17, pp 1–72

Hurai V, Harčarová E, Huraiová M, Ozdín D, Prochaska W, Wiegerová V (2002) Origin of siderite veins in the Western Carpathians I. P–T–X–δ13C–δ18O relations in ore-forming brines of the Rudňany deposits. Ore Geol Rev 21: 67–101

Jacko S, Sasvári T (1990) Some remarks to an emplacement mechanism of the West Carpathian Paleo-Alpine nappes. Geol Carpath 41: 179–197

Lexa O, Schulmann K, Ježek J (2003) Cretaceous collision and indentation in the West Carpathians: view based on structural analysis and numerical modeling. Tectonics 22: 1066, DOI: 10.1029/2002TC001472

Maluski H, Rajlich P, Matte P (1993) 40Ar–39Ar dating of the Inner Carpathian Variscan basement and Alpine mylonitic overprinting. Tectonophysics 223: 313–337

Martins BD, Lobato LM, Rosiere CA, Hagemann SG, Santos JOS, Villanova FLDP, Silva RCFE, Lemos LHD (2016) The Archean BIF-hosted Lamego gold deposit, Rio das Velhas greenstone belt, Quadrilatero Ferrifero: evidence for Cambrian structural modification of an Archean orogenic gold deposit. Ore Geol Rev 72: 963–988

Mikuš T, Kondela J, Jacko S, Milovska S (2018) Garavellite and associated sulphosalts from the Strieborna vein in the Rožňava ore field (Western Carpathians). Geol Carpath 69: 221–236

Németh Z (2002) Variscan suture zone in the Gemericum: contribution to reconstruction of geodynamic evolution and metallogenetic events of Inner Western Carpathians. Slovak Geol Mag 8: 247–257

Németh Z, Gazdačko L, Návesňák D, Kobulský J (1997) Polyphase tectonic evolution of the Gemericum (the Western Carpathians) outlined by review of structural and deformational data. In: Grecula P, Hovorka D, Putiš M (eds) Geological Evolution of the Western Carpathians. Geocomplex, Bratislava, pp 215–224

Plašienka D, Grecula P, Putiš M, Kováč M, Hovorka D (1999) Evolution and structure of the Western Carpathians: an overview. In: Grecula P, Hovorka D, Putiš M (eds) Geological Evolution of the Western Carpathians. Geocomplex, Bratislava, pp 1–24

Rajabzadeh MA, Rasti S (2017) Investigation on mineralogy, geochemistry and fluid inclusions of the Goushti hydrothermal magnetite deposit, Fars Province, SW Iran: a comparison with IOCGs. Ore Geol Rev 82: 93–107

Ramsay JG, Huber MI (1987) The Techniques of Modern Structural Geology. Volume 2: Folds and Fractures. Academic Press, London, pp 516–633

Roache TJ (2004) Shear zone versus fold geometries at the Cannington Ag–Pb–Zn deposit: implications for the genesis of BHT deposits. J Struct Geol 26: 1215–1230

Rodrigues BC, Peternell M, Moura A, Schwindinger M, Pamplona J (2016) P–T path development derived from shearband boudin microstructure. J Struct Geol 90: 95–110

Rozložník L (1976) Relationship of Siderite Metalogenesis and Tectonics of the Spis Ore Mountains and Their Position in Alpides. Faculty BERG, Košice, pp 1–301

Samanta SK, Majumder DB, Sarkar G (2017) Geometry of torn boudin – an indicator of relative viscosity. J Struct Geol 104: 21–30

Sasvári T, Maťo Ľ (1998) The characteristics of the Rožňava ore district, in relation to the structural–tectonic analysis and mineralization exampled by the deposition conditions of the Strieborna vein, Mária mine, Rožňava. Acta Mont Slov 3: 33–117

Smith MT, Rhys D, Ross K, Lee C, Gray JN (2013) The long canyon deposit: anatomy of a new off-trend sedimentary rock-hosted gold discovery in northeastern Nevada. Econ Geol 108: 1119–1145

Vozárová A (1993) Variscan metamorphism and crustal evolution of the Gemericum. Západ Karpaty Sér Mineral Petrogr Geochem Metalogen 16: 55–117 (in Slovak with English summary)

Vozárová A, Ivanička J (1996) Geodynamic position of acid volcanism of the Gelnica Group (Early Paleozoic, southern Gemericum; Inner Western Carpathians). Slovak Geol Mag 3–4: 245–250

Tourmaline composition records fluid-rock interaction: implications for cassiterite precipitation in the Triassic Chacaltaya district, Bolivia

Lisard Torró[1], Matthieu Harlaux[2], Angela Castro-Morante[1], Jean Vallance[1], Lorenzo Tavazzani[3], Anne-Sophie Bouvier[4], Thomas Bovay[4], Cyril Chelle-Michou[3], Thierry Sempere[5], Joan Carles Melgarejo[6]
[1]Geological Engineering Program, Pontifical Catholic University of Peru (PUCP), Peru
[2]BRGM – French Geological Survey, 45060 Orléans, France
[3]Department of Earth Sciences, ETH Zürich, Switzerland
[4]Institute of Earth Sciences, University of Lausanne, Switzerland
[5]ANDES C&P, Lima, Peru
[6]Departament de Mineralogia, Petrologia i Geologia Aplicada, Universitat de Barcelona, Spain

Abstract. The Triassic Chacaltaya Sn-polymetallic district, located in the Cordillera Real of Bolivia, is spatially and genetically associated with major tourmalinization. We document three petrographic types of tourmaline associated to pre-ore greisens (Tur-1) and syn-ore tourmaline-cemented breccias (Tur-2) and veins (Tur-3). Tourmalines belong to the alkali group and have Fe-rich compositions with overlapping Fe/(Fe+Mg) ratios. Tur-1 is relatively enriched in Zn and Li whereas Tur-3 is relatively enriched in Ca, Sc, V, Cr, Sr, Sn, Y, Cs, Be, and Zr, with Tur-2 showing intermediate compositions between those of Tur-1 and Tur-3. Strong positive Eu anomalies in all tourmaline types indicate dominantly reduced hydrothermal conditions while Tur-1 to Tur-3 record a shift towards HREE-enriched compositions. In situ $\delta^{18}O$ and $\delta^{11}B$ analyses of tourmaline indicate a dominant magmatic origin of the hydrothermal fluids. Collectively, these results suggest that cassiterite mineralization at Chacaltaya resulted from the interaction of magmatic fluids derived from a peraluminous S-type granite with the metamorphic host rocks.

1 Introduction

Tourmaline is a useful indicator mineral to trace geologic processes associated with the formation of ore deposits (Slack and Trumbull 2011). It is a common mineral in most ore deposits and associated igneous rocks along the Central Andean tin belt (Kelly and Turneaure 1970), which produced ~14% of the historic world tin supply (Lehmann 2021). Previous studies on tourmaline from the Central Andean tin belt have been mainly focused on the late Oligocene San Rafael Sn-Cu deposit (Mlynarczyk and Williams-Jones 2006; Harlaux et al. 2020, 2021). Here we combine petrographic and in situ geochemical analyses of tourmaline from the Triassic Chacaltaya Sn-polymetallic district in the Cordillera Real of Bolivia (Fig. 1) to provide new constraints on the geological processes leading to cassiterite deposition.

2 Geological setting

The Central Andean tin belt stretches over >900 km from southeast Peru across Bolivia to northernmost Argentina (Fig. 1) along the Eastern Cordillera. This belt can be divided into a northern branch trending NW-SE, and a southern branch trending N-S (Fig. 1; Mlynarczyk and Williams-Jones 2005). In the northern branch, Sn-W deposits consist mainly of lodes, veins/breccias, and stratabound bodies, which are spatially associated to granitic plutons of Triassic and late Oligocene ages (Fig. 1). Triassic-age Sn-W-polymetallic deposits occur immediately south and north of the orocline core hinge along the Cordillera Real of northern Bolivia, including the Chacaltaya district, and the Cordillera de Carabaya of southeast Peru, respectively (Lehmann et al. 1990).

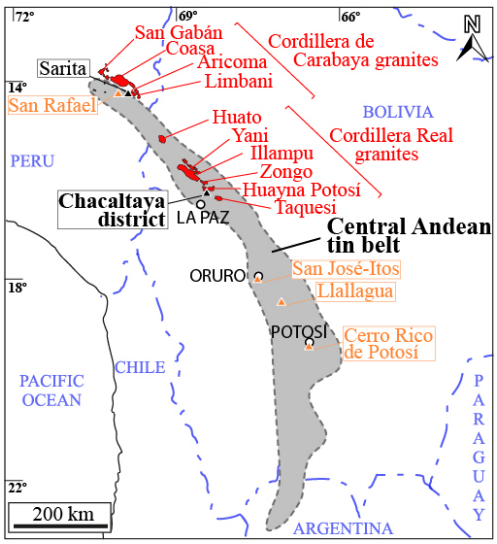

Figure 1. Map of the Central Andes showing the location of the Chacaltaya district in the Central Andean tin belt (grey field). The main Triassic plutons along the Cordillera Real and Cordillera de Carabaya are shown in red. The Triassic Sn deposits are labelled in black color, and late Oligocene-Miocene Sn deposits, in orange color.

The Chacaltaya district is located 20 km north of La Paz and ~5 km south of the Triassic (ca. 240-218 Ma) Huayna-Potosí two-mica granite batholith (Fig. 1). Rocks exposed in this district consist mostly of mid-Silurian dark shales and siltstones interbedded with thin sandstone beds of the Uncía Formation, and the overlying late-Silurian interbedded quartz-arenites and mudstones of the Catavi Formation. The Paleozoic metasedimentary rocks have been intruded by a small stock of cordierite-bearing peraluminous granite, which is

exposed in the central part of the Cerro Chacaltaya massif. Three types of hydrothermal features are distinguished in the Chacaltaya district: greisens, hydraulic breccias, and veins. Greisen occurs in most of the exposed Chacaltaya granitic stock (Lehmann 1985). Hydraulic breccias occur mostly on the eastern side of the Chacaltaya stock and are hosted by quartzites of the Catavi Formation. Finally, discordant veins and concordant-stratabound veins and veinlets are widespread across the Chacaltaya district (Lehmann 1985). The stratabound mineralization is chiefly associated with quartzitic lithologies of the Catavi Formation; a U-Pb LA-ICP-MS date of 218.3 ± 5.5 Ma was determined on cassiterite from the stratabound mineralization (Gemmrich et al. 2021).

3 Results

Three petrographic types of tourmaline (referred as Tur-1, 2, and 3) were identified in the Chacaltaya district based on detailed mineralogical and textural observations. Tourmaline in the greisen (Tur-1) occurs as disseminated millimeter- to centimeter-size grains and aggregates intergrown with white mica and quartz, or as pseudomorph after magmatic K-feldspar phenocrysts (Fig. 2A). At the microscopic scale, Tur-1 forms orange, subhedral, elongate to acicular crystals commonly showing a radial texture. Tur-1 crystals are optically homogeneous (Fig. 2B) except for discrete core to rim zoning observed locally in a few grains. Tourmaline in breccias (Tur-2) constitutes the cement of heterolithic rock fragments and mineral clasts (Fig. 2C) and forms a dense aggregate of very fine-grained, acicular crystals that commonly grew perpendicular to the clast borders in triangular and acute-angle spaces (Fig. 2D). Tur-2 crystals are dark green in color and show a discrete core to rim zoning. Isolated Tur-1 clasts up to 1 mm in size are cemented or epitaxially overgrown by Tur-2 within the breccia, thus demonstrating that Tur-1 formed prior to Tur-2. Finally, Tur-3 occurs in quartz veins hosted in the metasedimentary rocks and their alteration haloes (Fig. 2E). Tur-3 is characterized by a dark green color, and appears as subhedral, elongated to acicular crystals, which often form radial aggregates ranging from 30 µm to 2 mm in length intergrown with comb-textured quartz. Both Tur-2 and Tur-3 are locally finely intergrown with cassiterite indicating their co-crystallization from the same hydrothermal fluid (Figs. 2D, F).

Major and minor element analyses of tourmaline were performed at the University of Barcelona using a JEOL JXA-8230 electron microprobe. The three tourmaline types belong dominantly to the alkali group and have mostly Fe-rich compositions, close to the schorl endmember, and partly extending into the compositional fields of foitite and dravite. Tur-1 has mostly schorl to foitite compositions with Fe/(Fe + Mg) = 0.58 to 0.94 and X□/(X□ + Na + K) = 0.19 to 0.61. Tur-2 is also characterized by schorl to foitite compositions with Fe/(Fe + Mg) = 0.54 to 0.97 and X□/(X□ + Na + K) = 0.08 to 0.70. Finally, Tur-3 has dominantly schorl compositions with a few analyses extending into the foitite and dravite compositional fields, with Fe/(Fe + Mg) = 0.35 to 0.92 and X□/(X□ + Na + K) = 0.05 to 0.71.

Tourmaline trace element analyses were carried out at the ETH Zürich by LA-ICP-MS using the same equipment, instrumental setup, reference materials, measured isotopes, and data reduction process as in Harlaux et al. (2020). Tourmaline contains between 100s and some 1,000s ppm of K, Mn, and Zn, and between 10s to some 100s ppm of Li, Be, P, Sc, V, Cr, Ni, Sr, Sn, and Pb. Compared to major element compositions, trace elements in tourmaline show a wider range of variations. Principal component analysis (PCA) of trace element data shows that Tur-1 is distinguishably enriched in Zn and Li relative to Tur-2 and Tur-3 (Fig. 3A). In contrast, Tur-3 is relatively enriched in Sc, V, Cr, Sr, Sn, Y, Cs, Be, and Zr and depleted in Zn and Li. Tur-2 has trace element compositions intermediate between those of Tur-1 and Tur-3, except for a slight enrichment in U and Th. The contents of rare earth elements (REE) tend to increase from Tur-1 ($[\Sigma REE]_{avg.}$ = 5 ppm) to Tur-2 ($[\Sigma REE]_{avg.}$ = 14 ppm) and Tur-3 ($[\Sigma REE]_{avg.}$ = 12 ppm), principally marked by an enrichment in HREE (Fig. 3B). The UCC-normalized REE diagrams show systematic strong Eu positive anomalies (Fig. 3B).

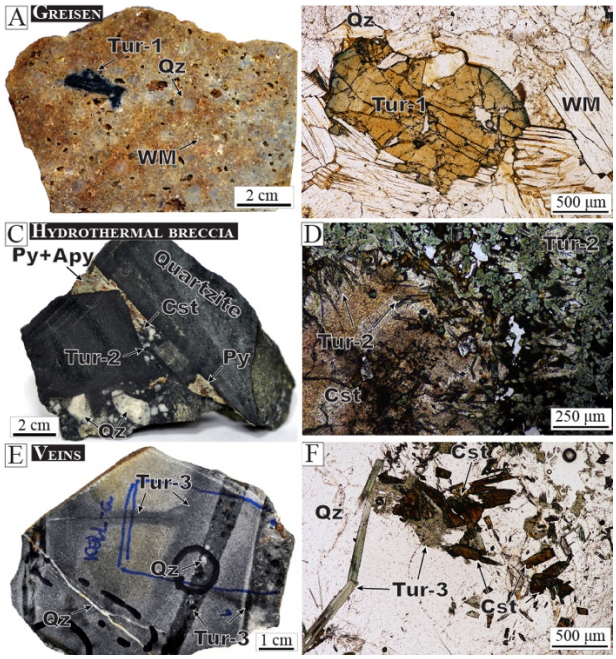

Figure 2. Mineralogical and textural features of tourmaline from the Chacaltaya district. A) Greisen composed of white mica, quartz, and tourmaline (Tur-1). B) Subhedral, millimetric tourmaline (Tur-1) crystal intergrown with secondary white micas and quartz in the greisen. C) Hydraulic breccia composed of angular rock fragments of quartzites (Catavi Formation) within a cement of fine-grained tourmaline (Tur-2), cassiterite, and sulfides. D) Needles of green tourmaline (Tur-2) intergrown with cassiterite composing the cement of the hydraulic breccia. E) Tourmaline (Tur-3)-rich veins and

veinlets crosscutting quartzites of the Catavi Formation. F) Tourmaline (Tur-3) intergrown with cassiterite in a quartz vein. Apy: arsenopyrite; Cst: cassiterite; Py: pyrite; Qz: quartz; Tur: tourmaline; WM: white mica.

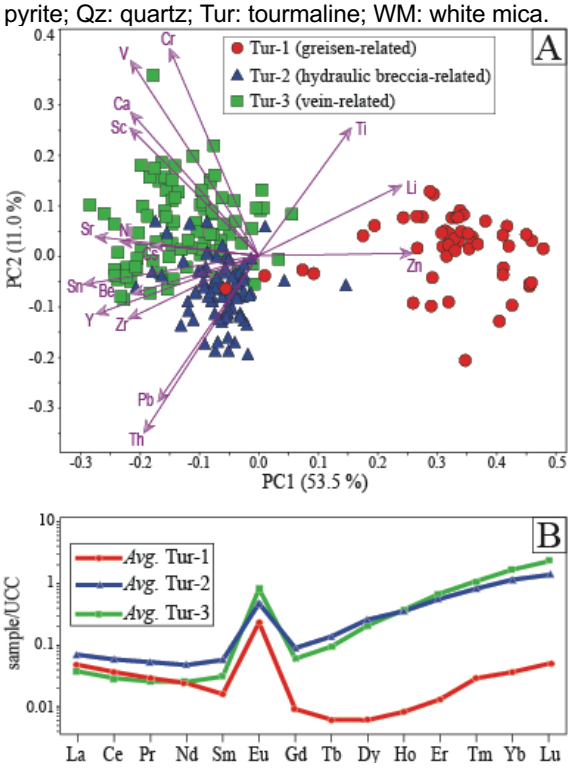

Figure 3. Principal component analysis (PCA) of log-transformed data set of selected minor and trace elements (A) and average UCC-normalized REE contents (B) of tourmaline from the Chacaltaya district. Upper continental crust values (UCC) after Rudnick and Gao (2014).

Oxygen and boron isotope analyses of tourmaline were performed at the SwissSIMS ion probe national facility at the University of Lausanne using the instrumental setup, reference materials, and data reduction process as in Harlaux et al. (2021). Tur-1 has $\delta^{18}O$ values ranging between 10.9 ‰ and 12.6 ‰, and $\delta^{11}B$ values between −13.5 ‰ and −10.5 ‰ (Fig. 4A). Tur-2 has $\delta^{18}O$ in a range between 13.5 ‰ and 17.0 ‰, and $\delta^{11}B$ in a range between −14.4 ‰ and −12.3 ‰. Finally, Tur-3 yields $\delta^{18}O$ values comprised between 12.5 ‰ and 14.4 ‰ and $\delta^{11}B$ in a range between −14.7 ‰ and −9.9 ‰.

4 Discussion

The three petrographic types of tourmaline identified in the Chacaltaya district are of hydrothermal origin. Tourmaline in the greisen (Tur-1) was formed by the replacement of primary igneous minerals during high-temperature interactions between the granitic rocks and B-rich hydrothermal fluids. In contrast, tourmaline in the cassiterite-bearing breccias (Tur-2) and veins (Tur-3) crystallized as open-space filling.

The conspicuous increase of Sn content from Tur-1 to Tur-3 (Fig 3A) may suggest increasing Sn activity in the hydrothermal fluid over time, eventually leading to cassiterite deposition coevally with Tur-2 and Tur-3 formation. High contents of Li (10s to >100 ppm) and Sn (100s to >1000 ppm), as observed in Tur-1, are typical of tourmaline that crystallized from magmatic-hydrothermal fluids (Harlaux et al. 2020; Codeço et al. 2021). In contrast, high contents of Sr, V, and Cr in tourmaline seem to be more likely attributed to crystallization from a fluid of metamorphic origin, or that equilibrated with metamorphic rocks (Sciuba et al. 2021). Following these findings, Tur-3, and to a lesser extent also Tur-2, which are enriched in Sr, V, and Cr relative to Tur-1, probably record interaction of a magmatic-hydrothermal fluid with the surrounding metamorphic rocks and/or mixing with a metamorphic fluid component. On the other hand, the fact that tourmaline from the Chacaltaya district systematically shows strong positive Eu anomalies in all tourmaline types indicate dominantly reduced conditions of the hydrothermal fluids (van Hinsberg 2011; Liu et al. 2017).

Considering crystallization temperatures of 500°C for Tur-1, 450°C for Tur-2, and 400°C for Tur-3, estimated from previous studies (Kelly and Turneaure 1970; Lehmann 1985), we calculated the $\delta^{18}O$ and $\delta^{11}B$ composition of water in equilibrium with tourmaline (Fig. 4B) using the O and B isotope fractionation factors of Zheng (1993) and Meyer et al. (2008), respectively. The isotopic compositions of water equilibrated with greisen-hosted Tur-1 fall in a range of $\delta^{18}O$ and $\delta^{11}B$ values typical of magmatic fluids derived from a peraluminous S-type granite, thus suggesting a magmatic origin for the greisen-forming fluids. A fluid equilibrated with breccia-hosted Tur-2 and vein-hosted Tur-3 yields $\delta^{11}B$ values that overlap those of Tur-1 but has $\delta^{18}O$ values that are mostly higher and fall outside of the typical compositional range for magmatic fluids. Geochemical modelling based on the measured O and B isotopic compositions of tourmaline and using the calculations detailed by Harlaux et al. (2021) is shown in Figure 4C. Rayleigh fractionation driven by tourmaline crystallization from a magmatic fluid at decreasing temperatures from 500 to 450 °C, results in a trend of near-constant $\delta^{18}O$ and increase in $\delta^{11}B$ values, which reproduces closely the composition of greisen-related Tur-1 for a fractionation degree of 10 to 70 %. Interaction between the magmatic fluid and the host metasedimentary rocks was modeled for different water/rock ratios (0.1 to 10) at 500 °C by assuming isotopic exchange with muscovite in the host rocks and initial values of $\delta^{18}O$ = 14.0 ‰ and $\delta^{11}B$ = -6.0 ‰ (see Harlaux et al. 2021). Results of the fluid-rock interaction modeling reproduce the measured isotopic compositions of Tur-2 to Tur-3 for moderate water/rock ratios of 0.1-0.5.

5 Conclusions

The textural, chemical, and isotopic characteristics of tourmaline from the Chacaltaya Sn district indicate that the hydrothermal conditions were sustainedly reduced during the deposition of pre-

and syn-ore tourmaline. In situ isotope data in tourmaline record interaction of a magmatic-hydrothermal fluid with the metasedimentary host rock or with fluids that equilibrated with the host rock. Therefore, water-rock interaction was probably key to the precipitation of cassiterite in the Chacaltaya district.

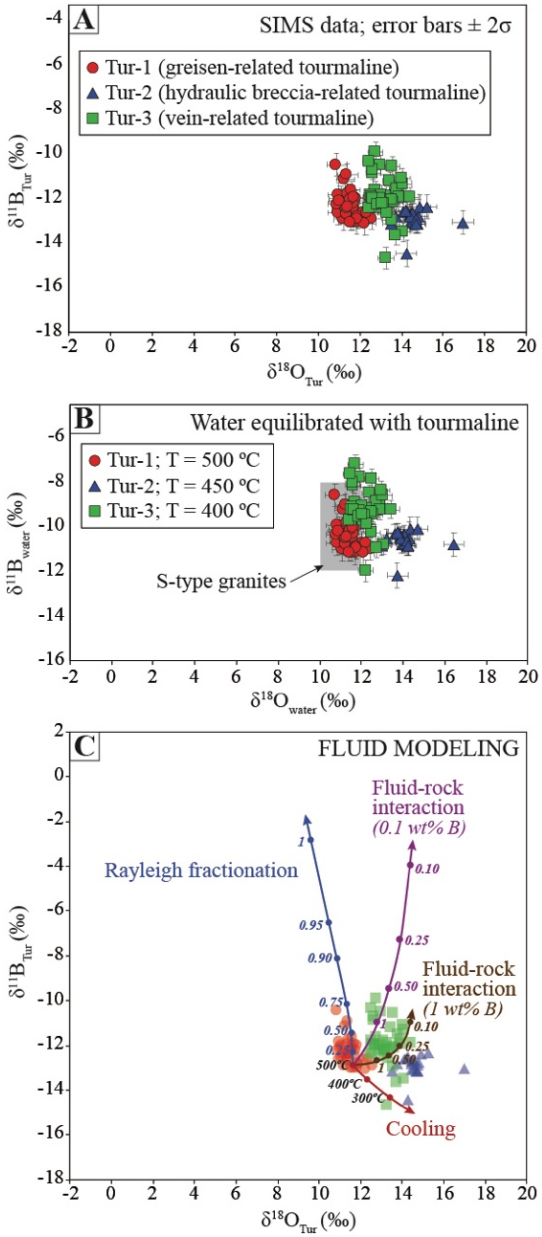

Figure 4. A) Plot of $\delta^{18}O$ vs. $\delta^{11}B$ composition of tourmaline from the Chacaltaya district determined by SIMS. B) Calculated $\delta^{18}O$ vs. $\delta^{11}B$ composition of water isotopically equilibrated with tourmaline by assuming crystallization temperatures of 500 °C for Tur-1, 450 °C for Tur-2, and 400 °C for Tur-3. The field for peraluminous S-type granites is from Harris et al. (1997) and Trumbull and Slack (2018). C) Modeling of $\delta^{18}O$ vs. $\delta^{11}B$ composition of tourmaline calculated for different evolution scenarios.

Acknowledgements

This research work was supported by the Peruvian PROCIENCIA-FONDECYT project (grant 1122-2020 E041-2020-01-01) and the FAI-0009-2021 project granted by PUCP.

References

Codeço MS, Weis P, Trumbull RB, Van Hinsberg V, Pinto F, Lecumberri-Sanchez P, Schleicher AM (2021) The imprint of hydrothermal fluids on trace-element contents in white mica and tourmaline from the Panasqueira W–Sn–Cu deposit, Portugal. Miner Deposita 56:481-508.

Gemmrich L, Torró L, Melgarejo JC, Laurent O, Vallance J, Chelle-Michou C, Sempere T (2021) Trace element composition and U-Pb ages of cassiterite from the Bolivian tin belt. Miner Deposita 56:1491-1520.

Harlaux M, Kouzmanov K, Gialli S, Laurent O, Rielli A, Dini A, Chauvet A, Menzies A, Kalinaj M, Fontboté L (2020) Tourmaline as a tracer of late-magmatic to hydrothermal fluid evolution: The world-class San Rafael tin (-copper) deposit, Peru. Econ Geol 115:1665-1697.

Harlaux M, Kouzmanov K, Gialli S, Marger K, Bouvier A-S, Baumgartner LP, Rielli A, Dini A, Chauvet A, Kalinaj M, Fontboté L (2021) Fluid mixing as primary trigger for cassiterite deposition: Evidence from in situ $\delta^{18}O$-$\delta^{11}B$ analysis of tourmaline from the world-class San Rafael tin (-copper) deposit, Peru. Earth Planet Sc Lett 563:116889.

Harris C, Faure K, Diamond RE, Scheepers R (1997) Oxygen and hydrogen isotope geochemistry of S- and I-type granitoids: the Cape Granite suite, South Africa. Chem Geol 143:95–114.

Kelly WMC, Turneaure FS (1970) Mineralogy, paragenesis and geothermometry of the tin and tungsten deposits of the Eastern Andes, Bolivia. Econ Geol 65:609-680.

Lehmann B (1985) Formation of the strata-bound Kellhuani tin deposits, Bolivia. Miner Deposita 20:169-176.

Lehmann B (2021) Formation of tin ore deposits: A reassessment. Lithos 402:105756.

Lehmann B, Ishihara S, Michel H, Miller J, Rapela C, Sanchez A, Tistl M, Winkelmann L (1990) The Bolivian tin province and regional tin distribution in the Central Andes: a reassessment. Econ Geol 85:1044-1058.

Liu W, Etschmann B, Migdisov A, Boukhalfa H, Testemale D, Müller H, Hazemann J-L, Brugger J (2017) Revisiting the hydrothermal geochemistry of europium (II/III) in light of new in-situ XAS spectroscopy results. Chem Geol 459:61–74.

Meyer C, Wunder B, Meixner A, Romer RL, Heinrich W (2008) Boron-isotope fractionation between tourmaline and fluid: an experimental re-investigation. Contrib Mineral Petr 156:259–267.

Mlynarczyk MSJ, Williams-Jones AE (2005) The role of collisional tectonics in the metallogeny of the Central Andean tin belt. Earth Planet Sc Lett 240:656-667.

Mlynarczyk MSJ, Williams-Jones AE (2006) Zoned tourmaline associated with cassiterite: implications for fluid evolution and tin mineralization in the San Rafael Sn-Cu deposit, southeastern Peru. Can Mineral 44:347-365.

Rudnick RL, Gao S (2014) Composition of the continental crust. In: Holland HD, Turekian KK (Eds) Treatise on Geochemistry, 2nd ed. Elsevier, Amsterdam.

Sciuba M, Beaudoin G, Makvandi S (2021) Chemical composition of tourmaline in orogenic gold deposits. Miner Deposita 56:537-560.

Slack JF, Trumbull RB (2011) Tourmaline as a recorder of ore-forming processes. Elements 7:321-326.

Trumbull RB, Slack JF (2018) Boron isotopes in the continental crust: granites, pegmatites, felsic volcanic rocks, and related ore deposits. In: Marschall HR, Foster GL (Eds) Boron Isotopes - The Fifth Element, Advances in Isotope Geochemistry: Gewerbestrasse, Springer-Verlag, p. 249–272.

van Hinsberg VJ (2011) Preliminary experimental data on trace-element partitioning between tourmaline and silicate melt. Can Mineral 49:153–163.

Zheng Y-F (1993) Calculation of oxygen isotope fractionation in hydroxyl-bearing silicates. Earth Planet Sc Lett 120: 247–263.

Lithium-bearing micas in the 'Lithium-rich Tuff' from the Macusani Volcanic Field, Puno, Peru

Lisard Torró[1], Cristina Villanova-de-Benavent[2], Loïs Monnier[3], Oscar Laurent[3], Mariana K. Segovia-More[1], Mercy K. Sanandres-Flores[1], Johan S. Ramírez-Briones[1], Jean Vallance[1], Stefano Salvi[3], Patrice Baby[1,3], Joaquín A. Proenza[2], Fernando Nieto[4]

[1]Geological Engineering Program, Faculty of Sciences and Engineering, Pontifical Catholic University of Peru, Peru
[2]Departament de Mineralogia, Petrologia i Geologia Aplicada, Facultat de Ciències de la Terra, Universitat de Barcelona, Spain
[3]GET-UMR CNRS/IRD/Univ. Paul Sabatier, Toulouse, France
[4]Departamento de Mineralogía y Petrología and IACT, Universidad de Granada-CSIC, Spain

Abstract. The Falchani Lithium Project has a resource of 0.9 Mt Li hosted in Neogene volcanic tuffs and breccias of the Macusani Volcanic Field. The main host is a newly-defined unit known as 'Lithium-rich Tuff' in which Li contents are mostly between 3,000 and 4,000 ppm. Although this tuff is pervasively altered to clays (dioctahedral smectite and kaolinite subgroup minerals) and zeolites, magmatic zinnwaldite and lepidolite crystals are preserved. The composition of the micas in the 'Lithium-rich Tuff' is systematically more evolved, i.e., richer in Li and other incompatible lithophile elements, relative to micas in other pyroclastic units and nearby intrusive rocks of the Macusani Volcanic Field.

1 Introduction

In November 2017, Macusani Yellowcake S.A.C., the Peruvian subsidiary of American Lithium Corp., announced the discovery of a major lithium resource in the Falchani Lithium Project, Puno department of south-eastern Peru (Fig. 1). As of February 2023, indicated resources amount to 0.2 Mt Li @ 2,954 ppm Li and inferred resources, to 0.7 Mt Li @ 2,706 ppm Li (https://americanlithiumcorp.com/falchani-lithium-project). Lithium resources are hosted by Tertiary rhyolitic tuff, breccia, and ignimbrite of the Macusani Volcanic Field (MVF), chiefly by the so-called 'Lithium-rich Tuff' in which Li contents are almost systematically between 3,000 and 4,000 ppm (Nupen 2019).

The general mineralogy of the 'Lithium-rich Tuff' is described and discussed in Segovia-More et al. (2023). It comprises relict igneous quartz, feldspar, and micas, and secondary phases such as fine-grained quartz, clays (kaolinite, dioctahedral smectites), and zeolites. In this abstract, we present the first data available on Li-bearing micas from the 'Lithium-rich Tuff' and nearby granites, breccias, and ignimbrites from the MVF. Variations in mica compositions are discussed focusing on their contribution to the Li endowment and source magmas.

2 Geological setting

The MVF (Fig. 1) is an ignimbrite basin exposed in the Quenamari Meseta, a plateau at an altitude of 4,400 m.a.s.l. in the Eastern Cordillera of southern Peru (Cheilletz et al. 1992). It is part of the Neogene ignimbrite centers of the Central Andes related to tectonic shortening, crustal thickening, and contemporaneous lithospheric removal and thinning (Salisbury et al. 2012; Göğüş et al. 2022). The MVF is located between the Cordillera de Carabaya and the Central Andean backthrust belt, and belongs to the Macusani Structural Zone (Perez et al. 2016) previously known as the Precordillera de Carabaya (Sandeman et al. 1997). It is underlain by Triassic syn-rift continental deposits of the Mitu Group, now exposed in the Eastern Cordillera due to tectonic inversion of the Triassic rift during Cenozoic Andean shortening.

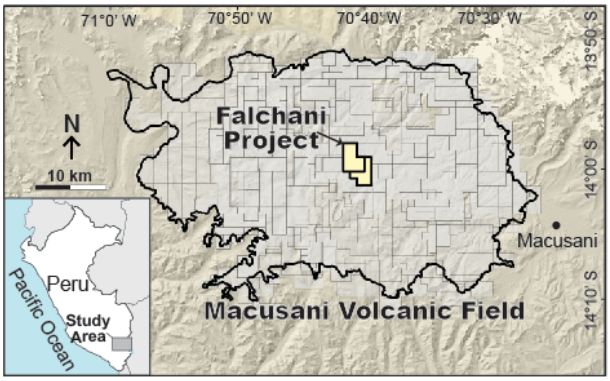

Figure 1. Location of the study area in SE Peru (inset) and of the Falchani Lithium Project concessions in the MVF.

Extrusive and intrusive suites exposed in the Macusani and neighboring volcanic fields represent the youngest igneous events recorded in the Macusani Structural Zone (Clark et al. 1990) and were grouped by Sandeman et al. (1997) into the Crucero Supergroup and the Crucero Intrusive Supersuite, respectively. Volcanic units, including lavas and pyroclastic deposits, were subdivided by these authors into the late Oligocene–early Miocene Picotani Group – comprising medium- to high-K calc-alkaline basalts, shoshonites and S-type rhyodacites and rhyolites – and the mid- to late Miocene Quenamari Group – comprising exclusively silicic peraluminous rocks. In the MVF, volumetrically dominant extrusive rocks belong to the Macusani Formation, the youngest unit of the Quenamari Group. This formation comprises a ~280 to 450 m-thick sequence of strongly peraluminous, rhyolitic, whitish-grey, poorly-consolidated, crystal-rich (~ 45 vol.%), ash-flow tuffs deposited between ca. 10.1 and 6.5 Ma (Cheilletz et al. 1992; Sandeman et al. 1997).

The lithium mineralization in the Falchani project is hosted by rocks of the Macusani Formation. The 'Lithium-rich Tuff' unit has a thickness comprised between 50 and 140 m and is sandwiched between an Upper and a Lower breccia, which are interpreted as deposited in a volcano-sedimentary environment and are also mineralized with average Li contents of ~1,400 and 1,900 ppm, respectively (Nupen 2019). The 'Lithium-rich Tuff' is interpreted to have deposited sub-aerially in an active crater-lake volcano (Nupen 2019).

3 Analytical methods

Point analyses of minerals of the mica group were performed using a CAMECA SXFive electron microprobe (EMPA) at the Centre de Microcaractérisation Raimond Castaing, Toulouse. X-ray (compositional) maps were acquired using a five-channel JEOL JXA-8230 electron microprobe at the Centres Científics i Tecnològics of the University of Barcelona (CCiT-UB). The structural formula of micas was normalized to 11 O, H_2O was determined by assuming (OH+F+Cl) = 2 atoms per formula unit (apfu), and lithium contents were calculated using equations tri1 [SiO_2 > 34 % and MgO < 6 %] and tri2 [SiO_2 > 34 % and MgO > 6 %] of Tischendorf et al. (1997). Raman spectra were obtained on polished thin sections with a HORIBA JobinYvon LabRam HR 800 dispersive spectrometer equipped with an Olympus BXFM optical microscope at the CCiT-UB. Mica grains from a 'lithium-rich tuff' sample were studied by Transmission Electron Microscopy (TEM) to determine the mineral composition by Analytical Electron Microscopy (AEM) in the Thalos microscope of the CIC of the University of Granada, calibrated by natural standards.

3 Results

In the 'Lithium-rich Tuff' unit of the MVF, mica-bearing tuff displays a variety of structures including fine, often contorted, alternating light and dark laminae, as well as nodular, porous, and massive layers. They consist mostly of igneous micas, quartz, and felspars in a matrix composed of quartz plus clay minerals (see Segovia-More et al. 2023). Mica grains are dark brown to black in color and their size ranges between 0.5 and 5 mm. They commonly disrupt the laminations in the tuff and are enclosed in sag structures. Although these mica grains are largely subhedral with straight outlines, some show embayments filled with clay and quartz. In the powder sample studied by TEM, mica appears without a definite morphology or size, but grains have high-crystallinity electron-diffraction and are larger than the co-existing clay minerals.

Mica grains from the 'Lithium-rich Tuff' are characterized by an octahedral occupancy > 2.8 apfu, which classifies them as tri-octahedral. Two contrasting compositions, labelled as zinnwaldite and lepidolite, were found. Zinnwaldites plot in the field of the siderophyllite-polylithionite series close to the siderophylllite end-member (Fig. 2). They yield higher Fe (0.85-1.02 apfu; EPMA data) than Mg (0.26-0.38 apfu) contents, relatively high Ti (0.04-0.09 apfu), and much lower Mn (0.02-0.04 apfu) and Zn (<0.02 apfu). Calculated Li contents are in the range of 0.41 to 0.61 apfu. In the interlayer position, K (0.81-0.90 apfu) is more abundant than Na (0.06-0.10 apfu), whereas the contents of Rb (0.01-0.02 apfu) and of Ca, Cs, and Ba (<0.01 apfu) are much lower. Their F content is of 1.01-1.51 apfu.

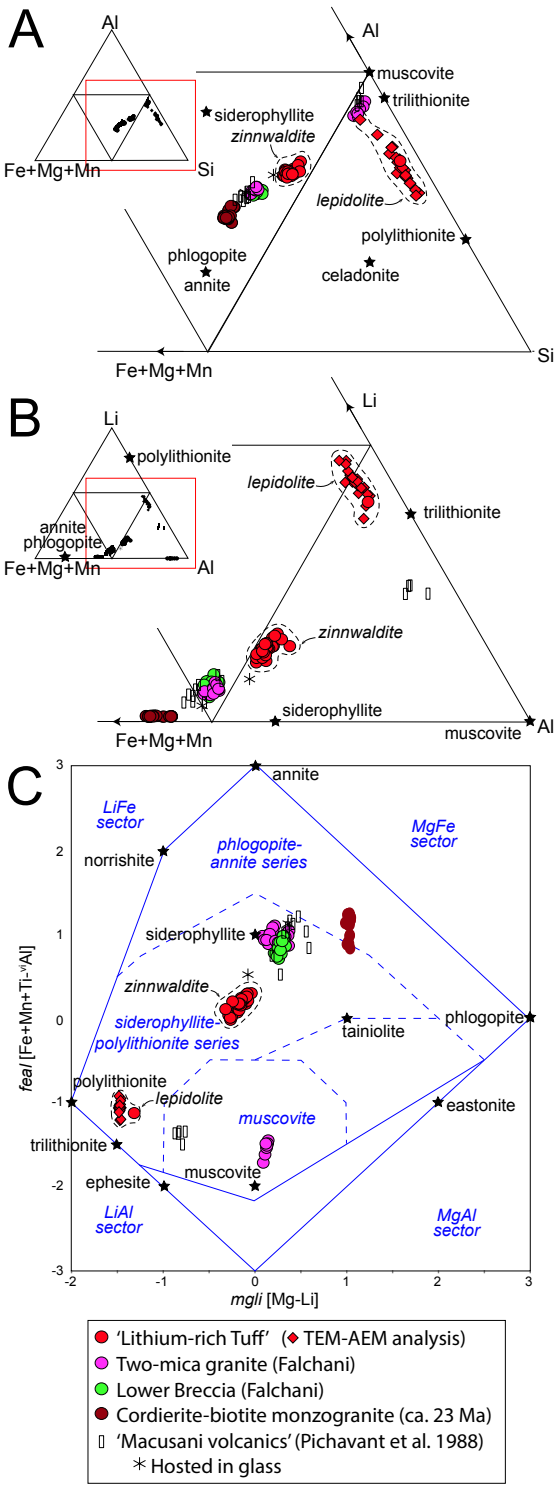

Figure 2. Classification of mica from the MVF in the ternary diagrams after Monier and Robert (1986) (A-B) and the binary diagram after Tischendorf et al. (2007) (C). TEM data were adjusted assuming Li = 1.5 apfu.

Only one EMPA analysis of lepidolite was obtained so far. Its composition plots close to the polylithionite end-member in the classification scheme of Tischendorf et al. (2007). It has a Li content of 1.35 apfu and much lower contents of Fe (0.13 apfu), Mg (0.04 apfu), Mn (0.02 apfu), Ti (0.01 apfu), and Zn (0.01 apfu). The K content (0.85 apfu) is higher than the Na (0.06 apfu), Rb (0.03 apfu), and Cs (0.01 apfu) contents and F is very high, at 2 apfu. This composition agrees nicely with the analyses obtained on TEM on another sample in which zinnwaldite was absent and lepidolite was the only mica present (Fig. 2).

The X-ray maps in Figure 3 show a subhedral mica grain from the 'Lithium-rich Tuff' that is compositionally zoned with a zinnwaldite core and a lepidolite rim. The latter is richer in F and Rb and poorer in Ti than the zinnwaldite core.

Micro-Raman spectra obtained on the core and the rim of the same grain are shown in Figure 4. Zinnwaldite displays one strong band at 190, two weaker bands at 92 and 687, and a shoulder at 646 cm^{-1}, whereas lepidolite is characterized by four strong bands at 93, 177, 255, and 705 cm^{-1}. The latter, at 705 cm^{-1}, is often observed in the lepidolite series, and in the trilithionite and polylithionite endmembers (RRUFF).

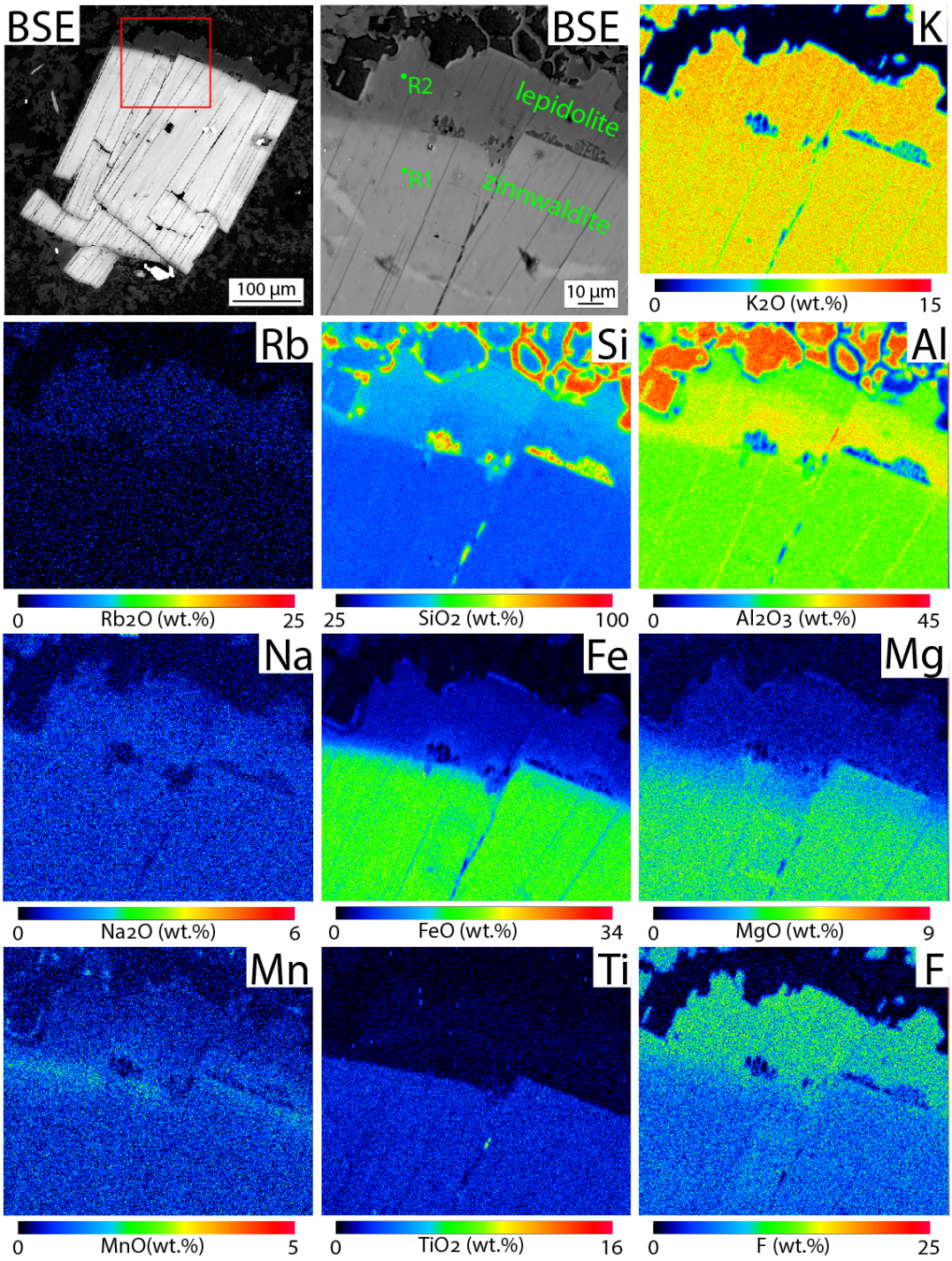

Figure 3. SEM (BSE mode) and quantitative X-ray images of a zoned mica grain from the 'Lithium-rich Tuff' in the Falchani Lithium Project, comprising a zinnwaldite core and a lepidolite rim.

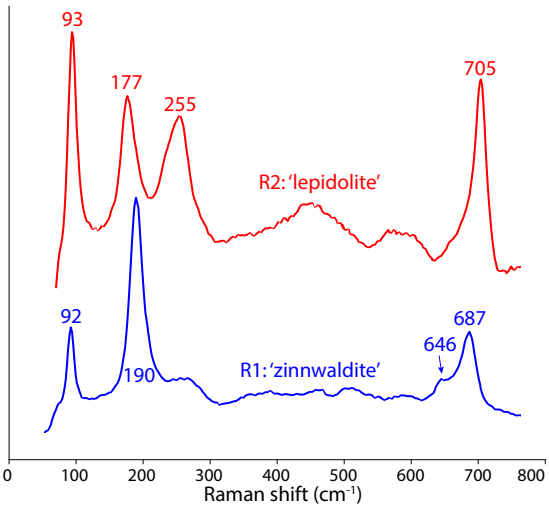

Figure 4. Raman spectra measured in a mica grain from sample 2021-MAC-11, for 20 s (5 accumulations) using a 532 nm laser, a 50x objective and a 50% grating. Location of point analyses (R1 and R2) shown in Fig. 3.

4 Discussion

The correlation between the lithium mineralization and rocks of volcanic origin ascribes the Falchani Lithium Project to the volcanogenic lithium deposit type (Bowell et al. 2020). In volcanogenic lithium deposits, Li enrichment from pre-enriched volcanic or volcanogenic rocks occurs during intense alteration that arises from the circulation of fluids of magmatic and/or meteoric origin in restricted basins such as volcanic calderas (Benson et al. 2017). These authors argue that the large volumes of Li-enriched rhyolites that are needed to form volcanogenic lithium deposits are typically emplaced in intracontinental settings through partial melting or assimilation of thick, felsic crust and, particularly, in strongly evolved melts through fractional crystallization.

The compositions of micas in the 'Lithium-rich Tuff' from the MVF contrast to those of micas in granites and ignimbrites in the area (new data plus published mica analyses in 'Macusani Volcanics' by Pichavant et al. 1988; Fig. 2). In particular, micas from the 'Lithium-rich Tuff' are systematically enriched in Li, Rb, and F relative to micas in the Lower Breccia (Nupen 2019) and nearby two-mica granites. All of them, in turn, are enriched in these elements compared to micas in older (ca 23 Ma; Sandeman et al. 1997), late Oligocene, cordierite-biotite monzogranites found in the southern margin of the MVF (Fig. 2). The marked enrichment in Li and other incompatible elements such as Rb in mica grains preserved in the 'Lithium-rich Tuff' would illustrate crystallization in equilibrium with a highly evolved rhyolitic magma during a particular period of magmatism in the Neogene MVF.

Acknowledgements

We want to thank the geologists from Macusani Yellowcake for the help and hospitality during sampling tasks and to Drs. Philippe de Parseval and Xavier Llovet for assistance during EMPA data acquisition. This research work was supported by the Peruvian PROCIENCIA-FONDECYT project 1122-2020 E041-2020-01-01, and logistically, by the project 2021 SGR 00239 (AGAUR).

References

Benson TR, Coble MA, Rytuba JJ, Mahood GA (2017) Lithium enrichment in intracontinental rhyolite magmas leads to Li deposits in caldera basins. Nat Commun 8:270.

Bowell RJ, Lagos L, de los Hoyos CR, Declercq J (2020) Classification and characteristics of natural lithium resources. Elements 16:259–264.

Cheilletz A, Clark AH, Farrar E, Arroyo Pauca G, Pichavant M, Sandeman HA (1992) Volcano-stratigraphy and $^{40}Ar/^{39}Ar$ geochronology of the Macusani ignimbrite field: monitor of the Miocene geodynamic evolution of the Andes of southeast Peru. Tectonophysics 205:307–327.

Clark AH, Farrar E, Kontak DJ, Langridge RJ, Arenas MJ, France LJ, McBride SL, Woodman PL, Wasteneys HA, Sandeman HA, Archibald DA (1990) Geologic and geochronologic constraints on the metallogenetic evolution of the Andes of southeastern Peru. Econ Geol 85:1520–1584.

Göğüş OH, Sundell K, Uluocak EŞ, Saylor J, Çetiner U (2022) Rapid surface uplift and crustal flow in the Central Andes (southern Peru) controlled by lithospheric drip dynamics. Sci Rep-UK 12:5500.

Monier G, Robert JL (1986) Evolution of the miscibility gap between muscovite and biotite solid solutions with increasing lithium content: an experimental study in the system K_2O-Li_2O-MgO-FeO-Al_2O_3-SiO_2-H_2O-HF at 600 ºC, 2 kbar P H_2O: comparison with natural lithium micas. Mineral Mag 50:641–651.

Nupen S (2019) Mineral Resource Estimates for the Falchani Lithium Project in the Puno District of Peru - under the Guidelines of National Instrument 43-101. The Mineral Corporation, Bryanston, pp 1-72.

Perez ND, Horton BK, Carlotto V (2016) Structural inheritance and selective reactivation in the central Andes: Cenozoic deformation guided by pre-Andean structures in southern Peru. Tectonophysics 671:264–280.

Pichavant M, Kontak DJ, Valencia Herrera J, Clark AH (1988) The Miocene-Pliocene Macusani Volcanics, SE Peru - I. Mineralogy and magmatic evolution of a two-mica aluminosilicate-bearing ignimbrite suite. Contrib to Mineral Petrol 100:300–324.

Salisbury MJ, Jicha BR, de Silva SL, Singer BS, Jiménez NC, Ort MH (2011) $^{40}Ar/^{39}Ar$ chronostratigraphy of Altiplano-Puna volcanic complex ignimbrites reveals the development of a major magmatic province. GSA Bull 123:821–840.

Sandeman HA, Clark AH, Farrar E, Arroyo-Pauca G (1997) Lithostratigraphy, petrology and ^{40}Ar-^{39}Ar geochronology of the Crucero Supergroup, Puno Department, SE Peru. J South Am Earth Sci 10:223–245.

Segovia-More MK, Torró L, Villanova-de-Benavent C, Ramírez-Briones J, Vallance J, Monnier L, Laurent O, Salvi S, Baby P, Proenza JA, Nieto F (2023). High-resolution mineralogy of 'lithium-rich tuff' from the Macusani Volcanic Field, Puno, Peru. This volume.

Tischendorf G, Gottesmann B, Förster H-J, Trumbull RB (1997) On Li-bearing micas: estimating Li from electron microprobe analyses and an improved diagram for graphical representation. Mineral Mag 61:809–834.

Tischendorf G, Förster H-J, Gottesmann B, Rieder M (2007) True and brittle micas: compositions and solid-solution series. Mineral Mag 71:285-320.

Fluid exsolution in the outer zones of the Emmons Pegmatite (Maine, USA)

Laura M. van der Does[1], Niels Hulsbosch[1], Jan Elsen[1], Philippe Muchez[1] and Mona-Liza C. Sirbescu[2]
[1]Department of Earth and Environmental Sciences, KU Leuven, Belgium
[2]Department of Earth and Atmospheric Sciences, Central Michigan University, MI, USA

Abstract. Pegmatites are an important source of critical and rare metals (e.g., Li, Ta, Sn, Nb). Understanding processes occurring during pegmatite crystallization are therefore key to understanding the mechanisms responsible to concentrating these elements. Several contrasting models for pegmatite formation have been put forward but it is still unclear when, and how fluid exsolution occurs. Here we investigate the timing of fluid exsolution through detailed studies of fluid inclusions (FIs) trapped in tourmaline crystals from the outer zones of the Emmons pegmatite, Maine, USA. Comb-like tourmaline from the border zone and quartz-tourmaline intergrowths (QTIs) from the border and wall zones are further subdivided based on morphology. Trapped FIs can be observed in all tourmaline types, with a consistent H_2O-CO_2-NaCl-(N_2-CH_4) and low to moderate salinity composition. The abundance of FIs sharply increases from the center outwards in the QTIs. This variation may result from the crystallization of the skeletal parts of the QTIs from a boundary layer formed around the central tourmaline. The fluid present during crystallization of the central tourmaline, which contains numerous melt inclusions and only rare primary fluid inclusions was exsolved as highly localized pools, whereas it was more prevalent in the boundary layer during skeletal tourmaline crystallization.

1 Introduction

Granitic pegmatites provide an important source for rare and critical metals, gemstones, and industrial minerals. LCT (Li-Cs-Ta) pegmatites, like the Emmons Pegmatite, are of particular importance as they may host high concentrations of Ta, Nb and Sn among other critical metals (Linnen et al. 2012). Studying the pegmatite-forming processes is important for understanding advanced magma evolution and the concentration of rare metals. Although previous studies indicate that many of these elements become concentrated as a result of magmatic processes, element enrichment in pegmatites at the magmatic-hydrothermal transition and the hydrothermal stage are not yet fully understood (Linnen et al. 2012).

The importance of an aqueous phase for pegmatite formation has been suggested by Jahns & Burnham (1969), inferring that an exsolved aqueous fluid is needed for the formation of pegmatites. Experimental and natural studies indicate that up to three different immiscible fluids can be present, simultaneously, during pegmatite formation, one of which is a low-saline aqueous fluid (Thomas et al. 2000; Veksler and Thomas 2002; Veksler et al. 2002; Veksler 2004).

A contrasting model has been put forward by London (1999, 2009, 2014, 2018) that suggests that the pegmatites form from a single-phase, hydrous melt. These studies acknowledge that the melt must be water and flux rich at least near the crystal surfaces to enhance the diffusion rates required to grow large crystals (London 2009) and that, ultimately, fluid exsolution occurs at late stages to form miarolitic cavities and replacement units (e.g., London 1986).

Most studies focus on fluid saturation in the transition from granite to pegmatite or between the internal zones of the pegmatite (Sirbescu and Nabelek 2003; Hulsbosch et al. 2016; Hulsbosch and Muchez 2020). This study instead examines, in detail, fluid inclusions (FIs) from the outer zones of the pegmatite, to learn more about the temporal evolution occurring on a much smaller scale.

The main aim, of this study, is to trace when and how fluid saturation happens in the border and wall zone of the internally zoned Emmons pegmatite. This is done through detailed studies of FIs trapped in tourmaline crystals, by petrography, microthermometry and Raman spectroscopy.

The Emmons Pegmatite is a relatively thin (5-10 m) internally zoned, miarolitic dike, located in the Oxford Pegmatite field, Maine, USA (Falster et al. 2019). Samples studied here all originate from the border and wall zone. This pegmatite is highly enriched in B, Li, Cs and Ta and hosts many rare minerals (Falster et al. 2019). The pegmatite is intruded into the metasedimentary rocks belonging to the Sebago Migmatite Domain (Solar and Tomascak 2009) and is thought to have been derived by anatexis of the metamorphic country rock (Falster et al. 2019) as opposed to fractionation from a parental pluton. No significant alteration or contact metamorphism occurred as the dike was intruded into the country rock (García-Serrano et al. 2017)

1.1 Tourmaline textures and morphology types

Two different textures were studied: subhedral prisms of comb-like tourmaline (5-10 cm) (Type 1) nucleating directly on the pegmatite border and quartz-tourmaline intergrowths (QTIs) from the wall zone (up to 30-40 cm in length). The QTIs are divided into three types, based on their morphology (Figure 1): larger, prismatic, central tourmaline (Type 2), less euhedral, second tier tourmaline, extending from Type 2 (Type 3) and skeletal tourmaline surrounding the central and second tier tourmaline (Type 4).

Type 1 tourmaline is the paragenetically earliest, nucleating directly on the border between

host rock and pegmatite. The QTIs occur further inwards in the wall zone and consequently crystallize later in the paragenetic sequence.

Studies on the QTIs by van der Does et al. *(in review)* infer that a boundary layer has an influence on the formation of the QTIs. A boundary layer forms around the first, rapidly growing tourmaline crystal (Type 2) in the QTIs. It will progressively become concentrated in elements incompatible in tourmaline, which includes H_2O and other fluxing elements, such as F and Li. This boundary layer becomes concentrated in components that are incompatible in tourmaline, which includes water. Based on the boundary layer model by van der Does et al. *(in review)*, Type 2 tourmaline is the paragenetically earliest, in the QTIs, followed by Type 3 and lastly Type 4.

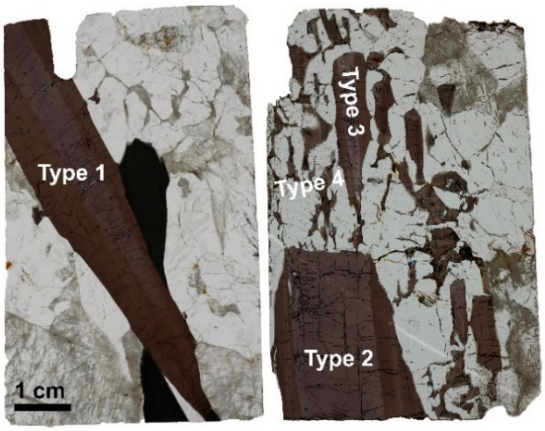

Figure 1. Micrographs of comb-like tourmaline (left) and a quartz-tourmaline intergrowth (right).

2 Methods

Doubly polished wafers were examined using an Olympus BX40 petrographic microscope to identify FI assemblages and types. Selected FI assemblages underwent cooling and heating using a Linkam MDS600 heating-freezing stage, mounted on an Olympus BX51 microscope, at the Department of Earth and Environmental Sciences, KU Leuven to measure phase transition temperatures including CO_2 melting (Tm_{CO2}), clathrate melting (Tm_{CL}) and CO_2 homogenization (Th_{CO2}) of the FI. The eutectic temperature (Tfm) and final ice melting (Tm_{ice}) temperatures were not clear for most FIs. Therefore, only a limited number of temperatures were acquired for these phase transitions. Inclusions were first cooled to -120˚C, to ensure they were entirely frozen. Heating rates varied from 10-30˚C/min but were reduced to 1˚C/min near phase transitions.

The composition of the homogenized carbonic phase was analyzed using a Horiba Jobin-Yvon LabRAM HR evolutions spectrometer coupled to an Olympus BX41 confocal microscope at the Department of Chemistry, KU Leuven. A 532 nm Nd:YAG laser was used to excite the carbonic phase and the scattered light was subsequently measured with a Peltier-cooled Synapse (EM)-CCD detector. Results were processed in LabSpec 6.5.2 software to calculate the molar fractions gaseous species in the carbonic phase.

3 Results

3.1 Fluid inclusion petrography

Fluid inclusions occur in all studied tourmaline types. This study only focusses on primary inclusions, that were recognized as clusters of FIs that occur unrelated to fractures. Generally, Types 1 and 2 have the least abundance of FIs (on average 7-8 analysed FIs per sample) and typically FI assemblages are only composed of 1-3 FIs (Figure 2). The inclusion assemblage is mainly dominated by primary clusters and pseudosecondary trails of melt inclusions (MIs). The amount of FIs increases in Type 3 (on average 10 FIs analysed per sample) and especially in Type 4 (on average 27 FIs analysed per sample). In the latter types, fields are usually composed of many more FIs together (Figure 2). MIs still occur, but the inclusion assemblage is dominated by FIs. The FIs found in Types 1 and 2 tend to be larger in size ($\bar{x}$ = 44 µm and $\bar{x}$ = 61 µm, respectively) compared to FIs in Types 3 and 4 ($\bar{x}$ = 34 µ and $\bar{x}$ = 27 µm, respectively).

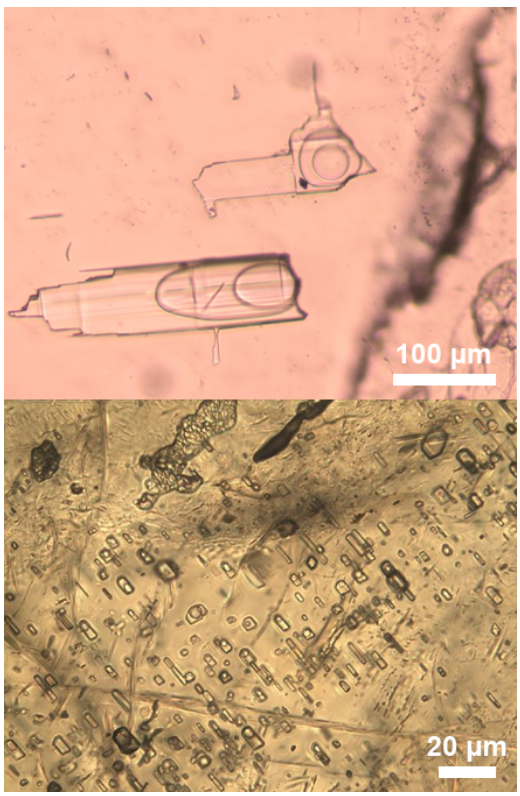

Figure 2. Typical FI fields in Type 2 tourmaline (top) and Type 4 tourmaline (bottom).

3.2 Fluid properties

The temperatures at which the different phase transitions occur are similar for the four tourmaline types (Table 1). Tm_{CO2} varies between -61.1˚C and -56.6˚C, Tm_{CL} between 6.2˚C and 9.9˚C, and Th_{CO2} has a large range between 7.9˚C and 30.2˚C., but

generally Th_{CO2}>20˚C. The largest variations are seen within Types 1 and 2. Type 2 trends to higher Th_{CO2}, but this appears to be mainly caused by one sample having higher Th_{CO2} than other FIs in Type 2 tourmaline.

Tfm could not always be clearly observed, so only a few temperatures were acquired (n=10). The acquired Tfm vary between -21.9˚C and -21.3˚C. Tm_{ice} overlap in Types 2, 3 and 4, with temperatures ranging from -11.5˚C to -3.6˚C (n=43), while Tm_{ice} in Type 1 extend to higher temperatures (-2.3˚C to -0.6˚C, n=3).

Table 1. Ranges, means and number of measurements for selected phase transitions in the different tourmaline types studied.

Tourmaline type	Tm_{CO2}	Tm_{CL}	Th_{CO2}
Type 1	-58.5˚C – -57.0˚C x̄ = -57.7˚C n = 14	6.6˚C – 9.2˚C x̄ =7.8 ˚C n = 14	7.8˚C – 28.1˚C x̄ = 22.2˚C n = 14
Type 2	-61.6˚C – -56.6˚C x̄ = -57.7˚C n = 36	6.2˚C – 9.9˚C x̄ = 7.7˚C n = 37	9.6˚C – 30.2˚C x̄ = 25.6˚C n = 36
Type 3	-58.8˚C – -56.6˚C x̄ = -57.6 ˚C n = 28	7.0˚C – 9.5˚C x̄ = 8.0˚C n = 30	8.8˚C – 28.8˚C x̄ = 25.5˚C n = 29
Type 4	-59.3˚C – -56.7˚C x̄ = -57.5 ˚C n = 74	6.6˚C – 9.9˚C x̄ = 8.1˚C n = 79	8.2˚C – 29.3˚C x̄ = 24.6˚C n = 79

Raman measurements (Figure 3) reveal that the vapor phase is heavily dominated by CO_2 (70-100%, majority >90%). N_2 composes up to 30%, while CH_4 usually makes up less than 5%. The carbonic phases are generally similar between the tourmaline types.

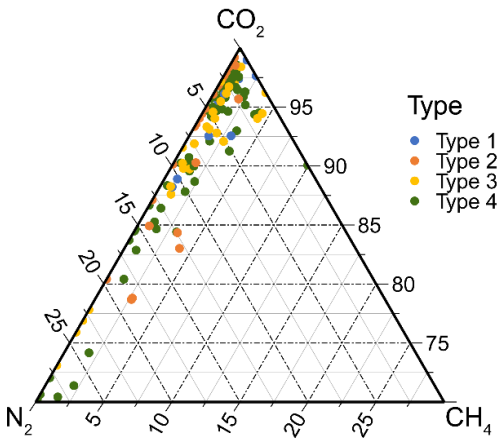

Figure 3. Ternary diagram of the composition of the carbonic phase in the fluid inclusions.

Salinity and density (Table 2) were calculated using the Q2 program from Bakker (1997). Where no Raman data was acquired, the equation from Darling (1991) was used. The salinity falls within the same range for the four tourmaline types, between 0.1 and 8.5 wt% NaCl eq. The densities show a large range, especially in Types 1 and 4, that overlaps in all tourmaline types.

Table 2. Ranges, means and number of measurements for the density and salinity of FIs in the different tourmaline types.

Tourmaline type	Density (g/cc)	Salinity (wt% NaCl eq.)
Type 1	0.5 – 1 x̄ = 0.8 n = 14	2.2 – 6.4 x̄ = 5.0 n = 14
Type 2	0.7 – 1 x̄ = 0.8 n = 35	0.7 – 8.5 x̄ = 4.8 n = 37
Type 3	0.6 – 1 x̄ = 0.8 n = 30	0.1 – 7.0 x̄ = 4.0 n = 27
Type 4	0.5 – 0.9 x̄ = 0.7 n = 67	0.4 – 7.4 x̄ = 4.2 n = 77

4 Discussion

The phase transition temperatures and composition of the fluid do not vary significantly among the different tourmaline types, so it is concluded that this is the same fluid type throughout all tourmaline types. However, the calculated densities show a large variation in this parameter, caused by the large variation of temperature of the phase transitions within each tourmaline type, such as the Th_{CO2} values. Tfm just below -21˚C infers that the fluid is dominantly H_2O-NaCl. The slight negative offset from the eutectic for this system could indicate that some amount of KCl is also present in the system. However, determining Tfm during microthermometric measurements was very difficult, therefore it is uncertain how precise the temperatures were determined. The high proportion of CO_2 in the carbonic phase, and only moderate to low proportions of N_2 and CH_4 indicate the vapor phase is strongly dominated by CO_2 in most FIs. Together, these observations demonstrate a H_2O-CO_2-NaCl-(N_2-CH_4) composition of the FIs.

The fluid has a relatively low salinity compared to other FIs found in the outer zones of pegmatites from the Gatumba-Gitarama pegmatite field in Rwanda (e.g. Hulsbosch et al. 2016; Hulsbosch and Muchez 2020). Lower salinity FIs in pegmatites have been reported by Sirbescu and Nabelek (2003), in pegmatites associated with the Harney Peak Granite in South Dakota, USA. They consider the low salinity fluids to represent the first exsolved magmatic fluid.

The presence of primary FIs in the tourmaline from the border and wall zone of the Emmons Pegmatite indicates that water saturation occurred very early in the crystallization of the pegmatite. The lack of significant alterations around the pegmatite (García-Serrano et al. 2017) indicates that no exsolved aqueous fluid was present upon intrusion of the dike. Studies on other pegmatites also found primary FIs in the outer zones, and

made a similar conclusion (e.g Mulja and Williams-Jones 2018; Hulsbosch and Muchez 2020). The increase in FI abundance from Types 1 and 2 to Types 3 and 4 tourmaline indicates changes in some factors, influencing the trapping potential. The lower abundance in Types 1 and 2 could indicate that the exsolved fluid was only present as localized droplets forming at the crystal-liquid interface during rapid crystallization. The FIs in Types 3 and 4 are less localized in the crystal and FI fields are larger, which could suggest an exsolved fluid was more abundant in their crystallization environment. Experimental studies have shown that a H_2O-undersaturated melt can reach local fluid exsolution in e.g. a melt boundary layer (London and Morgan 2017; Sirbescu et al. 2017). A melt boundary layer is suggested, for the formation of the QTIs by van der Does *(in review)*. The increase in FI abundance, and decrease in MI abundance, could therefore be caused by the progressive concentration H_2O, leading to fluid exsolution, in the boundary layer formed around the rapidly crystallizing Type 2 tourmaline. Although less prevalent, MIs continue to be present in Types 3 and 4 tourmaline, indicating that these types also crystallized in the presence of a magma and not solely from a fluid.

5 Conclusion

The fluid, trapped in the tourmaline of the border and wall zone of the Emmons Pegmatite, is a low to moderate saline fluid with an H_2O-CO_2-NaCl-(N_2-CH_4) composition. CO_2 dominates the vapour phase in most FIs. The fluid properties do not vary significantly between the different tourmaline types studied.

The presence of FIs in all tourmaline types studied indicates that fluid exsolution occurs very early in the formation of the Emmons Pegmatites. The fluid exsolution likely occurs as localized droplets on the crystal-melt interface, during the crystallization of Types 1 and 2, but changes to a more pervasive exsolution, constrained in a melt boundary layer, during crystallization of Types 3 and 4.

Acknowledgements

Herman Nijs (KU Leuven) is thanked for preparation of the wafers used in this study. The Raman equipment was acquired via the medium-scale research infrastructure FWO grant Raman-SIM^2 (number I000718N).

References

Bakker RJ (1997) Clathrates: Computer programs to calculate fluid inclusion V-X properties using clathrate melting temperatures. Comput Geosci 23:1–18. https://doi.org/10.1016/S0098-3004(96)00073-8

Darling RS (1991) An extended equation to calculate NaCl contents from final clathrate melting temperatures in H_2O-CO_2-NaCl fluid inclusions: Implications for P-T isochore location. Geochim Cosmochim Acta 55:3869–3871. https://doi.org/10.1016/0016-7037(91)90079-K

Falster AU, Simmons WB, Webber KL, et al (2019) The Emmons Pegmatite, Greenwood, Oxford County, Maine. Rocks Miner 94:498–519. https://doi.org/10.1080/00357529.2019.1641021

García-Serrano J, Roda-Robles E, Villaseca C, Simmons W (2017) Fe-Mn-(Mg) distribution in primary phosphates and silicates, and implications for the internal evolution of the Emmons rare-element pegmatite (Maine, USA). NGF Abstr Proc 2:37–40

Hulsbosch N, Boiron MC, Dewaele S, Muchez P (2016) Fluid fractionation of tungsten during granite-pegmatite differentiation and the metal source of peribatholitic W quartz veins: Evidence from the Karagwe-Ankole Belt (Rwanda). Geochim Cosmochim Acta 175:299–318. https://doi.org/10.1016/j.gca.2015.11.020

Hulsbosch N, Muchez P (2020) Tracing fluid saturation during pegmatite differentiation by studying the fluid inclusion evolution and multiphase cassiterite mineralisation of the Gatumba pegmatite dyke system (NW Rwanda). Lithos 354–355:105285. https://doi.org/10.1016/j.lithos.2019.105285

Jahns RH, Burnham CW (1969) Experimental Studies of Pegmatite Genesis: I. A model for the Derivation and Crystallization of Granitic Pegmatites. Econ Geol 64:843–864. https://doi.org/10.2113/gsecongeo.64.8.843

Linnen RL, Van Lichtervelde M, Černý P (2012) Granitic Pegmatites as Sources of Strategic Metals. Elements 8:275–280. https://doi.org/10.2113/gselements.8.4.275

London D (1986) Formation of tourmaline-rich gem pockets in miarolitic pegmatites. Am Mineral 71:396–405

London D (1999) Melt Boundary-Layers and the Growth of Pegmatitic Textures. Can Mineral 37:826–827

London D (2009) The Origin of Primary Textures in Granitic Pegmatites. Can Mineral 47:697–724

London D (2014) A petrologic assessment of internal zonation in granitic pegmatites. Lithos 184–187:74–104. https://doi.org/10.1016/j.lithos.2013.10.025

London D (2018) Ore-forming processes within granitic pegmatites. Ore Geol Rev 101:349–383. https://doi.org/10.1016/j.oregeorev.2018.04.020

London D, Morgan GB (2017) Experimental Crystallization of the Macusani Obsidian, with Applications to Lithium-rich Granitic Pegmatites. J Petrol 58:1005–1030. https://doi.org/10.1093/PETROLOGY/EGX044

Mulja T, Williams-Jones AE (2018) The physical and chemical evolution of fluids in rare-element granitic pegmatites associated with the Lacorne pluton, Québec, Canada. Chem Geol 493:281–297. https://doi.org/10.1016/j.chemgeo.2018.06.004

Sirbescu M-LC, Nabelek PI (2003) Crystallization conditions and evolution of magmatic fluids in the Harney Peak Granite and associated pegmatites, Black Hills, South Dakota - Evidence from fluid inclusions. Geochim Cosmochim Acta 67:2443–2465. https://doi.org/10.1016/S0016-7037(02)01408-4

Sirbescu M-LC, Schmidt C, Veksler I V., et al (2017) Experimental Crystallization of Undercooled Felsic Liquids: Generation of Pegmatitic Texture. J Petrol 58:539–568. https://doi.org/10.1093/petrology/egx027

Solar GS, Tomascak PB (2009) The Sebago Pluton and the Sebago Migmatite Domain, southern Maine: Results from New Studies. 2009 Annu Meet Northeast Sect Geol Soc Am Field Trip:1–24

Thomas R, Webster JD, Heinrich W (2000) Melt inclusions in pegmatite quartz: Complete miscibility between silicate melts and hydrous fluids at low pressure. Contrib to Mineral Petrol 139:394–401. https://doi.org/10.1007/s004100000120

Veksler I, Thomas R, Schmidt C (2002) Experimental evidence of three coexisting immiscible fluids in synthetic granitic pegmatite. Am Mineral 87:775–779. https://doi.org/10.2138/am-2002-5-621

Veksler I V. (2004) Liquid immiscibility and its role at the magmatic-hydrothermal transition: a summary of experimental studies. Chem Geol 210:7–31. https://doi.org/10.1016/j.chemgeo.2004.06.002

Veksler I V., Thomas R (2002) An experimental study of B-, P- and F-rich synthetic granite pegmatite at 0.1 and 0.2 GPa. Contrib to Mineral Petrol 143:673–683. https://doi.org/10.1007/s00410-002-0368-3

Large-scale HFSE and REE mobility linked to the formation of vein-type U-deposits in the Moldanubian Zone of the Bohemian Massif

Martin Kubeš[1,2], Vojtěch Wertich[1,2], Jaromír Leichmann[1], Markéta Holá[1], Julien Mercadier[3], Michel Cuney[3]
[1]Masaryk University, Brno, Czech Republic
[2]Czech Geological Survey, Prague, Czech Republic
[3]Université de Lorraine, Nancy, France

Abstract. Multi-element EMP maps and analyses of major accessory phases and their possible alteration products from ultrapotassic rocks (durbachites), in combination with LA-ICP-MS analyses of hydrothermal U-mineralization, provided constraints on potential U source of vein-type U-deposits in the Moldanubian Zone of the Bohemian Massif. The extensive metal mobilization in durbachites, recorded by EMP imaging, was controlled by self-induced radiation damage (metamictization) and subsequent fluid-driven alteration of U-bearing phases (thorite, allanite, zircon). Unusual trace element signatures of low-T hydrothermal U-mineralization (e.g., extremely high Zr, Nb, Ti, ∑REE) from the vein-type deposits reflect the large-scale HFSE and REE mobility via aqueous solutions. The character of late alteration of primary phases (zircon dissolution vs. resistance of apatite) and mineral assemblages of hydrothermal phases in durbachites (e.g., synchisite, F-rich titanite, monazite) indicates the importance of alkali-, F-, and P-rich fluids in the formation of U-deposits. The infiltration of oxidized, highly alkaline basinal brines likely played a key role in HFSE and REE mobility during the Permian hydrothermal event, as suggested by EMP chemical dating of U-mineralization.

1 Introduction

The Moldanubian Zone of the Variscan Bohemian Massif (Figure 1a, b) usually hosts significant hydrothermal U-deposits associated with shear zones in the high-grade metamorphic basement. The formation of hydrothermal U-deposits in the entire European Variscan belt is assumed to be related to the fluid-driven alteration of Late-Carboniferous peraluminous granites (Cuney 2009). However, within the Bohemian Massif, there is a lack of evidence of genetic and/or spatial link of vein-type U-mineralization to U fertile leucogranites, thus a potential U source remains a matter of debate. Accordingly, the high-grade metamorphic complexes hosting the Moldanubian U-deposits are currently considered as possible U source, related to hydrothermal decomposition of U-bearing accessories.

In the largest Moldanubian U-deposit (the Rožná deposit with total mine production of 23 000 t U), three major mineralization events were previously described (Kříbek et al. 2009): (1) pre-U quartz-sulfide and carbonate-sulfide mineralization, (2) U-mineralization, and (3) post-U quartz-carbonate-sulfide mineralization. As a result of the hydrothermal U-mineralizing event, three different types of U ore have formed in the Rožná deposit: (1) network-disseminated Coff>Urn in cataclasites of shear zones (2) Urn (±Coff) in carbonate veins, and (3) disseminated Coff (±Urn) in metasomatites adjacent to shear zones (Kříbek et al. 2009). The aim of this study was to identify the potential U source of the vein-type U-mineralization.

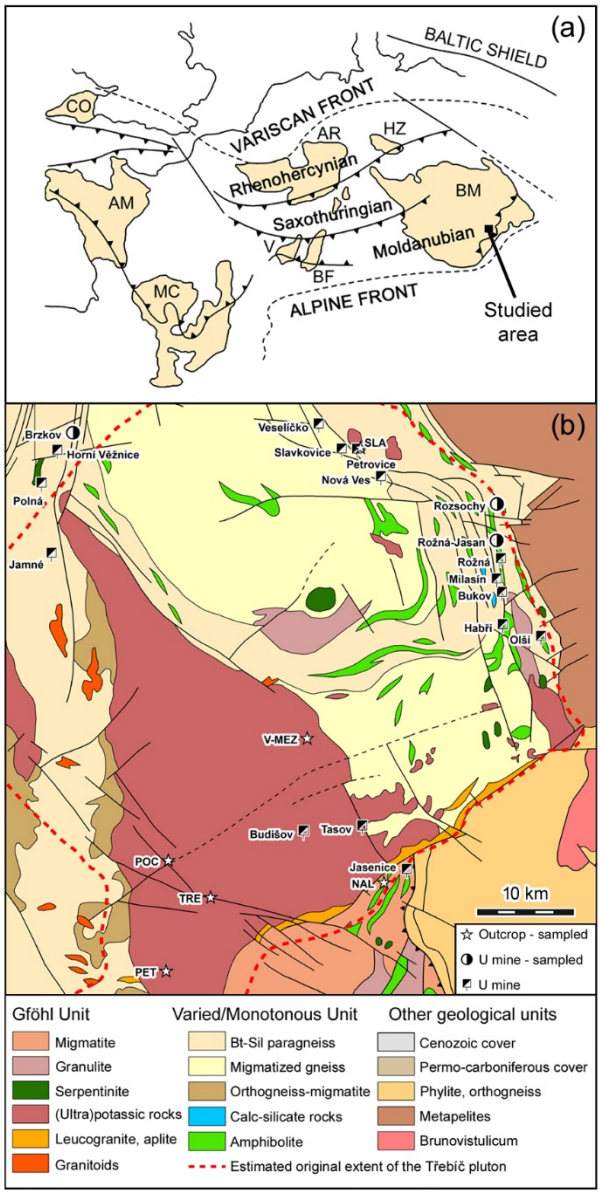

Figure 1. a Location of the Moldanubian U-deposits in the regional frame of western-central Europe. **b** Detail of sample locations in the Moldanubian Zone. Geological map modified after Kubeš et al. (2022).

Despite similar, low-temperature conditions of the origin of the vein-type U-mineralization in the Moldanubian Zone (150–170 °C; Kříbek et al. 2009), individual deposits are characterized by different chemical composition. They commonly exhibit highly variable rare earth element (REE) patterns and may incorporate a significant amount of high field strength elements (HFSE) in unaltered pristine uraninite (Wertich et al. 2022).
To explain such unusual trace element chemistry of U-deposits in the Moldanubian Zone, we focused on important U-bearing phases in highly alkaline (ultra)potassic rocks that experienced late fluid-driven alteration responsible for extensive HFSE and REE mobilization according to our previous findings (Kubeš et al. 2021). Particularly, element distribution imaging represents a powerful tool for obtaining direct evidence for the mobilization of incompatible elements from minerals during a fluid-driven alteration and could thereby help to determine which regions may correspond to primary sources of U and other metals in geological environment.

2 Methodology

In total, 9 samples of high-grade U ore from the Rožná-Jasan, Rozsochy and Brzkov deposits (3 samples from each locality) (Figure 1b) were gathered from the archives of Moravian Museum and DIAMO s.e. (organization dealing with the remediation of former U mining activities). These particular deposits were selected to decipher the origin of their anomalous trace element chemistry (high Zr, Nb, Ti, ∑REE; Wertich et al. 2022) and, importantly, identify the main source of these metals.
Building upon our previous observations of extreme mobility of HFSE and REE in highly alkaline K-rich syenites (Kubeš et al. 2021), (ultra)potassic plutons of durbachites series were sampled, some of which are spatially associated with U-deposits. The individual samples sites (Figure 1b) included localities within the Třebíč pluton (Pocoucov = POC, Petrůvky = PET, Třebíč = TRE, Velké Meziříčí = V-MEZ) and its smaller satellite bodies near Nové Město na Moravě (Slavkovice = SLA) and Náměšť nad Oslavou (Naloučany = NAL).
Major accessory phases from polished thin sections of durbachite samples were studied using backscattered electron (BSE) imaging and electron microprobe (EMP) imaging and analyses. Polished thin sections of selected ore samples were used for reflected light microscopy and BSE imaging in order to precisely earmark unaltered uraninite domains suitable for laser ablation-inductively coupled plasma-mass spectrometry (LA-ICP-MS) analyses.
BSE images together with the chemical composition of main U-bearing phases in durbachites were obtained by EMP Cameca SX 100 at the Department of Geological Sciences, Masaryk University, Brno. Operating conditions for spot analyses were as follows: wavelength-dispersive mode, an accelerating voltage of 15 kV, a beam current of 6–20 nA, and a beam size of 2–10 μm for primary accessory phases (zircon, apatite, thorite, uraninite, allanite, Th-rich monazite) and their alteration products (REE-fluorocarbonate, F-rich titanite, Th-poor monazite). X-ray element maps were acquired with an accelerating voltage of 15 kV, step size of 1 μm using a fully focused electron beam, and dwell time of 0.1 s.
Trace element concentrations of U-mineralization were measured by LA-ICP-MS at the Department of Chemistry, Masaryk University, Brno. The system consisted of Analyte G2 laser ablation device and Agilent 7900 ICP-MS analyser with an octopole reaction cell. The laser operated at a wavelength of 213 nm with a pulse duration ~4 ns. Spot ablations with a 50 μm spot diameter, repetition rate of 10 Hz, and fluence of 9 J cm were performed for 60 s. External calibration was performed using the standard reference materials (SRM) NIST 610 and NIST 612. More than 50 isotopes representing both the major components and trace elements of the samples were monitored with a total integration time of 4.5 s.

3 Deciphering potential U source

Within the following sections, based on the chemical composition of low-T hydrothermal vein-type U-mineralization and major primary U-bearing phases and their alteration products in durbachites, this contribution unravels the potential U source of the Moldanubian ore deposits and describes major physicochemical factors controlling large-scale HFSE and REE mobility in hydrothermal fluids.

3.1 Chemistry of U-mineralization

A typical feature of analysed uraninite samples from the studied hydrothermal low-T vein-type U-deposits is their significant HFSE enrichment (e.g., Zr, Nb, Ti) resembling those of granite/pegmatite-hosted U-deposits (Figure 2a, b). Moreover, REE patterns of uraninite significantly differ between individual vein-type deposits (Figure 2c). Uraninite from the Brzkov deposit typically shows LREE-enriched patterns (La_N/Yb_N 3.41–19.65) along with considerably high ∑REE (up to 1.12 wt%). By contrast, uraninite from the Rozsochy deposit has HREE-enriched patterns (La_N/Yb_N 0.01–0.59) similar to uraninite from the Rožná-Jasan deposit with relatively less pronounced HREE enrichment (La_N/Yb_N 0.29–1.48).
Observed anomalous HFSE enrichment along with highly variable REE patterns of uraninite simply rule out a different genetic type and formation temperature of hydrothermal vein-type U-deposits as the major mechanism controlling their unusual trace element signatures, considering the similar mineralogical and textural features of uraninite typical of low-temperature shear zone-hosted U veins (Kříbek et al. 2009).

Contrarily, the uncommon HFSE signatures and conspicuously variable REE patterns (Figure 2) are most likely a result of a combination of the chemistry of mineralizing fluids and element availability in the main source region. From this follows that our observations provide constraints on important physicochemical factors controlling HFSE and REE mobility in ore-forming fluids and major metal sources from which these incompatible elements were leached during fluid-rock interaction.

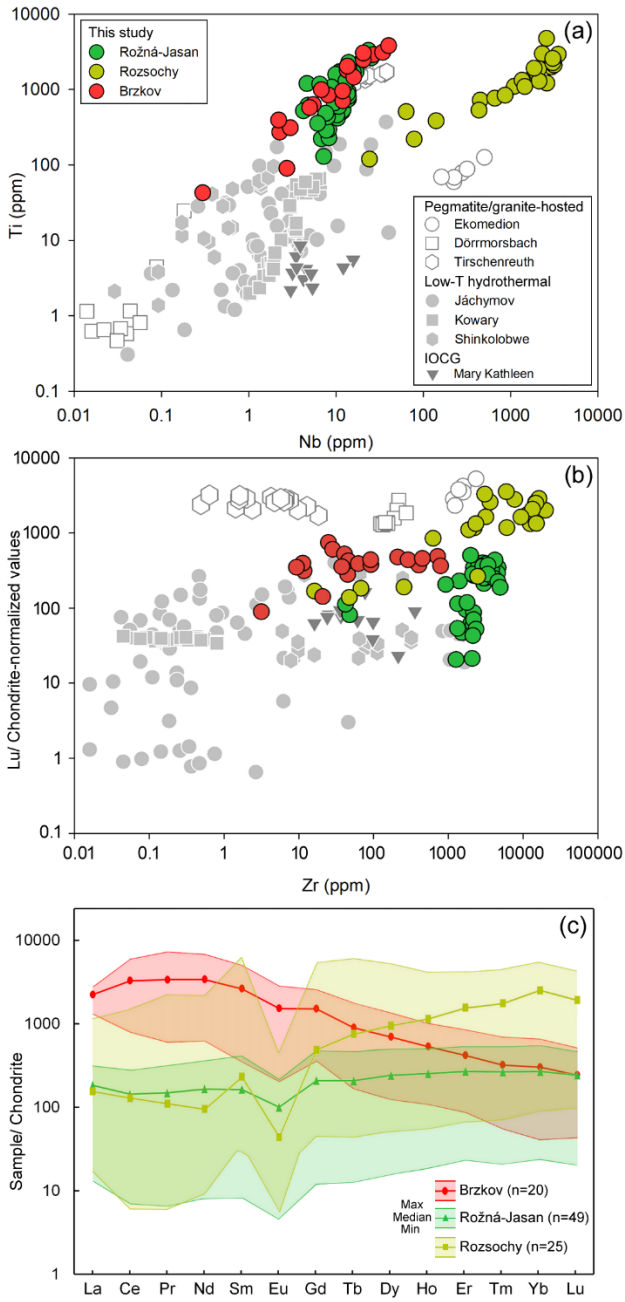

Figure 2. a, b Trace element chemistry of low-T hydrothermal uraninite from the Moldanubian deposits. Chemical composition of uraninite from different deposit types is from Frimmel et al. (2014). **c** Chondrite-normalized REE patterns of uraninite. Standardized values are from McDonough and Sun (1995).

3.2 Leaching metals from durbachites

Building up on our previous findings, highly alkaline potassic to ultrapotassic rocks of durbachite series experienced extensive post-magmatic hydrothermal alteration responsible for the leaching of HFSE and REE from their initial primary sources (Kubeš et al. 2021, 2022). The massive mobilization of U together with HFSE and REE in durbachites is well-documented by EMP imaging and analyses of their main U-bearing phases (Figure 3). Subsequent to metamictization of major U carrier in durbachites, radiation-damaged thorite experienced pervasive fluid-driven alteration, as evidenced by low BSE intensity, deficient EMP analytical totals, highly variable and low ThO_2 and UO_2 contents typical of altered thorite domains. In addition, rare occurrences of pristine magmatic uraninite, an easily leachable phase during oxidizing fluid circulation (Cuney 2009), observed in some durbachite samples suggest that most uraninite was probably entirely decomposed due to fluid-rock interaction. Apart from the abundant thorite, other refractory U-bearing minerals usually include zircon and allanite, both of which became metamict over a time interval sufficient to release U and other metals from their crystal structure during subsequent fluid-induced alteration, as documented by BSE imaging of extensively altered allanite and EMP maps showing the pervasive dissolution of metamict zircon triggering massive HFSE remobilization (Figure 3). Indeed, the variable REE signatures of Moldanubian vein-type U-deposits suggest the decomposition of two or more sources, at least one HREE- and one LREE-dominated (e.g., zircon vs. allanite). For instance, the extensive metal leaching from radiation-damaged zircon was triggered by interaction with post-magmatic hydrothermal fluids infiltrating through microfractures formed by volume expansion due to zircon metamictization (Kubeš et al. 2021). Accordingly, enhanced HFSE mobility in circulating hydrothermal fluids is reflected by presence of Zr-Th-U-Si phase that typically fills abundant microfractures intimately surrounding metamict zircon (Figure 3). Thus, the extreme HFSE and REE mobilization linked to the extensive dissolution of major U-bearing phases in durbachites provide the most likely explanation for the unusual chemistry of Moldanubian U-deposits.

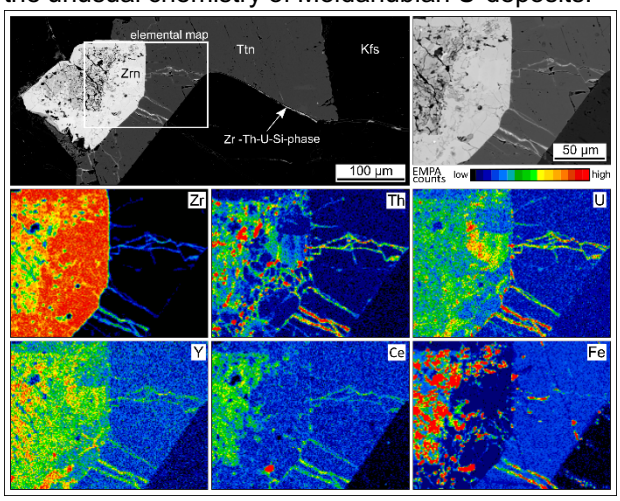

Figure 3. BSE image and EMP maps showing massive fluid-driven HFSE mobilization from altered zircon. Abbreviations: Zrn = zircon, Ttn = titanite, Kfs = K-feldspar.

The character of prevailing hydrothermally-derived accessory minerals in durbachites, such as REE-fluorcarbonates and Th-poor monazite after primary allanite and F-rich titanite after biotite, indicates that transport of incompatible elements was controlled by CO_2-, F-, and P-rich fluids. The replacement of chloritized biotite by hydrothermal F-rich titanite suggests that altered biotite supplied a significant F amount to interacting fluids through extensive chloritization. The key role of fluoride as one of the principal complexing ligands in fluids is further supported by: (1) high F content in hydrothermal Zr-Th-U-Si phase and altered primary thorite and Th-rich monazite (2) enhanced solubility of Th-rich monazite (3) extensive Th mobilization, and (4) presence of secondary fluorite in strongly altered durbachite samples. Furthermore, the pervasive zircon dissolution and resistance of apatite to alteration demonstrate alkaline conditions of the hydrothermal system (pH 8–12). Besides, dissolution of magmatic uraninite in durbachites and subsequent complexation of U in fluids, illustrated in Figure 3, points towards oxidizing conditions of the hydrothermal alteration. Taken together, the large-scale fluid-driven HFSE and REE mobilization, reflected by anomalous trace element signatures of low-T hydrothermal U-mineralization from the Moldanubian deposits (Figure 2a, b), was controlled by highly alkaline, oxidized aqueous solutions containing F- and P-dominated complexing ligands. The EMP chemical dating of U-mineralization revealed main Permian mineralizing event (ca. 270 Ma; Wertich et al. 2022) responsible for the formation of hydrothermal vein-type U-deposits in the Moldanubian zone. The recognition of the Permian age of the Moldanubian U-deposits suggests the importance of oxidized highly alkaline basinal brines, important ore-forming fluids in the entire Variscan belt (Cuney 2009), generated from Permo-Carboniferous sedimentary cover overlaying the crystalline basement hosting many hydrothermal U-deposits (Kříbek et al. 2009). Taking into account a much larger original extent of the highly alkaline (ultra)potassic intrusions, intervening up to the important tectonic boundary between Gföhl and Svratka Units (Leichmann et al. 2017) where most Moldanubian U-deposits are located (Figure 1b), HFSE- and REE-rich durbachites can account for an important source of U and other metals released during the infiltration alkaline brines triggering the pervasive dissolution of main U-bearing phases.

4 Conclusions

The unusual trace element chemistry of the low-T hydrothermal vein-type deposits (high Zr, Nb, Ti, ∑REE) and their close spatial association with HFSE- and REE-rich durbachite intrusions in the Moldanubian Zone of the Bohemian Massif most likely point towards their mutual genetic relation. We propose that radiation damage of major refractory minerals likely enhanced permeability due to their volume expansion, which facilitated fluid-mineral interaction and thus promoted HFSE and REE leaching from their source. The release of U and other metals from durbachites was documented by EMP distribution maps and analyses of main accessory phases. The large-scale mobility of incompatible elements, reflected by HFSE and REE enrichment typical of some Moldanubian U-deposits, could have been related to the infiltration of oxidized, alkaline basin-derived waters that became mineralizing fluids during the interaction with basement-hosted durbachites (release F and P during alteration) and gave rise to the formation of U-deposits during the Permian hydrothermal event.

Acknowledgements

This research was carried out under the OP VVV project CZ.02.1.01/0.0/0.0/16_026/0008459 (GeoBarr) from the European Regional Development Fund, and was supported also by the Czech Grant Agency (GACR) project GA22-33820S.

References

Cuney M (2009) The extreme diversity of uranium deposits. Miner Deposita 44:3–9.

Frimmel HE, Schedel S, Brätz H (2014) Uraninite chemistry as forensic tool for provenance analysis. Appl Geochem 48:104–121.

Kříbek B, Žák K, Dobeš P, Leichmann J, Pudilová M, René M, Scharm B, Scharmová M, Hájek A, Holéczy D, Hein UF, Lehmann B (2009) The Rožná uranium deposit (Bohemian Massif, Czech Republic): shear zone-hosted, late Variscan and post-Variscan hydrothermal mineralization. Miner Deposita 44:99–128.

Kubeš M, Leichmann J, Wertich V, Mozola J, Holá M, Kanický V, Škoda R (2021) Metamictization and fluid-driven alteration triggering massive HFSE and REE mobilization from zircon and titanite: Direct evidence from EMPA imaging and LA-ICP-MS analyses. Chem Geol 586, 120593.

Kubeš M, Leichmann J, Buriánek D, Holá M, Navrátil P, Scaillet S, O'Sullivan P (2022) Highly evolved miaskitic syenites deciphering the origin and nature of enriched mantle source of ultrapotassic magmatism in the Variscan orogenic root (Bohemian Massif, Moldanubian Zone). Lithos 432, 106890

Leichmann J, Gnojek I, Novák M, Sedlák J, Houzar S (2017) Durbachites from the Eastern Moldanubicum (Bohemian Massif): erosional relics of large, flat tabular intrusions of ultrapotassic melts–geophysical and petrological record. Int J Earth Sci 106:59–77.

McDonough W, Sun SS (1995) The composition of the Earth. Chem Geol 120:223–253.

Wertich V, Kubeš M, Leichmann J, Holá M, Haifler J, Mozola J, Hršelová P, Jaroš M (2022) Trace element signatures of uraninite controlled by fluid-rock interactions: A case study from the Eastern Moldanubicum (Bohemian Massif). J Geochem Explor 243, 107111.

Preliminary results of U-Pb dating and trace element analysis of cassiterites from the Western Sudetes, SW Poland

Władysław Zygo[1], Krzysztof Foltyn[1], Tonny Bernt Thomsen[2], Benjamin Dominguez Heredia[2], Adam Piestrzyński[1]
[1]Faculty of Geology, Geophysics and Environmental Protection, AGH University of Science and Technology in Kraków, Poland
[2]Geological Survey of Denmark and Greenland (GEUS), Department for Mapping and Mineral Resources, Copenhagen, Denmark

Abstract. Many tin deposits in Central Europe (e.g. Erzgebirge) are related to the emplacement of granites at the late stages of the Variscan Orogeny. The cassiterite crystals from selected, primary tin occurrences in Western Sudetes (Gierczyn-Przecznica, Czarnów, Piława Górna pegmatite) where investigated using LA-ICP-MS age of the mineralisation and trace elements composition. The results of cassiterite age from Czarnów and Piława Górna are slightly older than available data (dating of zircons, monazites and uraninites). The age of cassiterite from Gierczyn-Przecznica reveals that two distinguished types of cassiterite represent two separate events. The first event at 353±14 and 360±5 Ma can be related to the regional metamorphism event while the second is younger (318±6 Ma) and can be associated with the emplacement of the Karkonosze Granite.

1 Introduction

Cassiterite has been found in many places in Western Sudetes in SW Poland, either in primary rocks or in placers. In the mica-quartz-chlorite schists of the Stara Kamienica Schist Belt, accumulations were significant enough to warrant extraction of tin in the past but despite interest and exploration efforts in the 20th century, mining has not been resumed and the resources are considered subeconomic. Origin of this deposit is not yet fully understood and it is assumed that the tin-polymetallic mineralisation most likely originated from complex interplay of hydrothermal, magmatic and metamorphic processes (Małek and Mikulski 2021), but the details are still a matter of discussion and several genetic models have been suggested (for detailed reference list see Michniewicz et al. 2006 and Mochnacka et al. 2015). The "usual suspect" is hydrothermal activity related to granitic intrusion, either to the Cambrian-Ordovician granitic protolith of the Izera Gneisses (pre-metamorphic, e.g. Michniewicz et al. 2006) while others to the Variscan Karkonosze Granite (post-metamorphic e.g. Mochnacka et al. 2015).
The main aim of this work was to conduct U-Pb dating of cassiterite and study trace elements in them in order to provide new data on geochronology and origin of the mineralisation. Additional cassiterites collected in two other locations in Sudetes (Czarnów and Piława Górna) were also analyzed for comparison.

2 Geological setting

2.1 Gierczyn-Przecznica area

The Karkonosze–Izera Massif (KIM) is located in the south-central part of the West Sudetes on the NE margin of the Bohemian Massif, at the border of Poland and Czech Republic (Figure 1). The KIM can be subdivided into the Karkonosze Granite intrusion and its metamorphic envelope. Granite bodies crystallized around 312-306.9 Ma (Mikulski et al. 2020). The Izera Massif part consists of the texturally diversified Izera Gneisses, which were formed during Late Devonian to Early Carboniferous deformations of Early Palaeozoic porphyritic Izera and Rumburk granites (Oberc-Dziedzic et al. 2005). The Izera-Kowary Unit contains several W-E extending metasedimentary belts composed of mica schists with minor interbeds of amphibolite, calc-silicate rocks, quartzite and quartz–feldspar schist, all metamorphosed under conditions of upper greenschist and lower amphibolite facies (Żelaźniewicz et al. 2003). The Stara Kamienica Schist Belt dipping toward the north at angles of 37.5-57.5°, hosts low-grade cassiterite mineralisation disseminated in the chlorite–mica–quartz schist (in some cases also rich in almandine garnet), locally accompanied by a polymetallic sulphide/sulphosalt association with the dominance of chalcopyrite and pyrrhotite (Michniewicz et al. 2006, Mochnacka et al. 2015 and references therein). The tin-bearing schists are 100-200 m thick and surrounded on both sides by barren schist, distinction between them is based on geochemical data (Sn content > 0.004%) rather than lithological boundaries (Michniewicz et al. 2006).
Two types of cassiterite have been distinguished in the area, "brown" and "colourless".

2.2 Czarnów

The eastern parts of the Izera–Kowary Unit (IKU) include the Kowary Gneisses and the Czarnów Schist Formation, composed of mica schists, marbles, erlans, skarns, amphibolites and quartzofeldspathic rocks. Czarnów deposit consist of a steeply dipping (80° toward SE) SW-NE trending, 0.5–3 m thick quartz-ore vein, located at the tectonic contact of schists and calc-silicate rocks (Mochnacka et al. 2015).
The ore mineralisation is composed mostly of massive or coarse-grained euhedral crystals of

arsenopyrite and pyrrhotite that form lens-like bodies within the main quartz vein, or semi-massive impregnations in the country rocks (Mikulski et al. 2020). Minor quantities of pyrite, chalcopyrite, stibnite, cassiterite, magnetite or galena with sphalerite were also noted. Two separate generations of early formed cassiterite crystallized at temperatures of 440–384 °C and 340–300 °C at a pressure of 1.2–1.1 kbar from a fluid with total salinity 24–16 wt.% of NaCl equivalent (Mikulski et al. 2007). Several stages of ore crystallization have been identified, at least the main two of which were genetically associated with contact metasomatic and post-magmatic activity in the KP (Mikulski et al. 2007, Mikulski 2010).

The zircon grains from Czarnów porphyritic granite gave the weighted mean $^{206}Pb/^{238}U$ age from 14 analyses of 312.0 ± 2.9 Ma (Mikulski et al. 2020) while a similar Re-Os age (312 ± 3 Ma) has been obtained for Co-bearing arsenopyrite (Mikulski and Stein 2011). High-temperature Fe-Cu-As-Sn mineralisation was fractured, brecciated and overprinted by a younger generation of base metal sulphides, with visible Au and Bi-Ag-Te-Se sulphosalt mineralisation (Mikulski et al. 2020).

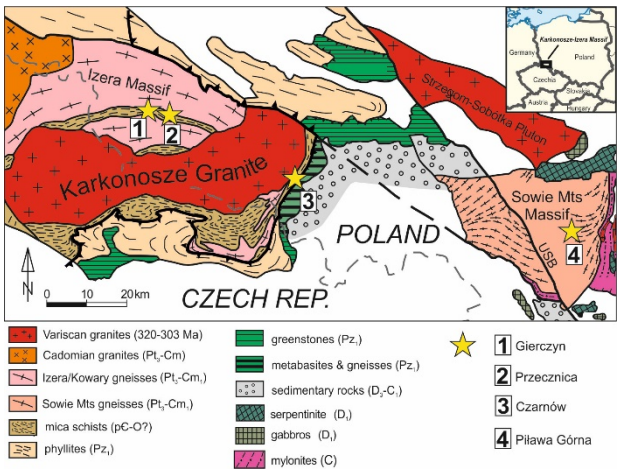

Figure 1. Geological map of Western Sudetes with the location of cassiterites collected for this study

2.3 Piława Górna

One of the major geological units of the Central Sudetes is the triangular Góry Sowie Block (Figure 1). It is composed predominantly of migmatitic para- and orthogneisses, amphibolites, and minor granulites, garnet meta-peridotites, pegmatites and calc-silicate rocks (Żelaźniewicz 1990). The late Proterozoic–Early Cambrian protolith underwent polymetamorphic evolution. An early high-pressure/high-temperature (HP–HT) episode at 400-395 Ma was followed by amphibolite-facies migmatisation ca. 385-380 Ma and rapid cooling ca. 370-360 Ma (Kryza and Fanning 2007, Szuszkiewicz et al. 2013). Decompression resulted in local partial melting and formation of pegmatites from anatectic granitic magmas (Szuszkiewicz et al. 2013). The metamorphic suite is cut by granites, aplites, pegmatites, rhyolitic and lamprophyric dikes as well as by barite and quartz hydrothermal veins.

The pegmatites are composed mainly of microcline, Na-plagioclase, quartz, biotite and muscovite, accompanied by schorl, almandine-spessartine garnet and beryl (Pieczka et al. 2018). Pegmatites show geochemical variability and range from primitive and moderately fractionated pegmatites, enriched in Nb-REE-Be-B and belonging to the NYF (niobium-yttrium-fluorine) pegmatitic family, to rare and much more strongly fractionated pods in the axial parts of the largest dykes that contain Li-Cs-Ta-Be-B mineralisation of the LCT (lithium-caesium-tantalum) type (Pieczka et al. 2018). In both types cassiterite crystals were observed.

3 Samples and methods

3.1 Samples

Cassiterite in samples from Gierczyn and Przecznica (Stara Kamienica Schist Belt) typically occurs as a small (20-200 μm) translucent grains with white/colorless internal reflections (Figure 2 A-B), disseminated in a quartz-mica-chlorite schist. “Spongy” cassiterite with brown internal reflections, sometimes intergrown with the more common translucent cassiterite, are more rare but was also targeted for LA-ICP-MS study (Figure 2 C-D). Due to small sizes, only coarser aggregates were selected for the U-Pb dating and trace elements analysis.

Cassiterite in Czarnów occurs as aggregates of subhedral to euhedral crystals (500-1000 μm in size), often forming intergrowths with arsenopyrite. Internal reflections reveal zonation in some of the cassiterite crystals.

Material from Piława Górna is represented by an approximately 7 mm large cassiterite crystal.

3.2 Methods

Chemical analyses of cassiterite in micro area were carried out using a JEOL JXA-8230 Super Probe electron microprobe at the Laboratory of Critical Elements AGH-KGHM in Kraków.

U-Pb dating of cassiterite as well as trace elements were analysed at the LA-ICP-MS facility at GEUS in Copenhagen employing an Element 2 single-collector magnetic sector field inductively coupled plasma mass spectrometer (SF-ICPMS) that is coupled to an NWR 213 nm Nd:YAG laser ablation system. All data were collected with laser spot diameter of 40 μm (pre-ablation of 50 μm), a laser repetition rate of 10 Hz and laser energy density of between 3.5 and 4.0 J/cm^2. The GJ1 zircon and NIST612 glass standard were used as a primary non-matrix-matched standards to correct for instrumental Pb-isotope fractionation and calculation of trace elemental compositions.

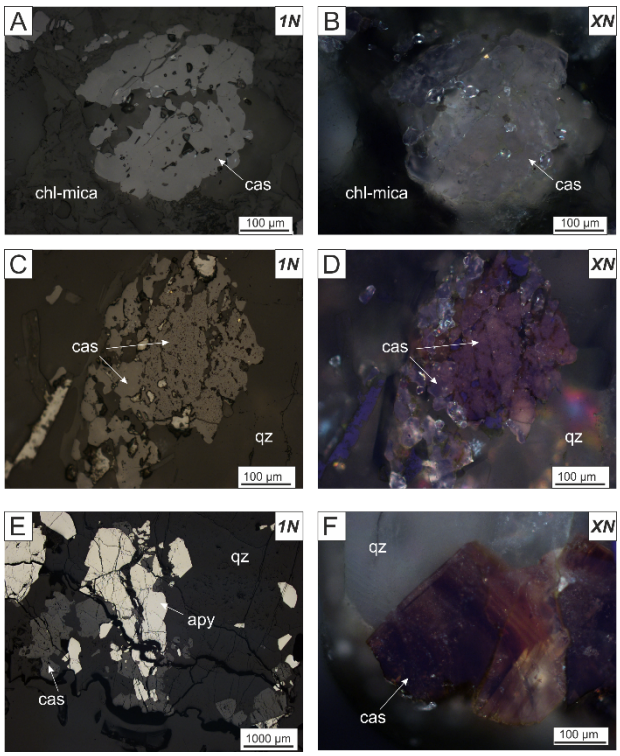

Figure 2. Photomicrographs of cassiterite from Gierczyn-Przecznica and Czarnów. A-B Typical quartz-chlorite mica schist hosted cassiterite with white/colorless internal reflections. C-D Przecznica, example of two intergrown types of cassiterite: one with white/colorless internal reflections and second "spongy" one with brownish internal reflections. E Typical cassiterite-arsenopyrite association from Czarnów. F Oscillatory zoned cassiterite from Czarnów

4 Results

4.1 Trace elements

Investigation of trace elements composition in cassiterites can help to distinguish different tin mineralisation types (Wang et al. 2022 and references therein). Although Wang et al. 2022 study only a few selected types of Sn mineralisation, pegmatite, greisen, skarn and quartz-vein types clearly cluster in different fields.

The LA-ICP-MS analyses of cassiterites from Gierczyn-Przecznica, Czarnów and Piława Górna reveal significant differences between them. The cassiterites from Piława Górna are enriched in Ta and Nb, in Czarnów the same trend is observed for W and V. In the Gierczyn-Przecznica area, Hf and Mn are depleted, while these elements are enriched in the other types.

The trace elements composition of cassiterite from Czarnów show significant variations (Figure 3) this can be explained by presence of crystal zonation (Figure 2F).

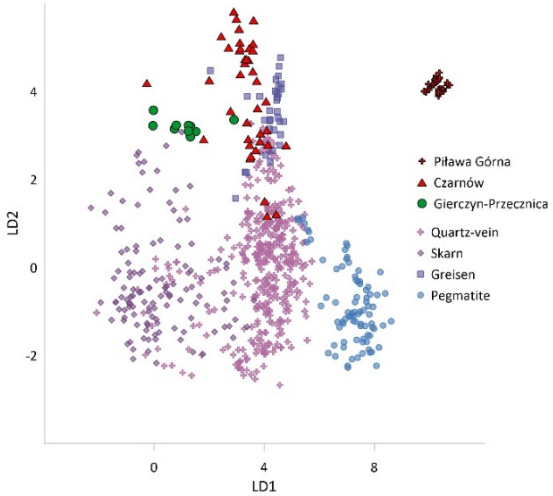

Figure 3. Discrimination diagram for the mineralisation types of cassiterite based on the fingerprint elements after Wang et al. (2022)

4.2 Geochronology

The small grain size made the analyses difficult, and those that were successful, point to 353±14 and 360±5 Ma age of the translucent cassiterite, whereas "spongy" grains yielded younger dates towards 318±6 Ma (Figure 4).

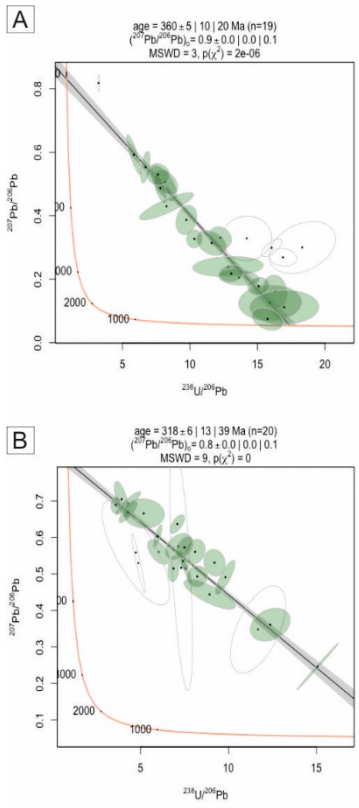

Figure 4. Tera–Wasserburg U–Pb plots for cassiterites from the Gierczyn-Przecznica tin deposit. (A) Plots reveal the cassiterite age at 360±5 Ma; (B) Plots reveal the cassiterite age at 318±6 Ma

Results from Czarnów (332±1 Ma) are older than the Re-Os age (312 ± 3 Ma) (Figure 5B) obtained for Co-bearing arsenopyrite by Mikulski and Stein (2011). Similarly, cassiterite from Piława Górna

(404±1 Ma) gave age slightly older (Figure 5A) than previous geochronological studies (e.g., 377.6-380.7 Ma).

Difference of approximately 6% between established ages and results for Czarnów and Piława Górna presented here might be partially due to non-matrix matched standard used for analyses. However, even assuming that similar differences exist for cassiterite from Gierczyn and Przecznica (there is no geochronological data for comparison), translucent cassiterite still seems to precede the emplacement of the Karkonosze Granite. Devonian/Early Carboniferous ages are coeval with the regional metamorphism which might suggest that the obtained data could in fact represent the resetting of U-Pb ages during metamorphism. Younger, 'spongy" cassiterite age is contemporaneous with the emplacement of the Karkonosze Granite.

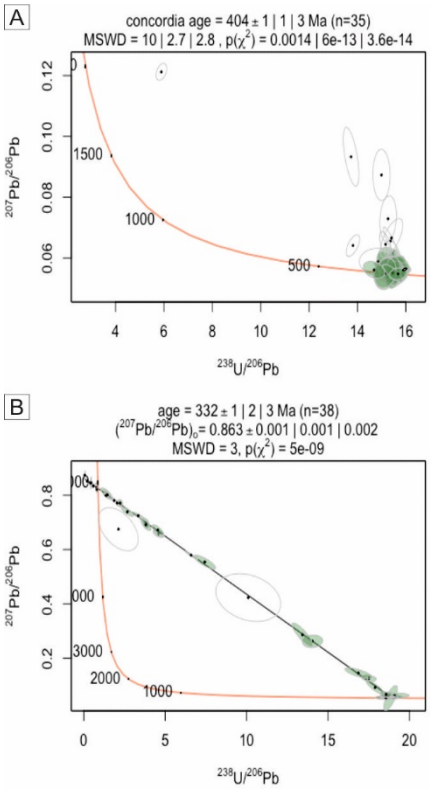

Figure 5. Tera–Wasserburg U–Pb plots for cassiterites from the Piława Górna (A) and Czarnów (B). The cassiterite age for Piława Górna – 404±1 Ma and for Czarnów – 33 ±1 Ma

Acknowledgements

This activity was carried out under the project "Enhanced Use of Heavy Mineral Chemistry in Exploration Targeting (MinExTarget)" that received funding from the European Institute of Innovation and Technology (EIT), a body of the European Union, under Horizon 2020, the EU Framework Programme for Research and Innovation. This work was partially funded by statutory funds of the Faculty of Geology, Geophysics and Environmental Protection, AGH University of Science and Technology, Kraków, Poland (No. 16.16.140.315).

References

Kryza R, Fanning CM (2007) Devonian deep-crustal metamorphism and exhumation in the Variscan Orogen: evidence from SHRIMP zircon ages from the HT-HP granulites and migmatites of the Góry Sowie (Polish Sudetes). Geodin Acta 20(3):159-175

Małek R, Mikulski SZ (2021) A rare indium-bearing mineral (Zn-In-Cu-Fe sulphide) from the Stara Kamienica Schist Belt (Sudetes, SW Poland). Geological Quarterly. http://dx.doi.org/10.7306/gq.1572

Michniewicz M, Bobiński W, Siemiątkowski J (2006) The mineralisation in the middle part of the Stara Kamienica Schist Belt (Western Sudetes). Prace PIG 185:5-136 (in Polish with English summary)

Mikulski SZ (2010) The characteristic and genesis of the gold-bearing arsenic polymetallic mineralisation in the Czarnów deposit (Western Sudetes). Biuletyn PIG 439:303-320 (in Polish with English summary)

Mikulski SZ, Kozłowski A, Speczik S (2007) Fluid inclusion study of gold-bearing quartz-sulphide veins and cassiterite from the Czarnow As deposit ore (SW Poland). In: Colin AJ et al. (ed) Mineral exploration and research: digging deeper, Proceedings of the 9th SGA Biennial Meeting, Dublin, Ireland. Cambridge Mineral Resources, Navan, pp 805-808

Mikulski SZ, Stein HJ (2011) Re-Os age for molybdenite from the Variscan Karkonosze massif and its eastern metamorphic cover (SW Poland). In: Barra F et al. (ed) Let's Talk Ore Deposits, Proceedings of the 11th SGA Biennial Meeting, Antofagasta, Chile. Ediciones Universidad Católica del Norte, Antofagasta, pp 130–133

Mikulski SZ, Williams IS, Stein HJ, Wierchowiec J (2020) Zircon U-Pb Dating of Magmatism and Mineralizing Hydrothermal Activity in the Variscan Karkonosze Massif and Its Eastern Metamorphic Cover (SW Poland). Minerals. https://doi.org/10.3390/min10090787

Mochnacka K, Oberc-Dziedzic T, Mayer W, Pieczka A (2015) Ore mineralisation related to geological evolution of the Karkonosze–Izera Massif (the Sudetes, Poland) - Towards a model. Ore Geol Rev 64:215-238

Oberc-Dziedzic T, Pin C, Kryza R, (2005) Early Palaeozoic crustal melting in an extensional setting: petrological and Sm-Nd evidence from the Izera granite-gneisses, Polish Sudetes. Int J Earth Sci 94:354–368

Pieczka A, Gołębiowska B, Jeleń P, Włodek A, Szełęg E, Szuszkiewicz A (2018) Towards Zn-dominant tourmaline: A case of Zn-rich fluor-elbaite and elbaite from the Julianna system at Piława Górna, Lower Silesia, SW Poland. Minerals. https://doi.org/10.3390/min8040126

Speczik S, Wiszniewska J (1984) Some comments about stratiform tin deposits in the Stara Kamienica Chain (southwestern Poland). Miner Deposita 19(3):171-175

Szuszkiewicz A, Szełęg E, Pieczka A, Ilnicki S, Nejbert K, Turniak K, Michałowski P (2013) The Julianna pegmatite vein system at the Piława Górna mine, Góry Sowie Block, SW Poland–preliminary data on geology and descriptive mineralogy. Geological Quarterly 57:467-484

Wang C, Zhao K, Chen J, Ma X (2022) Examining fingerprint trace elements in cassiterite: Implications for primary tin deposit exploration. Ore Geol Rev 149:105082

Żelaźniewicz A (1990) Deformation and metamorphism in the Góry Sowie gneiss complex, Sudetes, SW Poland. Neues Jahrb Geol Palaontol Abh 179:129–157

Żelaźniewicz A, Nowak I, Achramowicz S, Czapliński W, Ciężkowski A, Wojewoda J (2003) The northern part of the Izera-Karkonosze Block: a passive margin of the Saxothuringian terrane. In: Ciężkowski W et al. (ed) Sudety Zachodnie–od wendu do czwartorzędu WIND, Wrocław, pp 17-32. (in Polish with English summary)

Genthelvite from the world-class beryllium-polymetallic deposit - Perga, Ukraine

Adam Piestrzyński1, Barbara Zygo[1], Władysław Zygo[1], Jadwiga Pieczonka[1], Anatolyi Berezovsky[2]
[1]AGH University of Science and Technology, Faculty of Geology, Geophysics and Environmental Protection, Krakow, Poland
[2] Kryvyi Rih National University, Kryvyi Rih, Ukraine

Abstract. Beryllium deposit Perga is located in the north-west part of Ukraine (Zhytomyr region). Geologically, it is situated within the Perga complex, which is the part of the Sushchano-Perga zone (NW of the Ukrainian Shield). The mineralization is related to rare metal granites (apogranites), in which are responsible for the variety of mineral species and geochemically unusual signature. About 70 minerals are distinguished within the boundaries of the complex. They belong to different classes (silicates and aluminosilicates, oxides, phosphates, sulphides, haloids and native elements).

1 Introduction

The Perga beryllium deposit is a unique phenomenon on a global scale – it is the only object in the world, in which commercial concentrations of beryllium are associated with a very rare mineral – a genthelvite ($Zn_4Be_3(SiO_4)_3S$). This deposit was discovered in the late 1960's, covers an area of approximately 21 km2 and is confined to the Perga granites. Systematic exploration of the Perga deposit has begun in 1950's and continues to present days. In the period of 1960-1977, detailed exploration work was carried out (Metalidi et al. 1977) and based on the results of these works, reserves of beryllium ores were calculated and approved in 1977.

2 Geological settings

2.1 Regional geology

The Perga beryllium deposit is located in the northern part of the Ukrainian shield, within the Sushchano-Perga faults zone, which separates the Korosten and Osnitsk blocks (Figure 1 and 2). The Korosten block is part of the Volyn megablock and includes mostly Palaeoproterozoic rocks. The Osnitsk block belongs to the Osnitsk-Mikashevitsky volcanic belt. The deposit is restricted to the middle part of the Sushchano-Perga zone, which is distinguished as the Perga ore field (Figure 2). Deep fault zones isolate the Volyn megablock from other large tectonic elements of the Ukrainian Shield (Metalidi et al. 1997, Pieczonka et al. 2016). From the north and northwest, the Volyn mega block is separated from the Osnitsk-Mikashevitsky volcanic belt by the Sushchano-Perga faults zone. In the south, it is set apart from the Podole megablock by the Andrushivsky faults zone. In the east, the Zvizdal-Zalesk faults zone splits the Volyn megablock from the Brusilov suture zone (Metalidi et al. 1997). Repeated tectonic activations of the Volyn megablock led to numerous displacements of the block and its parts in both vertical and horizontal directions. The Sushchano-Perga faults zone is a system of faults striking in north-easterly directions. It has a width of 0.5-15 km and a length of about 200 km. The planes of individual faults in the Sushchano-Perga zone dip north-westward and have dip angles of 50–80º. Dynamo-metamorphism and intrusive magmatism manifested repeatedly within the boundaries of the Sushchano-Perga zone. This zone is an ore control structure and contains deposits and ore occurrences of rare, rare-earth, non-ferrous and noble metals. The Sushchano-Perga zone is composed of various rocks of different ages. Among them, the most widespread are quartzites, disthenic quartzites, greisens, syenites, alkaline syenites, alkaline metasomatites, granites, granite-porphyries, and subalkaline granites. The main ore mineralization of the Sushchano-Perga zone is associated with granites, which are distinguished under the name Perga granites. The Perga ore field is characterized by extensive development of alkaline metasomatites. The most common metasomatites are quartz-feldspar, albite - K-feldspar, and biotite-K-feldspar metasomatites (Metalidi and Nechaev 1983).

Figure 1. Location of Perga deposits within the Ukrainian Shield (not to scale)

The most productive part of the Perga complex is located between the Plotnitsky and Ubort faults, where metasomatically altered syenites and Perga granites contains Be, Zr-REE and Nb-Ta-F mineralization (Dagelaysky 1997).

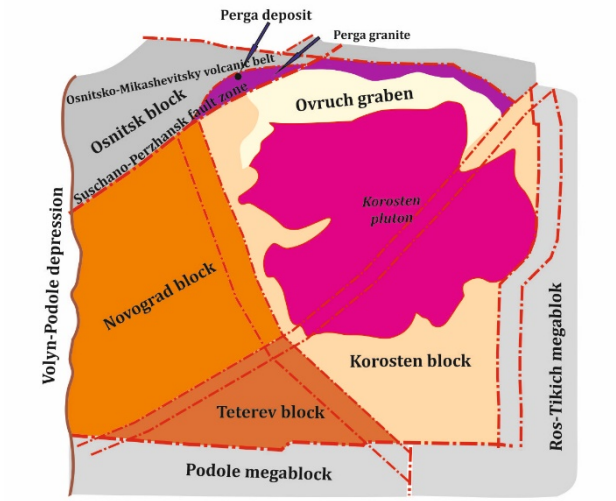

Figure 2. Structural map of Volyn megablock (not to scale).

The Perga ore field is composed of alkali syenites and granites enriched in volatile substances that are subjected to widespread metasomatosis. These granites were identified as apogranites (albitized and greizenised granites around the edges of intrusions, commonly enriched in rare metals - including Nb, Ta, Li, Rb, Be, Sn, W, Mo) (Galetsky 1974 vide Dagelaysky 1997).

2.2 Ore mineralization

The rocks that build the Perga complex (Figure 3) are characterized by the occurrence of a diverse set of ore and accessory minerals, among which the following are distinguished: zircon, fluorite, cryolite, weberite, pachnolite, thorite, cassiterite, molybdenite, columbite, bastnaesite, hematite, magnetite, galena, sphalerite, phenakite, genthelvite, and gahnite (Esipchuk et al. 1993). Geochemical research conducted by Metalidi and Nechaev (1983) showed that the presence of: F, Be, Ta, Nb, REE, Zr, Pb, Zn, Li, Rb, Ce, Ga, Tl and Cd is typical for the Perga type of syenite and apogranite metasomatites (Remezova 2016).

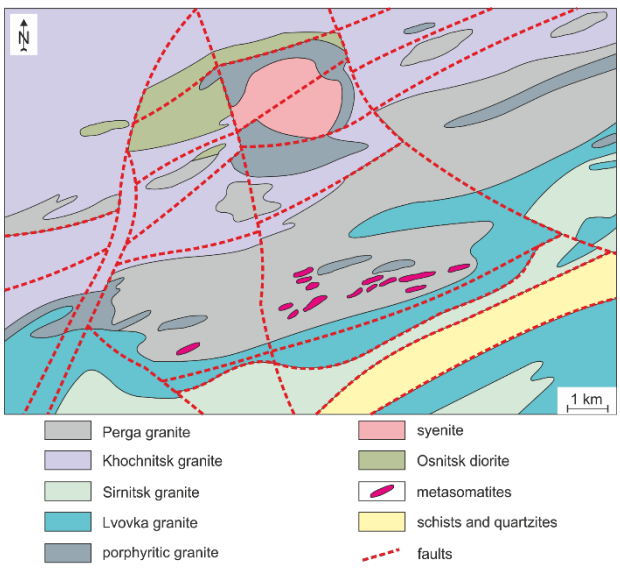

Figure 3. Geological map of the Perga deposit (Metalidi and Nechaev 1983)

Beryllium ores are restricted to mica-quartz-feldspar metasomatites (Figure 4). Within deposit, 8 ore zones up to 3000 metres length and 40 to 80 metres width were identified. In each zones from 1 to 35 ore bodies are distinguished. The distance between ore bodies varies from 5 to 30 metres (Figure 3). The main ore minerals are genthelvite and in restricted areas also phenakite. The genthelvite ore represents 69% of the ore, phenakite ore is just about 2% solely. The four types of genthelvite can be distinguished based on mineral's colour: brown, green, crimson (Figure 5) and light-pink (Figure 6). The genthelvite occurs as crystals and grains ranging in size from 0.01 mm to 5 mm.

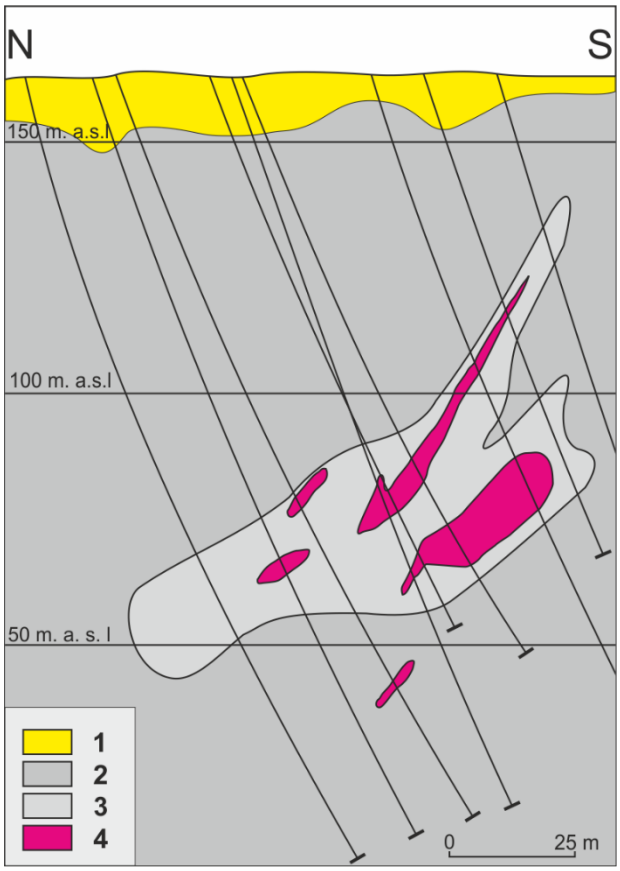

Figure 4. Schematic geological cross section of beryllium ore body. 1 - quaternary sediments, 2 - Perga granite, 3 - ore body, 4 - metasomatites

The first generation of genthelvite occurs in feldspar metasomatites and pure albitites. It is constituted by light yellow or brown crystals and irregular grains ranging in size from 0.1 mm to 1 mm, which have a barely visible zoning (their inner core is lighter than the outer zone). The characteristic elemental impurities include cadmium and titanium.

Figure 5. Crystals of crimson genthelvite in microcline metasomatite, galena crystals are located almost in the centre of the sample. Sample size 15 cm (Phot. by V.V. Levitsky)

Figure 6. Pink variety of genthelvite in quartz-microcline metasomatite

The genthelvite of the second generation occurs in albite-feldspar metasomatites and is represented by tetrahedrons and corroded grains. It is characterized by a pronounced zoning. The core of crystals or grains is light yellow or yellow. The outer zone is brown or light brown. The zones are separated from each other by a white stripe. There is often a multiple alternation of these zones of different colours. The characteristic impurity elements are cadmium, germanium and thorium.

Genthelvite of the third generation is found in feldspar-quartz-mica, feldspar metasomatites and is represented by brown-red and brown grains of irregular shape, as well as fragments of tetrahedron crystals, which have a weakly noticeable zoning.

It should be noted that, according to various studies, eight generations of genthelvite have been identified in the Sushchano-Perga zone (Metalidi and Nechaev 1983).

In the Sushchano-Perga zone, beside Beryllium deposit, 8 placer deposits of Sn-Nb-Ta-Zr were recognized (Galetskiy et al. 2016) and numerous showings were identified.

3 Methods and samples

The samples from the Perga beryllium deposit in Ukraine were collected in 2015-2018, during the annual student's field work organized by the AGH University of Science and Technology. Selection of the ore specimens were done with the help of local geologists. Due to the fact that beryllium cannot be determined using an electron microprobe, its percentage in genthelvite was calculated from the formula proposed by Dunn (1976):

$$(Mn,Fe^{2+},Zn,Ca,Mg):Be= 4/3$$

Reflected and transmitted light microscopy was used to identify and characterize ore and rock forming minerals. Chemical analyses of genthelvite and sulphides were carried out using a JEOL JXA-8230 Super-Probe electron microprobe at the Laboratory of Critical Elements AGH-KGHM in Kraków. The microprobe was operated in the wavelength-dispersion mode at an accelerating voltage of 15kV and probe current of 20 nA. The following standards and spectral lines were used for genthelvite: albite (SiKα, AlKα), rodonite (MnKα), diopside (CaKα, MgKα), sanidine (KKα), willemite (ZnKα), fayalite (FeKα), anhydrite (SKα). Electron microprobe data were corrected using the ZAF procedure and JEOL software.

4 Results

Genthelvite belongs to the helvite group with the general formula Be3M4(SiO4)3S (where M = Fe2+, Zn or Mn), which also includes helvite (Mn member) and danalite (Fe2+ member). Of these, genthelvite is the rarest species. Theoretically, it contains: 54.54% ZnO, 12.58% BeO, 30.19% SiO2 and 5.37% S (Dunn 1976).

Three types of genthelvite were recognized during microscopic and microprobe study. Due to the colour of the crystals, the following types were identified: pink (type 1), green (type 2) and brown (type 3).

In order to determine the chemical composition and the influence of admixtures on genthelvites colour, 75 analyses were performed – 11 for type 1, 28 for type 2 and 36 for type 3 (Table 1, Figure 7 and 8).

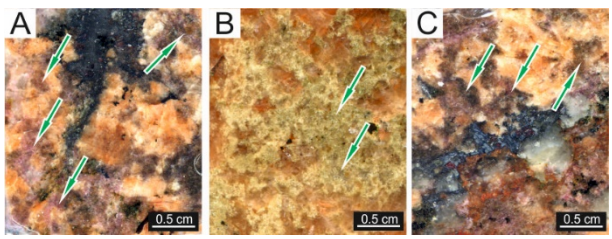

Figure 7. Different types of genthelvite (A - Type 1 – pink, B - Type 2 – green, C - Type 3 - brown).

Table 1. Representative, average composition (in wt. %) of genthelvite from Perga deposit. BeO content was calculated following Dunn (1976).

	T.C.	**Type 1** (n = 11)	**Type 2** (n = 28)	**Type 3** (n = 36)
SiO_2	30.19	31.63	30.94	31.59
MnO	-	1.15	0.62	1.0
ZnO	54.54	42.44	50.56	36.56
FeO	-	8.55	1.37	14.21
S	5.37	5.71	5.66	5.71
BeO	12.58	12.28	12.17	12.37
S=O	2.68	2.85	2.82	2.85
Total	100.00	98.93	98.56	98.61

T.C. – theoretical composition after Dunn (1976)

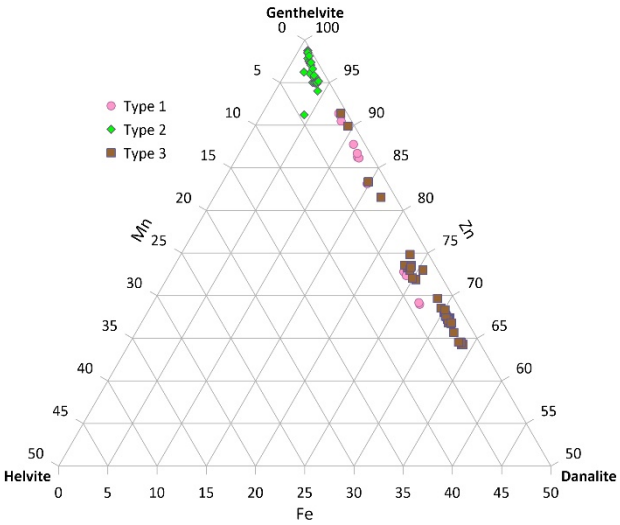

Figure 8. Ternary Fe-Mn-Zn plot of genthelvite from Perga deposit.

5 Conclusion

Quantitative measurements of macroscopically coloured varieties of genthelvite confirmed the differences in their composition.

The pink variety of genthelvite (type 1) comprises 12.28% of BeO, 42.44% of ZnO, 8.55% of FeO and 1.15 % of MnO in average. The type 3 (brown) is characterized by lower content of ZnO (36.56%) and a higher share of BeO (12.37%) and FeO (14.21%). It contains also less ZnO (36.56%) and MnO (1.0%) in comparison with type 1. The average content of the type 2 genthelvite is presented as follows: 12.17% of BeO, 50.56% of ZnO, 1.37% of FeO and 0.62% of MnO.

Of all the varieties studied, ZnO content is sometimes close to the theoretical green variant of genthelvite. The result is aligned with Dunn's (1976) statement that pure genthelvite can vary in colour from colourless to light green. As a result of the performed chemical analyses, it was found that the darker genthelvite, the more Fe and Be as well as less Zn it contains.

Acknowledgements

This work was partially funded by statutory funds of the Faculty of Geology, Geophysics and Environmental Protection, AGH University of Science and Technology, Kraków, Poland (No. 16.16.140.315). We would like to thank geologists B. Wysocki and M. Masko for their help as well as effort with field works and sample collection.

References

Dunn PJ (1976) Genthelvite and the helvine group. Mineralogical Magazine 40:627-636

Dagelaysky VB (1997) Ukrainian Shield. In: Rundqvist DV, Gillen C (rd) Precambrian Ore Deposits of the East European and Siberian Craton. Elsevier Science B.V., Amsterdam, pp 107-153

Esipchuk KYe, Sheremet YeM, Sveshnikov KI (1993) Rare metal granites and related rocks of the Ukrainian Shield. Bulletin of the Geological Society of Finland 65/ II:131-141

Metalidi SV, Slysh RA, Bilchenko PB, Lebed NI, Garkusha AP, Liskevich RM (1977) Perga deposit of beryllium / Report on the results of exploration carried out in 1962-1977 in the Olevsk district of the Zhytomyr region of the Ukrainian SSR. Book 1. Text. Kiev, 519 p

Metalidi SV, Nechaev SV (1983) Sushchano-Perzhanskaia zona (heolohiia, mineralohiia, rudonosnost). Naukova dumka, Kyiv, 136 (in Russian)

Pieczonka J, Piestrzyński A, Paranko I (2016) Geology of the selected mineral deposits of Ukraine. WG AGH Krakow,157p (in Polish)

Galetskiy LS, Khrushchov DP, Remezova OO, Yaremenko OV, Kravchenko OA (2016) Modern interpretation of the Perga cassiterite-columbite placer deposit geological construction. Geological Journal 3:7-20